STUDIES OF THE FIELD-DEPENDENT SURFACE RESISTANCE OF NITROGEN-DOPED NIOBIUM FOR SUPERCONDUCTING ACCELERATORS

A Dissertation

Presented to the Faculty of the Graduate School

of Cornell University

in Partial Fulfillment of the Requirements for the Degree of

Doctor of Philosophy

by

James Thomas Maniscalco

May 2020

STUDIES OF THE FIELD-DEPENDENT SURFACE
RESISTANCE OF NITROGEN-DOPED NIOBIUM
FOR SUPERCONDUCTING ACCELERATORS

James Thomas Maniscalco, Ph.D.
Cornell University 2020

This dissertation presents new research on the field-dependent surface resistance of nitrogen-doped niobium. We prepared a set of single-cell 1.3 GHz niobium accelerator cavities with nitrogen doping and measured the surface resistance of these cavities. We studied the relation between the field-dependent reduction in the surface resistance (the "anti-Q-slope") and the doping level, finding a strong empirical link between high nitrogen content and the suppression of quasiparticle overheating. We prepared another set of cavities with nitrogen infusion and studied their surface resistance, finding similar behavior to that of the nitrogen-doped cavities despite the stark differences in impurity content. We found evidence suggesting that the anti-Q-slope is a *surface* effect, depending on the surface concentration of nitrogen and sensitive to surface contamination. We developed a new thermal modeling framework for studying local models of the surface resistance in superconducting niobium cavities with depth-dependent material parameters. We assessed several recent models of the anti-Q-slope, finding that none provide a fully satisfying explanation of the behaviors observed in experiment. Finally, we developed, constructed, and began commissioning the DC Field Dependence Cavity, a new apparatus for investigating the field-dependent surface resistance of nitrogen-doped niobium and other materials under superposed DC and RF surface magnetic fields.

BIOGRAPHICAL SKETCH

James Thomas Maniscalco was born and raised in Essex County, New Jersey, in the glow of New York City. After years in the excellent West Orange public school system, he attended Regis High School in New York, graduating in 2009. In 2014, he obtained his B.S. in physics at Northeastern University in Boston, where he met his wife Béline. He moved to Cornell University for his graduate studies in accelerator physics and completed his Ph.D. in 2019.

To my wife, Béline — je t'aime.

ACKNOWLEDGEMENTS

"Ph.D.": three small letters that indicate a huge amount of work that was only possible with the enormous amount of support that I was lucky to receive from friends, family, colleagues, and mentors over the last few decades. I can't name everyone who helped me along the way, but I can try.

First and foremost, I want to extend my gratitude to my doctoral advisor Professor Matthias Liepe. From the day I arrived at Cornell as a prospective graduate student, Matthias has made me feel welcome in the SRF Group. Through my time here his guidance, support, and thoughtful conversation have been excellent resources to draw upon, and his commitment to a healthy work/life balance has been instrumental in ensuring that I become the best scientist I can be. I am proud to call Matthias my *doktorvater* as well as my friend.

Next, I want to thank my family, who have supported me in so many ways for so many years. My lovely wife Béline, my partner in the adventure of life, has stood by my side throughout my time in graduate school, brewing the tea and bringing home the bacon. She moved across the world to be with me, and I hope one day to return the favor. My parents Mark and Lisa have taught me to be thoughtful, kind, inquisitive, courageous, and creative, qualities that have helped me to no end as a scientist and as a human. My grandmother Patricia has showered me with unconditional love and has supported my education from the beginning, bringing me to the first day of kindergarten and cheering me on at every graduation since then. And all the rest of the aunts, uncles, cousins, in-laws, all those Maniscalcos, Azierskis, Galantes, O'Briens, Huesslers, Falzons, Dargents, and Preteseilles have shown me that the love and support of a family can make life a wonderful thing.

I have had many mentors throughout my life whose guidance has led me to

where I am today. I especially want to thank my high school physics teacher Frank Barona for introducing me to physics and fostering a creative learning environment in which I was able to make my important early developments as an experimental physicist. I want to thank Professor Indara Suarez, who encouraged me to pursue graduate school and showed me how exciting life as a scientist can be. I also want to thank Professors Emanuela Barberis, Latika Menon, and Darien Wood of Northeastern University and Dennis Wall of Stanford University (formerly of Harvard Medical School) for their kindness and guidance through the early years of my scientific career.

In an experimental laboratory like the Cornell SRF group, nothing gets done without the help of an army of graduate students, post-docs, technicians, and scientists. I want to extend a huge thanks to my fellow SRF graduate students Sam Posen, Dan Gonnella, Daniel Hall, Pete Koufalis, Ryan Porter, Thomas Oseroff, Shura Zeryck, and Neil Stilin, the Newman Laboratory technical and engineering staff including Paul Bishop, Holly Conklin, Terri Gruber-Hine, Adam Holic, John Kaufman, Greg Kulina, Tim O'Connell, Peter Quigley, and James Sears, as well as post-doc Zeming Sun and scientists Fumio Furuta and Mingqi Ge for their companionship and unfailing help in getting all this work done. I also want to thank Eric Smith and Professors Don Hartill and Hasan Padamsee for many interesting conversations and much scientific guidance.

I have been lucky to take part in several collaborative research projects in my time at Cornell. I want to thank Professor Tomás Arias and his students Michelle Kelley and Nathan Sitaraman as well as Professor Jim Sethna and his post-doc Danilo Liarte for the opportunity to work together with brilliant physicists on interesting problems.

Finally, life in graduate school would not have been the same without the

dear friendships that I have made in my time at Cornell. I especially thank Morgan Carter, Alex Mauney, Jocienne Nelson, Alex Plumridge, Peter Rau, and Brian Schaefer for many, many, many memorable coffee hours, board game nights, and cocktail parties through the years.

TABLE OF CONTENTS

LIST OF TABLES

LIST OF FIGURES

LIST OF ABBREVIATIONS

BCP	buffered chemical polishing
BCS	Bardeen-Cooper-Schrieffer (theory, resistance, *etc.*)
BEPC-II	Beijing Electron-Positron Collider II
CBETA	Cornell-Brookhaven ERL Test Accelerator
CEBAF	Continuous Electron Beam Accelerator Facility
CERN	Conseil européen pour la recherche nucléaire (European Organization for Nuclear Research)
CESR	Cornell Electron Storage Ring
CHESS	Cornell High-Energy Synchrotron Source
CW	continuous-wave
DC	direct-current
DI	de-ionized (water)
EBW	electron-beam welding
EP	electropolishing
ERL	Energy Recovery Linac
EXFEL	European X-Ray Free Electron Laser
FCC	Future Circular Collider
FLASH	Free-electron LASer in Hamburg
FM	frequency modulation
FNAL	Fermi National Accelerator Laboratory
FPC	fundamental/forward power coupler
GL	Ginzburg-Landau (theory, coefficient, *etc.*)
HF	hydrofluoric acid
HPR	high-pressure rinsing
HZB	Helmholtz-Zentrum Berlin
ILC	International Linear Collider
J-PARC	Japan Proton Accelerator Research Complex
LCLS	Linac Coherent Light Source
LCLS-II	Linac Coherent Light Source II
linac	linear accelerator
LHC	Large Hadron Collider
OP	oxipolish
PLL	phase-locked loop
PTFE	Polytetrafluoroethylene (trade name: Teflon)
RGA	residual gas analyzer
RHIC	Relativistic Heavy Ion Collider
RF	radio-frequency
RRR	residual resistivity ratio

SIMS	secondary ion mass spectrometry
SRF	superconducting radio-frequency (accelerator physics)
TESLA	TeV Electron Superconducting Linear Accelerator
TRIUMF	Tri-University Meson Facility
UHV	ultra-high vacuum
VCO	voltage-controlled oscillator
VEP	vertical electropolishing

LIST OF SYMBOLS

A	area
$\vec{A}$	magnetic vector potential
$\vec{B}$	magnetic flux density
$\vec{E}$	electric field
$c = 2.99 \times 10^8$ m/s	speed of light in vacuum
$e = -1.6{\times}10^{-19}$ C	electron charge
f	frequency
G	geometry factor of a cavity
$\vec{H}$	magnetic field strength
H_c	thermodynamic critical magnetic field
H_c1	lower critical magnetic field
H_c2	upper critical magnetic field
H_pk	peak surface magnetic field in a cavity
H_sh	superheating field
$i = \sqrt{-1}$	imaginary unit
$\hat{i}, \hat{j}, \hat{k}$	unit vectors in x, y, and z directions
$\vec{J}$	current density
$k_\mathrm{B} = 8.6{\times}10^{-2}$ meV/K	Boltzmann constant
ℓ	electron mean free path
ℓ_ph	phonon mean free path
$m_\mathrm{e} = 9.1{\times}10^{-31}$ kg	electron mass
P	power
P_diss	dissipated power
Q	quality factor
Q_0	intrinsic quality factor
Q_L	loaded quality factor
R_s	surface resistance
R_0	residual surface resistance
R_BCS	BCS surface resistance
$\mathrm{Re}(X)$	real part of (X)
T	temperature
T_c	superconducting critical temperature
U	(stored) energy
v_F	Fermi velocity
β	coupling factor
Δ	superconducting energy gap
κ	Ginzburg-Landau parameter

λ_{GL}	Ginzburg-Landau penetration depth
λ_L	London penetration depth
$\Lambda = c/f$	RF wavelength
$\mu_0 = 4\pi\times10^{-7}$ H/m	vacuum magnetic permeability
ξ	(dirty) coherence length
ξ_0	clean coherence length
σ	conductivity
τ_L	"loaded" decay constant
$\phi_0 = 2.07\times10^{-15}$ Wb	flux quantum
ψ	superconducting order parameter
$\omega = 2\pi f$	angular frequency

CHAPTER 1

INTRODUCTION

The discovery of nitrogen-doped niobium in 2013 has been a boon for superconducting radio-frequency (SRF) particle accelerators. Nitrogen doping can improve the efficiency of a niobium SRF accelerator cavity as measured by its intrinsic quality factor Q_0 by a factor of three, which can greatly reduce the operational costs of SRF accelerator installations. In just a few years, nitrogen doping has seen much attention and success in the SRF community, inspiring much study and making its way into the large-scale Linac Coherent Light Source II (LCLS-II) project.

One notable feature of this increase in Q_0 is its dependence on the strength of the surface magnetic field in the SRF cavity. At low RF field levels, Q_0 in nitrogen-doped niobium cavities is about equal to that in other niobium cavities with similar electron mean free path ℓ. As the field strength increases, the efficiency also increases, peaking at a surface magnetic field in the range of 70-130 mT. This increase comes as a result of a field-dependent *decrease* in the microwave surface resistance, inversely proportional to Q_0.

As the field of SRF pushes towards ever higher efficiency, understanding this field-dependent surface resistance is of paramount import. In this dissertation, I will describe several studies performed at Cornell aimed at exploring this effect in niobium cavities prepared with nitrogen doping and related treatments.

1.1 Organization of this Dissertation

This dissertation can be separated roughly into three parts, bookended by this introductory chapter and a conclusion.

In the first part, I will present some foundational information. Chapter 2 motivates SRF particle accelerator technology with some historical context. Chapter 3 describes the essentials of SRF science, covering the relevant physics of superconductors and their surface resistance and the methods of building and testing SRF cavities. Chapter 4 introduces the methods, benefits, and downsides of nitrogen doping and the related nitrogen infusion.

In the second part, I will discuss several studies of the physics of the field-dependent surface resistance in nitrogen doped and infused cavities. Chapter 5 covers a study of strongly nitrogen-doped cavities, linking the magnitude of the reduction in surface resistance to the doping level by way of quasiparticle overheating. Chapter 6 discusses a study of nitrogen-infused cavities, comparing their performance to that of nitrogen-doped cavities and studying the dependence of that performance on the chemical content of the RF surface. Chapter 7 details a new thermal modeling system for predicting the behavior of nitrogen-doped and nitrogen-infused cavities. Chapter 8 assesses several proposed theories of the field-dependent surface resistance in nitrogen-doped cavities, comparing their predictions to experimental results.

Chapter 9 stands alone as the third part of this dissertation, presenting a new experimental apparatus designed and built at Cornell for studying the field-dependent surface resistance of nitrogen-doped niobium and other SRF materials. The DC Field Dependence Cavity focuses on another side of the coin than

previous studies in SRF cavities by measuring the dependence of the surface resistance on externally-applied DC magnetic fields parallel to the RF surface. This tool will provide a new window for the study of these materials, deepening our understanding of the physics at work and driving the field towards even higher efficiency.

Chapter 10, finally, offers some summarizing and concluding thoughts on the research presented in this dissertation, discussing its implications and proposing further research.

CHAPTER 2

WHY SRF?

Superconducting radio-frequency accelerator physics, or SRF for short, is a field that sits at the intersection of several main avenues of modern physics. Chiefly it uses the discoveries and breakthroughs in the study of superconductors, which are special materials whose electrical resistance drops to zero[1] below a certain "critical temperature", to create better particle accelerators. These superconducting accelerators are used for many purposes, though the most popular applications are as X-ray light sources (such as CESR/CHESS at Cornell) and as colliders for particle physics (such as the LHC at CERN on the Swiss/French border) and nuclear physics (such as CEBAF at the Thomas Jefferson National Accelerator Facility). In turn, the drive for advances in SRF from accelerator users, SRF physicists, and funding agencies pushes forward our understanding of "superconductors under extreme conditions"[2].

In this chapter my aim is to give a pedagogical/historical introduction and motivation to SRF accelerator physics: why build particle accelerators in the first place? why operate them at radio frequencies? and why make them out of superconductors? After considering these questions I will give an overview of the experimental and analytical methods we use in the Cornell SRF group to investigate the fundamental physics of superconducting accelerators and the materials that we use to make them.

[1] Here I refer to the resistance to DC/low-frequency currents; in the microwave regime, the resistance is non-zero but small compared to the normal-conducting case. More on this later.

[2] A favorite saying of mine from Prof. J. P. Sethna.

2.1 Why Accelerators?

Though accelerator physics is, like so many other fields of study, built upon the work of centuries of scientists, we can begin this account of the history of particle accelerators with the discovery of "cathode rays" by J. W. Hittorf in 1869 [Dah97, p. 55]. Throughout the mid-1800's, scientists including M. Faraday and J. Plücker were performing experiments with high-voltage electrodes in low-pressure gas environments, investigating glow discharge and other effects. Hittorf was experimenting with point-like cathodes, whose glow is in the shape of a cone with its tip at the cathode and its base on the opposing fluorescent glass wall, when he saw that an object placed between the cathode and the glass wall casts a shadow on the wall. Figure 2.1 shows a replica device illustrating Hittorf's experiment. By this observation he made the remarkable discovery that the glow was not only produced by the cathode but also *emitted* by the cathode in straight lines. In 1876, E. Goldstein named these "cathode rays" (*Kathodenstrahlen*) [Gol76], a name which has stuck since then. Though the phrase had not yet been coined, Hittorf's experiment was one of the first particle accelerators.

In the following years, many other scientists continued to investigate these effects in vacuum tubes, which led to a number of notable and influential discoveries. In 1895 W. Röntgen discovered that cathode ray tubes also produced a new kind of penetrating radiation which he dubbed the "X-ray"; he was later awarded the very first Nobel Prize for Physics in 1901 for this discovery [Odh01]. In 1897-98, J. J. Thomson demonstrated that cathode rays were made up of traveling sub-atomic particles, which we now know as electrons, and measured their charge-to-mass ratio; for these findings, he was awarded the Nobel

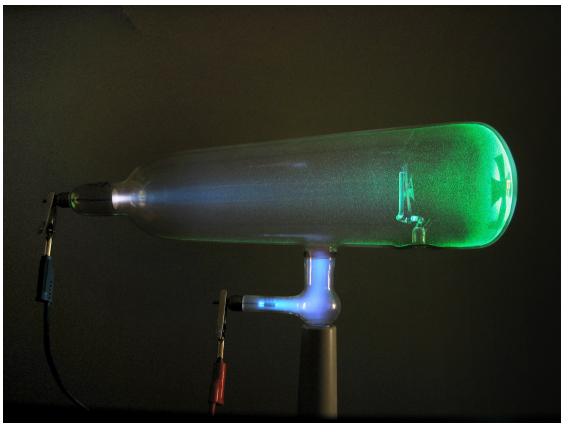

Figure 2.1: Photo of a Crookes tube in operation, equipped with a standing cross to replicate the experiment of J. W. Hittorf. Photo attribution: D-Kuru/Wikimedia Commons, licensed under CC BY-SA 3.0 AT.

Prize for Physics[3] in 1906 [Kla06].

Aside from the cathode ray tube ubiquitous in consumer electronics from the 20th century, these two discoveries laid the foundation for a large part of modern accelerator physics, and for one of the popular accelerator applications listed above: X-ray light sources. When charged particles such as electrons are accelerated, whether it be the deflection of collision with a screen, a curving of the trajectory by an electric or magnetic field, or otherwise, they emit electromagnetic radiation known today as *bremsstrahlung* ("braking-radiation") [Jac99]. Most modern medical and security (*e.g.* luggage scanning) X-ray sources are advanced versions of Röntgen's original apparatus, called "X-ray tubes": vacuum tubes in which electrons are emitted by a cathode and are accelerated towards a positively-charged anode with which they collide. In the collision the electrons interact with the strong electric fields near the nuclei of atoms in the anode, are deflected, and release *bremsstrahlung* X-rays. In addition, the collision temporarily excites some of the native electrons in the anode to higher energy levels, and

[3] In an interesting and comedic moment in 20th-century physics, while J. J. Thomson was awarded the Nobel Prize for discovering that the electron is a particle, his son George won the Prize himself in 1937 for discovering that it is also a wave [Ple37].

their relaxation emits characteristic X-rays as well [SZY84].

Many large-scale accelerators serve as X-ray light sources, producing a specific type of *bremsstrahlung* called "synchrotron radiation"[4]. This type of radiation was first discovered by a number of researchers in the 1940's, notably those at General Electric in 1947, who observed that a beam of electrons traveling at relativistic speed (*i.e.* at an appreciable fraction of the speed of light) being deflected by a transverse magnetic field emit a beam of X-rays in the original direction of motion of the electrons [Wie15, EGLP47]. These X-rays are highly collimated and distributed over a broad, continuous spectrum. Such X-rays are held in high demand by accelerator users performing a wide range of experiments, including X-ray diffraction, X-ray crystallography, small-angle X-ray spectroscopy, and many other imaging, diffraction, and spectroscopic techniques.

Around the world, dozens of synchrotron radiation sources exist as active user facilities (not all of which are actually synchrotrons). These include purpose-built machines such the Linac Coherent Light Source (LCLS), parasitic machines such as the Beijing Electron-Positron Collider II (BEPC II), and converted colliders such as the Cornell High-Energy Synchrotron Source (CHESS)[5]. These machines use devices known as "undulators" and "wigglers" which use a series of magnets oriented with fields transverse to the direction of the beam and with alternating orientation to "wiggle" the beam side to side, thereby releasing highly collimated synchrotron radiation with an intensity much greater than that released in a bend (as in the experiments at General Electric) [Wie15].

[4]We will discuss synchrotrons in the next section.

[5]CHESS was originally a parasitic light source using electrons and positrons intended for the particle physics experiments at the Cornell Electron Storage Ring (CESR). Collision physics at CESR ceased in 2008, but the facility still circulates positrons for CHESS as of 2019.

Moreover, by adjusting the strength of the undulator/wiggler magnets, one can adjust the spectrum of the resulting X-ray radiation to meet user demands in a way that is not possible for bending magnets, whose field strength is fixed by the geometry of the accelerator and energy of the beam.

Returning to history: contemporaneously with the cathode ray experiments, other scientists were laying the foundations for one of the other pillars of modern physics, the study of the atomic nucleus and of radioactivity. In 1896, while investigating phosphorescence, H. Becquerel discovered that uranium emitted a form of penetrating radiation similar to Röntgen's X-rays; in 1898, Marie Skłodowska Curie found that the new "radioactivity" was an atomic process, and with her husband Pierre Curie discovered two new radioactive elements which they named "polonium" and "radium" [SZY84]. For their work Becquerel and the Curies were awarded the Nobel Prize for Physics in 1903 [Tör03].

Beginning in 1909 and continuing with improvements through 1913, E. Rutherford and colleagues H. Geiger and E. Marsden performed the "gold foil experiment", one of the first particle collision experiments: a source of α-particles (one of the three types of radioactive radiation identified by Rutherford) is enclosed except for a small slit, which produces a beam of α-particles. In the path of this beam is placed a sheet of gold foil. Around the gold foil a fluorescent screen illustrates the flux of α-particles which pass through the foil and others which are deflected by the sheet [Gei10]. Figure 2.2 illustrates the apparatus. The α-particles were mostly scattered in a small cone behind the screen, with a small number being deflected to wider angles; by this result, Rutherford *et al.* concluded that atoms were composed of a small, positively charged

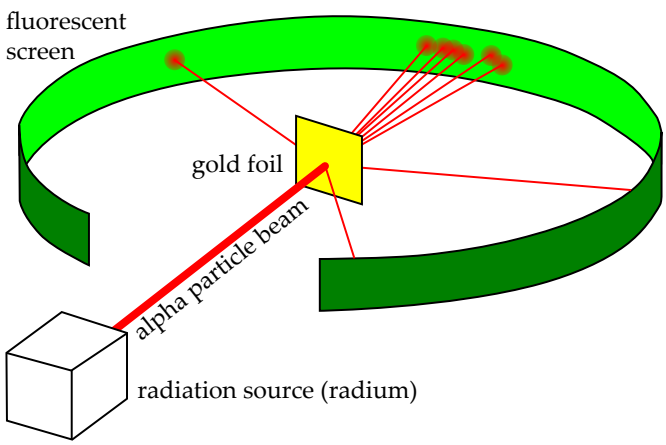

Figure 2.2: Illustration of Rutherford, Geiger, and Marsden's gold foil experiment. Image attribution: Kurzon/Wikimedia Commons, licensed under CC BY-SA 3.0. Alterations: changed typeface of image labels.

nucleus surrounded by electrons. This was in opposition to the earlier "plum pudding" model of the atom, which featured a diffuse positively charged cloud studded with electrons: the deflection seen in the experiment was an interaction between the incoming α-particles and the atomic nuclei.

Thus began the long legacy of another main application of particle accelerators, as particle colliders. In the 1920's advances in high-voltage power supplies by R. Van de Graaff, J. Cockroft, and E. Walton, among others, allowed for the acceleration of α-particle, proton, and ion beams towards fixed targets, much like the gold foil experiment. These early accelerators served as tools to investigate the physics of atoms and subatomic particles; accelerator users today continue in these same and related pursuits. Fixed-target facilities such as the Continuous Electron Beam Accelerator Facility (CEBAF), the TRIUMF Cyclotron, and the Hadron Facility (HD) of the Japan Proton Accelerator Research Complex (J-PARC) are used (among other things) to study subatomic physics and to create rare atomic isotopes often useful for medical applications. Perhaps more famously, there also exist many beam-beam collider facilities, such as the

Large Hadron Collider (LHC), the Relativistic Heavy Ion Collider (RHIC), and the Beijing Electron-Positron Collider II (BEPC II), which provide users with high-energy collisions between beams of electrons, positrons, protons, gold and lead ions, and other particles for probing the boundaries of our understanding of particle physics.

A further common application of particle accelerator technology is the electron microscope, a device that takes on elements of the X-ray sources and colliders previously discussed. In these machines, found at universities and research facilities around the globe, electrons are accelerated in a narrow beam towards a sample [LCS12]. The interaction between the incident electrons and the sample produces many signals which can be analyzed by the user, including *bremsstrahlung* X-rays and characteristic X-rays (as in Röntgen's X-ray tube and similar modern devices) as well as transmitted electrons and back-scattered electrons (like the transmitted and scattered α-particles in the gold foil experiment). These signals carry a great deal of information about the surface under electron illumination.

Yet another particle accelerator application is in making macroscopic changes to materials, in both electron beam lithography and electron beam welding. In the former case, a beam of electrons is accelerated towards a substrate in order to etch high-resolution structures, often used in the manufacturing process of semiconductor devices [RC97]. In the latter, an electron beam is used to join metal pieces, much like traditional welding [WBP16]. Amusingly, at Cornell we use such an accelerator (an electron beam welder) to fabricate our accelerator cavities – we use accelerators to make accelerators!

One final application of particle accelerators I will discuss here is the

klystron, a radio-frequency amplifier featuring an electron beam [Vel87]. The beam passes through a "buncher" cavity[6] which separates the steady beam of electrons into a train of bunches. These bunches continue to compress as they travel through a "drift" section, after which they reach a "catcher" cavity. Here the compressed electron bunches excite a strong electromagnetic field, and a field pickup couples this amplified signal outward so that the user may direct it towards their desired application. Klystrons are often used to power radar devices as well as radio-frequency particle accelerators.

2.2 Why Radio-Frequency?

I hope that in the previous section I have sufficiently motivated the broad range of applications for particle accelerators and the historical context upon which much of the field draws. In this section, I will give some more context for early accelerators and why the switch was made quite early on from electrostatic machines to the radio-frequency accelerators much more commonly seen today.

As mentioned above, great progress was made in the 1920's towards building high voltage power supplies. J. Cockroft and E. Walton constructed a voltage multiplier that, at a potential ranging up to 700 kV in 1932, enabled the pair to accelerate protons into a lithium target and "split the atom" (*i.e.* cause artificial radioactive decay) for the first time [CW32]. They repeated this process with many other elements, successfully "transmuting" them into lighter elements and radioactive decay products. For this and related work, Cockroft and Walton were awarded the 1951 Nobel Prize in Physics [Wal51]. R. Van de Graaff

[6] In the next section we will discuss radio-frequency accelerator components, such as accelerating cavities, in detail.

developed his famous generator at a similar time, and in 1931 succeeded in exciting a 1.5 MV potential intended for use in nuclear physics applications; he eventually achieved an accelerating potential of 5.1 MV with the Round Hill Electrostatic Generator [Ano31, ANAG36]. In more recent memory, tandem van de Graaff generators such as those at Oak Ridge National Laboratory and at Brookhaven National Laboratory have reached accelerating voltages of nearly 25 MV [JAB+88].

Unfortunately, high-voltage breakdown limits the maximum voltage achievable in an electrostatic accelerator such as a van de Graaff or Cockroft-Walton device [Wie15]. How might a higher accelerating voltage be reached? One tempting idea would be to line up several of these devices and accelerate a beam through one after the other; unfortunately, particles would be decelerated in the space between subsequent electrostatic accelerators due to the conservative nature of the electromagnetic force, and the total voltage gained over the chained device would be no better than the potential difference between the start and end of the machine. Likewise, circulating the beam multiple times through the same electrostatic accelerator would only give as much acceleration as a single pass, since all energy gained by the beam traveling through the machine is lost in bringing it back to the beginning. If, however, one were able to accelerate the beam through one electrostatic potential, then switch off or reverse the polarity of the system while the beam passes from one device to the next (in either the drift regions between chained accelerators or the return loop in a circulating machine), and finally restore the original accelerating voltage in time for the beam to be accelerated again, it would be possible to surpass the high-voltage-breakdown limit by quite a lot. Indeed, this principle of operation was realized in the 1920's and 1930's in both the linear "chained" case (by the drift-tube linear

accelerator) and the circulating case (by the cyclotron) [Wid28, LL32]. Because of the high speed of these accelerated particles, it is necessary to cycle the polarity of the accelerating gaps at radio frequencies, often in the range of several MHz up to several GHz.

The drift-tube linac, a type of accelerator first successfully built by R. Widerøe in 1928, consists of a long string of hollow tubes aligned axially and separated by gaps [Wie15]. These tubes are wired to a radio-frequency (RF) power source, with adjacent tubes wired in opposite polarity. A beam of charged particles passes along the axes of the tubes, inside which the electromagnetic field is zero. In the gaps between the tubes, the particles are exposed to the electric field between the tubes with opposite charge. The linac is carefully timed so that the particles arrive at a gap when the potential difference across the gap is at its greatest magnitude; as the particles pass through the following tube, the polarity of the RF source reverses, and as the particles arrive at the following gap they are accelerated further. This repeats through the full length of the accelerator.

The accelerating structures in modern linear accelerators and synchrotrons (more or less a linac with a return loop) are direct extensions of this principle of operation, with the gaps replaced by "accelerating cavities"[7]. Figure 2.3 shows several examples of accelerating cavities. In these hollow metal structures, an RF field is excited at a resonant frequency of the cavity; the beam is separated into bunches of particles (much like the klystron, another kind of linear accelerator discussed previously), and the bunches are timed so that they enter and exit the cavity when the field is at an optimal phase. By operating on resonance, it is possible to excite a very strong electromagnetic field while

[7]We will discuss modern accelerating cavities in further detail later in this chapter.

(a) 9-cell 3 GHz cavity (niobium).

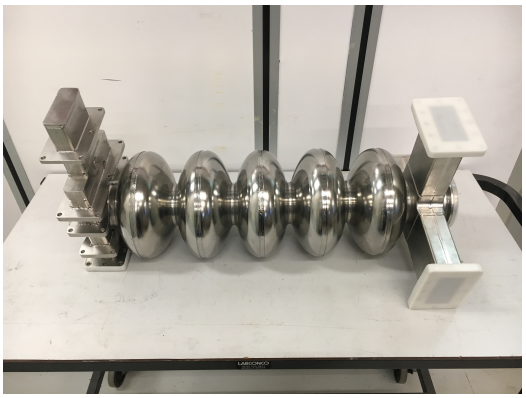

(b) 5-cell 1.5 GHz CEBAF cavity (niobium).

Figure 2.3: Example accelerating cavities.

only supplying a relatively small amount of power per cycle of oscillation. To date, researchers have achieved accelerating gradients of 250 MV/m in pulsed cryogenic copper cavities and 52 MV/m in continuous-wave superconducting cavities [CRD+18, Gen05].

Returning to history: due to the unavailability of high-voltage RF power supplies before the invention of the klystron in 1937, drift-tube linacs were rather limited in their achievable beam energy [Wie15]. More successful in achieving high acceleration were circulating machines, such as the cyclotron, in which the same particles are accelerated many hundreds of times and thus reach quite considerable beam energies.

The cyclotron, developed by E. O. Lawrence and associates (especially M. S. Livingston) beginning in 1929, is a circular device consisting of a wide, flat, cylindrical vacuum chamber placed between two magnet poles such that the magnetic field points axially through the chamber [LL32]. Inside the chamber are two half-cylindrical "dees", so named for their resemblance to the capital letter; between the flats of the two dees is a small gap. An RF power source is applied across the two dees, and the resulting electric field in the gap acceler-

ates particles there towards one of the dees. Inside the dees, much like the tubes of the drift-tube linac, the electric field is zero; in the cyclotron, however, the perpendicular magnetic field curves the particles in a circular trajectory. The frequency of the power source is chosen so that, just as the particles approach the gap after being curved around by the magnetic field, the polarity of the electric field is reversed, accelerating the particles into the opposite dee. The process repeats, with the radius of the beam's trajectory steadily increasing; for sufficiently slow (*i.e.* non-relativistic) particles, the "cyclotron frequency" is independent of the velocity of the particles or the radius of curvature of the trajectory. When the beam reaches the edge of the chamber, it is directed outwards for use. Starting with a 10-inch-diameter cyclotron which produced a proton beam greater than 1 MeV in energy, Lawrence and Livingston (first together and later independently) built a succession of larger and larger machines, culminating in Lawrence's 184-inch "synchrocylcotron" which could reach proton energies of more than 700 MeV [Liv75]. In 1939 Lawrence was awarded the Nobel Prize in Physics for his invention of the cyclotron, which had a great impact on the world of nuclear physics and lead to the discovery of many new elements and isotopes [Sie39].

The beam energy from a cyclotron is limited by the laws of special relativity, as alluded to above. As the particles are accelerated to an appreciable fraction of the speed of light, their momentum becomes relativistic, and the particles lose synchronization with the cyclotron's power source. To reach higher beam energies in a circulating machine, it is necessary to use a "synchrotron" [Wie15]. In this type of particle accelerator, the beam is accelerated by a (usually small) number of cavities and is returned to the start of the acceleration section by a long chain of "bending magnets" and other magnetic devices. Like the mag-

netic field in a cyclotron, these magnets curve the trajectory of the beam. However, in the case of the synchrotron, instead of the magnet running at a fixed field strength, the magnetic field magnitude is raised synchronously (hence the name) with the increasing momentum of the beam, ensuring that the trajectory of the beam stays unchanged. The maximum achievable beam energy in a synchrotron is limited by two balanced relationships: first, the radius of curvature (larger machines can reach higher energies) balances against the strength of the bending magnets (stronger bending allows for a smaller radius at the same beam energy); second, energy lost due to synchrotron radiation balances against the available acceleration. For a given beam energy, synchrotron radiation scales inversely with the rest mass of the particles being accelerated, and as a result electron and positron synchrotrons are typically limited by synchrotron radiation losses; on the other hand, hadron synchrotrons (which typically accelerate protons, anti-protons, and ions) are limited by the bending magnet / radius of curvature relation.

Historically, the concept of the synchrotron was developed in the 1940's by several independent researchers [Wil96]. The first successful synchrotron acceleration was achieved in 1946 with an 8 MeV electron beam; later in that same year, researchers at General Electric reached a 70 MeV beam energy. In the years since, many laboratories around the world have built synchrotrons, and the peak beam energy has steadily climbed. As of 2019, the largest particle accelerator in the world, the Large Hadron Collider (LHC), circulates counter-rotating beams of protons at beam energies up to 6.5 TeV per beam [O'L15].

2.3 Why Superconducting?

Scientific curiosity and demand from accelerator users continue to drive the pursuit of higher beam energies, both at the energy frontier and in more economical applications for everyday users and small installations. Further, many accelerator users today demand high-repetition-rate/high-duty-cycle and continuous-wave (CW) beams, preferable over pulsed beams with low repetition rates and low duty cycles for applications such as light sources and colliders. High beam energies mean lots of particle acceleration, in linacs (which only have one pass to fully accelerate the beam) as well as in storage rings and synchrotrons (which need to constantly re-accelerate the beam to make up for energy lost due to synchrotron radiation). Unfortunately, the power dissipated in the walls of an accelerator cavity while sustaining the electromagnetic field inside scales quadratically with the magnitude of the accelerating field [PHK98]. Though traditional accelerator cavity materials like copper can achieve quite high accelerating gradients (up to 250 MV/m so far) in low-duty pulses, for high-duty and CW applications such a gradient would require megawatts of continuous RF power per meter of copper cavity, not including the power actually transferred to the beam [CRD+18]. Not only would this be economically unfeasible, it would also melt the copper.

Fortunately, another scientific discovery from the turn of the 20th century offers a solution: superconductivity. After succeeding in liquefying helium in 1908, H. Kamerlingh Onnes discovered in 1911 that mercury, when cooled to a temperature of 3 K, exhibits zero electrical resistance [Nis11]. Shortly thereafter, Kamerlingh Onnes found that tin and lead exhibited this same property, which he named "superconductivity". In 1913, Kamerlingh Onnes was awarded the

Nobel Prize in Physics for his groundbreaking work in low-temperature physics [Nor13]. Since then, thousands more materials have been shown to exhibit superconductivity at sufficiently low temperatures.

Below a certain "critical temperature" T_c, the DC resistance of superconductors drops abruptly to zero, and the resistance to RF currents drops significantly as well. For example, at 2 K and 1.3 GHz, high-quality copper (a normal metal) exhibits a microwave surface resistance near 2 mΩ; under the same conditions, high-quality niobium (the standard superconductor for accelerator applications) shows a surface resistance closer to 15 nΩ, and even lower resistances at lower temperatures. This extremely low resistance means that superconducting accelerator cavities are very efficient: a typical modern niobium cavity operating at 2 K, 1.3 GHz, and 20 MV/m dissipates only about 20 W/m of RF power due to the surface resistance of the walls[8]. This efficiency makes SRF technology desirable for cutting-edge "big science" accelerators like the planned Future Circular Collider (FCC) and the under-construction Linac Coherent Light Source II (LCLS-II) as well as for more modest applications on the university or industrial scale; for example, one proposed SRF accelerator would produce a 10 MeV CW electron beam over a distance of less than 2 m [KBC+15].

Much of contemporary research in SRF is aimed at improving peak accelerating fields sustainable in cavities and at decreasing the surface resistance of SRF materials. Far from van de Graaff's 1.5 MV generator constructed for "about $100" [GCA33], the price tags for the biggest accelerators currently planned have boomed towards $10 billion or more, with electrical power requirements in the 100's of MW [Ban19, ABB+16]. Improving the peak achievable fields and

[8]Keeping the cavities cool while this power is being dissipated requires a good deal more refrigerator power, but superconducting RF cavities are still quite attractive in the balance for high-gradient and high-duty/CW operations.

surface resistance in SRF cavities will help to drive construction and operating costs downwards and make even higher beam energies possible. In the Cornell SRF group, our focus is on understanding the fundamental science of superconductors in the context of very strong electromagnetic fields; to return to a phrase, we study "superconductors under extreme conditions". In the following chapter, I will introduce the experimental and analytical methods used at Cornell as well as the theoretical background for the research presented in this dissertation; in later chapters, I will refer back to this explanatory section as I discuss my research.

CHAPTER 3

SRF THEORY AND EXPERIMENT

Here I would like to explore the current theoretical understanding of superconductivity by addressing the classic experimental observations of superconductors and the theoretical work developed to help explain these phenomena. Following this, I will motivate and develop the technique of SRF cavity testing for fundamental superconductor research and accelerator applications as performed at Cornell. For more extensive treatment of these subjects, the interested reader will find a detailed overview of superconducting theory M. Tinkham's book; in addition, H. Padamsee's text is quite thorough in applying these concepts to superconducting accelerators [Tin04, PHK98].

3.1 Basics of Superconductivity for Accelerators

On the whole, superconductors are a fascinating class of materials. Chief among the intriguing observations of superconductors is the "Meissner effect" [MO33], in which ambient magnetic fields are expelled from the bulk of the superconductor as it transitions below its critical temperature T_c. Moreover, the superconductor will repel any magnetic fields up to a limiting "critical field" applied after transition (exhibiting perfect diamagnetism). Above the critical field, the superconducting state breaks down and the material returns to the normal state.

When defects are present in the material, such as normal-conducting or insulating inclusions or regions with suppressed superconducting parameters, magnetic flux in the material above transition can be pushed into these regions instead of being expelled as the material goes through transition. This magnetic

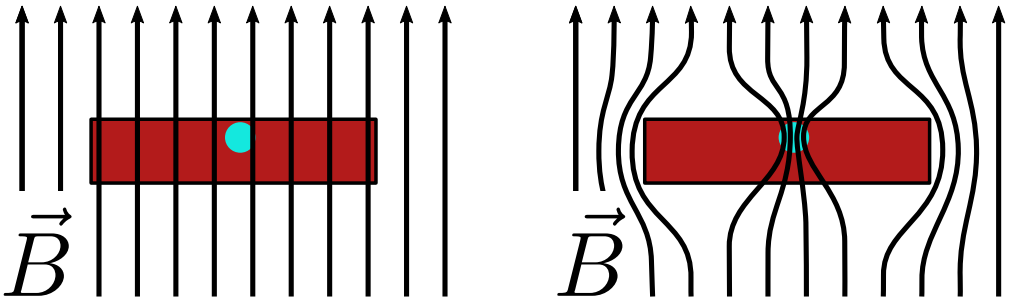

(a) $T > T_c$ (b) $T < T_c$

Figure 3.1: Below its critical temperature T_c, a superconductor (in red) will expel magnetic flux (black arrows). During the transition from normal-conducting to superconducting, flux but can become trapped at sites that exhibit weaker superconductivity or are normal-conducting or insulating (teal circle).

flux becomes trapped in the material; this is often called "flux pinning" or "flux trapping". Figure 3.1 illustrates this effect. Trapped flux will become an important topic later in this dissertation.

As in the case of complete flux expulsion, changes to the externally-applied or ambient magnetic field will not change the flux distribution inside the superconductor. A practical example of this phenomenon can be seen in superconducting magnetic levitation: flux is pinned in the superconductor, which resists changes to the pinned field with a strength greater than that of gravity and other ambient forces.

The other chief observation of the behavior of superconductors is their infinite conductance to steady currents (see Sec. 2.3). Below their critical temperatures, superconductors exhibit zero electrical resistance to constant voltages, and any induced currents (*e.g.* from externally applied magnetic fields) will persist indefinitely.

These two properties – perfect diamagnetism and perfect DC conductivity –

are in fact deeply linked in the physics of superconductivity. In 1935 the London brothers developed a model to explain these phenomena [LL35]. In their model, current in a superconductor is carried by a certain density of electrons that flow freely (*i.e.* without the scattering that gives rise to resistivity in the Drude model), and the electric and magnetic fields in the superconductor are governed by the following equations:

$$\vec{E} = \frac{\partial}{\partial t}\left(\frac{m_\mathrm{e}}{n_\mathrm{s}e^2}\vec{J}_\mathrm{s}\right) \tag{3.1}$$

$$\vec{B} = -\frac{m_\mathrm{e}}{n_\mathrm{s}e^2}\nabla \times \vec{J}_\mathrm{s} \tag{3.2}$$

Here $\vec{E}$, $\vec{B}$ are the local electric and magnetic fields and $\vec{J}_\mathrm{s}$ is the local current density carried by the "superconducting" electrons, known also as "supercurrent". The terms m_e and e refer to the electron mass and charge, respectively, and n_s is the number density of the superconducting electrons. Equations 3.1 and 3.2 are nowadays commonly referred to as the "London equations". They can also be combined into a single expression using the magnetic vector potential $\vec{A}$:

$$\vec{J}_\mathrm{s} = -\frac{n_\mathrm{s}e^2}{m_\mathrm{e}}\vec{A} \tag{3.3}$$

By applying Ampère's law $\nabla \times \vec{B} = \mu_0\vec{J}$ to Eq. 3.2, one finds the following:

$$\vec{B} = \frac{m_\mathrm{e}}{\mu_0 n_\mathrm{s}e^2}\nabla^2\vec{B} \tag{3.4}$$

$$= \lambda_\mathrm{L}^2\nabla^2\vec{B} \tag{3.5}$$

Solving this differential equation for an infinite superconductor-vacuum interface yields a magnetic field that decays exponentially into the superconductor:

$$\vec{B}(x) = B_0 \exp\left(-\frac{x}{\lambda_\mathrm{L}}\right)\hat{j} \tag{3.6}$$

In the expression above, $\vec{B}$ runs parallel to the surface and B_0 is the magnitude of $\vec{B}$ at the surface. The parameter $\lambda_\mathrm{L} = \sqrt{m_\mathrm{e}/\mu_0 n_\mathrm{s}e^2}$ is the exponential decay

length of the field and is known as the "London penetration depth". Physically, this exponentially decaying magnetic field can be explained by "screening currents" (given by $\vec{J}_s$) which are excited on near the surface and flow with zero resistance, generating their own magnetic fields that perfectly cancel out the applied field far from the surface[1]. Empirically, λ_L varies strongly with temperature T near T_c [Tin04]:

$$\frac{\lambda_L(T)}{\lambda_L(0)} \approx \left(1 - \left(\frac{T}{T_c}\right)^4\right)^{-1/2} \tag{3.7}$$

The London model as described is a "local" model: as is apparent from Eq. 3.3, the current density and electromagnetic field strength depend only on the local value of $\vec{A}$. Due to the Heisenberg uncertainty principle, this must be nonphysical to some degree. In 1953 A. B. Pippard developed a nonlocal modification to the London model to account for this, based on a similar modification to Ohm's law that had been performed in 1952 [Pip53]. Pippard's modification introduces a characteristic length scale for the electromagnetic interaction in a superconductor, known as the "coherence length" ξ, and replaces Eq. 3.3 with the following (with the substitution for λ_L as described above):

$$\vec{J}_s = -\frac{3}{4\pi\mu_0\lambda_L^2\xi_0}\int \frac{\vec{r}(\vec{r}\cdot\vec{A})}{r^4}\exp\left(-\frac{r}{\xi}\right)d^3\vec{r} \tag{3.8}$$

In addition to the "clean" coherence length ξ_0, here there is a second "dirty" coherence length ξ (with no subscript) that takes into account electron scattering in the material, quantified by the "electron mean free path" ℓ:

$$\xi = \left(\frac{1}{\xi_0} + \frac{1}{\ell}\right)^{-1} \tag{3.9}$$

This is also referred to as the "Pippard coherence length". The penetration depth

[1]Roughly, one might imagine applying Lenz's law to a box surrounded by superconducting wire loops; a field that turns on near the box induces currents in the loops which never decay, and the field inside the box remains 0.

of the RF field is also affected by electron scattering:

$$\lambda = \lambda_{\mathrm{L}} \left(1 + \frac{\xi_0}{\ell}\right)^{1/2} \tag{3.10}$$

The electron mean free path ℓ represents the average distance traveled by an electron moving through the material at the Fermi velocity v_{F} between subsequent scattering events. It is dependent on a number of material properties such as the crystal grain size and, importantly for discussion later in this dissertation, on the interstitial impurity content of the crystal. Impurities increase the rate of scattering and thus decrease ℓ and ξ and increase λ; in the "clean" limit, $\ell \gg \xi_0$, so $\xi \to \xi_0$ and $\lambda \to \lambda_{\mathrm{L}}$. Throughout this dissertation, I will refer very often to ℓ simply as "the mean free path"; when discussing other mean free paths I will distinguish them with subscripts and textual modifiers (*e.g.* the phonon mean free path ℓ_{ph}).

Though the London model describes some of the major behaviors of superconductors, it does not provide a microscopic understanding of the physics at work. In a series of papers in the 1950's, J. Bardeen, L. Cooper, and J. Schrieffer developed a microscopic model of superconductivity, now known as the "BCS theory" after the initials of its authors [Bar55, Coo56, BCS57a, BCS57b]. The trio received the Nobel Prize in Physics in 1972 for their work describing superconductivity [Lun72].

In the quasi-classical picture of the BCS theory, electrons moving through a crystal deform the crystal slightly by attracting the lattice atoms via the Coulomb force. The deformed region, now with a higher density of positively-charged atomic nuclei than the rest of the crystal, attracts electrons as well. The net interaction results in an attractive potential between electrons. The resulting attractive force is small, but below a certain critical temperature, thermo-

dynamic excitations are weak enough that the electrons reach an equilibrium density of "Cooper pairs" which are able to travel through the crystal with no impedance. Since they are charged ($q = 2e$) they can carry current with zero resistance. The length scale of this electron-electron interaction is the Pippard coherence length ξ.

In the quantum-mechanical picture of the BCS theory, the attractive potential between electrons is mediated by phonons, particles that represent vibrations in the crystal lattice (analogous to the photons that mediate the electromagnetic force). The paired electrons (which together behave as a single boson) occupy the ground state in a second-quantization formalism, and excitations known as "quasiparticles" exist above an energy gap Δ. These quasiparticles represent unpaired electrons in the quasi-classical model; it takes an excitation of 2Δ to "break" a Cooper pair and excite two opposite-spin quasiparticles. By standard thermodynamic balance, the number density of quasiparticles is as follows:

$$n_{\mathrm{n}} \propto \exp\left(-\frac{\Delta(T)}{k_{\mathrm{B}}T}\right) \tag{3.11}$$

The quasiparticles often have the name Bogolyubov associated with them, after one of the physicists involved with deriving the "canonical transformation" of the BCS Hamiltonian [Bog58].

The BCS authors calculated the following relation between the energy gap Δ at $T = 0$ and the critical temperature T_{c} of a superconductor:

$$\frac{\Delta(0)}{k_{\mathrm{B}}T_{\mathrm{c}}} = 1.764 \tag{3.12}$$

Experimental results have shown that this value is in general correct, though the true value of the coefficient varies from material to material and has typical values between 1.6 and 2.3 [Kit04]. In general Δ is dependent on temperature and decreases as T increases, though for $T/T_{\mathrm{c}} < 1/2$, $\Delta(T) \approx \Delta(0)$ [Tin04].

The BCS theory provides a thorough understanding of a large portion of the physics of superconductors. However, its quantum-mechanical formalism makes it somewhat difficult to use when addressing the meso- and macroscopic behavior of these materials; for this, the Ginzburg-Landau or "GL" theory proves quite useful. The model, originally proposed by V. L. Ginzburg and L. Landau, is phenomenological in nature (similar to the simpler London model) though L. Gor'kov showed that it could be derived within the formalism of the microscopic BCS theory [GL50, Gor59]. Nowadays much of the science of superconductivity for particle accelerators is done using the language of the Ginzburg-Landau theory.

In their model, calculated for $T \approx T_c$, Ginzburg and Landau expressed the physics of superconductivity in terms of the balance of free energy and a second-order phase transition with order parameter ψ that occurs when the energy of the superconducting state is lower than that of the normal-conducting state. Conceptually starting from a point where the superconducting state is optimal, anything that increases the free energy above a certain threshold will drive the material normal-conducting. This includes increasing the temperature above the critical temperature T_c, but also includes the increased energy due to the presence of electric currents and magnetic fields in the material. Analogous to the critical temperature, it is possible to use the GL framework to derive a critical magnetic field H_c, above which the superconducting state is no longer energetically favorable:

$$\mu_0 H_c = \frac{\phi_0}{\pi \sqrt{8}\, \xi_{GL} \lambda_{GL}} \tag{3.13}$$

This relies on the Ginzburg-Landau coherence length ξ_{GL}, which defines the characteristic length scale for variations in ψ. The confusion between the defini-

tions of ξ and ξ_{GL} is abated by the fact that at temperatures $T \ll T_c$ (where most SRF accelerator cavities operate), the GL coherence length is well approximated by the Pippard coherence length [Tin04]. Near T_c, ξ_{GL} is approximated by the following [OMFB79]:

$$\xi_{GL} = 0.739\left(\xi_0^{-2} + \frac{0.882}{\xi_0 \ell}\right)^{-1/2}\left(1 - \frac{T}{T_c}\right)^{-1/2} \tag{3.14}$$

The definition of H_c also relies on an effective "Ginzburg-Landau penetration depth" λ_{GL} which must be measured experimentally. Near T_c this is well approximated by the following [OMFB79]:

$$\lambda_{GL} = \frac{1}{\sqrt{2}}\lambda_L\left(1 + 0.882\frac{\xi_0}{\ell}\right)^{1/2}\left(1 - \frac{T}{T_c}\right)^{-1/2} \tag{3.15}$$

Experimentally, for niobium, H_c is better approximated by using the effective penetration depth from the microscopic treatment given in Eq. 3.10:

$$\mu_0 H_c = \frac{\phi_0}{\pi\sqrt{8}\,\xi_{GL}\lambda} \tag{3.16}$$

The thermodynamic critical field H_c also depends on temperature T. As the temperature rises and increases the thermal free energy, the threshold energy required to destroy the superconducting state is lowered. Empirically, H_c varies with T as follows [Tin04]:

$$\frac{H_c(T)}{H_c(0)} \approx 1 - \left(\frac{T}{T_c}\right)^2 \tag{3.17}$$

Note that the exponent here is not consistent with the temperature dependence of the approximations of ξ_{GL} and λ_{GL} defined above; these are all empirical relations.

A property of superconductors that emerges from the Ginzburg-Landau formulation is the "intermediate" or "mixed" state. For certain materials, when calculating the free energy balance for a certain applied magnetic field, the energy

"cost" for completely expelling the field (*i.e.* staying in the Meissner state) is higher than that of admitting a small amount of magnetic flux in small normal-conducting "cores", thereby entering an intermediate state between pure superconductor and normal-conductor. Whether this state is possible is determined by the relationship between λ_{GL}, which relates to the energy of the boundary between normal-conducting and superconducting regions, and ξ_{GL}, which in this scenario relates to the energy of the normal-conducting regions themselves. Indeed, one can derive the "Ginzburg-Landau parameter" κ to help distinguish between superconductors in which this mixed state may or may not occur:

$$\kappa = \frac{\lambda_{\mathrm{GL}}}{\xi_{\mathrm{GL}}} \tag{3.18}$$

For materials with $\kappa < 2^{-1/2}$, the intermediate state is never energetically favorable; these are known as Type-I superconductors. On the other hand, in Type-II superconductors, $\kappa > 2^{-1/2}$, and above a certain threshold magnetic flux will enter the material in so-called Abrikosov vortices, named for the physicist who predicted them in the GL formalism [Abr57]. These are thin, normal-conducting regions of cylindrical cross-section with diameter on the scale of the coherence length ξ_{GL}, and with total cross-sectional magnetic flux equal to the flux quantum $\phi_0 = 2.06 \times 10^{-15}$ Wb flowing axially through the core. A cylindrical supercurrent sheet surrounds the core in a vortex, shielding the rest of the superconductor from the magnetic flux in the core.

Several important magnetic field strengths determine the limits of the intermediate state for Type-II materials. The first of these is H_{c1}, the lower critical field. At $H > H_{\mathrm{c1}}$, it becomes energetically favorable for the superconductor to enter the mixed state. In general, finding H_{c1} requires numerical simulation [HA63], but for dirty superconductors such as niobium doped with impurities,

the following approximation can be used [Tin04]:

$$\mu_0 H_{c1}(0) \approx \frac{\phi_0}{4\pi\,\lambda_{GL}^2(0)} \ln(\kappa) \tag{3.19}$$

Relating this to H_c, we find the following for superconductors with $\kappa \gg 1$:

$$\frac{H_{c1}}{H_c} = \frac{\ln(\kappa)}{\sqrt{2}\,\kappa} \tag{3.20}$$

Approaching the Type-I/Type-II boundary at $\kappa = 2^{-1/2}$, $H_{c1} \approx H_c$.

Though H_{c1} indicates the field strength at which the mixed state is more energetically favorable than the Meissner state, vortices may only enter the material from the outer surface (since magnetic flux lines must move continuously). Forming vortices on the surface and pushing them into the bulk requires an additional finite activation energy. As a result, if a superconductor is exposed to a magnetic field that increases smoothly from a low strength up and over H_{c1}, it will stay in a flux-free "superheated" metastable state[2] until a higher "superheating field" H_{sh} at which the excess free energy is sufficient to form vortices and push them across the surface energy barrier.

The superheating field for Type-II superconductors has been calculated numerically and for $\kappa > 1$ is very well approximated by the following when $T \approx T_c$ [TCS11]:

$$\frac{H_{sh}}{H_c} \approx \frac{\sqrt{5}}{3} + \frac{0.5448}{\sqrt{\kappa}} \tag{3.21}$$

It should be noted here that Type-I superconductors also experience a similar superheating effect. Equation 3.21 above is approximately correct for these materials as well, but the rest of this dissertation will concern Type-II superconductors and as such I will limit my discussion to high-κ materials.

[2]This is analogous to phase transitions in other materials, such as water lowered slightly below its freezing point that only crystallizes when jostled.

Parameter	Clean Nb	Doped Nb
T_c (K)	8.9-9.3	8.9-9.3
$\Delta/k_B T_c$	1.85-2.05	1.85-2.05
ℓ (nm)	500-2000	1-200
κ	0.9-1.0	1.1-33
λ_L (nm)	38	38
λ (nm)	38-40	42-160
λ_{GL} (nm)	28-29	5-27
ξ_0 (nm)	39	39
ξ (nm)	36-38	1-33
ξ_{GL} (nm)	28-29	5-27
$\mu_0 H_c$ (mT)	210	200-210
$\mu_0 H_{c1}$ (mT)	210	15-210
$\mu_0 H_{sh}$ (mT)	220	170-220
$\mu_0 H_{c2}$ (mT)	300	>500

Table 3.1: Typical superconducting parameter and critical field values for clean and doped niobium. Values taken at low RF field strength and $T = 0$ where appropriate.

Just as the lower critical field H_{c1} defines the boundary between the Meissner and mixed states, there is an *upper* critical field H_{c2} that separates the mixed and normal-conducting states. This field strength is approximated by the following [Tin04]:

$$\frac{H_{c2}}{H_c} \approx \sqrt{2}\kappa \tag{3.22}$$

Table 3.1 lists some typical superconducting parameter and critical field values for clean (low κ) and impurity-doped (high κ) niobium.

3.2 The Microwave Surface Resistance

The above section outlined the physics of superconductors under time-invariant currents and magnetic fields. Under alternating currents and fields, superconductors exhibit a small but measurable electrical impedance: while the super-

current carriers (Cooper pairs) flow with no impedance to carry currents induced by applied voltages and magnetic fields, their finite inertia causes them to "slosh" under AC excitation. This in turn allows the oscillating fields/voltages to induce a small amount of current on the normal-conducting carriers (unpaired electrons) which flow with impedance. The motion of these unpaired electrons results in power dissipation as heat, as in a traditional resistive material. This dissipation increases with frequency and generally becomes relevant for superconducting devices operating in the microwave range of frequencies, also known as radio-frequency or RF, from f = several 10's of MHz and upwards into the GHz.

Mathematically, this impedance can be studied most easily using the terms of the London and Ginzburg-Landau models, interpreting the superconductor as a two-fluid system: one "fluid" of superconducting charge carriers (*i.e.* Cooper pairs) following the physics of the London/Ginzburg-Landau equations, and a second "fluid" of traditional electrons (*i.e.* Bogolyubov quasiparticles) following traditional models of conductivity. We consider that these two fluids have two distinct densities, n_s for the superconducting charge carriers and n_n for the normal electrons, as well as current densities $\vec{J}_\mathrm{s}$ and $\vec{J}_\mathrm{n}$.

We imagine that there is a sinusoidally oscillating magnetic field applied to the surface of the superconductor, $\vec{B} = B\exp(-i\omega t)$. By Eq 3.2, $\vec{J}_\mathrm{s} = J_\mathrm{s}\exp(-i\omega t)$, and by Eq. 3.1, we have the following for the electric field generated by the supercurrent:

$$\vec{E} = i\omega\frac{m_\mathrm{e}}{n_\mathrm{s}e^2}J_\mathrm{s}\exp(i\omega t) = i\omega\frac{m_\mathrm{e}}{n_\mathrm{s}e^2}\vec{J}_\mathrm{s} \tag{3.23}$$

We can group the coefficients here as a measure of conductivity:

$$\sigma_\mathrm{s} = \frac{n_\mathrm{s}e^2}{\omega m_\mathrm{e}} \tag{3.24}$$

Then Eq. 3.23 becomes the following:

$$\vec{J}_{\mathrm{s}} = -i\sigma_{\mathrm{s}}\vec{E} \tag{3.25}$$

This in turn mirrors Ohm's law, which determines the relationship between current and electric field for the normal-conducting charge carriers:

$$\vec{J}_{\mathrm{n}} = \sigma_{\mathrm{n}}\vec{E} \tag{3.26}$$

Adding these, we get an expression linking the electric field generated by the moving superconducting carriers to the current densities of both the superconducting and normal-conducting carriers:

$$\vec{J} = \vec{J}_{\mathrm{n}} + \vec{J}_{\mathrm{s}} = (\sigma_{\mathrm{n}} - i\sigma_{\mathrm{s}})\vec{E} \tag{3.27}$$

Given the combined conductivity $\sigma = (\sigma_{\mathrm{n}} - i\sigma_{\mathrm{s}})$ expressed above, we can examine the power dissipated in the surface due to the applied oscillating field. Applying Eq. 3.2 and Ampère's law to Eq. 3.6, and making the substitution $\vec{B} = \mu_0\vec{H}$ (noting that $\mu \approx \mu_0$ for the metallic superconductors considered in this dissertation), we arrive at the following expression for the magnitude of the local current density J in the London limit:

$$J = \frac{H_0}{\lambda_{\mathrm{L}}} \exp\left(-\frac{x}{\lambda_{\mathrm{L}}}\right) \tag{3.28}$$

For the power dissipated in a resistive material with current density $J(\vec{r})$ and conductivity σ, we have the following, beginning with Joule's First Law and inserting the above expression for J:

$$P = \mathrm{Re}\left[\frac{1}{\sigma}\int_V J^2(\vec{r})\, d^3\vec{r}\right] \tag{3.29}$$

$$= \mathrm{Re}\left[\frac{H_0^2}{\sigma\lambda_{\mathrm{L}}^2}\int_V \exp\left(-\frac{2x}{\lambda_{\mathrm{L}}}\right) dx\, dy\, dz\right] \tag{3.30}$$

We can calculate an expression for the power dissipated per unit area on the surface, integrating over the exponential decay into the bulk:

$$\frac{P}{A} = \mathrm{Re}\left[\frac{H_0^2}{\sigma\lambda_\mathrm{L}^2}\int_0^\infty \exp\left(-\frac{2x}{\lambda_\mathrm{L}}\right) dx\right] \tag{3.31}$$

$$= \mathrm{Re}\left[\frac{1}{\sigma\lambda_\mathrm{L}}\frac{H_0^2}{2}\right] \tag{3.32}$$

From this we can nicely group the terms as a superconducting surface resistance R_SC that encapsulates the field distribution in the material, giving the power dissipated per unit area of the surface for a given applied field measured at the surface:

$$R_\mathrm{SC} = \mathrm{Re}\left[\frac{1}{\sigma\lambda_\mathrm{L}}\right] \tag{3.33}$$

$$= \frac{P}{A}\frac{2}{H_0^2} \tag{3.34}$$

Here is a more commonly used form of the above expression:

$$\frac{P}{A} = \frac{1}{2}R_\mathrm{SC}H_0^2 \tag{3.35}$$

Using our expression in Eq. 3.27 above for the complex conductivity σ and taking the real part of the complex impedance, we find the following:

$$R_\mathrm{SC} = \mathrm{Re}\left[\frac{1}{(\sigma_\mathrm{n} - i\sigma_\mathrm{s})\lambda_\mathrm{L}}\right] \tag{3.36}$$

$$= \frac{\sigma_\mathrm{n}}{\lambda_\mathrm{L}(\sigma_\mathrm{s}^2 + \sigma_\mathrm{n}^2)} \tag{3.37}$$

Then substituting Eq. 3.24 for σ_s and the Drude model for normal electrical conductivity $\sigma_\mathrm{n} = n_\mathrm{n}e^2\ell/v_\mathrm{F}m_\mathrm{e}$ [Kit04], and then assuming that $\sigma_\mathrm{s} \gg \sigma_\mathrm{n}$ (indeed $1/\omega \gg \ell/v_\mathrm{F}$ for niobium with $f < 100$ GHz and $\ell < 1$ μm), we find a concise form for the surface resistance:

$$R_\mathrm{SC} \approx \frac{\sigma_\mathrm{n}}{\lambda_\mathrm{L}\sigma_\mathrm{s}^2} \tag{3.38}$$

$$\approx \frac{n_\mathrm{n}e^2\ell}{m_\mathrm{e}v_\mathrm{F}}\mu_0^2\omega^2\lambda_\mathrm{L}^3 \tag{3.39}$$

Including the relation from Eq. 3.11 we can find the temperature-dependence of this surface resistance:

$$R_{\mathrm{SC}} \propto \ell\omega^2\lambda_{\mathrm{L}}^3 \exp\left(-\frac{\Delta(T)}{k_{\mathrm{B}}T}\right) \tag{3.40}$$

The above expression can be improved by replacing λ_{L} with λ from Eq. 3.10 to account for the effects of short ℓ on the penetration depth. Further corrections can be done to introduce the Pippard relation in Eq. 3.8 and to account for the anomalous skin effect, reaching the following approximation for R_{s} in the limit of $T/T_{\mathrm{c}} < 1/2$ and $\omega < \Delta/\hbar$ [Gur12]:

$$R_{\mathrm{SC}} \approx \mu_0^2\omega^2\lambda^3 \left(\frac{n_{\mathrm{n,NC}}e^2\ell}{m_{\mathrm{e}}v_{\mathrm{F}}}\right)\frac{\Delta(T)}{k_{\mathrm{B}}T}\ln\left(\frac{2.246\,k_{\mathrm{B}}T}{\hbar\omega}\right)\exp\left(-\frac{\Delta(T)}{k_{\mathrm{B}}T}\right) \tag{3.41}$$

Here, $n_{\mathrm{n,NC}}$ is the density of electrons in the normal-conducting state.

In 1970, J. Halbritter developed a computer code to calculate the surface resistance numerically from BCS theory [Hal70]. An online version of this code is available to the interested reader at `https://www.classe.cornell.edu/~liepe/webpage/researchsrimp.html`. For high-quality niobium cavities at 1.3 GHz and 2 K, the BCS surface resistance is approximately 20 nΩ; at 1.5 K this reduces to about 1 nΩ. In the field of SRF accelerator physics, this temperature-dependent superconducting surface resistance (R_{SC} above) is usually referred to as R_{BCS}.

As anticipated directly in Eq. 3.40 and by the inclusion of λ_{GL} and σ_1 in Eq. 3.41, R_{BCS} depends strongly on the electron mean free path ℓ. In particular, there is a minimum when $\ell \approx \xi_0/2$, where R_{BCS} is approximately half as big as in the clean limit of $\ell \gg \xi_0$. Figure 3.2 shows the results of a calculation of R_{BCS} vs. ℓ for typical niobium parameters.

Two important effects have been observed experimentally but are not ad-

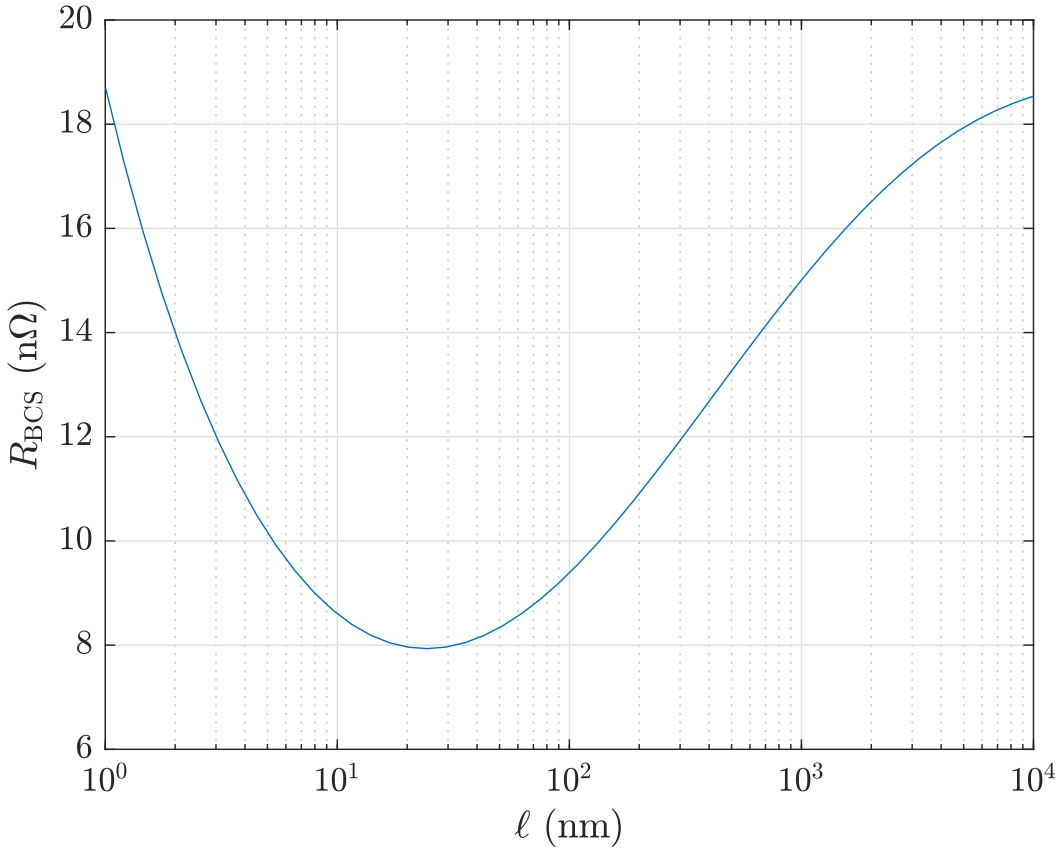

Figure 3.2: Theoretical BCS surface resistance as a function of mean free path, calculated for typical niobium parameters: $T_c = 9.2$ K, $\Delta/k_B T_c = 1.9$, $\lambda_L = 39$ nm, $\xi_0 = 38$ nm, $T = 2$ K, and $f = 1.3$ GHz.

dressed by the Ginzburg-Landau/London and BCS treatments above. The first of these is the "residual resistance" R_0, which is a temperature-independent offset to the surface resistance:

$$R_s = R_0 + R_{\mathrm{BCS}}(T) \tag{3.42}$$

There are many possible sources of residual resistance, including normal-conducting inclusions, magnetic impurities, niobium hydride crystals, trapped magnetic flux, surface defects, and more. Well-prepared niobium cavities at 1.3 GHz can have $R_0 < 0.5$ nΩ [GL13]. Figure 3.3 shows the results of a calculation for typical niobium.

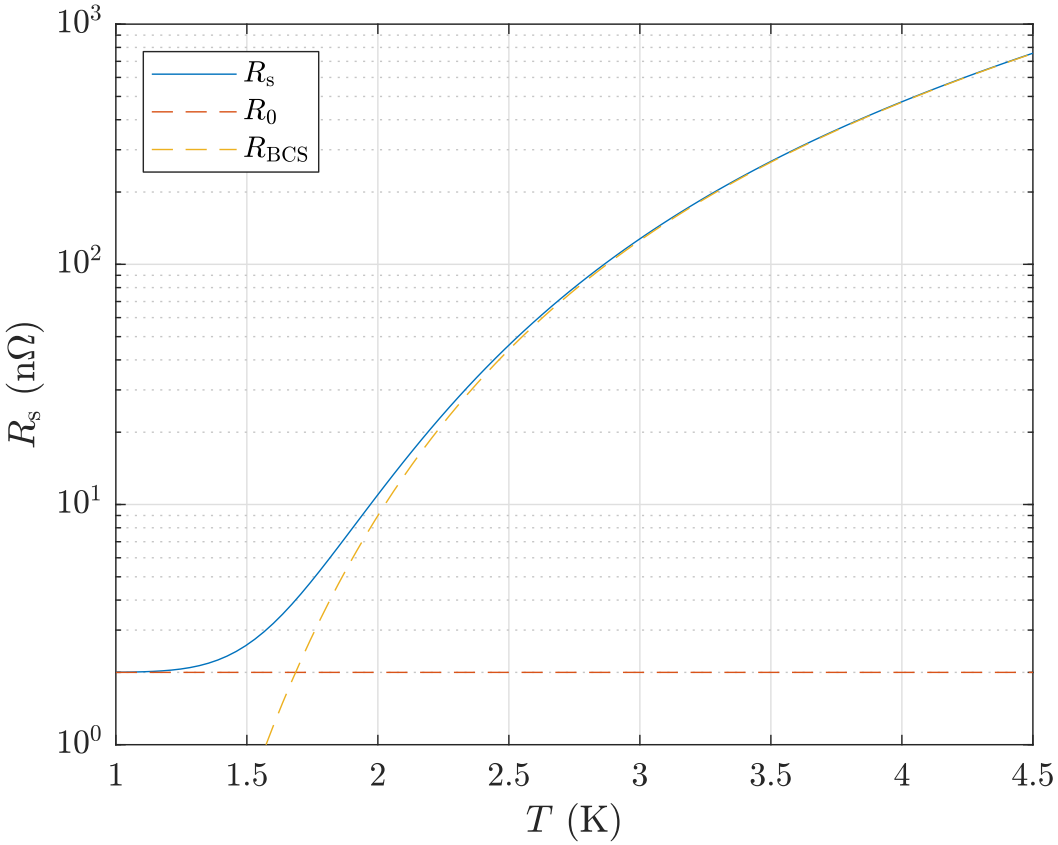

Figure 3.3: Theoretical surface resistance as a function of temperature, calculated for typical niobium parameters: $T_c = 9.2$ K, $\Delta/k_B T_c = 1.9$, $\lambda_L = 39$ nm, $\xi_0 = 38$ nm, $\ell = 80$ nm, $f = 1.3$ GHz, and $R_0 = 2$ nΩ.

The second important effect unaddressed by the traditional treatments is the field dependence of the surface resistance. Equation 3.35 can more accurately be written as follows:

$$\frac{P}{A} = \frac{1}{2} R_s (H_0) H_0^2 \tag{3.43}$$

Both R_0 and R_{BCS} can in general depend on the strength of the surface magnetic field. Much of the work later in this dissertation will address this field-dependent surface resistance.

3.3 SRF Accelerator Cavity Fundamentals

In the previous section, we used the fundamentals of the theory of superconductivity to develop a microwave surface resistance, a loss mechanism for superconducting surfaces under radio-frequency magnetic fields. This superconducting surface resistance is the chief loss mechanism for superconducting accelerators; as a result, it is of paramount interest to study this resistance in great detail. One useful method of study is to use cavities very similar to those used in accelerators to investigate the surface resistance.

3.3.1 Intrinsic Losses

To understand how SRF cavities are used in fundamental research, we will first consider a hypothetical superconducting cavity: a hollow space surrounded by a superconductor with an oscillating electromagnetic field trapped inside. The energy stored in the field of the cavity can be calculated as follows:

$$U = \frac{1}{2}\mu_0 \int_V dV\, H^2 \tag{3.44}$$

Because there are surface magnetic fields, this cavity will dissipate a certain amount of power, which can be calculated by integrating Eq. 3.35 over the surface area of the cavity:

$$P_{\text{diss}} = \frac{1}{2}\int_S dS\, R_s H^2 \tag{3.45}$$

For a resonator such as an SRF cavity, a useful figure of merit is the "quality factor" Q, which relates the stored energy to the dissipated power:

$$Q = \frac{\omega U}{P} \tag{3.46}$$

When only considering the power dissipated in the cavity walls (*i.e.* the intrinsic loss mechanism of the cavity), we can define an "intrinsic quality factor" Q_0:

$$Q_0 = \frac{\omega U}{P_{\text{diss}}} \tag{3.47}$$

We can plug Eqs. 3.44 and 3.45 into Eq. 3.47, normalizing by the peak field on the cavity wall H_{pk}:

$$Q_0 = \omega\mu_0 \frac{\int_V dV \left(\frac{H}{H_{\text{pk}}}\right)^2}{\int_S dS\, R_{\text{s}} \left(\frac{H}{H_{\text{pk}}}\right)^2} \tag{3.48}$$

Under the assumption that the surface resistance is independent of the field strength and uniform over the cavity surface, or that the field is equal everywhere on the surface, we can pull R_{s} out of the integral in the denominator. With this adjustment the two normalized integrals and the resonant frequency ω are strictly dependent on the distribution of fields determined by the cavity geometry. We can group these terms (and the constant μ_0) into a "geometry factor" G:

$$G = \omega\mu_0 \frac{\int_V dV \left(\frac{H}{H_{\text{pk}}}\right)^2}{\int_S dS \left(\frac{H}{H_{\text{pk}}}\right)^2} \tag{3.49}$$

Then the intrinsic Q_0 is the relation between G and the surface resistance R_{s}:

$$Q_0 = \frac{G}{R_{\text{s}}} \tag{3.50}$$

A nice feature of G is that it is independent of scale: adjusting the linear dimensions L will scale ω by L^{-1}, the dV integral by L^3, and the dS integral by L^2, resulting in an overall scaling of $L^0 = 1$. Elliptical cavities and other similar high-transit-time-factor accelerating structures tend to have $G \approx 270\ \Omega$.

In the case when no other power aside from P_{diss} is flowing into or out of the cavity, Q_0 gives the behavior of the stored energy U over time as power is

dissipated. We can solve the following differential equation with appropriate substitutions:

$$\frac{dU}{dt} = -P_{\text{diss}} \tag{3.51}$$

$$\left[\mu_0 \int_V dV \left(\frac{H}{H_{\text{pk}}}\right)^2\right] \frac{d}{dt} H_{\text{pk}}^2 = -H_{\text{pk}}^2 \int_S dS \; R_{\text{s}} \left(\frac{H}{H_{\text{pk}}}\right)^2 \tag{3.52}$$

Moving things around, again pulling R_{s} out of the dissipated power integral, and substituting in from Eqs. 3.49 and 3.50, we have the following:

$$\frac{d}{dt} H_{\text{pk}}^2 = -\frac{\omega}{Q_0} H_{\text{pk}}^2 \tag{3.53}$$

The solution to the above equation is the time-dependent value of the peak field magnitude H_{pk}:

$$H_{\text{pk}}(t) = H_{\text{pk}}(0) \exp\left(-\frac{\omega}{2Q_0} t\right) \tag{3.54}$$

For the instantaneous energy U and dissipated power P_{diss} as functions of time we get the following:

$$U(t) = U(0) \exp\left(-\frac{\omega}{Q_0} t\right) \tag{3.55}$$

$$P_{\text{diss}}(t) = P_{\text{diss}}(0) \exp\left(-\frac{\omega}{Q_0} t\right) \tag{3.56}$$

3.3.2 Nonuniform Surface Fields

The above equations work well to describe SRF cavities with sufficiently uniform surface magnetic fields. Equipped with a method for measuring Q_0, an experimentalist can find the surface resistance as a function of the surface magnetic field by measuring Q_0 vs. H_{pk} and plugging into Eq. 3.50. However, when the fields are not uniform across the surface, using this method implicitly averages R_{s} over the distribution of the magnetic field on the surface. To get a

"localized" $R_s(H)$, a more complicated approach is necessary, which requires knowledge of the surface field distribution in the cavity from *e.g.* an RF simulation computer program such as SuperLANS [Euc17]. I described one such method in a 2018 paper [ML18], which I will summarize here. Note that this method still assumes that the superconductor is uniform over the cavity surface, such that all points on the surface exhibit the same $R_s(H)$.

The implicit averaging mentioned above occurs in the geometry factor G (Eq. 3.49). If we combine Eqs. 3.47-3.49 we can see the averaging more explicitly:

$$R_{av}(H_{pk}) = \frac{G}{Q_0(H_{pk})} = \frac{\int_S dS\ R_s(H)\, H^2}{\int_S dS\ H^2} \tag{3.57}$$

We can consider the right hand side of this equation to be an averaging operator $\mathbf{A}$ mapping the resistance function of the localized field $R_s(H)$ to an average resistance function of the peak field $R_{av}(H_{pk})$:

$$R_{av}(H_{pk}) = \mathbf{A}\, R_s(H) \tag{3.58}$$

Measuring Q_0 vs. H_{pk} yields $R_{av}(H_{pk})$ by way of G, and from that we can obtain the localized R_s by inverting $\mathbf{A}$. We can solve this by discretizing the problem, turning R_s and R_{av} into column vectors of R values at N increasing H values and turning $\mathbf{A}$ into an $N \times N$ matrix:

$$\mathbf{R}_{av} = \mathbf{A}\mathbf{R}_s \tag{3.59}$$

$$\begin{bmatrix} R_{av}(H_1) \\ R_{av}(H_2) \\ \vdots \end{bmatrix} = \begin{bmatrix} A_{1,1} & A_{1,2} & \cdots \\ A_{2,1} & A_{2,2} & \cdots \\ \vdots & \vdots & \ddots \end{bmatrix} \begin{bmatrix} R_s(H_1) \\ R_s(H_2) \\ \vdots \end{bmatrix} \tag{3.60}$$

The elements of $\mathbf{A}$ can be determined with knowledge of the surface field distribution in the cavity. If we imagine that the peak field in the cavity is H_n, we can split the surface S into n areas $S_{m/n}$ in such a way that the surface field

in each $S_{m/n}$ is approximately equal to H_m. We can then split the numerator of the averaging surface integral in 3.57 into a sum of integrals over the different surfaces:

$$R_{\mathrm{av}}(H_n) = \frac{1}{\int_S dS\ H^2} \sum_{m=1}^{n} \int_{S_{m/n}} dS\ R_{\mathrm{s}}(H)\, H^2 \tag{3.61}$$

Since $H \approx H_m$ across each $S_{m/n}$, $R_s(H) \approx R_{\mathrm{s}}(H_m)$ as well. Thus we can pull R_s out of these integrals, effectively averaging over each $S_{m/n}$ instead of over all S:

$$R_{\mathrm{av}}(H_n) = \frac{1}{\int_S dS\ H^2} \sum_{m=1}^{n} R_{\mathrm{s}}(H_m) \int_{S_{m/n}} dS\ H^2 \tag{3.62}$$

Now $R_{\mathrm{av}}(H_n)$ is a linear combination of the first n elements of $\mathbf{R_s}$, and as such the first m elements of the n^{th} row of $\mathbf{A}$ are given by the coefficients of the sum:

$$A_{\mathrm{m,n}} = \frac{\int_{S_{m/n}} dS\ H^2}{\int_S dS\ H^2} \tag{3.63}$$

To complete $\mathbf{A}$, we note that all other entries $A_{\mathrm{m,n}}$ where $m > n$ are equal to zero, since $R_{\mathrm{av}}(H_{\mathrm{pk}} = H_{\mathrm{n}})$ cannot depend on any $R_{\mathrm{s}}(H > H_{\mathrm{n}})$. As a result, $\mathbf{A}$ is a positive lower triangular matrix and is thus invertible. The local surface resistance $R_{\mathrm{s}}(H)$ can be calculated with $\mathbf{A^{-1}}$:

$$\mathbf{R_s} = \mathbf{A^{-1}}\, \mathbf{R_{av}} = \mathbf{A^{-1}} \frac{G}{\mathbf{Q_0}} \tag{3.64}$$

Above, $\mathbf{Q_0}$ is the intrinsic quality factor $Q_0(H)$ assembled into a column vector, and G is the implicitly-averaging geometry factor; the division is element-wise.

Figure 3.4 demonstrates the usefulness of the above procedure by comparing an example "localized" surface resistance to the implicitly averaged surface resistance obtained from traditional measurement methods. Elliptical cavity geometries such as the TESLA single-cells and nine-cells ("LTE1" and "LTE9" in the figure), the Cornell elliptical geometry ("LE"), and a low-βelliptical cavity (here an SNS cavity) have high field uniformity and as such see only a small

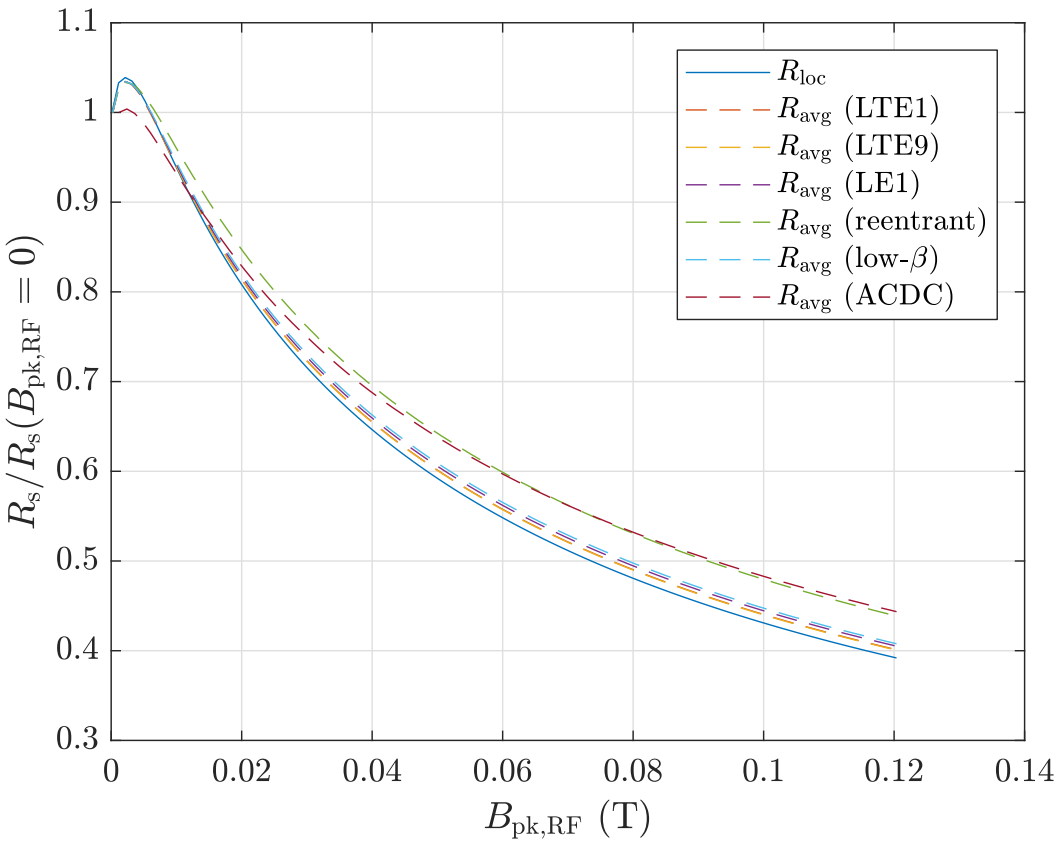

Figure 3.4: A comparison of the implicitly averaged surface resistance R_{avg} to an example "localized" surface resistance R_{loc} for several cavity shapes.

correction to the measured value of R_s. On the other hand, cavities with more non-uniform fields such as a high-gradient reentrant cavity or the DC field-dependence cavity to be discussed later in this dissertation ("ACDC") have up to a 10% adjustment to the measured R_s at high fields. Considering the effects of cavity geometry on the implicit averaging of R_s is essential in accurately characterizing SRF cavities and cavity materials.

3.3.3 Couplers and Power Measurements

So far, this discussion has only concerned the intrinsic losses of a superconducting cavity with a trapped electromagnetic field. To excite and measure such a field, a "coupler" can be used to couple electromagnetic power into or out of the cavity. Such a coupler might be a waveguide or an antenna[3]. Couplers can also be used to measure Q_0 for a cavity when a more direct measurement of P_{diss} is not available; this is one of the main experimental methods used in SRF cavity research and will be elaborated upon below.

In general, SRF cavities are excited with a "fundamental power coupler" (alternatively "forward power coupler" or simply "FPC"). Cavities are also often equipped with a small "pickup" or "transmitted power coupler" to measure the strength of the field. Figure 3.5 depicts a typical single-cell SRF cavity in the accelerating mode with on-axis forward and transmitted power couplers.

In the case when the cavity is not driven (*i.e.* there is no forward power incident on the FPC), the couplers act as energy loss mechanisms: in addition to the power dissipated in the cavity walls due to the surface resistance, power will be coupled out of the cavity into the transmission lines connected to the couplers. Equation 3.51 then becomes the following:

$$\frac{dU}{dt} = -P_{\text{diss}} - P_{\text{e}} - P_{\text{t}} = -P_{\text{total}} \tag{3.65}$$

By convention, power lost out through the FPC is called the "emitted power" or P_{e}; transmitted power is given the symbol P_{t}. We define the "loaded quality

[3]Which is just a waveguide anyway.

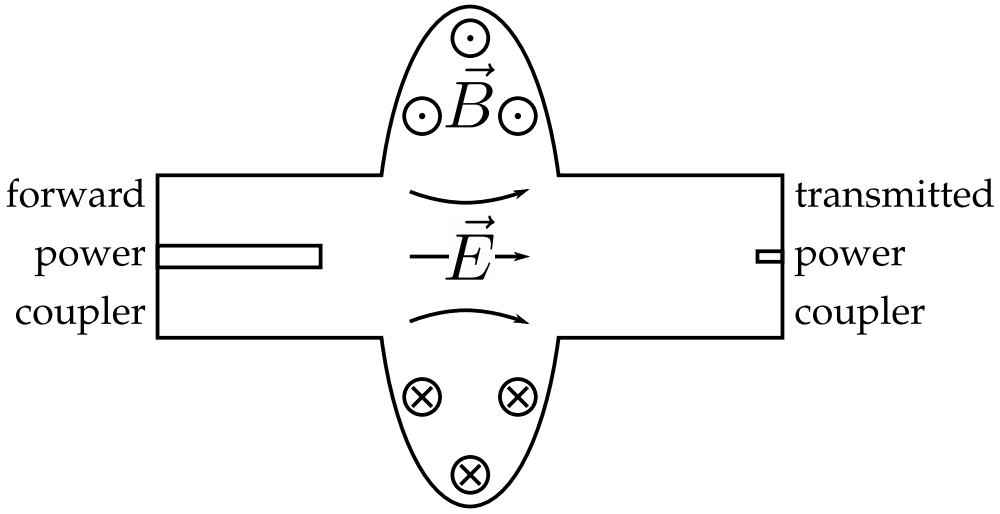

Figure 3.5: A representative cartoon of a single-cell SRF cavity excited in the TM_{010} mode with $\vec{B}$ and $\vec{E}$ fields illustrated as well as forward and reflected power couplers; $\vec{B}$ and $\vec{E}$ vary in time with a 90° phase difference.

factor" from Eq. 3.46 by including all power loss mechanisms:

$$Q_{\mathrm{L}} = \frac{\omega U}{P_{\mathrm{total}}} \tag{3.66}$$

We can update Eq. 3.55 to reflect the total power loss:

$$U(t) = U(0)\exp\left(-\frac{\omega}{Q_{\mathrm{L}}}t\right) = U(0)\exp\left(-\frac{1}{\tau_{\mathrm{L}}}t\right) \tag{3.67}$$

The loaded time constant $\tau_{\mathrm{L}} = Q_{\mathrm{L}}/\omega$ is a common grouping of cavity test parameters because (as we shall see later) this exponential decay can be measured directly.

Splitting up the components of P_{total}, the loaded quality factor can be broken down into the reciprocal sum of component Q values that relate the power lost through each mechanism to the energy stored in the cavity field:

$$Q_{\mathrm{L}} = \left(\frac{1}{Q_0} + \frac{1}{Q_{\mathrm{e}}} + \frac{1}{Q_{\mathrm{t}}}\right)^{-1} \tag{3.68}$$

$$= \left(\frac{P_{\mathrm{diss}}}{\omega U} + \frac{P_{\mathrm{e}}}{\omega U} + \frac{P_{\mathrm{t}}}{\omega U}\right)^{-1} \tag{3.69}$$

Parameter	LTE1	STE1	DCFDC (mode 1)	DCFDC (mode 2)	DCFDC (mode 3)
f_r (MHz)	1300	2600	550	1300	2040
G (Ω)	278	278	118	273	424
$\mu_0 H_{pk} U^{-1/2}$ (mT J$^{-1/2}$)	34.3	96.1	244	271	267
$\mu_0 H_{pk} E_{pk}^{-1}$ (mT MV^{-1}m)	2.27	2.27	243	137	139
$\mu_0 H_{pk} E_{acc}^{-1}$ (mT MV^{-1}m)	4.23	4.25	–	–	–
$E_{pk} E_{acc}^{-1}$	1.86	1.87	–	–	–

Table 3.2: Cavity field parameters for the cavity types used in this dissertation: TESLA-shape single-cell (LTE1), TESLA-shape single-cell scaled to 2600 MHz (STE1), and the DC Field Dependence Cavity (see Chap. 9). The latter has no accelerating mode and thus no values for E_{acc}. G values for the DC Field Dependence Cavity assume a superconducting inner conductor, when $G \approx G_{inner}$.

By convention, Q values related to couplers (Q_e and Q_t in this discussion) are called "external" quality factors. A measurement of P_e or P_t (when no power is coming into the cavity by way of the coupler in question) and knowledge of Q_e or Q_t yields the energy in the cavity:

$$U = \frac{P_e Q_e}{\omega} = \frac{P_t Q_t}{\omega} \tag{3.70}$$

From there it is easy to find the magnitudes of the electric and magnetic fields in the cavity with knowledge of the field distributions from calculations or computer simulations; for a given cavity geometry it is typical to calculate a conversion factor $H_{pk}/\sqrt{U}$ and similar constants for electric field measurements. Table 3.2 gives the conversion factors as well as other relevant field parameters for the cavity geometries used in this dissertation.

We also define "coupling factors" β to quantify the ratios of the power trans-

mitted out through the couplers to the dissipated power:

$$\beta_e = \frac{P_e}{P_{diss}} = \frac{Q_0}{Q_e} \tag{3.71}$$

$$\beta_t = \frac{P_t}{P_{diss}} = \frac{Q_0}{Q_t} \tag{3.72}$$

In common SRF applications and experiments, β_t is typically chosen to be very small ($\beta_t \ll 1$) so that the loaded Q is not strongly affected:

$$\frac{1}{Q_L} = \frac{1}{Q_0}(1 + \beta_e + \beta_t) \approx \frac{1}{Q_0}(1 + \beta_e) \tag{3.73}$$

In the driven case, a forward power P_f is sent down the transmission line towards the FPC and into the cavity. A certain amount of power is reflected, P_r, and a certain amount $P_{in} = P_f - P_r$ goes into the cavity. Considering the steady-state case where $\frac{dU}{dt} = 0$, it is easy to see that P_{in} is identical to P_{diss}. By applying transmission line theory to the system, one finds that P_{in} is related to P_f as follows when the cavity is driven on resonance [PHK98]:

$$P_f - P_r = P_{in} = P_f \frac{4Q_L^2}{Q_0 Q_e} = P_f \frac{4\beta_e}{(1+\beta_e)^2} \tag{3.74}$$

With measurements of P_r and P_f in the steady state we can calculate β_e:

$$\beta_e = \frac{1 \pm \sqrt{\frac{P_r}{P_f}}}{1 \mp \sqrt{\frac{P_r}{P_f}}} \tag{3.75}$$

When the cavity is overcoupled, the upper signs are used and $\beta_e > 1$; when the cavity is undercoupled, the lower signs are used and $\beta_e < 1$. When $\beta_e = 1$, the cavity is considered to be "critically coupled".

If one knows the value of Q_e for an SRF cavity, it is straightforward to use the steady-state β_e above and Eq. 3.71 to determine Q_0. These can in turn be used to find R_s as well as Q_L, U, and the magnitudes of the electric and magnetic fields.

However, if Q_e is unknown, or if it is desirable to make a second measurement of Q_0, another method is required. At Cornell we use the "RF Off" method: first the steady-state on-resonance P_r and P_f are measured, then the RF drive on the FPC is abruptly turned off and P_e is measured as the field in the cavity decays [PHK98]. The power emitted out through the FPC is given by the following:

$$P_e(t) = \frac{\omega U(t)}{Q_e} \tag{3.76}$$

$$= \omega U(0) \frac{\beta_e}{Q_0} \exp\left(-\frac{\omega}{Q_L} t\right) \tag{3.77}$$

Here we have made substitutions using Eqs. 3.71 and 3.67. In the steady-state, the stored energy of the cavity can be related to P_f and β_e; this is equal to the value of U at the start of the decay:

$$U(0) = \frac{Q_0 P_{diss}}{\omega} = \frac{Q_0 P_{in}}{\omega} = P_f \frac{Q_0}{\omega} \frac{4\beta_e}{(1+\beta_e)^2} \tag{3.78}$$

We can substitute this into Eq. 3.77:

$$P_e(t) = P_f \frac{4\beta_e^2}{(1+\beta_e)^2} \exp\left(-\frac{\omega}{Q_L} t\right) \tag{3.79}$$

Measuring the undriven P_e at $t = 0$ yields the coefficients to the left of the exponential; this gives an alternative measurement of the coupling factor β_e:

$$\beta_e = \frac{1}{2\sqrt{\frac{P_f}{P_e}} - 1} \tag{3.80}$$

The measurement of the decay curve over time $P_e(t)$ can then be fitted to an exponential function, which yields the decay constant τ_L and thus Q_L. With Q_L and β_e in hand, it is simple to use Eq. 3.73 to find Q_0.

In addition, the sign of $P_e(0) - P_f$ informs the choice of sign for calculating the coupling factor by Eq. 3.75: when $P_e(0) > P_f$, the cavity is overcoupled ($\beta_e > 1$), and vice-versa. In the Cornell SRF group we typically measure β_e using the

methods in both Eq. 3.75 and Eq. 3.80, averaging them for use in calculating Q_0 and H_{pk} (by way of U and the geometry-dependent conversion factor $H_{\mathrm{pk}}/\sqrt{U}$). We only accept points for which the two measurements of β_{e} agree within 10%.

3.3.4 Excitation by Phase-Locked Loop

For most of the cavity tests in the Cornell SRF group, we excite the cavity in an RF circuit known as a phase-locked loop (PLL). In general, a PLL uses an RF mixer to compare the frequency of a voltage-controlled oscillator (VCO) to that of a reference source, using the mixer output to adjust the VCO frequency to match the reference oscillator. In the case of SRF cavities, the cavity (reference oscillator) is driven by the signal generator (VCO), so the two oscillate at the same drive frequency ω_{d}. However, ω_{d} may be slightly off from the resonant frequency of the cavity ω_{r} to begin with, and ω_{r} may shift further over time due to microphonics (changes in the cavity geometry caused by mechanical vibrations) [PHK98]. The difference between ω_{d} and ω_{r} results in a phase difference between the cavity and the drive signal. In the steady state this looks like the following [SZY84, FLS06]:

$$\Delta\phi = \phi_{\mathrm{c}} - \phi_{\mathrm{d}} = \tan^{-1}\left(Q_{\mathrm{L}}\frac{\omega_{\mathrm{d}}^2 - \omega_{\mathrm{r}}^2}{\omega_{\mathrm{d}}\,\omega_{\mathrm{r}}}\right) \tag{3.81}$$

The energy U of the field in the cavity and thus the voltage of the signal at the pickup antenna V_{cav} will also be lower than their on-resonance maxima:

$$U = 4P_{\mathrm{f}}\frac{\omega_{\mathrm{r}}\omega_{\mathrm{d}}^2}{Q_{\mathrm{e}}}\left(\frac{\omega_{\mathrm{r}}^2\omega_{\mathrm{d}}^2}{Q_{\mathrm{L}}^2} + \left(\omega_{\mathrm{d}}^2 - \omega_{\mathrm{r}}^2\right)^2\right)^{-1} \tag{3.82}$$

$$V_{\mathrm{cav}} \propto \sqrt{U} \tag{3.83}$$

Figures 3.6 and 3.7 show an example of these phase and amplitude differences for a 1.3 GHz cavity over a range of realistic values of Q_{L}. Cavities with high Q_{L}

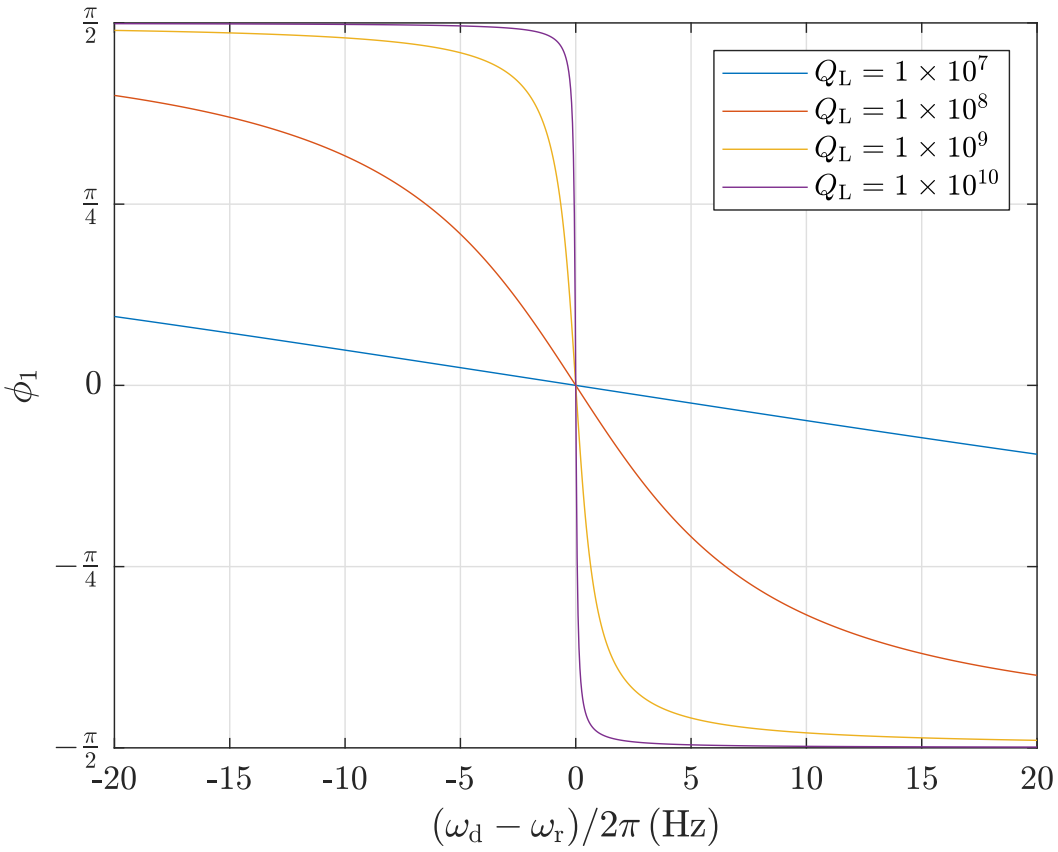

Figure 3.6: Phase difference between cavity and drive signal as a function of the drive frequency ω_d relative to the cavity resonant frequency ω_r, shown for several values of the loaded quality factor at 1.3 GHz.

have a phase and field strength that varies very quickly near $\Delta\omega = \omega_d - \omega_r = 0$, and are more sensitive to microphonics as a result. A PLL used to drive high-Q_L SRF cavities (such as those under vertical test at Cornell) tracks this phase difference $\Delta\phi$ and adjusts ω_d to keep $\Delta\phi$ (and thus $\Delta\omega$) constant. We then use a further manual phase adjustment to set $\Delta\omega = 0$, thus driving the cavity on its (time-varying) resonance frequency, essential for accuracy in the RF measurements described in Sec. 3.3.3.

V. F. Kroupa's text offers a very nice overview of PLL principles [Kro03], and C. Gökçek's paper gives a description of using a digital PLL to track a moving reference frequency [Gok03]. Here I will go over the basic mathematics of using

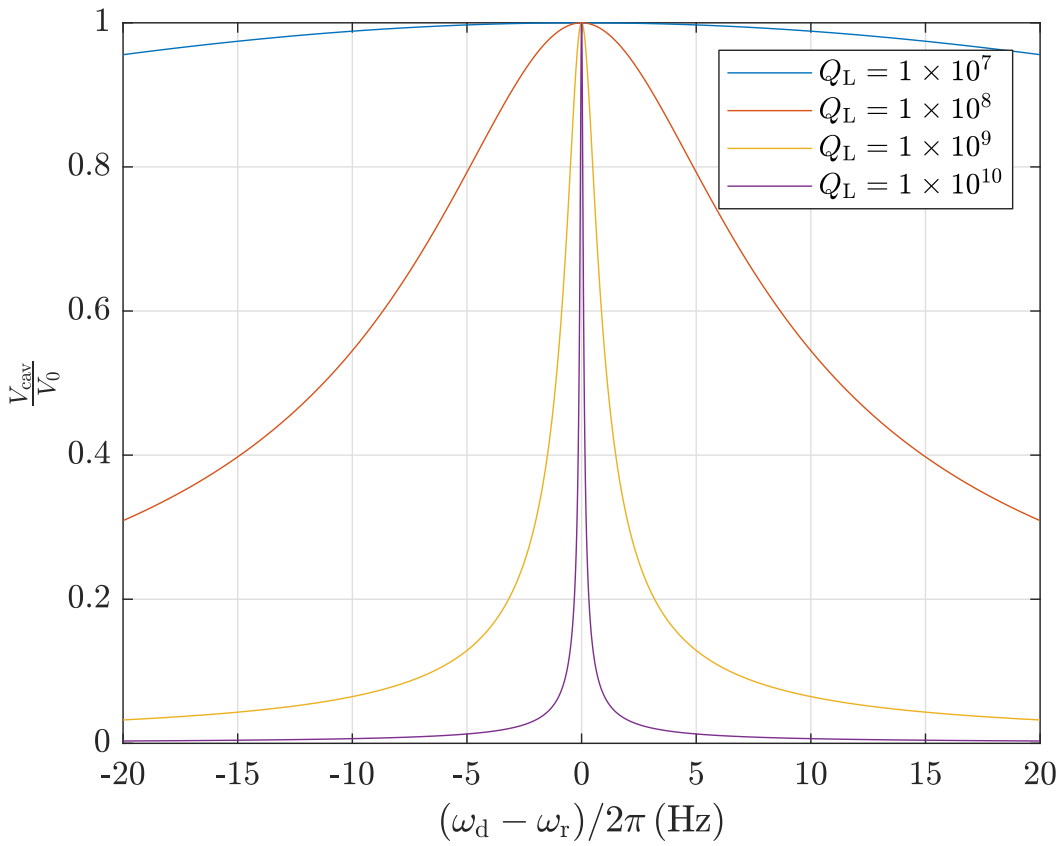

Figure 3.7: Amplitude of cavity voltage relative to the on-resonance voltage as a function of the drive frequency ω_{d} relative to the cavity resonant frequency ω_{r}, shown for several values of the loaded quality factor at 1.3 GHz.

an analog PLL to track a moving reference frequency, as we do in the Cornell SRF group. Figure 3.8 shows an overview of the main components of the system for reference.

The RF mixer is the key component of the phase-locked loop. It compares the signals at its two inputs, labeled LO (local oscillator) and RF (radio-frequency), and generates the product of these signals at its output, labeled IF (intermediate frequency), along with a mixer gain factor K_{M}. The LO and RF inputs will be

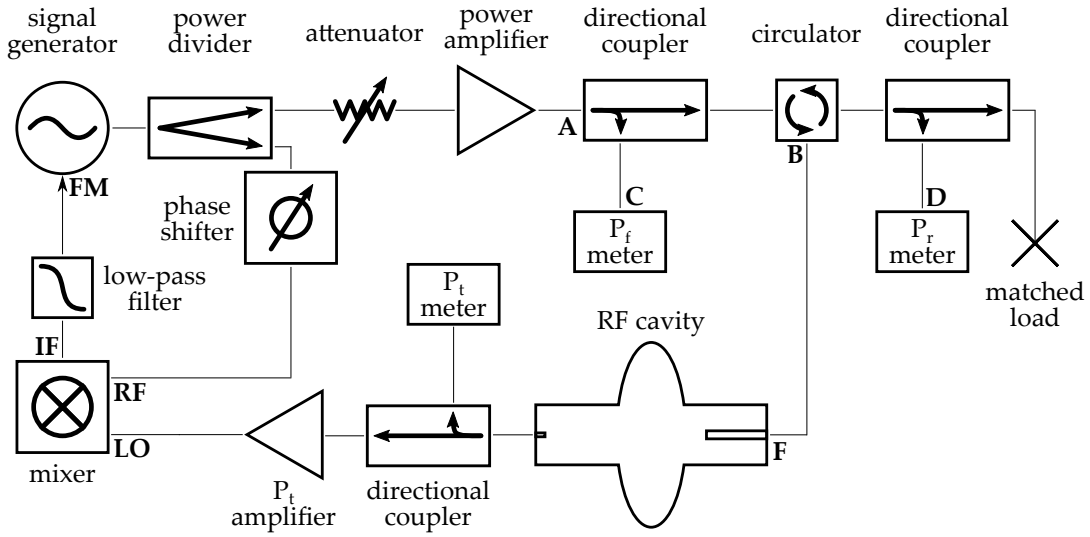

Figure 3.8: Diagram of the phase-locked loop circuit used for cavity testing at Cornell.

sinusoids at the drive frequency with time-varying phase shifts ϕ_{LO} and ϕ_{RF}:

$$v_{\mathrm{IF}} = K_{\mathrm{M}} v_{\mathrm{LO}} v_{\mathrm{RF}} \tag{3.84}$$

$$= K_{\mathrm{M}} V_{\mathrm{LO}} V_{\mathrm{RF}} \sin(\omega_{\mathrm{d}} + \phi_{\mathrm{LO}}) \cos(\omega_{\mathrm{d}} + \phi_{\mathrm{RF}}) \tag{3.85}$$

$$= K_{\mathrm{M}} V_{\mathrm{LO}} V_{\mathrm{RF}} [\sin(\phi_{\mathrm{LO}} - \phi_{\mathrm{RF}}) + \sin(2\omega_{\mathrm{d}} + \phi_{\mathrm{LO}} + \phi_{\mathrm{RF}})] \tag{3.86}$$

I have set v_{RF} as a cosine for mathematical simplicity. Assuming that ϕ_{LO} and ϕ_{RF} move slowly with respect to each other, the low-pass filter removes the high-frequency $\sin(2\omega_{\mathrm{d}})$ wave and leaves only the first term. This is the signal that reaches the FM (frequency modulation) port on the signal generator:

$$v_{\mathrm{FM}} = K_{\mathrm{M}} V_{\mathrm{LO}} V_{\mathrm{RF}} \sin(\phi_{\mathrm{LO}} - \phi_{\mathrm{RF}}) \tag{3.87}$$

This phase difference is equal to the phase difference between the cavity and the drive signal $\Delta\phi$, plus the external phase shift added by the path lengths of the lines between the components of the PLL ϕ_{ext}, plus the shift added by the manually adjustable phase shifter ϕ_{m}:

$$v_{\mathrm{FM}} = K_{\mathrm{M}} V_{\mathrm{LO}} V_{\mathrm{RF}} \sin(\Delta\phi + \phi_{\mathrm{m}} - \phi_{\mathrm{ext}}) \tag{3.88}$$

The VCO adjusts the drive frequency ω_d away from its center frequency ω_c based on v_{FM} multiplied by an FM gain factor K_{FM}:

$$\omega_d = \omega_0 + \delta\omega_d \tag{3.89}$$

$$\delta\omega_d = K_{FM} v_{FM} \tag{3.90}$$

Here $\delta\omega_d$ gives the difference between the time-varying drive frequency and the fixed center frequency of the VCO. We can define a similar factor for the difference between the time-varying resonance frequency of the cavity and VCO's center frequency:

$$\omega_r = \omega_0 + \delta\omega_r \tag{3.91}$$

We can reorganize Eq. 3.81 with the change of variables suggested by Eqs. 3.89 and 3.91:

$$\Delta\phi = \tan^{-1}\left(Q_L \frac{2\omega_0(\delta\omega_r - \delta\omega_d) + \delta\omega_r^2 - \delta\omega_d^2}{\omega_0^2 + \omega_0(\delta\omega_r + \delta\omega_d) + \delta\omega_r\delta\omega_d}\right) \tag{3.92}$$

In the approximation that $\omega_0 \approx \omega_r \approx \omega_d$ (*i.e.* $\delta\omega_d, \delta\omega_r \ll \omega_0$), the higher-order $\delta\omega$ terms drop out:

$$\Delta\phi = \tan^{-1}\left(\frac{2Q_L}{\omega_0}(\delta\omega_r - \delta\omega_d)\right) \tag{3.93}$$

If the argument of the inverse tangent function is small ($\delta\omega_r \approx \delta\omega_d$), then the phase difference is approximately linear:

$$\Delta\phi = \frac{2Q_L}{\omega_0}(\delta\omega_r - \delta\omega_d) \tag{3.94}$$

We can substitute this into Eqs. 3.88 and 3.90 to get a self-consistent solution for $\delta\omega_d$:

$$\delta\omega_d = K_{FM} K_M V_{LO} V_{RF} \sin\left(\frac{2Q_L}{\omega_0}(\delta\omega_r - \delta\omega_d) + \phi_m - \phi_{ext}\right) \tag{3.95}$$

We have already made the approximation that the first term in the sine function is small. If we then also adjust the manual phase shift ϕ_m to compensate for

ϕ_{ext}, we can use the small-angle approximation for the full argument of the sine function to linearize the problem:

$$\delta\omega_{\text{d}} = K_{\text{FM}} K_{\text{M}} V_{\text{LO}} V_{\text{RF}} \left(\frac{2Q_{\text{L}}}{\omega_0} (\delta\omega_{\text{r}} - \delta\omega_{\text{d}}) + \phi_{\text{m}} - \phi_{\text{ext}} \right) \tag{3.96}$$

Then we can solve for $\delta\omega_{\text{d}}$:

$$\delta\omega_{\text{d}} = \delta\omega_{\text{r}} \frac{2KQ_{\text{L}}}{\omega_0 + 2KQ_{\text{L}}} + \frac{\omega_0 K (\phi_{\text{m}} - \phi_{ext})}{\omega_0 + 2KQ_{\text{L}}} \tag{3.97}$$

Here I have grouped the gain factors and mixer input voltages into $K = K_{\text{FM}} K_{\text{M}} V_{\text{LO}} V_{\text{RF}}$. With the exception of K_{M}, these can be adjusted easily by the SRF test operator. Typical values of K are in the range of 1-10 MHz: $K_{\text{M}} \approx 1\ \text{V}^{-1}$, $V_{\text{LO}}, V_{\text{RF}} \approx 1$ V, and K_{FM} is set to 1-10 MHz/V. As a result, $KQ_{\text{L}} \gg \omega_0$, and we can make the following final approximation:

$$\delta\omega_{\text{d}} = \delta\omega_{\text{r}} + \frac{\omega_0 (\phi_{\text{m}} - \phi_{\text{ext}})}{2Q_{\text{L}}} \tag{3.98}$$

This result is stable when the following conditions are met (the approximations from above): the center frequency of the VCO is set near the resonance frequency of the cavity and the FM deviation is small,

$$\omega_0 \approx \omega_{\text{r}} \approx \omega_{\text{d}} \tag{3.99}$$

the deviations of the resonance and drive frequencies from the center frequency of the VCO are approximately equal,

$$\delta\omega_{\text{r}} \approx \delta\omega_{\text{d}} \tag{3.100}$$

the PLL gain is sufficiently high,

$$K = K_{\text{FM}} K_{\text{M}} V_{\text{LO}} V_{\text{RF}} \gg \frac{\omega_0}{2Q_{\text{L}}} \tag{3.101}$$

and the manual phase adjustment approximately compensates for the other phase shifts in the PLL system:

$$\phi_{\text{m}} \approx \phi_{\text{ext}} \tag{3.102}$$

In this case, the PLL correctly adjusts for any slight shifts in ω_r, due for example to microphonics, by adjusting ω_d such that $\Delta\omega = \omega_d - \omega_r$ remains constant (equal to the second term on the right hand side of Eq. 3.98). The phase difference $\Delta\phi$ is stable and the phase of the VCO is thus "locked" to the cavity phase.

To reach this stable phase-locked condition, the operator typically must adjust ω_0 and ϕ_m to satisfy the above conditions. Adjustment to K_{FM} may also be necessary to account for changes in V_{LO} and V_{RF}, which are proportional to the cavity voltage and the signal generator amplitude, respectively. Time-dependent system noise will typically satisfy the $\delta\omega_r \approx \delta\omega_d$ condition at some point, bringing the system into the phase-locked state. The operator can then manually adjust ϕ_m to minimize the second term of Eq. 3.98. In practice, operators usually adjust ϕ_m to maximize the field level in the cavity as measured by the transmitted power meter[4], which by Eqs. 3.82 and 3.83 occurs when the cavity is driven on resonance (i.e. $\delta\omega_r = \delta\omega_d$).

The above mathematical description is a good approximation of the PLL used in the Cornell SRF group. The true system is slightly more complicated: the low-pass filter does not perfectly and instantaneously select the low-frequency signal but in fact effectively integrates the input signal, resulting in a response time on the order of the cutoff frequency of the filter. The path lengths of the cables between the different components of the PLL as shown in Fig. 3.8 also add speed-of-light signal delays, and the VCO has a lag associated with the FM control unit and its gain setting. In all, this results in a delay on the order of nanoseconds to microseconds for 1.3 GHz cavities in normal testing operations. As long as $\delta\omega_r$ changes slowly on this time scale, the PLL will stay in the locked state.

[4] Alternatively, the operator can minimize the reflected power.

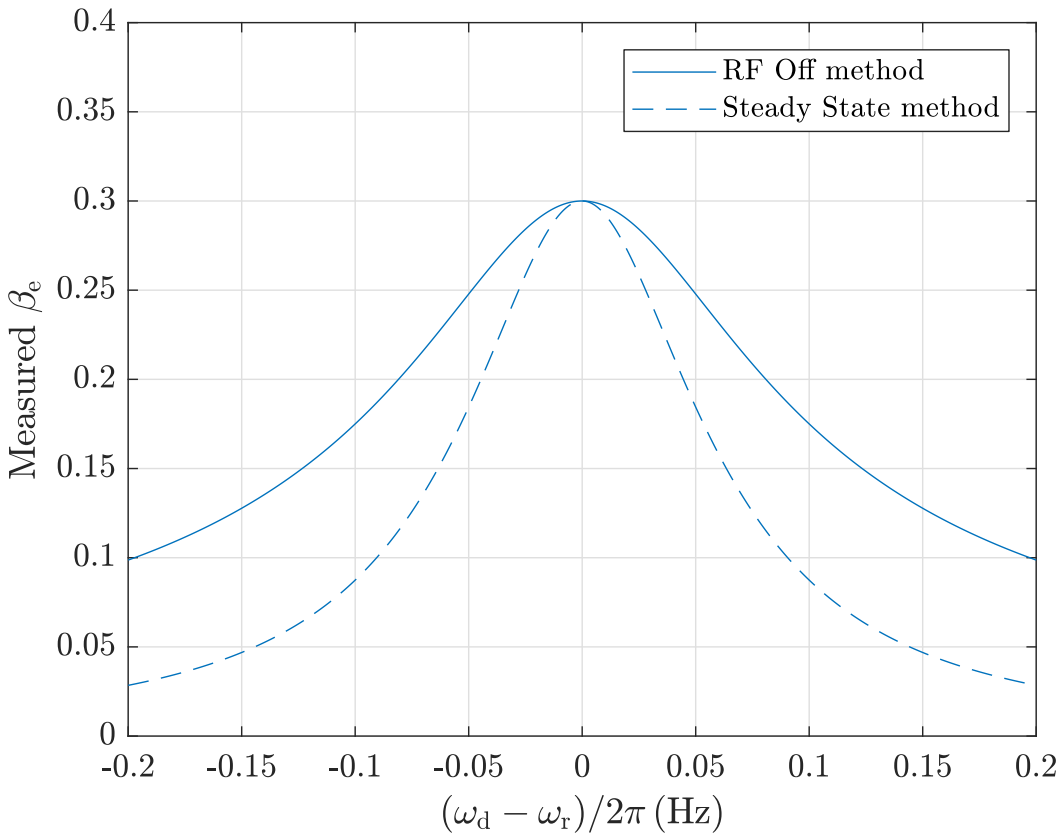

Figure 3.9: Error in the measured coupling factor of the FPC due to error in the cavity drive frequency, calculated by the RF Off and steady state methods. Results shown for $Q_0 = 1 \times 10^{10}$ and $f_0 = 1.3$ GHz with a true coupling factor of 0.3.

As mentioned in Sec. 3.3.3, we can use Eq. 3.80 to get a second measurement of β_e from the values of P_f in the steady state and P_e at the start of the decay. If the PLL has not been properly optimized so that $\omega_d = \omega_r$, then the two measurements of β_e will contain errors due to the decrease in U (Eq. 3.82). In the case when $Q_L = (Q_0^{-1} + Q_e^{-1})^{-1}$, as when cavities are under vertical test, then Eq. 3.82 becomes the following:

$$U = 4P_f \frac{\omega_r \omega_d^2}{Q_e} \left(\omega_r^2 \omega_d^2 \left(\frac{1}{Q_0} + \frac{1}{Q_e} \right)^2 + \left(\omega_d^2 - \omega_r^2 \right)^2 \right)^{-1} \tag{3.103}$$

The power coupled into the cavity P_{in} is equal to $P_{diss} = \omega U/Q_0$ as before, due to the conservation of energy, though U is now dependent on the frequency er-

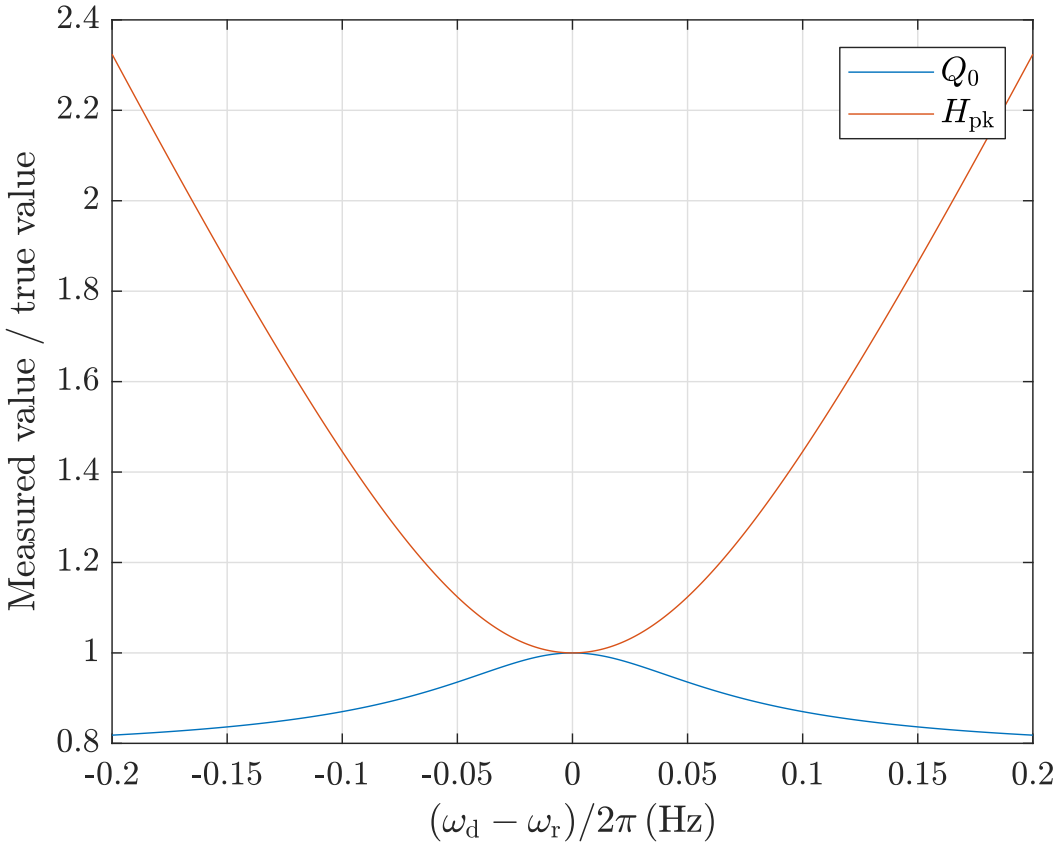

Figure 3.10: Error in the calculations of the intrinsic quality factor Q_0 and the peak surface magnetic field H_{pk} due to error in the cavity drive frequency. Results shown for the same parameters as Fig. 3.9.

ror. The steady-state reflected power $P_r = P_f - P_{in}$ as earlier in Eq. 3.74, and the emitted power at the moment the RF drive is turned off is $\omega U/Q_e$ as in Eq. 3.79. If one tries to determine β_e from the steady state measurement with Eq. 3.75 or from the RF Off measurement with Eq. 3.80, the error in U when $\omega_d \neq \omega_r$ will create an error in the calculated coupling factor. In particular, the two values of β_e will not agree; for the SRF test operator, noticing a mismatch between the two calculated values of β_e is a good sign that the PLL has not been optimized. Figure 3.9 shows the error in the calculation of β_e due to error in the PLL optimization for representative cavity parameters. This error in the measured value of β_e then affects the measurements of Q_0 and H_{pk}. Figure 3.10 shows example

results of the error in Fig. 3.9 propagated through the Q_0 and H_{pk} calculations. As mentioned in Sec. 3.3.3, we reject data for which the two measurements of β_{e} differ by $\geq$ 10%; for the example values in Figs. 3.9 and 3.10, this rejection threshold results in a 2.3% error in the measured value of Q_0 and a 3.4% error in the measured value of H_{pk}. A stricter threshold of 5% error between the β_{e} measurements would result in errors of 1.1% in Q_0 and 1.6% in H_{pk}, and a more relaxed threshold of 20% disagreement would result in errors of 5.0% and 8.6%, respectively.

3.3.5 Surface Heating and Thermal Concerns

In Section 3.2, we noted that the microwave surface resistance is highly dependent on temperature. In typical SRF applications, formed sheet-metal cavities are fitted with couplers and sealed into place on test inserts or in cryomodules. Vacuum is pulled inside, then the cavities are immersed in a liquid helium bath set to temperatures in the 1.5-4.5 K range for testing or operation. When an accelerating field is excited in the cavity, power is dissipated as heat on the interior of the cavity due to the surface resistance and pulled away by the bath and ultimately the refrigeration system. Any inefficiencies in heat transfer from the RF surface out to the bath result in an increased surface temperature $T_{\mathrm{s}} > T_{\mathrm{bath}}$; this increase in temperature leads to an increase in surface resistance. In SRF material studies, this complicates attempted measurements of the intrinsic surface resistance of samples under investigation. In accelerator applications, this decreases Q_0 and increases cryogenic power requirements; moreover, electron heating on the RF surface is a potential mechanism for the medium-field Q-slope (a gradual field-dependent decrease in Q_0 commonly observed in SRF cavities)

and can limit the achievable accelerating gradient in a cavity by thermal runaway quench (the cavity surface temperature becomes unstable and increases until it exceeds T_c) [VXP07, DHL17]. Three of the principal sources of inefficiency in this heat transfer are the thermal conductivity of the cavity bulk κ, the Kapitza resistance h_K, and the electron-phonon energy transfer rate Y.

Metals are typically known to have high thermal conductivity, especially at low temperatures: high-purity copper, for example, can exhibit thermal conductivity κ well in excess of 1 kW/m K at temperatures below 50 K [SDR92]. Heat in metals is primarily carried by electrons. However, as described previously, below T_c a large portion of a superconductor's electrons are condensed into Cooper pairs. Though they can carry electric current, these Cooper pairs do not contribute to the entropic process of heat transfer [KB96]. As a result, the thermal conductivity of superconductors is greatly reduced at temperatures below T_c. This is improved at very low temperatures, however, where phonon scattering is greatly reduced; this reduction allows phonons to make a significant contribution to the overall thermal conductivity. Figure 3.11 shows a calculation of the thermal conductivity of superconducting niobium as a function of temperature for several different values of RRR (the residual resistivity ratio, a measure of the purity of a metal that is related to the electron mean free path ℓ), as well as different values of the phonon mean free path ℓ_{ph}, using the model of Koechlin and Bonin [KB96]. Phonon scattering at grain boundaries is thought to be a major contribution to the lattice thermal resistance, so the average grain size is considered a reasonable approximation for ℓ_{ph} in niobium; for samples produced at Cornell, the niobium grains are on the order of 100-500 μm in size. Thermal conductivity for cavity-grade high-RRR niobium at an operating temperature of 2 K is typically estimated to be near 5-20 W/m K [KB96], and is

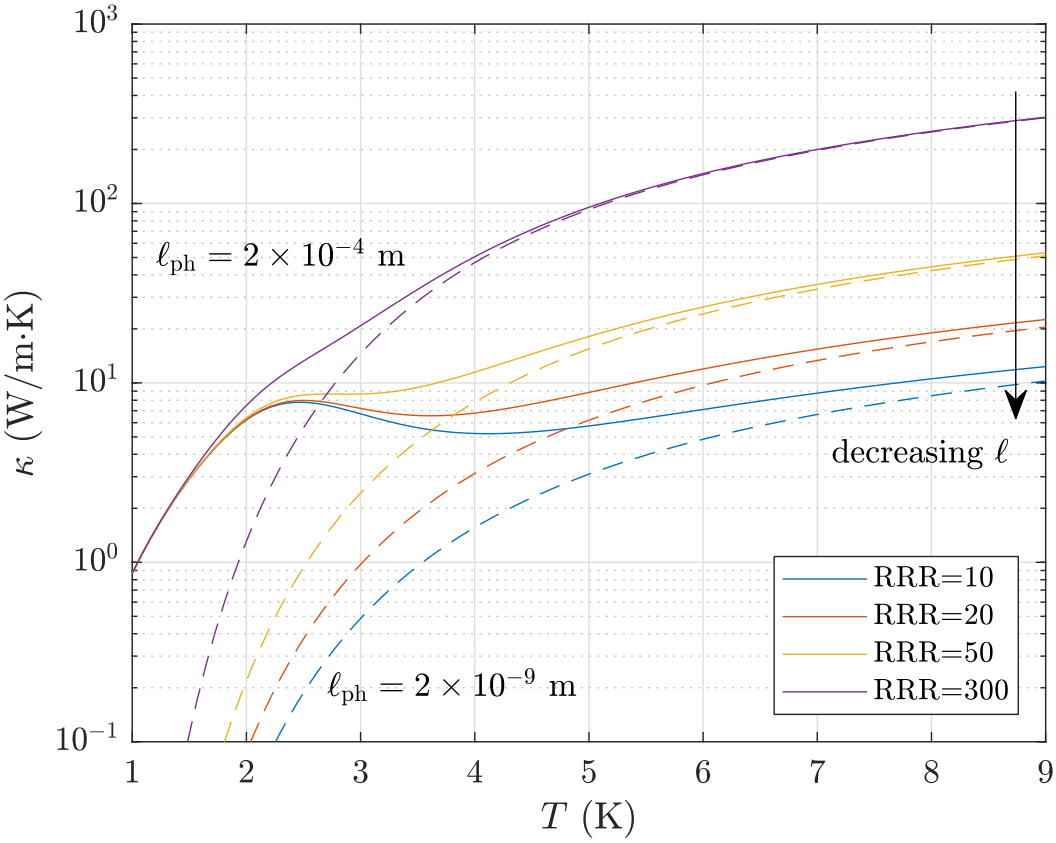

Figure 3.11: Calculation of the thermal conductivity of superconducting niobium from the model of Koechlin and Bonin [KB96]. Solid lines show results for large ℓ_{ph} resulting in a strong contribution to κ from phonons; dashed lines show the opposite.

dominated by the phonon contribution. The typical wall thickness for SRF cavities at Cornell is 3 mm, giving a thermal resistance in the range of 3-7 kW/m^{2}K.

The "Kapitza resistance" or alternatively the "Kapitza interface conductance" h_{K} is another contributing factor to the inefficient transfer of heat away from the cavity surface. The Kapitza resistance is thought to arise from a mismatch in phonon transport properties across the boundary between two different materials (*e.g.* niobium and liquid helium). This results in a temperature difference across the boundary proportional to the heat flow. The Kapitza resistance across the boundary between superconducting niobium and superfluid

helium has been measured to be in the range of 5 kW/m^{2}K [AF00].

Prior work studying heat transfer across SRF cavity walls has for the most part only considered these first two phenomena [VXP07]. However, the electron-phonon energy transfer rate provides yet another important source of inefficiency in heat transfer. The power dissipated by the oscillating electromagnetic field in an SRF cavity due to the surface resistance heats up the normal-conducting electrons near the vacuum interface. Since the thermal conductivity of the niobium bulk is dominated by the *phonon* contribution (as noted above), any inefficiency in the transfer of heat from the electrons to the phonons leads to a temperature difference between the two [KLT57, GHL$^+$06, TGK$^+$09]. Few experiments have been performed to quantify this inefficiency in niobium; later in this dissertation I will use the electron-phonon heat transfer coefficient as a free parameter in theoretical fits to experimental data in order to establish links between material parameters and observed effects that may be related to electron/quasiparticle overheating.

3.4 Testing SRF Cavities

Now that I have outlined some of the analytical methods of SRF accelerator physics experiment – adapting basic superconductivity theory to SRF cavity applications and detailing the mathematics of SRF measurements in cavities with couplers and non-uniform surface fields – I would like to elaborate on the practical procedures used in the Cornell SRF group to fabricate and test cavities.

3.4.1 Cavity Fabrication and Test Preparation

The current state-of-the-art procedure for the fabrication of niobium SRF cavities is deep-drawing of niobium sheets into the component parts of the cavity followed by electron-beam welding (EBW) of the parts to form the full structure[5]. At Cornell, our fundamental SRF research program primarily makes use of 1.3 GHz single-cell elliptical cavities of the TESLA/ILC design [ABB+00] that we fabricate in-house. We begin with fine-grain high-RRR niobium sheets, place them between machined 7075-grade aluminum dies, and deep-draw the sheets into half-cells using a hydraulic press. Figure 3.12a shows an example of a die pair used in the deep-drawing process (in this case for 2.6 GHz cavities). After pressing, the cups are trimmed and chemically cleaned in preparation for welding. Using EBW, we weld the two half-cells to cylindrical "beam tubes" at the irises, weld vacuum flanges to the other ends of the beam tubes, and finally weld the two assemblies together at the equator, completing the cavity. The flanges are either made from reactor-grade Nb or from NbTi, depending on the desired vacuum sealing method for the cavities; this choice of sealing method tends to have negligible impact on cavity performance but affects ease of assembly and disassembly.

After welding, the cavity is chemically polished to remove a 100-150 μm layer of niobium from the surface of the cavity, thereby cleaning away defects introduced by the machining process (scratches, small chips, *etc.*). We employ two different chemical polishing techniques, namely BCP (buffered chemical polishing) and EP (electropolishing). Modern high-performance niobium cavities are usually etched by BCP and then EP in succession, or alternatively entirely by EP

[5]The interested reader will find a detailed overview of SRF cavity fabrication procedures in W. Singer's course notes for the 2013 CAS-CERN Accelerator School [Sin14].

(a) Aluminum dies

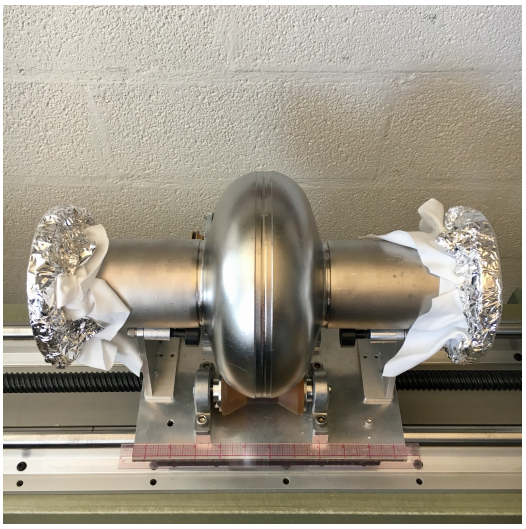

(b) Welded cavity with protective caps

Figure 3.12: Cornell's SRF cavities are formed by pressing niobium sheets between aluminum dies (at left). After pressing, the half-cells are welded by EBW into the final cavity shape (at right). The welds leave visible seams at the equator and irises.

(this method is slower but yields higher performance).

The BCP process consists of filling the cavity with BCP solution, a 1:1:2 mixture of 70% nitric acid, 48% hydrofluoric acid, and 85% phosphoric acid solutions, and allowing the acid to etch the surface by oxidization and dissolution of the oxide [KWS70]. At 20 °C, BCP etches niobium at a rate of about 1 μm per minute. The rate can be controlled by adjusting the temperature; we typically chill the acid in a refrigerator between mixing (an exothermic process) and etching (another exothermic process) and cool the exterior of the cavity by a continuous spray of chilled water during the etch to prevent excessive or runaway etching.

Unlike BCP, EP is an electrochemical process (see [CSF12, Cra17] for detailed explanations of the mechanism of niobium EP). At Cornell we EP our cavities in a vertical configuration. To perform this vertical EP or "VEP", we insert an

aluminum cathode rod into the vertically oriented cavity on its axis. We fill the cavity with a 10:1 mixture of 98% sulfuric acid and 48% hydrofluoric acid. We apply a 12 V potential between the cathode and the niobium cell, which engages the electrolytic polishing process: the surface undergoes anodization, and the hydrofluoric acid etches away the newly grown oxide layer, resulting in a new removal of niobium. The typical time-averaged surface current density at the niobium cavity during EP is 10 mA/cm^2. As with BCP, we chill the acid before VEP and externally cool the cavity by chilled water spray in order to control the removal rate and prevent runaway conditions; we usually keep the temperature in the 15-20 °C range. Niobium removal by EP is slower than in BCP, at about 5 μm per hour; however, due to the dynamics of the electrolyte near the niobium surface, surface peaks are etched away preferentially over the "valleys" and, as a result, overall surface roughness is reduced in the EP process.

After chemical etching, we clean the cavity first by rinsing with DI (deionized) water to remove acid and reaction residue. We then immerse the cavity in an ultrasonic cleaner with soap and water; this is followed by a second ultrasonic cleaning in DI water. The cavity is then transferred to a ISO class 10 clean room and finally cleaned with an HPR (high-pressure rinsing) system: $\sim$ 1000 PSI DI water jets are sprayed on the surface, rotating on the cavity axis and moving back and forth along the cavity axis to thoroughly clean any remaining residue from the surface. After HPR, we leave the cavity in the clean room to air-dry.

After chemistry and cleaning, we bake the cavity in a UHV (ultra-high vacuum) furnace to remove interstitial impurities, especially hydrogen, which can be absorbed during the EP process and can cause a certain type of performance

degradation called "Q disease" [Pad09]. This "degas" bake is usually performed at 800 °C for 3-6 hours.

To combat the effects of high-field Q-slope, a steep field-dependent degradation of Q_0 beginning at surface fields in the range of 80-100 mT [Pad09], the degas bake is optionally followed by a second bake at 120 °C for 48 hours. Between the two bakes the furnace is brought to room temperature and vented, allowing the native oxide layer to re-grow on the niobium surface. Possible explanations for this effect include the dissolution of an "oxygen pollution layer" in the 10-20 nm near the RF surface [Saf01, CMS+10] as well as a reduction or suppression of "nanohydride" growth on the surface [RECS13, BGS+19]; however, these results are as yet preliminary, and for now the reason for the suppression of the high-field Q-slope by the 120 °C bake remains unclear.

A recent development in the field of SRF is the discovery of "nitrogen doping", a treatment which greatly increases Q_0 for niobium cavities and which causes a further increase in Q_0 with increasing field strength [GRS+13][6]. This field-dependent effect is commonly known as the "positive Q-slope" or "anti-Q-slope" to distinguish it from the previously studied medium-field and high-field Q-slopes. Figure 3.13 compares the Q vs. H performance of a typical nitrogen-doped cavity to that of a cavity treated with an 800 °C degas bake; both cavities were treated with VEP before the baking step.

In general these doping treatments modify the degas bake, adding a doping step during which high-purity nitrogen gas is introduced into the vacuum furnace at low pressure (< 1 Torr) as well as an optional annealing step in UHV afterwards. These steps are performed in succession without returning the fur-

[6]Similar observations were presented in [DCM+13], but it remains unclear whether these effects were the result of nitrogen doping.

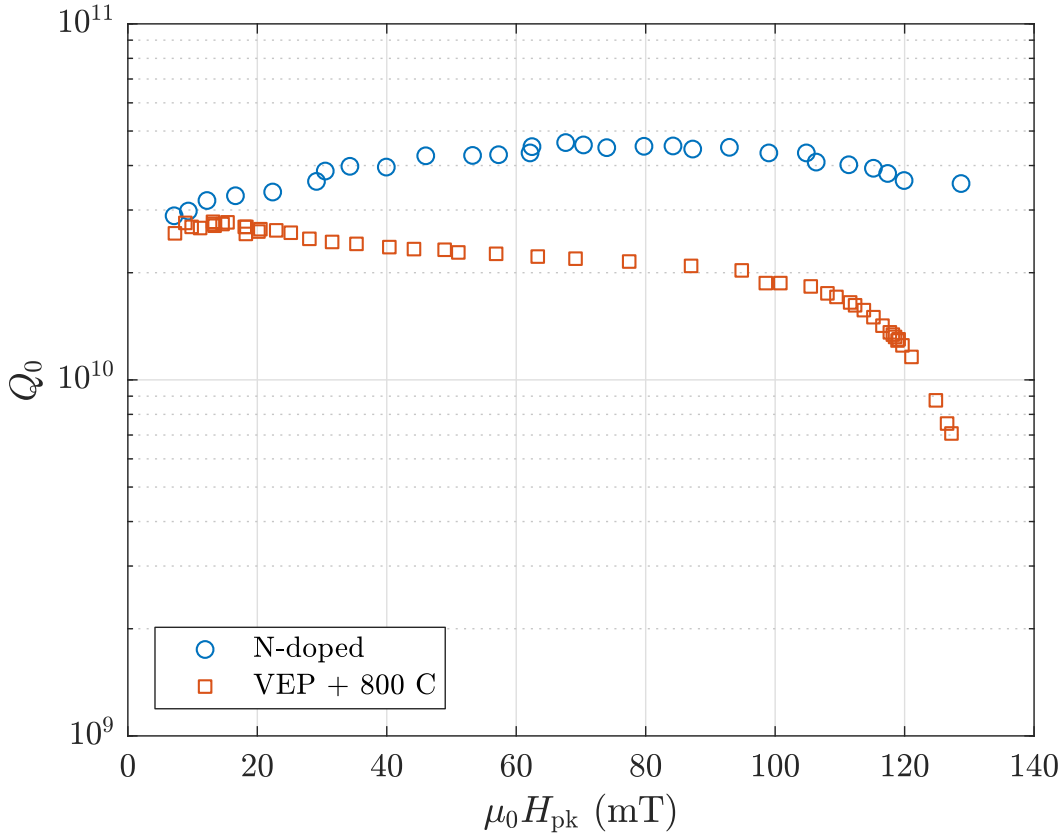

Figure 3.13: Comparison of Q vs. H curves at 2 K for a nitrogen-doped cavity and a "baseline" cavity treated with 800 °C degas.

nace to room temperature or venting in between. For cavities doped at high temperature (800-1000 °C), the 120 °C vacuum bake is typically omitted; high-field Q-slope may be present in some N-doped cavities[7] but this has not been studied in detail at time of writing. High-temperature doping is followed by a light EP to remove 5-20 μm of the surface, etching away a layer of niobium nitride and bringing the surface nitrogen concentration to a desirable level. Alternative "infusion" treatments take place at lower temperatures (120-160 °C) and may have some of the same benefits as the 120 °C vacuum bake. I will go into greater detail about the state of the art of nitrogen doping in the following chapter, and I will (as the title of this dissertation suggests) explore the funda-

[7]For example, see Fig. 3 in [GAB+19].

mental physics of nitrogen-doped niobium in the chapters to come.

After all chemical etches and heat treatments have been completed, we return the cavity to the class 10 clean room for another HPR and air-dry followed by assembly onto a vertical test stand "insert" like that pictured in Fig. 3.14a. The structure features an FPC with variable coupling, and the cavity is also typically fitted with a transmitted power coupler as described in Sec. 3.3.3. We then pump out the cavity to vacuum at a controlled rate to the region of $1{\times}10^{-7}$ Torr, which takes several hours. We check the cavity for leaks using a helium wand and an RGA (residual gas analyzer), spraying high-purity helium on the vacuum connection seals and measuring the amount of helium that leaks through into the cavity vacuum.

When the cavity has been pumped and found to be leak-tight, we dress the cavity and insert with various sensors for additional information collection during the test. In particular these include Cernox brand cryogenic temperature sensors [Laka], calibrated to the ±5 mK level down to 1.4 K, and Bartington brand fluxgate magnetometers [Bar], calibrated to a resolution of 0.1 nT. Additional instrumentation includes a pressure sensor for the cryogenic dewar and a helium level stick for measuring the depth of the liquid helium bath surrounding the cavity inside the dewar. Permanently installed in the test area are radiation monitors which can be used to detect field emission.

After dressing, we install the cavity insert into a cryogenic dewar, pump the dewar to vacuum, and begin the transfer of liquid helium into the dewar to cool the cavity below its superconducting critical temperature. This cooling can be done as a "fast cooldown" or a "slow cooldown". In a fast cooldown, we cool the dewar with a high flow of cold ($\approx$ 4.5 K) helium gas, building a

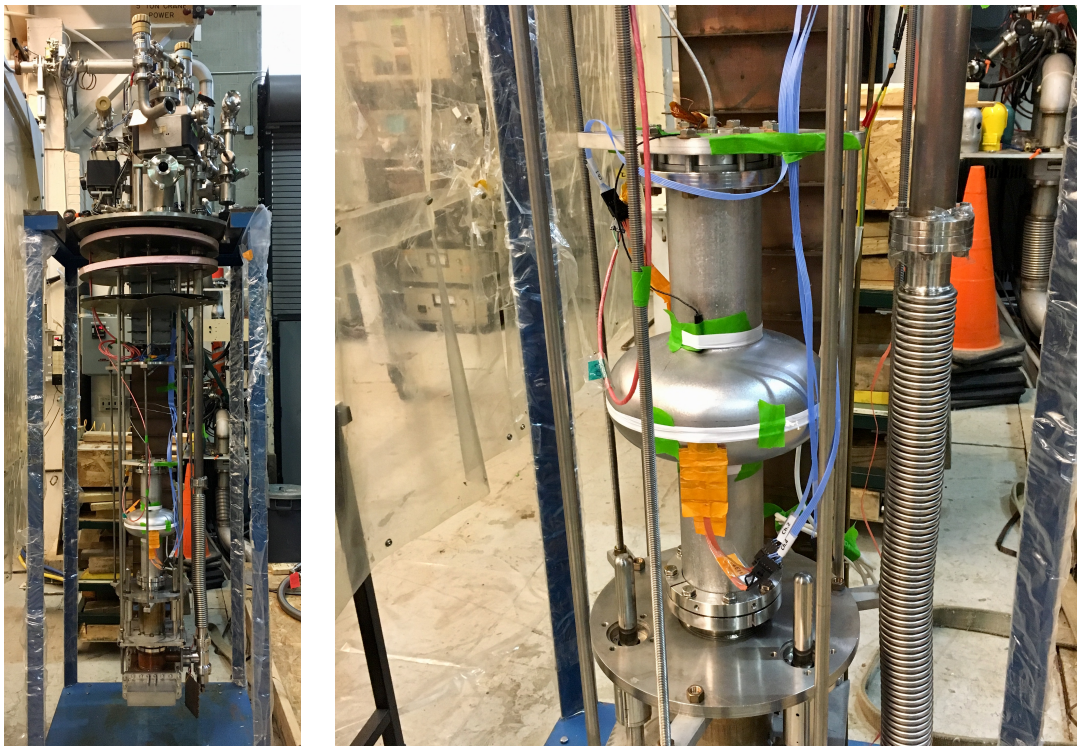

(a) Vertical test insert (b) Closeup of dressed cavity on insert

Figure 3.14: Single-cell cavities are usually tested vertically on stands like those pictured here. The cavities are dressed with instrumentation and the insert assembly is installed in a cryogenic dewar for testing.

large temperature gradient ($\geq$ 1 K/cm) across the cavity cell from iris to iris; as the cavity cools through T_c, the transition to the superconducting state occurs at a sharply defined boundary and magnetic flux is maximally expelled (see Sec. 3.1), minimizing trapped magnetic flux and any residual resistance caused by the trapped flux. Cooling quickly through the temperature range of 100-150 K also minimizes the effects of Q-disease by limiting the time available for hydride formation [Pad09]. Fast cooling has a potential negative side effect, however: large temperature gradients across parallel conducting components of the test setup can excite thermoelectric currents by way of the Seebeck effect, and these currents can generate magnetic fields that are not fully expelled by the cavity during the superconducting transition. This is also an important is-

sue for bi-metallic SRF cavities such as those made from Nb_3Sn, which feature a metal-metal interface parallel to the temperature gradient across the entire cavity. Fortunately for the tests of doped niobium cavities covered in this dissertation, these issues have largely been avoided.

In a slow cooldown, we first cool quickly through 100 K in order to limit the effects of Q-disease and then use heaters and throttle the flow of cold helium gas in order to stabilize the temperature of the cavity above T_c. Our criterion for stabilization is a temperature gradient of less than 10 mK across the cell (about 10 cm in length from iris to iris for a 1.3 GHz cavity). Once we have stabilized the temperature, we adjust the flow throttle and the heater power to slowly decrease the temperature of the cavity through T_c, maintaining a small temperature gradient across the cell. We use this process to intentionally trap a large amount of magnetic flux, usually to study the sensitivity of the residual resistance to trapped magnetic flux. In these tests we also install a Helmholtz coil around the cavity to provide an external DC magnetic field to trap; without the coil, the magnetic shielding in the dewar typically limits the ambient magnetic field to ≈ 5 mG. Slow cooling also limits thermoelectric currents and their resulting fields.

After cooldown, fast or slow, we finish filling the dewar with liquid helium at 4.2 K. Using a vacuum pumping system we can control the temperature of the helium bath to a precision of 10 mK between 1.4 K and 4.2 K. Below 2.17 K, helium becomes a superfluid and has excellent cooling capability; we do most of our testing with high RF field at temperatures of 2.1 K and below. With the cooldown completed and the cavity at the desired temperature, we begin testing the cavity under RF power.

3.4.2 Cavity Measurement Procedures

We excite the cavity with a phase-locked loop as described above in Sec. 3.3.4. Once the VCO is locked to the cavity and the drive frequency adjusted to match the resonant frequency of the cavity, we proceed with RF Off measurements as described in Sec. 3.3.3. The forward, reflected, and transmitted powers P_{f}, P_{r}, and P_{t} are measured at the meters indicated in Fig. 3.8. We adjust these measured values by the attenuation factors between points **A**, **B**, **C**, **D**, and **F** (measured before the test) to find the true values of P_{f} and P_{r} at the FPC (point **F**). We measure these values in the steady state, which by Eq. 3.75 gives a measurement of the coupling factor β_{e} and by Eq. 3.74 the power coupled into the cavity P_{in}. We then turn the RF drive power off; now in the undriven state, the field in the cavity decays exponentially. We measure the decay in P_{e} (picked up at the P_{r} meter); Fig. 3.15 shows example results from such a measurement. Fitting the time constant of the exponential decay yields a measurement of Q_{L} as in Eq. 3.79. Using β_{e} and Q_{L} in Eq. 3.73 gives us the intrinsic quality factor Q_0. The values of P_{f}, Q_0, and β_{e} give the steady-state value of U by Eq. 3.82, and finally we use the geometrical constants of the cavity to convert U into a measurement of H_{pk}, the peak surface magnetic field in the cavity. We then repeat this process at many field levels, building a Q_0 vs. H_{pk} curve to characterize the performance of the cavity under test.

Recent Cornell SRF test activities have also included measurements using the "continuous Q vs. H" method. This technique is fundamentally similar to the RF Off method but uses data from the full decay of the cavity field to calculate a continuous Q_0 vs. H_{pk} curve. As in the traditional RF Off method, we use power meter data from the start of the cavity decay curve to calculate $Q_{\mathrm{L}}(t = 0)$,

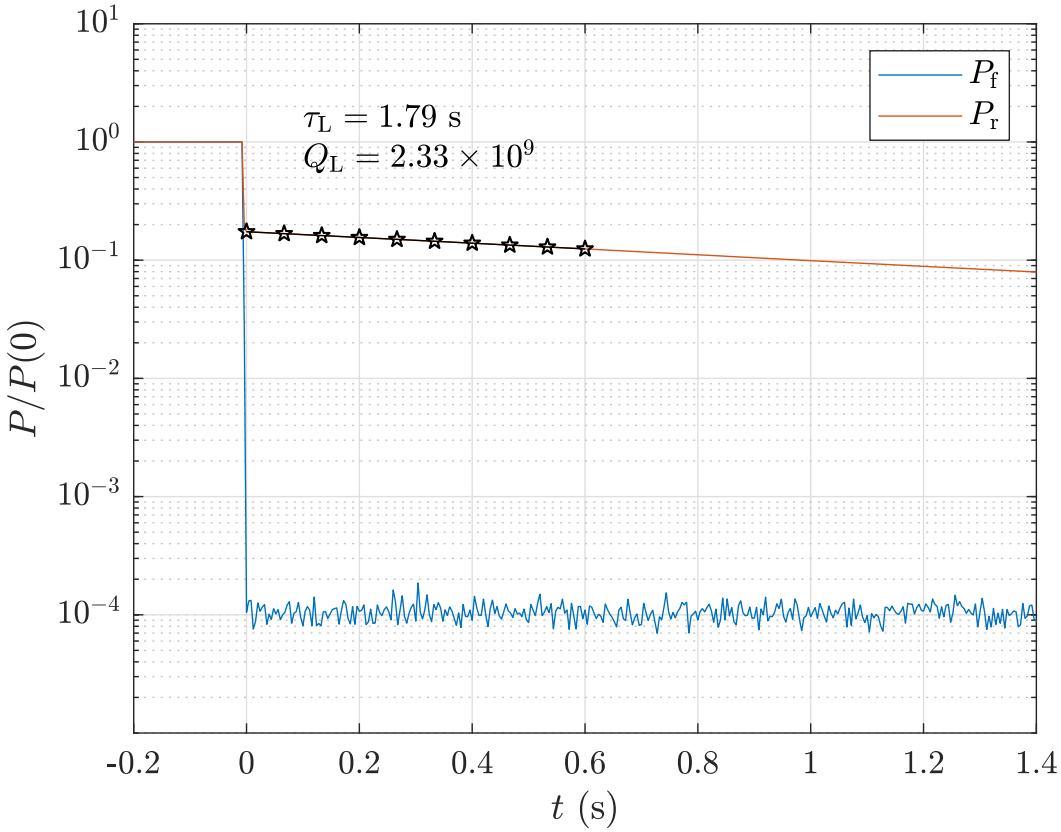

Figure 3.15: An example RF Off measurement of the forward and reflected power near the time when the RF drive is switched off. Black line with stars indicates the exponential fit of the loaded time constant.

β_e, and $H_{pk}(t = 0)$. Then at each point along the decay curve, we perform another exponential fit, resulting in a measurement of the loaded quality factor as a function of time, $Q_L(t)$. Assuming Q_e and the attenuation factors to remain fixed during the measurement, we first calculate $Q_0(t)$ from $Q_L(t)$ and then use the $P_e(t)$ data to get a measurement of the peak field as a function of time, $H_{pk}(t)$. Finally, we combine these parametrically, resulting in a continuous $Q_0(H_{pk})$ curve. In general this method is very consistent with the traditional RF Off method. Figure 3.16 shows example results using both methods. This process is then repeated at many temperatures, resulting in a three-dimensional Q_0 vs. H_{pk} vs. T set of data to characterize the RF performance of the cavity under test.

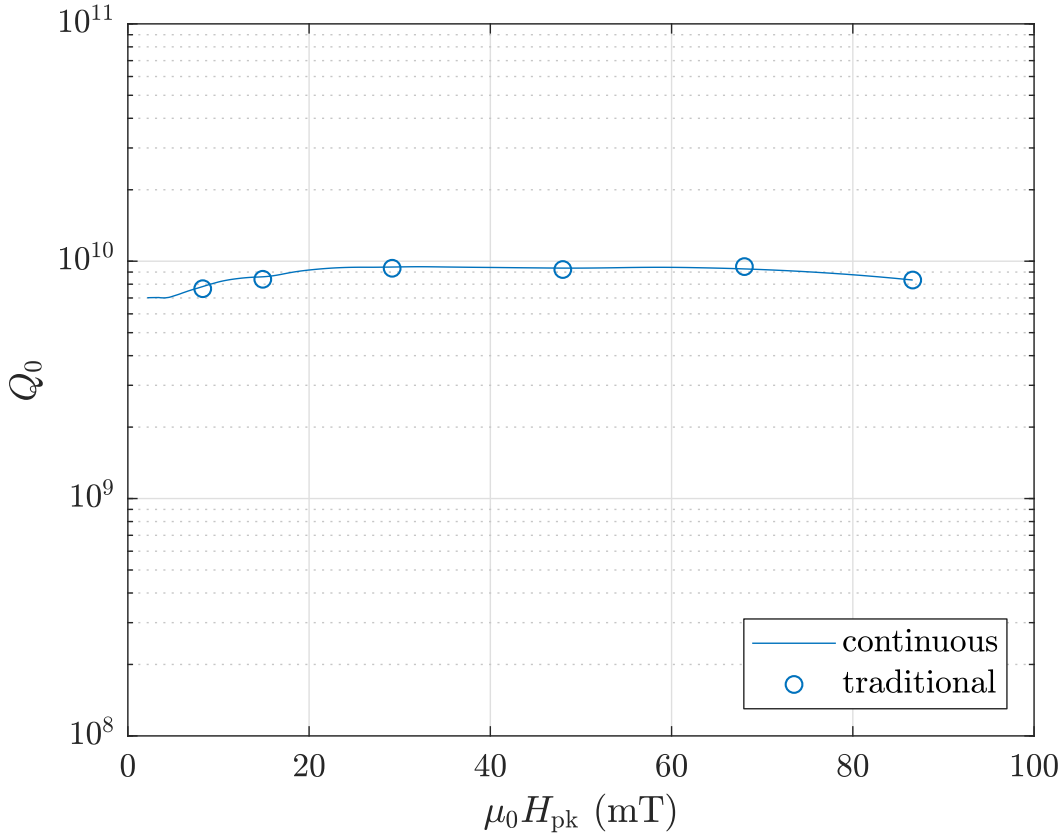

Figure 3.16: Example measurements of Q_0 vs. H_{pk} for a 1.3 GHz niobium cavity at 2.0 K, using both the continuous Q vs. H and traditional RF Off methods.

After the bulk of RF testing is completed for a cavity, we perform a final measurement, tracking the resonance frequency f_{r} of the cavity as a function of temperature. Near T_{c}, the penetration depth of the cavity λ increases in a manner that is dependent on the electron mean free path ℓ near the cavity surface. As a result of this increase, the cavity effectively increases in volume, and the resonance frequency decreases; for 1.3 GHz TESLA cavities, this decrease is on the order of tens of kHz per μm increase of λ.

With this extensive data set in hand, we turn to theoretical calculations to extract the material parameters of the RF surface of the cavity. In particular we are interested in the temperature-dependent surface resistance R_{BCS}, the

temperature-independent residual resistance R_0, the critical temperature T_c, the reduced energy gap $\Delta(0)/k_B T_c$, and the electron mean free path ℓ. We first extract T_c by measuring the temperature above which f_r ceases to change; this indicates that the RF surface of the cavity is fully normal-conducting. We then use a MATLAB routine written by N. R. Valles that performs alternating theoretical fits of f_r vs. T and of R_{BCS} vs. T at low RF field (usually near 10 mT) [Val14]. At its base this program uses the SRIMP code, an algorithm developed by J. Halbritter that performs numerical calculations of BCS theory to find R_{BCS} and λ as functions of temperature based on the material properties of a cavity [Hal70]. This extracts a measurement of ℓ as well as low-field values of $R_{BCS}(T)$, R_0, and Δ. We then use T_c and ℓ to fit the model against the field-dependent data, extracting $R_{BCS}(T, H_{pk})$, $R_0(H_{pk})$, and $\Delta(H_{pk})$. Figure 3.17 shows example fit results from typical cavity test data; note that SRIMP uses RRR as a stand-in for ℓ, with the relation RRR= $\ell/5.99$ nm.

These measurements and calculations are the bread and butter of the SRF testing program at Cornell. In the next chapters I will discuss many cavity test measurements; in general, these use the methods described above.

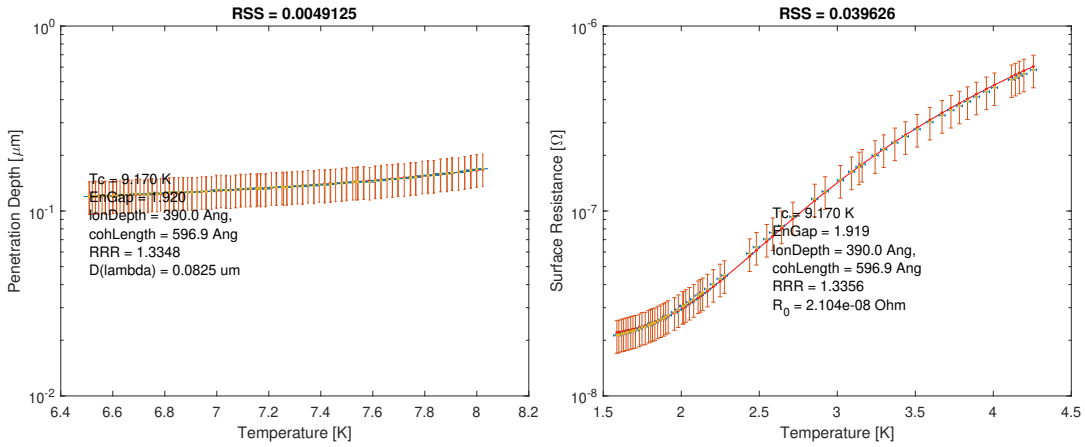

(a) Fitting λ vs. T

(b) Fitting R_{BCS} vs. T at low field

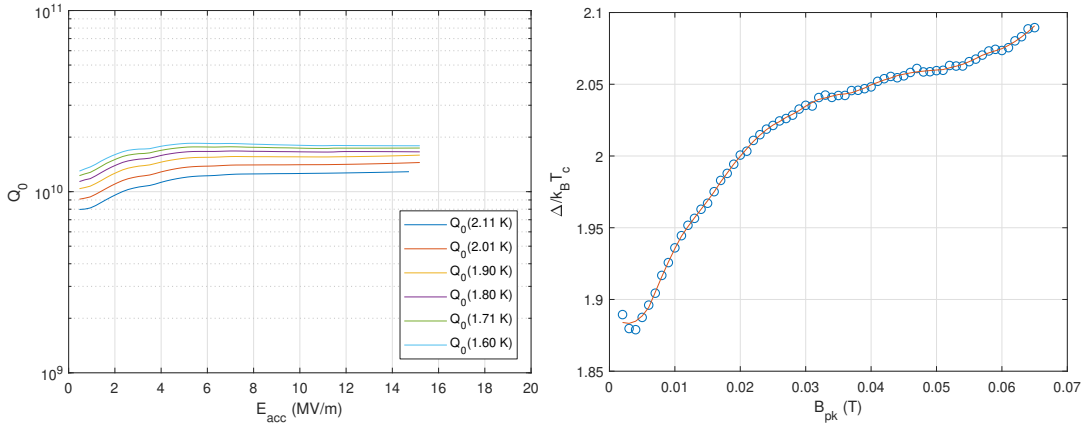

(c) $Q_0(T)$ vs. E_{acc}

(d) $\Delta/k_{\mathrm{B}}T_{\mathrm{c}}$ vs. $B_{\mathrm{pk}} = \mu_0 H_{\mathrm{pk}}$

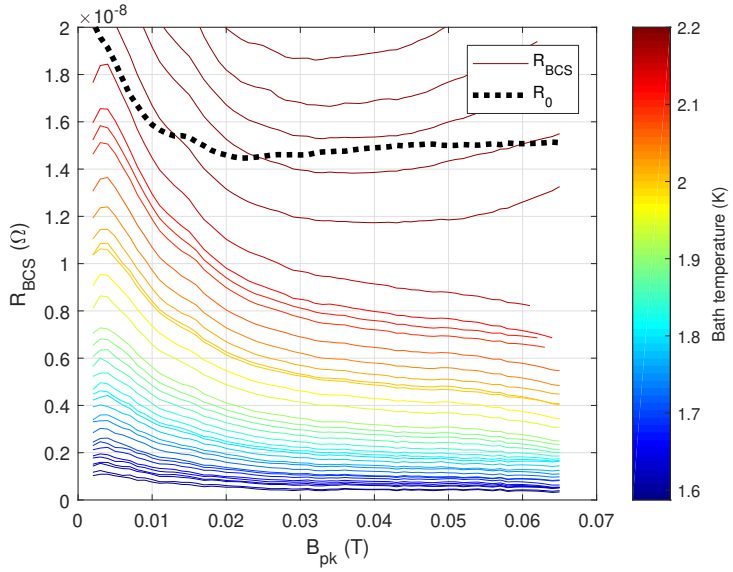

(e) $R_{\mathrm{BCS}}(T)$ and R_0 vs. $B_{\mathrm{pk}} = \mu_0 H_{\mathrm{pk}}$

Figure 3.17: Example measurement and fit results for a 1.3 GHz cavity. $E_{\mathrm{acc}} = \mu_0 H_{\mathrm{pk}}/4.23$ mT for this geometry.

CHAPTER 4

NITROGEN DOPING AND INFUSION: AN OVERVIEW

One of the most significant advances in niobium SRF technology in the last decade has been the discovery in 2013 of "nitrogen doping", a mild cavity treatment protocol with a large impact on RF performance [GRS+13]. The nitrogen doping procedure enriches the first few tens of micrometers of the niobium cavity surface with nitrogen at a level of approximately $\sim$ 0.1 at.%; beneath the doped surface layer the niobium bulk remains "clean" with very low impurity content. Experimentally, the BCS surface resistance in nitrogen-doped cavities at low field levels is usually reduced compared to cavities prepared with the baseline treatment (EP + 800 °C vacuum bake, as described in Ch. 3). Moreover, many of these cavities also exhibit a further decrease in R_{BCS} with increasing RF field strength. This results in an intrinsic quality factor Q_0 that increases with field, an effect known as the "positive Q-slope" or "anti-Q-slope". The efficiency of these nitrogen-doped cavities (as measured by Q_0) is improved by as much as a factor of 3 at higher fields over the previous state-of-the-art treatments. Figure 4.1, a reproduction of Fig. 3.13, demonstrates this improvement in Q_0 for a representative nitrogen-doped cavity as compared to a baseline treatment of the same cavity.

In this chapter I will detail the nitrogen doping procedure, its effect on the chemical composition of the RF surface, and its effects on the RF performance of niobium cavities. I will also cover some variations to the doping protocol, in particular introducing the "nitrogen infusion" treatment. Finally, I will lay out the questions that will guide the investigations presented in the remainder of this dissertation.

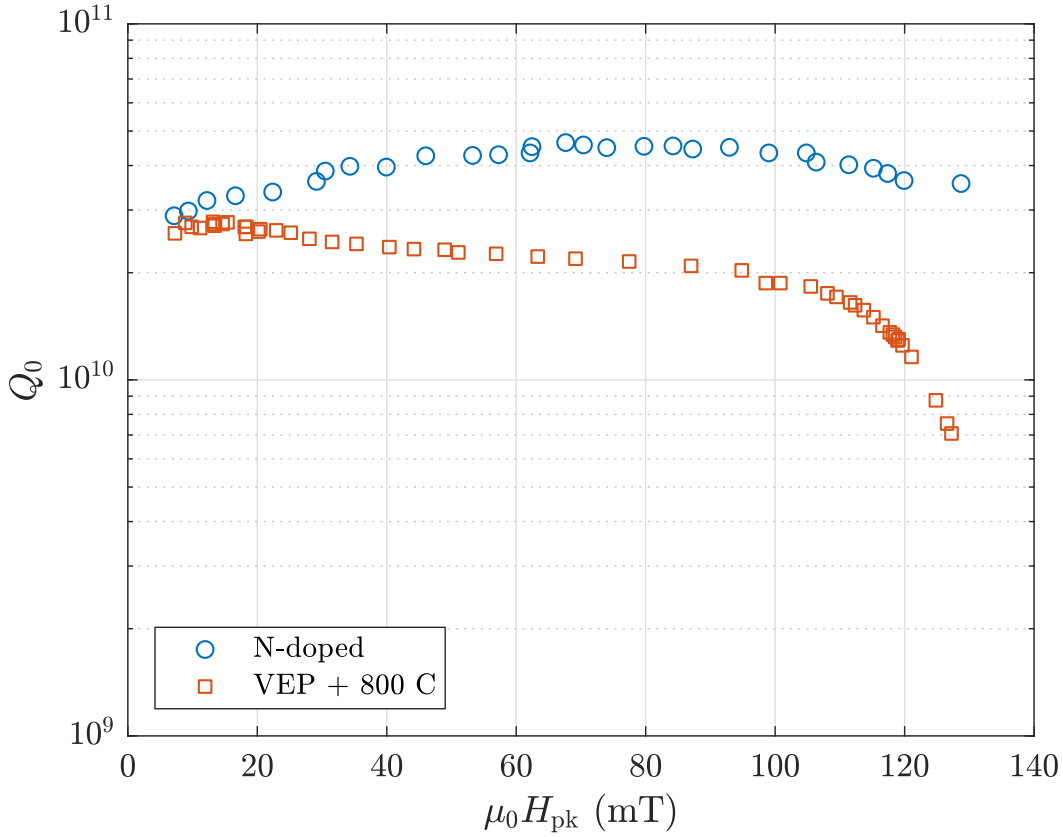

Figure 4.1: Comparison of Q vs. H curves at 2 K for a nitrogen-doped cavity and a "baseline" cavity (reproduction of Fig. 3.13).

4.1 Nitrogen Doping Procedures

As outlined briefly in Sec. 3.4.1, nitrogen doping is a variation of the standard 800 °C degas treatment in modern niobium cavity fabrication procedures. Discovered at FNAL (Fermi National Accelerator Laboratory) in 2013 [GRS+13], the treatment adds a short doping step after the degas bake. The furnace is maintained at the degas temperature or brought to the desired doping temperature (typically 800 °C). A small amount of high-purity dry nitrogen gas is let into the furnace through a particle filter, typically up to a pressure of 20-60 mTorr (the process is not sensitive to variations in nitrogen pressure over this range [Gon16]). The niobium cavity, which following the degas bake has

very low internal impurity content and almost[1] no surface oxide barrier, readily absorbs nitrogen into its surface. This absorption is allowed to continue for a short time, with 2 minutes being a standard length of the doping step. After this short step, the furnace is brought back to high vacuum, removing the nitrogen gas. The furnace is left at the doping temperature for an optional annealing step, with 6 minutes being a typical duration in previous R&D studies. During this time, the nitrogen in the cavity surface is able to diffuse further into the bulk. After the annealing step, or directly after the doping step if no anneal is performed, the furnace is ramped back down to room temperature and then vented with filtered air. The cavity is then removed from the furnace for further treatment.

After the doping process, the chemical composition of the surface of the cavity is greatly altered. Figure 4.2 shows an example of the concentration of nitrogen in the cavity surface as a function of depth; this data was measured using SIMS (secondary ion mass spectrometry) on a single-crystal electropolished niobium witness sample treated alongside the cavity. This cavity was doped at 800 °C for 20 minutes and then annealed for 30 minutes. Also presented in Fig. 4.2 is a calculation of the electron mean free path ℓ calculated from the nitrogen concentration by the following:

$$\ell = \frac{\sigma}{\Delta\rho} \tag{4.1}$$

$$\Delta\rho = \left(5.2 \times 10^{-8}\ \Omega\mathrm{m}\right) c' \tag{4.2}$$

Equation 4.1 relates the electron mean free path ℓ to the change in normal-conducting resistivity $\Delta\rho$ due to the presence of impurities in the niobium, with $\sigma = 0.37 \times 10^{-15}\ \Omega\mathrm{m}^2$ [GK68]; in turn, Eq. 4.2 gives the change in resistivity for a

[1] An oxygen monolayer exists on niobium surfaces at least up to 2000 °C [VKFS19].

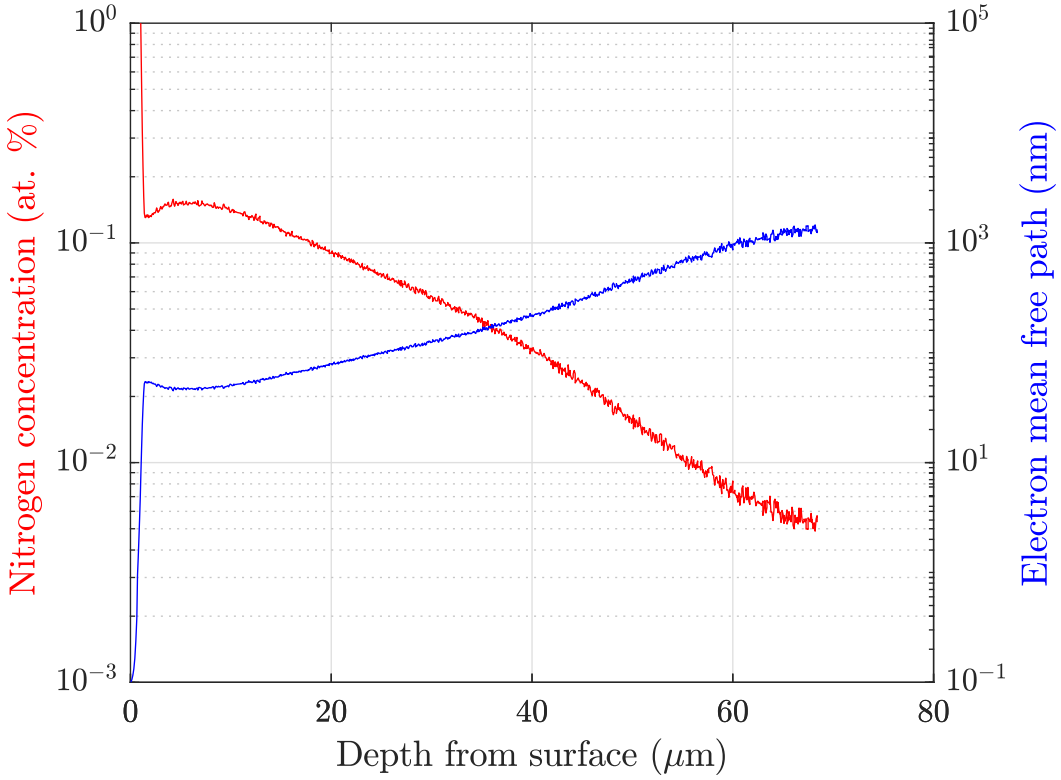

Figure 4.2: SIMS results of nitrogen concentration and resulting electron mean free path ℓ near the RF surface after doping at 800 °C and before EP. Figure adapted from [Gon16].

given concentration of nitrogen c' in units of at.% [Pad09].

The doping process leaves a thin surface layer (2-5 μm) with a very high concentration of nitrogen, commonly understood to be a layer of lossy niobium nitride [TGMR15]. The cavity is treated with EP to remove this layer and expose the doped layer underneath. After this final EP, typical values of ℓ on the cavity surface range from 1-200 nm. At this point the cavity is ready for HPR and installation.

Doping protocols (or "recipes") are typically named to indicate the doping time, annealing time, and post-dope EP depth; for example, the cavity indicated in Fig. 4.2 received a "20/30 dope" followed by later etching of 24 μm (not

indicated in the SIMS results). In this dissertation I will generally refer to doping protocols by these names, also indicating the doping temperature which is sometimes omitted in the literature.

4.2 RF Performance of Nitrogen-Doped Cavities

Despite the relatively small changes made to the material composition of niobium after the nitrogen doping process, nitrogen-doped niobium and non-doped clean niobium behave remarkably differently under accelerator conditions. Here I will lay out some of the major positive and negative changes that nitrogen doping brings to the RF performance of niobium SRF cavities.

4.2.1 Positive Effects of Nitrogen Doping

Nitrogen doping of niobium has been studied most extensively at 1.3 GHz, the design frequency of the TESLA cavity geometry [ABB+00] and a very common frequency for niobium SRF cavities used for electron acceleration over the last few decades (for example EXFEL, LCLS-II, and CBETA). At this frequency and when operating below the liquid helium superfluid transition temperature of 2.17 K, the BCS surface resistance of nitrogen-doped cavities shows two substantial changes compared to that of "clean" non-doped cavities. First, at low fields ($\mu_0 H_{\mathrm{pk}} \approx 10$ mT), R_{BCS} is reduced in all but the most strongly doped cavities; this follows from the reduction of the mean free path as discussed in Sec. 3.2 (in particular, see Fig. 3.2). Figure 4.3 shows the low-field R_{BCS} for several nitrogen-doped cavities compared with the theoretical prediction from numer-

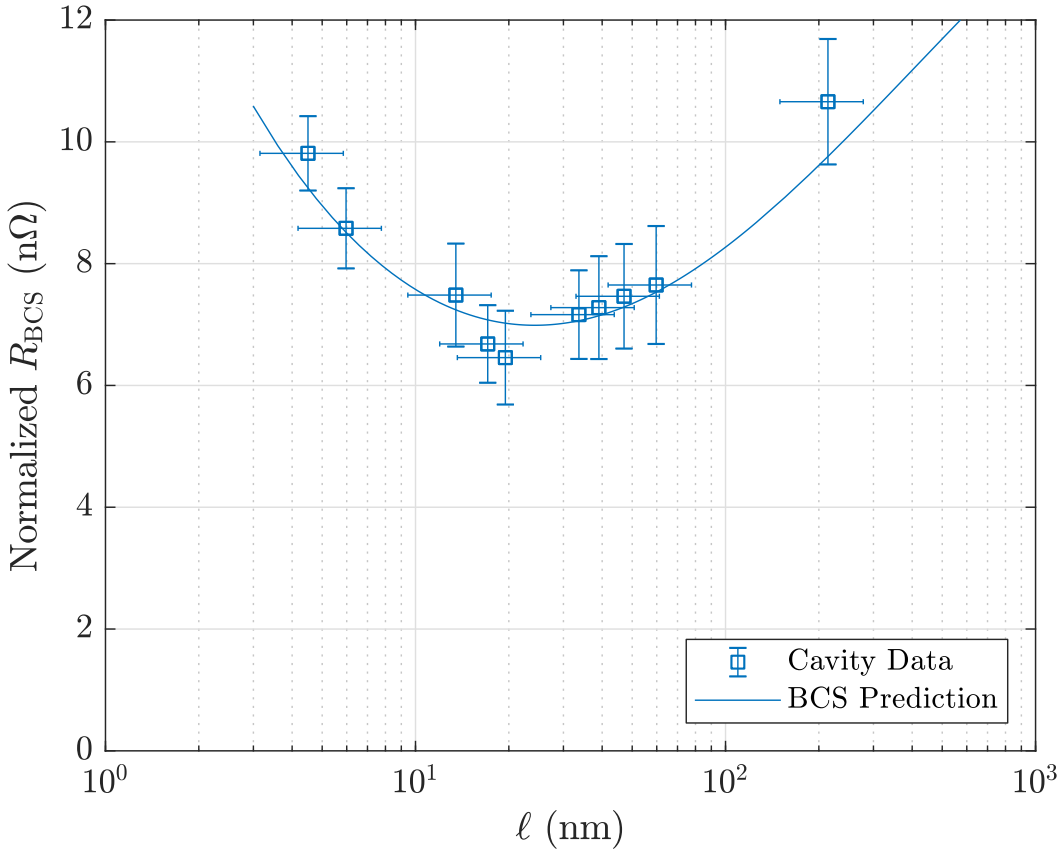

Figure 4.3: Low-field BCS surface resistance for nitrogen-doped cavities at 2 K as a function of mean free path compared to theoretical prediction; R_{BCS} has been normalized for variations in $\Delta/k_B T_c$. First published in [MGL17].

ical calculations of BCS theory, normalized for differences in $\Delta/k_B T_c$ [MGL17]. Cavities doped to a mean free path of $\sim$ 20 nm have the strongest reduction in R_{BCS} at low fields, with about half the BCS surface resistance of non-doped cavities.

Second, as the RF field strength increases, R_{BCS} tends to decrease, and can be reduced by as much as another factor of 2. This is the most exciting change between clean and doped niobium cavities, as it allows for unprecedentedly high efficiency of acceleration. As we shall see in Ch. 5, the magnitude of the decrease in R_{BCS} is strongly dependent on ℓ [MGL17]. This decrease is most dramatic in

cavities doped to the shortest mean free paths, saturating near $\ell = 10$ nm. At lighter doping levels, with $\ell \geq 200$ nm, the relative decrease in R_{BCS} with increasing field is negligible. Unlike the low-field change in R_{BCS}, this high-field behavior of nitrogen-doped cavities is not yet well understood. The primary focus of the investigations in this dissertation is to work towards building a theoretical understanding of the field-dependent reduction of the BCS surface resistance.

4.2.2 Negative Effects of Nitrogen Doping

Nitrogen doping also has some negative effects on the RF performance of niobium SRF cavities. One critical issue in nitrogen-doped cavities is the sensitivity of the residual resistance R_0 to trapped magnetic flux. As described in Sec. 3.1, magnetic flux can become trapped in the cavity wall during cooldown if there is not a strong thermal gradient parallel to the surface or if there are flux-trapping defects present in the cavity. Magnetic flux thus trapped in the cavity surface can oscillate under RF excitation, and under certain conditions this can cause losses that appear as an additional temperature-independent surface resistance [GC13, LHK+18]. SRF cavities show a sensitivity to trapped magnetic flux that scales linearly with the strength of the trapped field:

$$R_0 = R_{0,\mathrm{native}} + S \cdot B_{\mathrm{trapped}} \tag{4.3}$$

Here, $R_{0,\mathrm{native}}$ is the residual resistance of the cavity not caused by trapped magnetic flux, B_{trapped} is the average magnetic flux density trapped in the cavity wall, and S is the cavity's trapped flux sensitivity. Figure 4.4 shows an example of this linear relation. In addition to the magnitude of the trapped field, S depends on

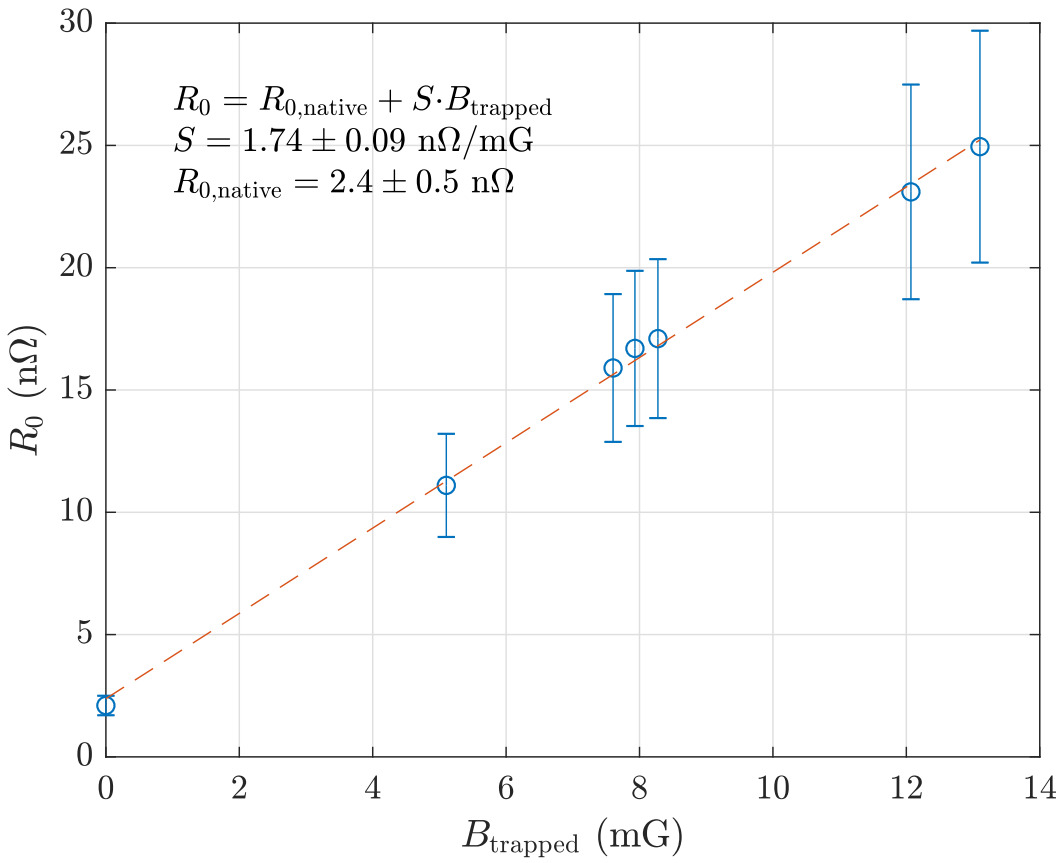

Figure 4.4: Sensitivity of the residual resistance of an example nitrogen-doped cavity to trapped magnetic flux (ℓ = 8.8 nm). The cavity was prepared at FNAL and tested at Cornell.

the orientation of the cavity with respect to the trapped field; most trapped flux studies (and all such studies presented in this chapter) align the field with the axis of the cavity. S also depends on ω to varying degree for different SRF materials [LHK+18, Hal17, Gon16].

Experimental studies have revealed a strong non-linear dependence of the sensitivity S on the electron mean free path ℓ in nitrogen-doped cavities. Figure 4.5 shows this sensitivity as a function of ℓ for a number of 1.3 GHz nitrogen-doped cavities prepared at Cornell. Towards the non-doped clean limit, S tends towards 0.2-0.5 nΩ/mG of trapped flux. The sensitivity peaks near a mean free

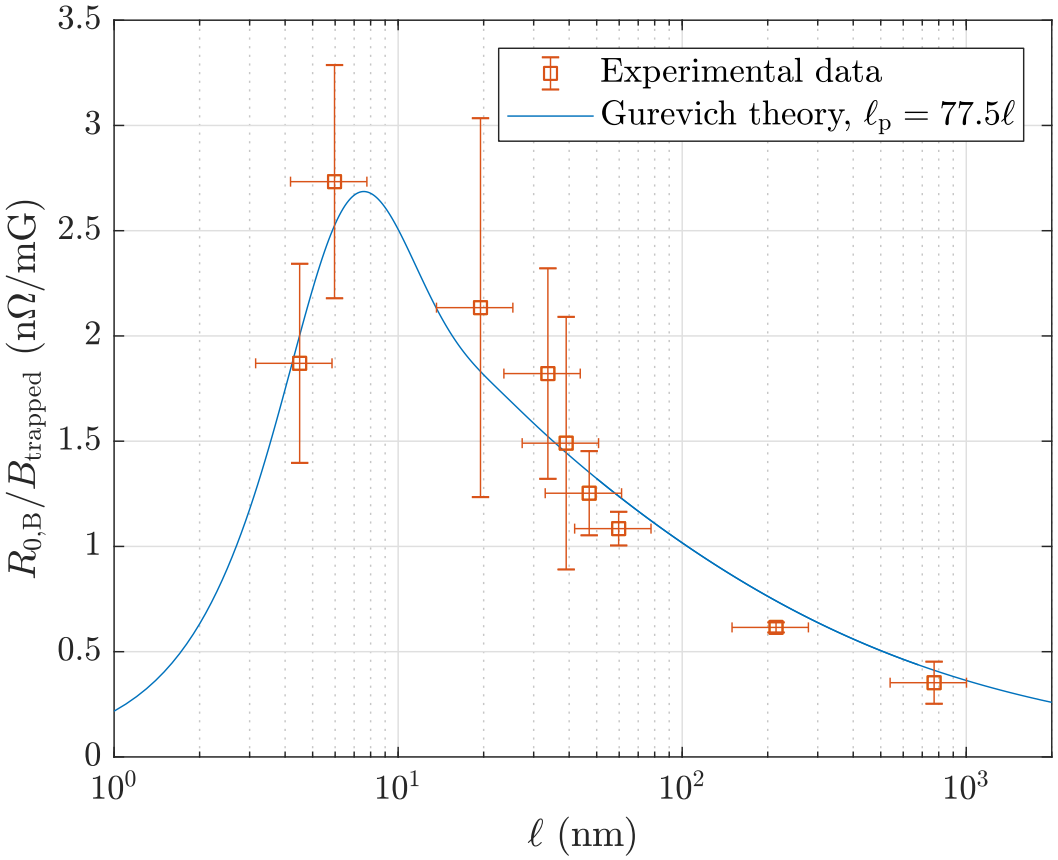

Figure 4.5: Sensitivity of the residual resistance of nitrogen-doped cavities prepared at Cornell to trapped magnetic flux as a function of electron mean free path ℓ. Line indicates theoretical prediction from [GC13], using $77.5 \cdot \ell$ as the pinning spacing ℓ_p. This figure is an updated version of a figure presented in [MGL17], now accounting for geometrical corrections to the measurements of trapped flux [Por19] and to the theoretical sensitivity [LHK+18].

path[2] of 5-10 nm, where $S \approx 2.5$ nΩ/mG. Ambient magnetic fields in shielded cryomodules and test dewars are typically in the range of 5 mG; since R_{BCS} at a standard operating temperature of 2 K is 6-12 nΩ, the high sensitivity of nitrogen-doped cavities can cause quite a significant increase to the total surface resistance if the ambient flux is not efficiently expelled during cooldown.

[2]Something interesting to note is that nitrogen-doped cavities prepared at FNAL have shown qualitatively similar sensitivity to trapped magnetic flux but with the peak at a different value of ℓ (see for example Fig. 1 in [MGC+16]); this discrepancy is not yet understood.

Also shown in Fig. 4.5 is a theoretical calculation of $S(\ell)$ using the model presented in [GC13]. In this model, magnetic vortices are strongly pinned at locations through the surface, and their oscillations fall into two regimes of behavior sensitive to the mean distance between pinning sites ℓ_p. When ℓ_p is very short, the vortices are strongly pinned in place, with only a small portion of each trapped vortex contributing to the dissipative losses. As ℓ_p increases, vortex oscillations between pinning sites increase in magnitude, increasing losses. On the other hand, when ℓ_p is long, vortices are largely unpinned and free to oscillate with large amplitude and low line tension; dissipative losses are limited, decreasing further with increasing ℓ_p. There is a crossover between these two regimes where the losses peak at an intermediate value of ℓ_p. We have found good agreement between Cornell trapped flux sensitivity data in nitrogen-doped niobium cavities at 1.3 GHz and the Gurevich flux sensitivity model by setting[3] $\ell_p = 77.5 \cdot \ell$ [GKL16].

A further limitation of nitrogen-doped cavities is a tendency towards low quench fields [Gon16]. This effect is highly dependent on the doping protocol, with more strongly doped cavities tending towards lower quench fields, but has not yet been studied thoroughly. The cavities studied in this dissertation typically reached quench fields in the range of 65-100 mT, whereas non-doped cavities prepared at Cornell regularly reach 130 mT or more.

[3]This coefficient is updated from the one originally presented in [GKL16] after refitting with the geometric corrections offered in [Por19] and [LHK+18].

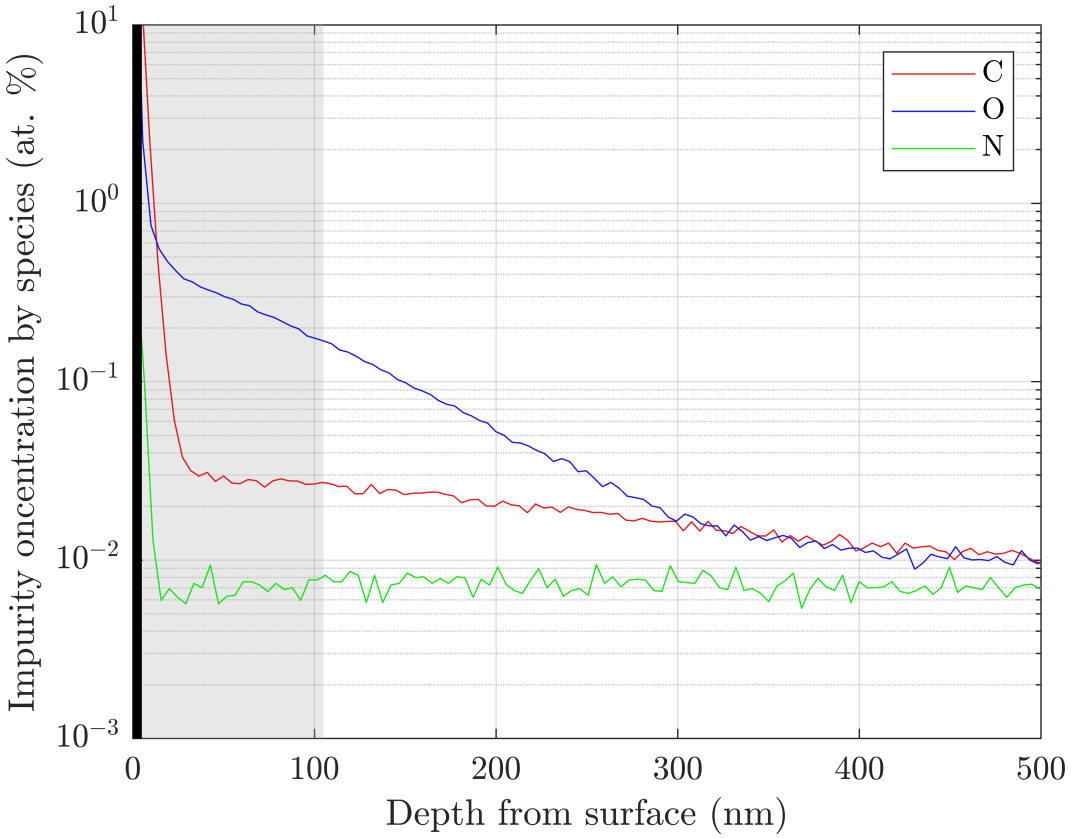

Figure 4.6: SIMS results of nitrogen, oxygen, and carbon content of a cavity treated with 160 °C nitrogen infusion for 48 hours. Gray area approximates the RF penetration layer.

4.3 Nitrogen Infusion

A more recent development related to the nitrogen doping of niobium is the so-called "nitrogen infusion" process. This is a similar treatment protocol to nitrogen doping, but with the doping step taking place at a much lower temperature and for a much longer time [GRT+17, KFG+16]. For the nitrogen-infused cavities studied in this dissertation, the furnace was ramped after the degas step down to 160 °C for doping. The length of the doping step varied from study to study, but was typically 1-7 days.

Figure 4.6 shows the concentrations of nitrogen as well as oxygen and carbon

impurities in a representative nitrogen-infused niobium surface; in this case, the cavity underwent a 48-hour doping step. Like the earlier impurity concentration results, the measurements here were taken by SIMS on a single-crystal sample of electropolished niobium treated alongside the cavity. Two things are of particular note here in comparison to the impurity content compared to that of nitrogen-doped niobium as exemplified in Fig. 4.2. First is that the spike in nitrogen concentration near the surface is not high enough to indicate a substantial layer of niobium nitride; indeed, except in cases of surface contamination, we were able to omit the light EP step from the doping process when preparing cavities by nitrogen infusion. Second is that beyond the initial spike, the concentration of nitrogen decreases very rapidly, reaching background levels a mere 10-20 nm from the surface, while the concentrations of carbon and oxygen are substantially higher for several hundred nm; later work in this dissertation will suggest that this very limited presence of nitrogen nevertheless has an important impact on the RF performance of nitrogen-infused cavities.

Given these dramatic differences in impurity content, one might be understandably astonished to see that these nitrogen-infused cavities perform very similarly to nitrogen-doped cavities. Figure 4.7 shows the 2 K Q_0 vs. H_{pk} behavior of a cavity that was infused for 48 hours at 160 °C compared against that of a cavity that received a 20/30 dope at 800 °C followed by a 24 μm VEP; the two curves are nearly identical in their anti-Q-slope behavior. The doped and infused cavities received the same treatments as the samples in Figs. 4.2 and 4.6, respectively, with the doped cavity receiving an additional 24 μm VEP after the bake. Looking at the SIMS results, the two cavities had similar concentrations of nitrogen on the surface ($\sim$ 0.1 at. %) but quite different impurity content after the first few nm: where the impurity concentrations in the nitrogen-infused

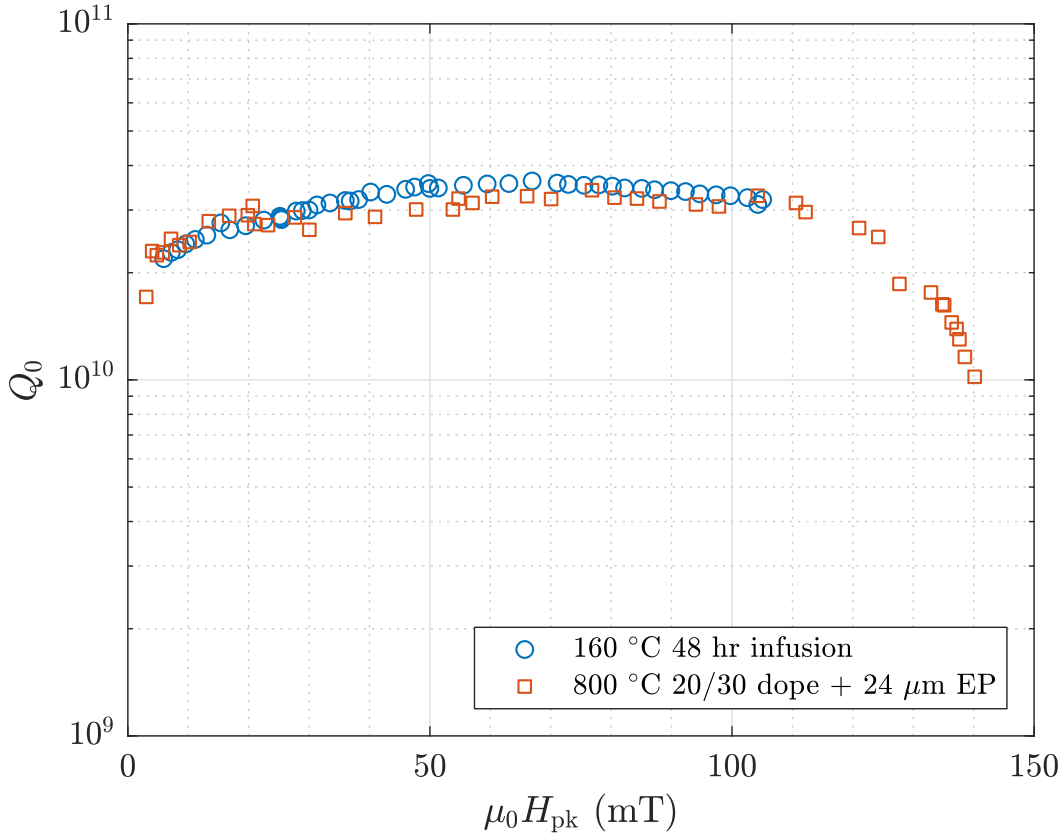

Figure 4.7: Q vs.H curves at 2 K for a nitrogen-infused cavity and a nitrogen-doped cavity.

cavity decay very rapidly in the first few 100's of nm, the nitrogen concentration of the nitrogen-doped cavity remains essentially constant on that scale.

As in the cavities doped with nitrogen at high temperatures, the field-dependent increase in Q_0 in 160 °C nitrogen-infused niobium cavities is caused by a decrease in R_{BCS} with increasing RF field strength. Figure 4.8 shows R_{BCS} and R_0 for an example nitrogen-infused cavity.

Also similarly to high-T-doped cavities, the residual resistance of nitrogen infused cavities shows a significant sensitivity to trapped magnetic flux. Unlike the nitrogen-doped cavities, however, nitrogen-infused cavities prepared at

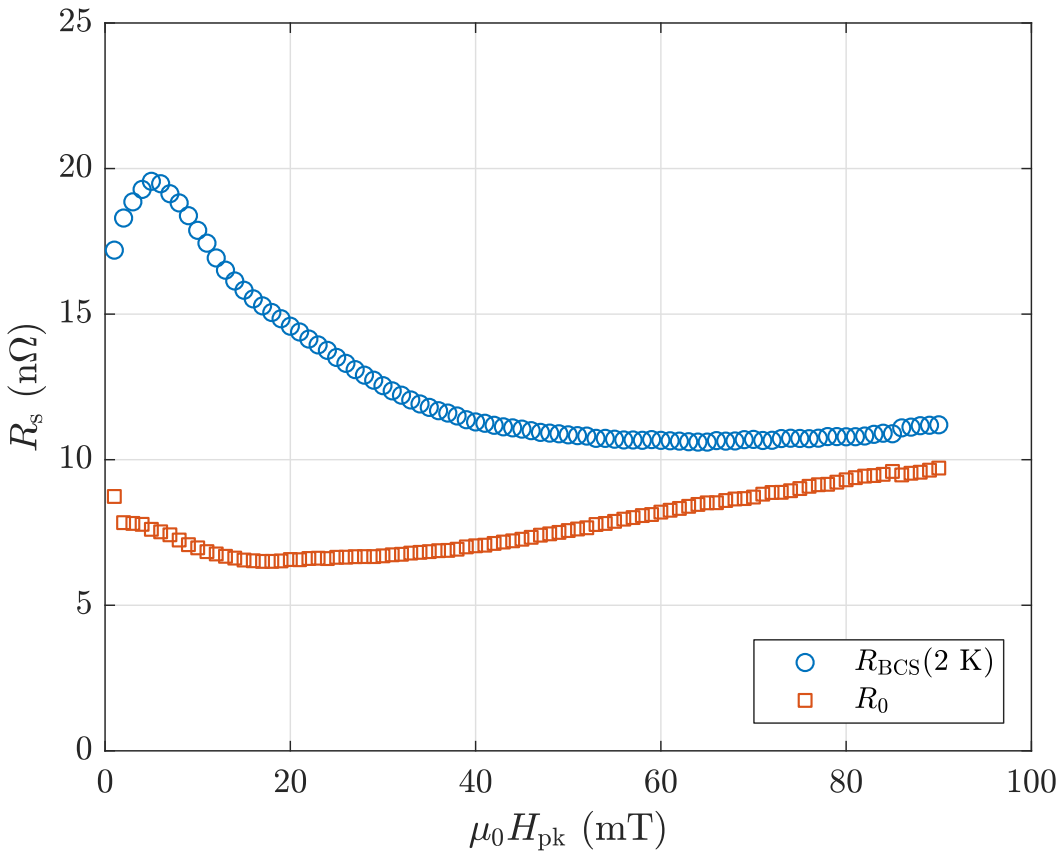

Figure 4.8: BCS and residual surface resistance of a nitrogen-infused cavity (160 °C, 4.5 days) as a function of RF field strength.

Cornell have also shown a linear sensitivity to the strength of the RF field:

$$R_0 = R_{0,\mathrm{native}} + a \cdot B_{\mathrm{RF}} \cdot B_{\mathrm{trapped}} + b \cdot B_{\mathrm{trapped}} \tag{4.4}$$

Figure 4.9 shows an example of this sensitivity in a cavity that underwent a 24-hour 160 °C nitrogen infusion run. Such a sensitivity has been observed in thin-film cavities such as niobium cavities coated with niobium-3 tin [HLP+17] and in copper cavities sputtered with niobium [BCC+97]. Some other laboratories have also found such a sensitivity in nitrogen-doped niobium [MGC+16], though Cornell flux trapping sensitivity results for nitrogen-doped niobium have shown only a very weak or negligible dependence on the RF field strength [Gon16]. For nitrogen-infused cavities prepared at Cornell, the non-

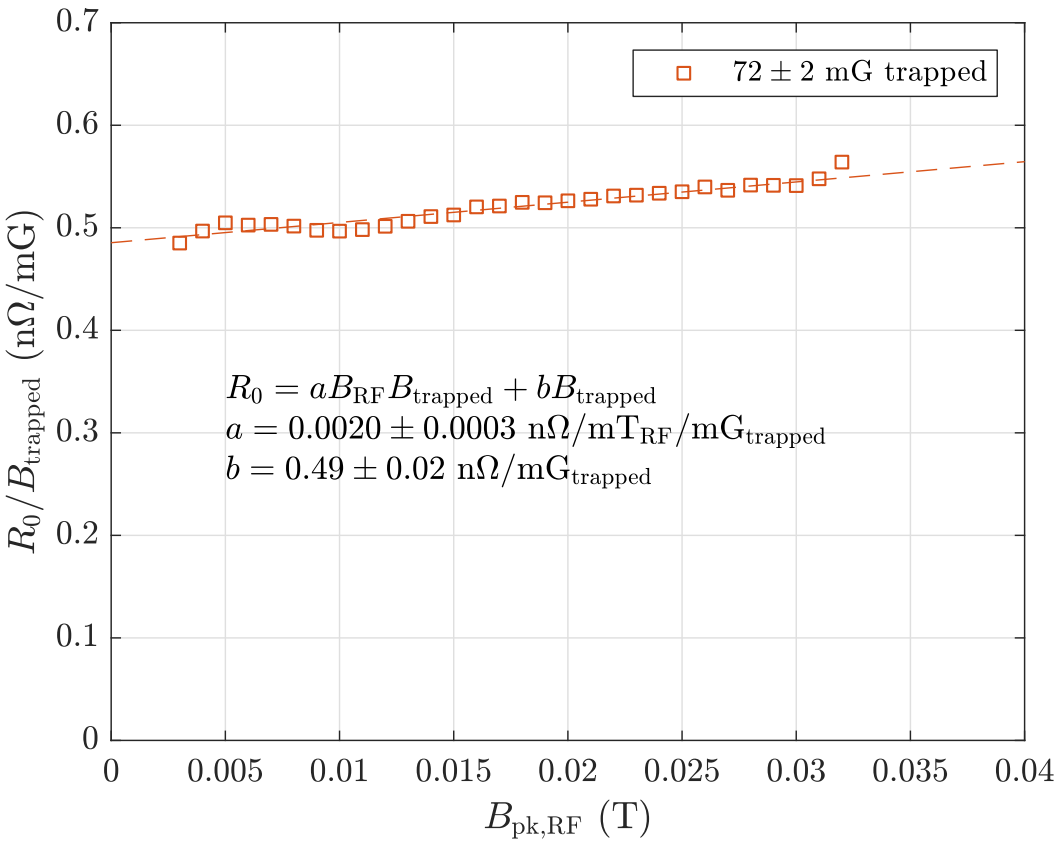

Figure 4.9: Residual resistance due to trapped magnetic flux for a nitrogen-infused cavity (160 °C, 24 hours).

field-dependent flux trapping sensitivity (b in Eq. 4.4) has generally been on the low end of the range of the sensitivity observed in nitrogen-doped cavities, in the range of 0.2-1 nΩ/mG at 1.3 GHz.

4.4 Open Questions

As discussed above, the anti-Q-slope behavior exhibited by nitrogen-doped and nitrogen-infused niobium SRF accelerator cavities gives the potential to build high-efficiency particle accelerators. Together, the experimental results of these cavities indicate that their RF performance is impacted significantly by the pres-

ence of impurities, particularly nitrogen. As such, there remain a number of open questions concerning nitrogen doping and infusion:

1. How does the concentration of impurities affect the properties of the anti-Q-slope in nitrogen-doped cavities?
2. How does the concentration of impurities affect the properties of the anti-Q-slope in nitrogen-infused cavities?
3. Can we build a framework to simulate nitrogen-doped and nitrogen-infused cavities?
4. Do we have a theoretical understanding of the anti-Q-slope?
5. Can we design an experiment to investigate the anti-Q-slope from another angle?

In Ch. 5, I will discuss a study of strongly nitrogen-doped 1.3 GHz single-cell niobium cavities, quantifying the properties of the anti-Q-slope with respect to the electron mean free path ℓ. In Ch. 6, I will discuss initial studies of nitrogen-infused cavities, investigating the impacts of the different impurities present in the RF surface. In Ch. 7, I will detail my development of a framework to model the RF behavior of doped and infused cavities including the important thermal effects discussed in Sec. 3.3.5. In Ch. 8, I will use the framework and other tools to test competing theories of the anti-Q-slope. In Ch. 9, I will describe a new test apparatus to investigate the field-dependence of the surface resistance in nitrogen-doped and nitrogen-infused niobium. Finally, in Ch. 10, I will summarize the results of the previous chapters and present an outlook on future investigations of these novel SRF materials.

CHAPTER 5

QUASIPARTICLE OVERHEATING IN NITROGEN-DOPED CAVITIES

Nitrogen-doped niobium cavities exhibit a peculiar and exciting behavior: their BCS surface resistance *decreases* with increasing RF field strength, leading to a field-dependent increase in their efficiency as measured by the intrinsic quality factor Q_0. As discussed in Ch. 4, this "anti-Q-slope" can improve Q_0 by up to a factor of 3 at gradients relevant to SRF accelerator applications. The characteristics of this field-dependent R_{BCS}, particularly the value of R_{BCS} at low field and the relative change in magnitude of R_{BCS} as the field strength increases, are strongly affected by the level of nitrogen concentration in the RF penetration layer (first few λ) of the cavity surface. In nitrogen-doped cavities, this concentration is fairly constant on the scale of λ, and can be non-destructively quantified through measurements of the electron mean free path ℓ. In this chapter, I will discuss an "overdoping" study we performed at Cornell in which we prepared and tested[1] a set of cavities with a range of levels of nitrogen-doping as quantified by ℓ, using the results to build an empirical model of the anti-Q-slope as a function of doping level [MGL17]. This model hinges on the thermal effects outlined in Sec. 3.3.5, especially quasiparticle overheating by inefficiency in the electron-phonon heat transfer mechanism.

5.1 Overview of Experiment

To comprehensively study the anti-Q-slope in nitrogen-doped cavities, we prepared a set of cavities with electron mean free path ℓ ranging from 4 to 200 nm.

[1] The cavity preparations and RF tests in this study, presented in Sec. 5.1, were supervised and performed, respectively, by D. Gonnella during his dissertation work [Gon16]; the subsequent analysis presented in Secs. 5.2-5.5 is my new contribution.

Cavity	Preparation	T_c (K)	$\Delta/k_B T_c$	ℓ (nm)
C3(P2)	990°C N-doping[1] + 5 μm VEP	9.1 ± 0.1	2.05 ± 0.01	4 ± 1
C2(P2)	900°C N-doping[2] + 18 μm VEP	9.1 ± 0.1	2.00 ± 0.01	6 ± 1
C2(P3)	900°C N-doping[2] + 6 μm VEP	9.2 ± 0.1	1.94 ± 0.01	17 ± 5
C2(P1)	800°C N-doping[3] + 6 μm VEP	9.3 ± 0.1	1.88 ± 0.01	19 ± 6
C3(P1)	800°C N-doping[3] + 12 μm VEP	9.3 ± 0.1	1.91 ± 0.01	34 ± 10
C1(P1)	800°C N-doping[3] + 18 μm VEP	9.3 ± 0.1	1.88 ± 0.01	39 ± 12
C4(P1)	800°C N-doping[3] + 24 μm VEP	9.2 ± 0.1	1.89 ± 0.01	47 ± 14
C5(P1)	800°C N-doping[3] + 30 μm VEP	9.2 ± 0.1	1.88 ± 0.01	60 ± 18
C5(P2)	800°C N-doping[3] + 40 μm VEP	9.2 ± 0.1	1.94 ± 0.01	213 ± 64

[1] 100 μm VEP, 800 °C in vacuum for 3 hours, 990 °C in 30 mTorr of N_2 for 5 minutes.
[2] 100 μm VEP, 800°C in vacuum for 3 hours, 900 °C in 60 mTorr of N_2 for 20 minutes, 900 °C in vacuum for 30 minutes.
[3] 100 μm VEP, 800 °C in vacuum for 3 hours, 800 °C in 60 mTorr of N_2 for 20 minutes, 800 °C in vacuum for 30 minutes.

Table 5.1: Overview of cavity preparations for the overdoping study with final critical temperature, energy gap, and mean free path values. Labels are chronological in nature; for example, "C3(P2)" is the second preparation of cavity number three. This table was first published in [GKL16].

In this "overdoping" study (so-called because the cavities were doped more strongly than the industrialized "2/6" recipe used in the LCLS-II protocol), we used five 1.3 GHz single-cell TESLA-style [ABB+00] cavities built at Cornell. To cover the range of values of ℓ, we varied the doping and annealing times, doping temperatures, and final etch depths of the nitrogen doping procedures laid out in Sec. 4.1. These preparations are summarized in Table 5.1.

After preparation, these cavities were tested vertically in the Cornell SRF facilities using the methods described in Sec. 3.4.2. In particular, we used measurements of f vs. T to find the critical temperature T_c, then used these measurements along with low-field measurements of Q_0 vs. T to find the low-field energy gap $\Delta/k_B T_c$ and the electron mean free path ℓ. We then analyzed the measurements of Q_0 over varying values of T and H_{pk} to find R_{BCS} as a function of temperature and RF field strength and R_0 as a function of RF field strength. The cavities were typically tested from $\mu_0 H_{pk} \approx 10$ mT up to just below the quench field at 2.1 K, 2.0 K, 1.9 K, 1.8 K, 1.7 K, and 1.6 K. Of the nine cavity preparations considered in this study, eight exhibited an anti-Q-slope under RF test; in all cases, this was due to a field-dependent decrease in R_{BCS}. The ninth preparation, C5(P2), was the cavity with the lightest doping (ℓ=213 nm).

For all cavities tested, the low-field BCS surface resistance varied with mean free path as expected by BCS theory as discussed in Sec. 3.2, with a pronounced minimum near $\ell \approx 25$ nm. This result inspires confidence in our experimental techniques. Figure 5.1 demonstrates these low-field results at 2 K and $\mu_0 H_{pk} \approx 20$ mT, normalized for variations in the energy gap and critical temperature by the following:

$$R_{BCS,norm} = R_{BCS,meas} \exp\left(\frac{\Delta}{k_B T_c} - \frac{\Delta_{avg}}{k_B T_{c,avg}}\right) \tag{5.1}$$

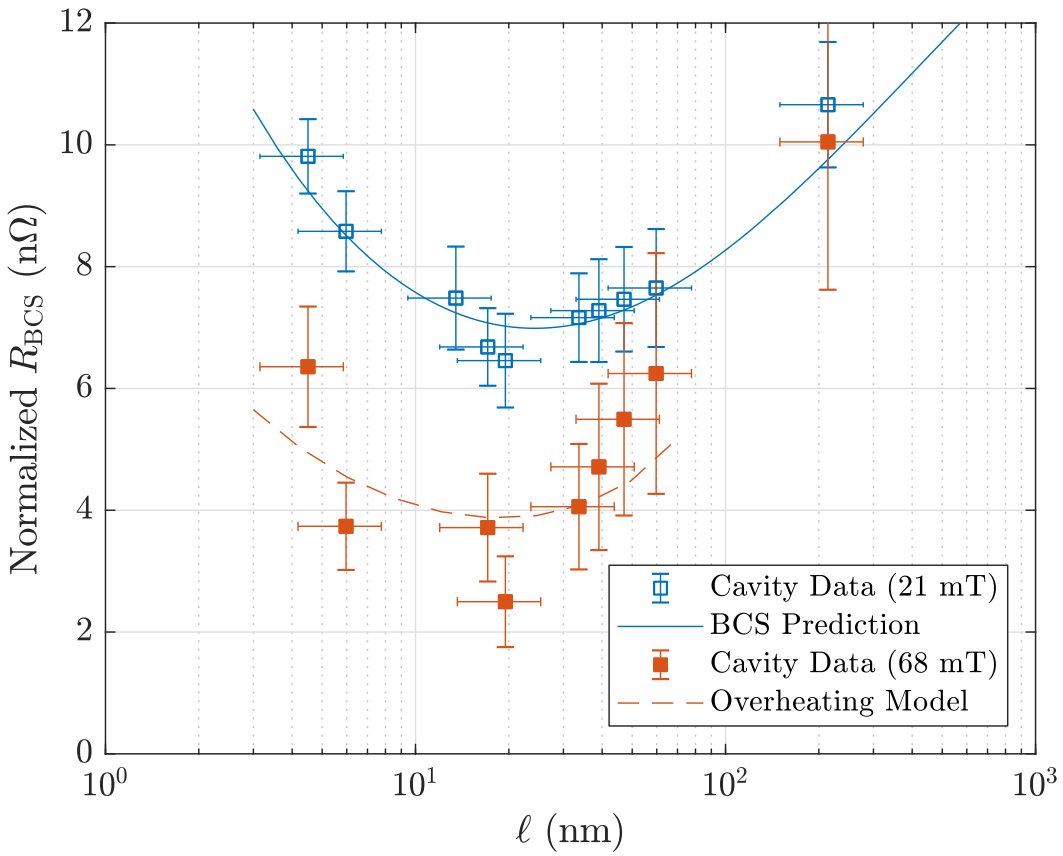

Figure 5.1: Low-field BCS surface resistance, R_{BCS} at H_{pk} = 68 mT, BCS prediction, and overheating model prediction as a function of mean free path (see Sec. 5.3); R_{BCS} has been normalized for variations in Δ/k_BT_c and is given at 2 K. First published in [MGL17].

Figure 5.1 also shows the $R_{BCS}(2\text{ K})$ results for the same cavities at high field ($\mu_0 H_{pk} \approx 70$ mT). Due to the stronger anti-Q-slope at higher doping levels (shorter mean free paths), the minimum in R_{BCS} at high field is shifted to a lower value of ℓ, closer to 17 nm.

Of the eight cavity preparations which exhibited an anti-Q-slope, the magnitude of the relative decrease in R_{BCS} showed a pronounced dependence on ℓ as well: as suggested by Fig. 5.1, cavities doped to a shorter ℓ showed a relative decrease that was much more pronounced than that in more lightly doped cavities. Figure 5.2 shows this relative decrease in R_{BCS} over increasing RF field

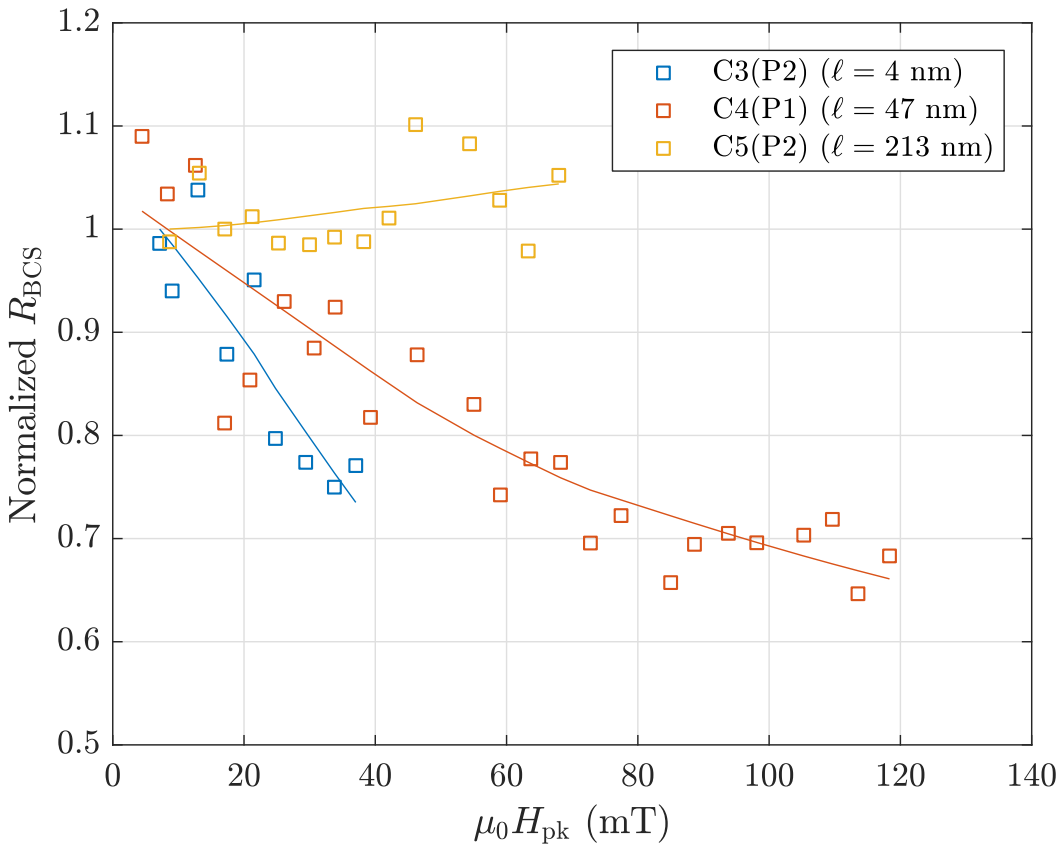

Figure 5.2: BCS surface resistance for several nitrogen-doped cavities at 2 K as a function of RF field; R_{BCS} has been normalized to the value at $\mu_0 H_{\mathrm{pk}} \approx 10$ mT. Lines represent data smoothed by a 1st-degree LOWESS filter. "CX(PY)" labels refer to cavity preparations listed in Table 5.1.

strength for several of the cavities included in this study.

5.2 Gurevich Model with Quasiparticle Overheating

After processing the RF test data from these cavities, we sought to build an empirical model of this observed dependence of the change in R_{BCS} on the electron mean free path ℓ. For the basis of the model, we used a recent theory by A. Gurevich to describe the anti-Q-slope behavior of these cavities; the theory's

prediction of R_{BCS} vs. H_{pk} has shown good agreement with experimental results from nitrogen-doped cavities at 1.5 GHz [Gur14]. Gurevich's model proposes the following mechanism for a field-dependent surface resistance:

Magnetic fields on the surface of a superconductor induce Meissner effect screening currents in the penetration layer (see Sec. 3.1); for high field levels, these screening currents can be strong enough to break Cooper pairs and significantly alter the Bogolyubov quasiparticle density of states. This density of states, which under BCS theory features a singularity at the energy gap Δ followed by an exponential decay at higher energies, instead undergoes two major changes: the energy gap decreases and the peak in the density of states is "smeared". The first of these effects increases the overall population of quasiparticles by moving states close to the zero-field energy gap down to lower energies; the second of these effects *decreases* the quasiparticle population by reducing the number of states available above the zero-field Δ. The magnitude of these two effects depends on field strength and frequency, and the overall change in the balance of the quasiparticle population controls the BCS surface resistance (see Sec. 3.2, in particular Eqs. 3.38 and 3.41).

The model presents two cases, the first of which features Meissner currents excited by a strong DC magnetic field and the second of which considers screening currents excited by a strong RF field (like the accelerating field in an SRF cavity) instead. In this study, we used the second case of the theory; for dirty-limit niobium at 1.3 GHz, this case calculates a strong anti-Q-slope that agrees well with experimental results. In Ch. 9 I will discuss the first case and develop an experimental apparatus that may be able to confirm or disprove the predictions of the model.

The model makes some assumptions that are important to bear in mind, most notably that the distribution function of the quasiparticles does not change over the RF period and is equal to the distribution function at zero field, that the quasiparticle lifetimes are long compared to the RF period, and that the superconducting material is in the dirty limit where high scattering rates ensure that the superconducting physics behave locally. For now, I will let these assumptions stand, but I will address some potential issues with the distribution function during my assessment of anti-Q-slope theories in Chap. 8.

On top of this base effect of the model, the author addresses the thermal effects enumerated earlier in Sec. 3.3.5. For simplicity, the contributions to quasiparticle overheating made by the electron-phonon heat transfer inefficiency Y, the thermal conductivity κ of the niobium wall of thickness d, and the Kapitza resistance h_K between the cavity wall and the helium bath are combined in a single dimensionless[2] overheating parameter[3] α:

$$\alpha = \frac{R_{BCS,0} H_c^2}{2T_0} \left(\frac{1}{Y} + \frac{d}{\kappa} + \frac{1}{h_K} \right) \tag{5.2}$$

The effect of this overheating, encapsulated in α, is to raise the temperature T of the quasiparticles on the inner surface of the cavity. In the lower limit, this overheating, *i.e.* the increase of T with respect to the bath temperature T_0, is linearly proportional to α and to R_{BCS} and scales quadratically with H_{pk}:

$$T - T_0 = \frac{\alpha T_0}{R_{BCS,0}} \left(\frac{H_{pk}}{H_c} \right)^2 R_{BCS}(H_{pk}, T) \tag{5.3}$$

This overheating serves to counteract the reduction of R_{BCS} with increasing H_{pk}: stronger fields dissipate more power, and inefficiency in the transfer of that

[2] It seems that H_c, $R_{BCS,0}$, and T_c are included here just to make α dimensionless: they all get canceled out the next equation. We will get rid of them later in this section.

[3] This and the following equation are reproductions of Eqs. 14 and 13 in the original paper, respectively [Gur14].

power away from the Bogolyubov quasiparticles raises the temperature of the quasiparticles and thus the surface resistance. Stronger overheating leads to a weaker reduction in R_{BCS} and thus a weaker anti-Q-slope. This overheating can be strong enough to give R_{BCS} a positive slope at high fields; Fig. 5.3 in the next section illustrates this with calculations of R_{BCS} vs. H_{pk} for several values of α.

In essence, the base Gurevich model provides a strong anti-Q-slope that matches well the strongest anti-Q-slopes measured in 1.3 GHz nitrogen-doped cavities; quasiparticle overheating then modulates that fundamental behavior, yielding more moderate anti-Q-slope curves that can curve into negative Q-slope at high fields. Using the base model of the theory and the above interpretation of the thermal effects in the cavity wall, the field-dependent surface resistance can be fully calculated using the material parameters observed experimentally (f, T_c, $\Delta/k_B T_c$, ℓ, etc.) and the overheating parameter α.

5.3 Overheating and the Electron Mean Free Path

In our study, we developed software to calculate the Gurevich theory using the material parameters derived from our experimental RF test results of the cavities listed in Table 5.1. For a given set of material parameters, a temperature T_0 of the helium bath, and an overheating parameter α, the algorithm calculates the Bogolyubov quasiparticle density in the RF surface as a function of the peak RF magnetic field strength. Important to note here is that the temperature of the quasiparticles T_{qp} is calculated locally as a function of local field level due to the abstraction of the thermal effects into one parameter; in Ch. 7, I will develop a more advanced thermal modeling framework that will consider quasiparticles

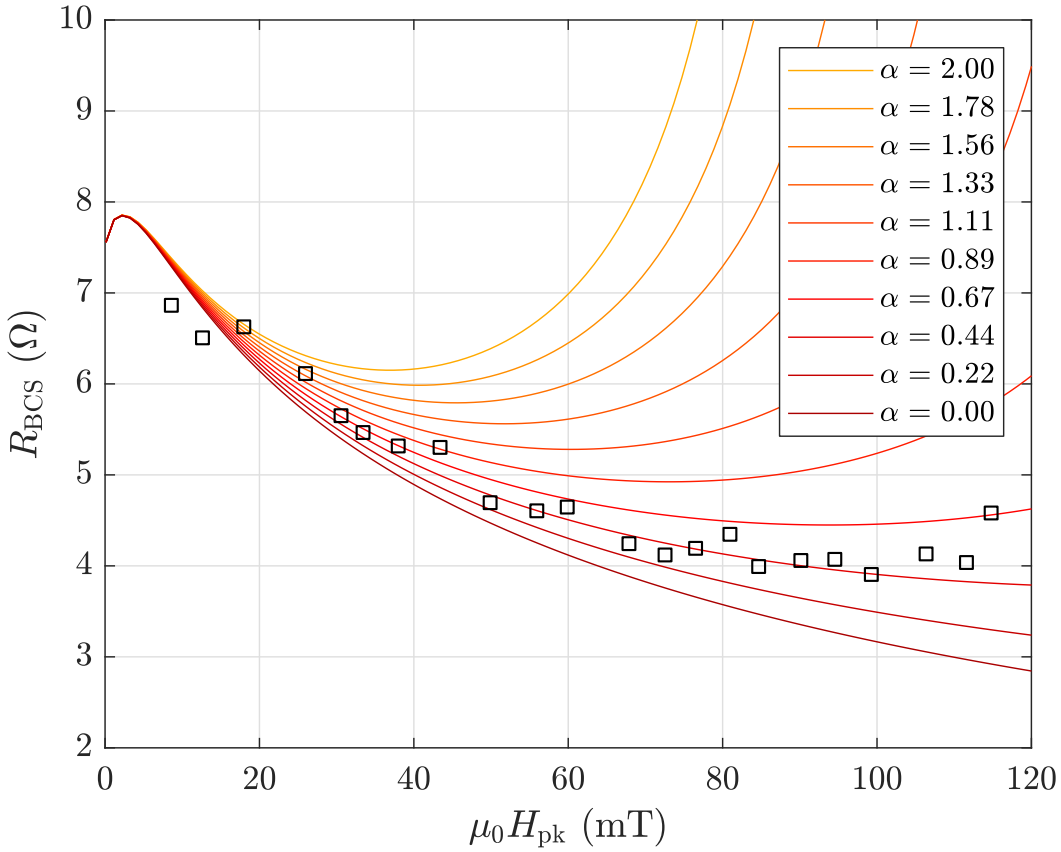

Figure 5.3: R_{BCS} at 2 K for preparation C3(P1) with theoretical calculations for a range of values of the quasiparticle overheating parameter α.

in thermal equilibrium.

The software then compares the theoretical results to experimental data, using a nonlinear least squares regression to find an optimal value of the overheating parameter α to fit the theory to experiment. The fit also includes a linear "scaling parameter" s to account for systematic experimental error in measurements of Q_0 and Δ:

$$s = \frac{R_{\mathrm{BCS,meas}}}{R_{\mathrm{thy}}} \tag{5.4}$$

The same scaling parameter was applied to all R_{BCS} vs. H_{pk} data points for a given cavity preparation. Figure 5.3 shows one such experimental curve alongside theoretical curves calculated for the proper material parameters.

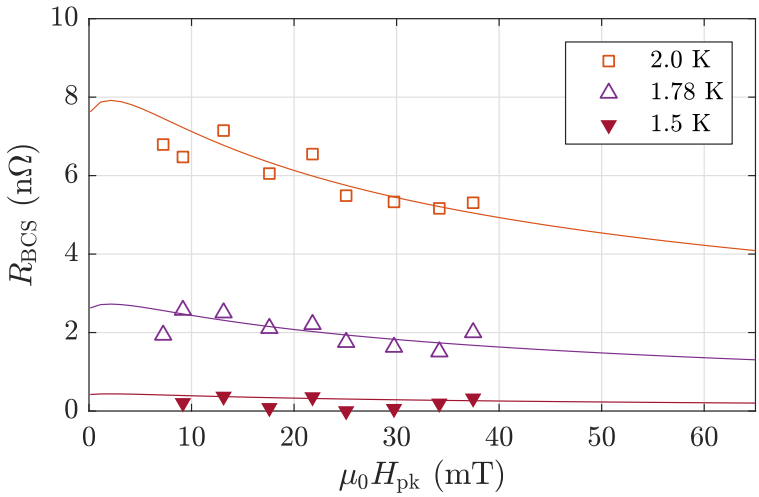

(a) C3(P2)
$\ell = 4 \pm 1$ nm

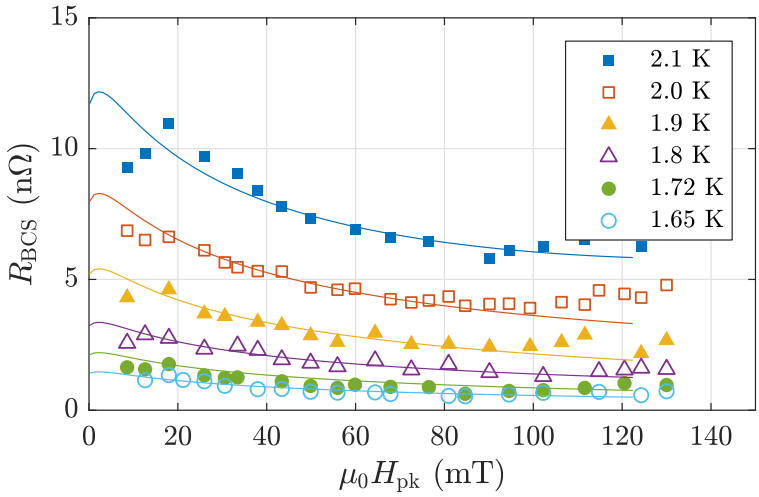

(b) C3(P1)
$\ell = 34 \pm 10$ nm

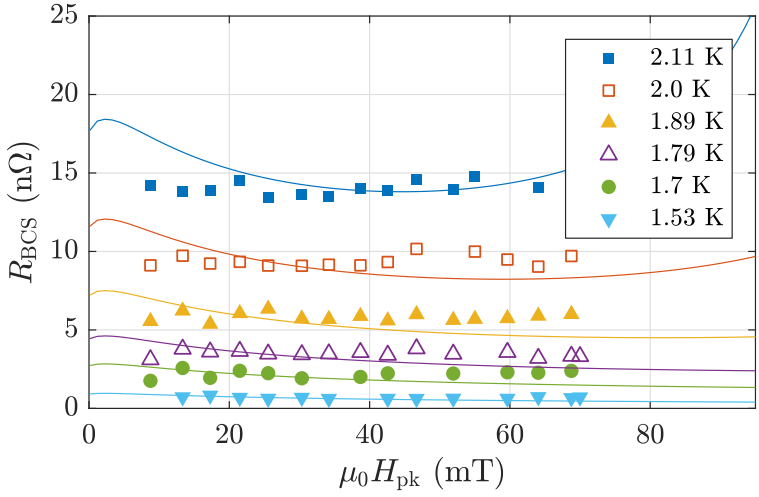

(c) C5(P2)
$\ell = 213 \pm 64$ nm

Figure 5.4: Experimental BCS surface resistance with theoretical fits using the Gurevich model with quasiparticle overheating.

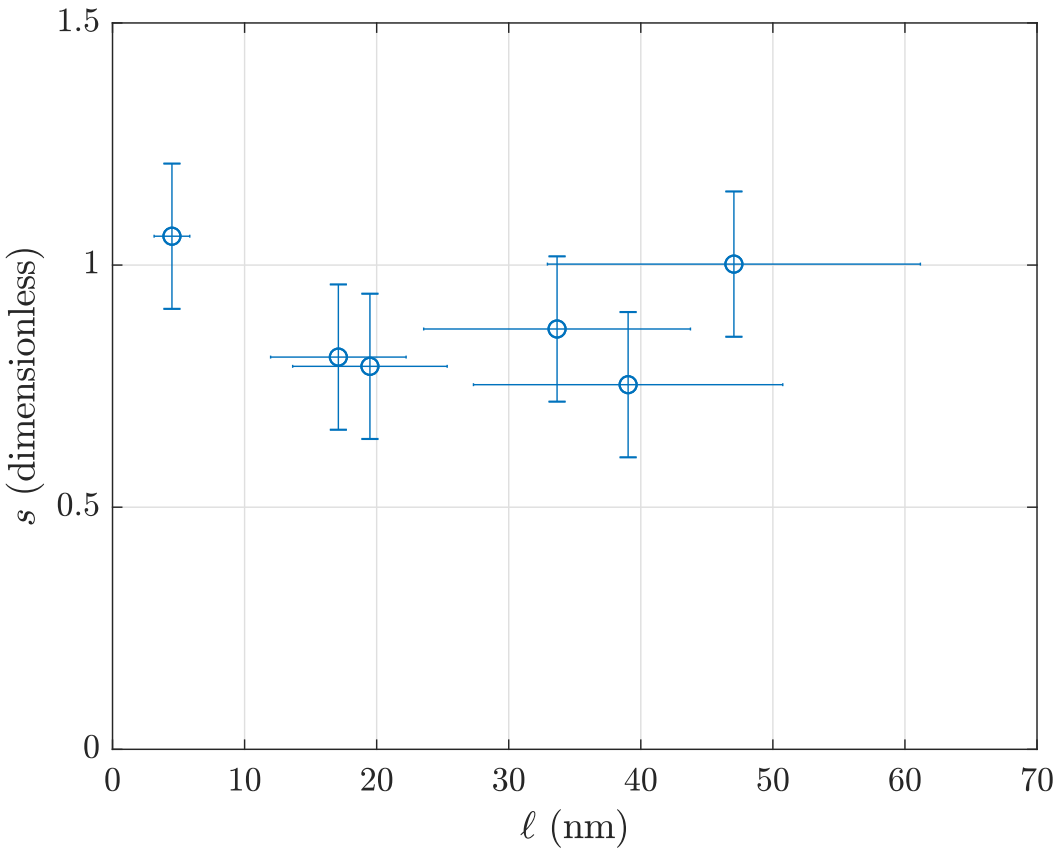

Figure 5.5: Fit results for the scaling parameter s as a function of the electron mean free path for the cavities tested in the overdoping study.

In this way, the fitting routine yielded one value of α for each R_{BCS} vs. H_{pk} curve for each cavity preparation at each temperature tested, as well as one value of s for each cavity preparation. Figure 5.4 shows fit results for several of the cavity preparations considered in the study, spanning the range of tested values of ℓ. Notably, the theory agrees well with the experimental results of the strongly-doped cavities ($\ell \leq 60$ nm) with pronounced anti-Q-slopes. We performed these fits on all cavity preparations except for C2(P2) and C5(P1), which did not have enough temperature-dependent data to produce fits with low uncertainty.

For the cleanest cavity preparation C5(P2), with the longest mean free path

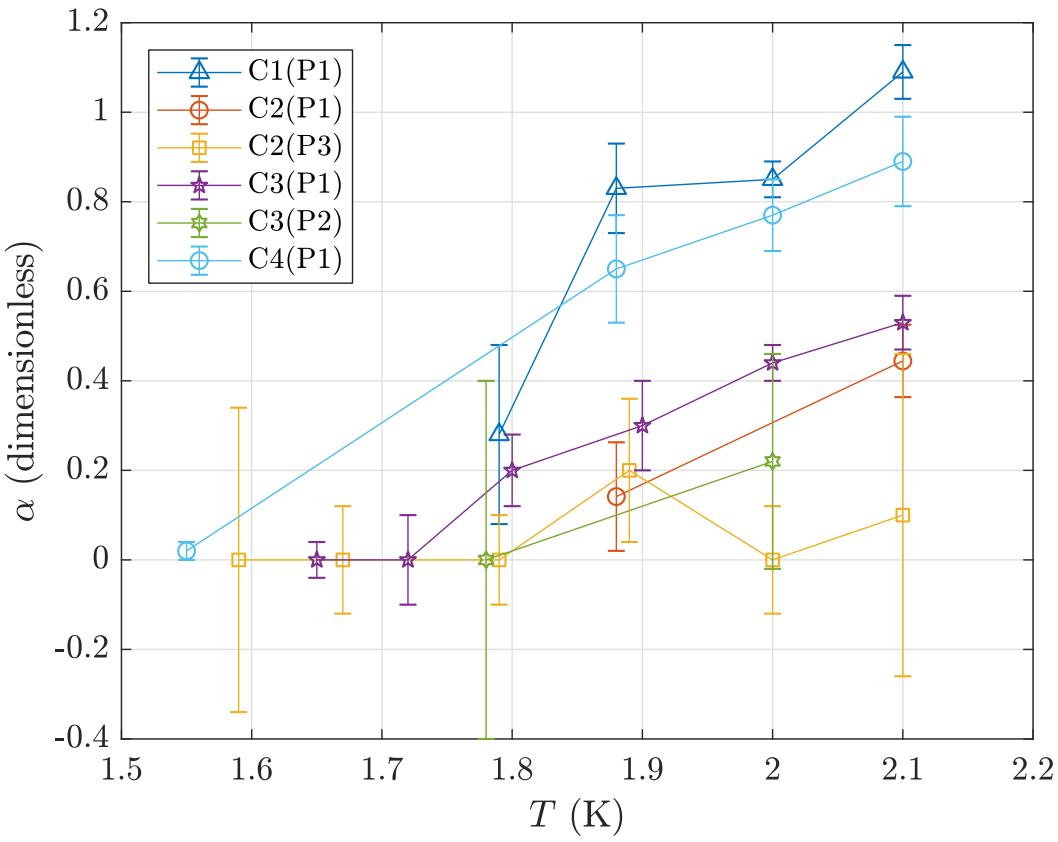

Figure 5.6: Fit results for the overheating parameter α as a function of the helium bath temperature T_0 for the cavities tested in the overdoping study.

and no anti-Q-slope, the theory does not agree well with experiment. Indeed, the Gurevich theory does not predict the standard mild Q-slope behavior observed experimentally in non-doped (clean) niobium cavities; this limitation may be due to the aforementioned assumptions in the model or due to additional effects (thermal or otherwise) not considered in the theory. I will discuss this discrepancy again in Ch. 8. In the remaining plots in this chapter, I will omit the results of C5(P2).

Considering first the scaling parameter s, we found no strong dependence on the doping level as quantified by ℓ. Figure 5.5 shows the fitted values of the scaling parameter for the cavities in the study. All values were close to

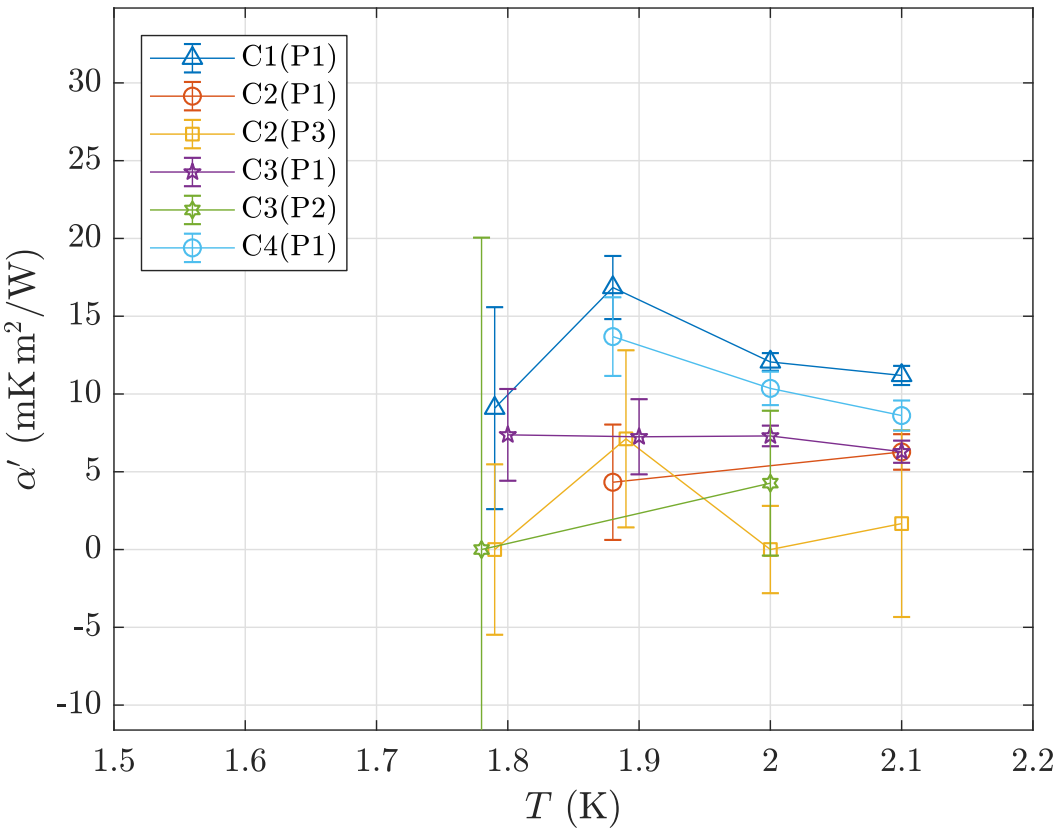

Figure 5.7: Fit results for the *normalized* overheating parameter α' as a function of the helium bath temperature T_0 for the cavities tested in the overdoping study.

unity, indicating that our interpretation of s as a correction to systematic errors is valid.

Next considering the fit results of the overheating parameter α, we see quite a different story. As might be expected from the formulation in Eq. 5.2, α here has a strong positive dependence on T_0, as can be seen in Fig. 5.6 (the exponential dependence on T_0 of R_{BCS} in Eq. 5.2 outweighs the inverse dependence of α on T_0). The overheating parameter also has a wide variation from preparation to preparation. To try to isolate the dependence on cavity treatment protocol, we can reformulate Eqs. 5.2 and 5.3 to represent a "normalized overheating parameter" α', now no longer unitless but perhaps more appropriately encapsulating

the thermal effects:

$$\alpha' = \alpha \frac{2T_0}{R_{\mathrm{BCS},0} H_\mathrm{c}^2} = \left(\frac{1}{Y} + \frac{d}{\kappa} + \frac{1}{h_\mathrm{K}} \right) \tag{5.5}$$

$$T - T_0 = \frac{1}{2} \alpha' H_\mathrm{pk}^2 R_\mathrm{BCS}(H_\mathrm{pk}, T) = \alpha' \frac{P_\mathrm{diss}}{A} \tag{5.6}$$

In this formulation it becomes clear that α' relates the dissipated power to the increase in temperature from the helium bath to the quasiparticles in the RF surface, much like a more traditional thermal conductivity.

Figure 5.7 shows the α results previously shown in Fig. 5.6, now normalized by Eq. 5.5 in the form of α'. There is no longer a strong dependence on T_0, at least in the region $T_0 \geq 1.8$ K where α is large compared to its uncertainty. This suggests that α' is related only to the intrinsic properties of the doped niobium and not to extrinsic properties of the experimental setting.

Because there is no strong dependence on T_0, we can average the α' values by cavity preparation and plot them against the mean free path ℓ. The results, shown in Fig. 5.8, reveal an exciting relation: quasiparticle overheating increases linearly with the electron mean free path. This finding may appear understated, but it suggests by its simplicity a deep connection between the doping level (quantified by ℓ) and the observed variation of anti-Q-slope magnitude through the effect of quasiparticle overheating.

We can fit the results of α' vs. ℓ to the following affine function:

$$\alpha' = \gamma + \beta \ell \tag{5.7}$$

For the parameters of the fit we find $\beta = 0.24 \pm 0.14\,\mathrm{mK\,m^2/W\,nm}$ and $\gamma = 0.2 \pm 4.2\,\mathrm{mK\,m^2/W}$. Important to note here is that these results are valid only in the strongly-doped limit with $\ell \leq 60$ nm, where the results of the Gure-

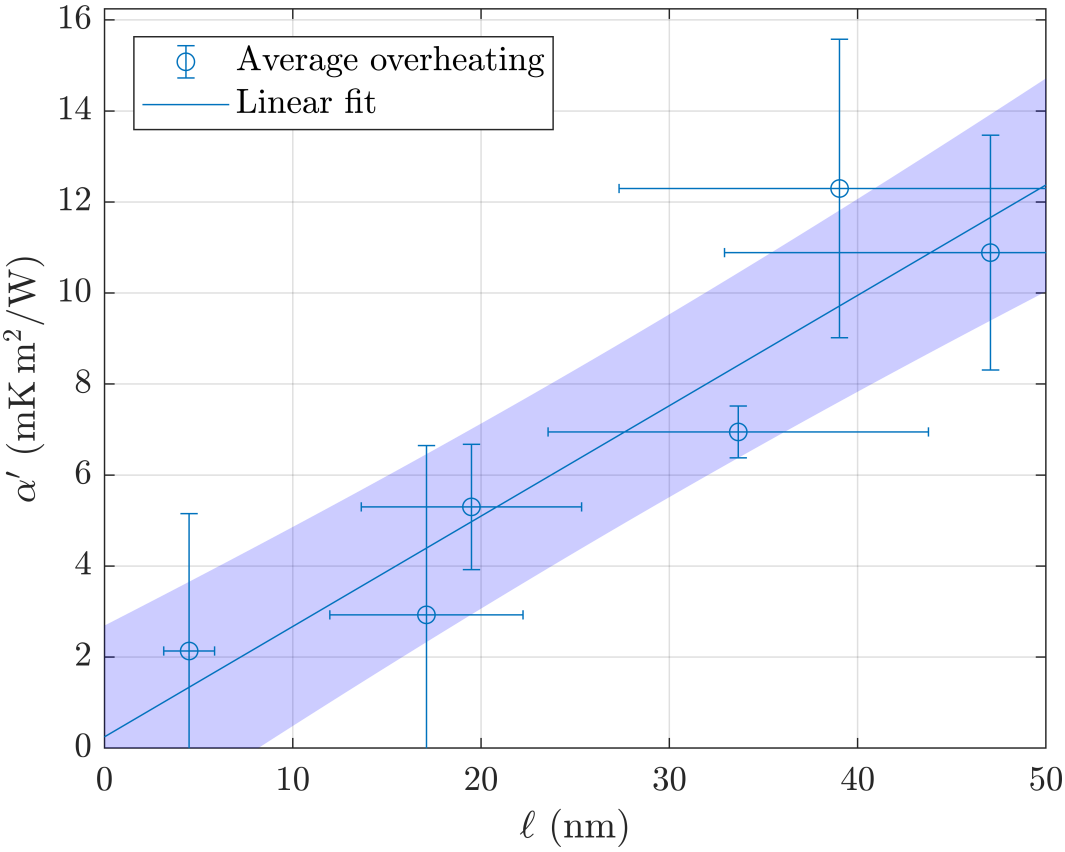

Figure 5.8: Normalized overheating parameter α' as a function of the mean free path ℓ for the cavities tested in the overdoping study. Affine fit parameters: $\alpha' = \gamma + \beta\ell$, with $\gamma = 0.2 \pm 4.2$ mK m^2/W and $\beta = 0.24 \pm 0.14$ mK m^2/W nm.

vich theory with linearized quasiparticle overheating are consistent with experimental results.

From this linear fit, we can look to our earlier definition of α' to find potential connections between the empirical relation above and the theoretical derivation. Of the three terms in the right hand side of Eq. 5.5, we should expect that d/κ and h_K do not depend strongly on the doping level, if at all. All the cavities considered in this study were manufactured from the same stock material to the same specifications, and doping only strongly affects the first 10's of μm of the surface; as such, d and κ should not be drastically different between cavities, and

in particular κ should be dominated by the properties of the clean interior of the cavity material (long ℓ, long ℓ_{ph}). For the cavities here, $d = 3$ mm and κ should be near 5-10 W/m·K [KB96] (see also Fig. 3.11), resulting in $d/\kappa \leq 1$ mK m^2/W. Likewise, the Kapitza resistance h_{K} likely makes a small contribution; though it may be dependent on ℓ and other near-surface material properties, most literature values of h_{K} fall in the range of 1-8$\times 10^3$ W/m^{2}K [BF95], leading to a contribution to α' of $1/h_{\mathrm{K}} \leq 1$ mK m^2/W. Since these will not change dramatically with ℓ, we can consider them to combine to form the fit constant γ:

$$\gamma = \frac{d}{\kappa} + \frac{1}{h_{\mathrm{K}}} \tag{5.8}$$

Indeed, the value of γ found in the empirical fit is falls in the range of expected values for the sum of the κ and h_{K} terms above.

From this we can draw the conclusion that the principal dependence of α' on the mean free path comes from the electron-phonon inefficiency:

$$\beta\ell = \frac{1}{Y} \tag{5.9}$$

In this case, at short ℓ, Y is large and α' is small, limited by κ and h_{K}. The electron-phonon energy transfer mechanism has high efficiency, the effects of overheating are limited, and the nitrogen-doped material exhibits a strong decrease in R_{BCS} with increasing RF field strength. On the other hand, as ℓ increases (within the linear region of anti-Q-slope overheating behavior), Y decreases, and α' gets larger. The electron-phonon mechanism becomes less efficient, resulting in stronger quasiparticle overheating, a weaker reduction in R_{BCS}, and a weaker anti-Q-slope with a lower maximum Q_0.

This electron-phonon effect has not yet been widely considered in the SRF literature (see for example [VXP07, Pad09]), but it provides a reasonable explanation for the quasiparticle overheating in this model of the anti-Q-slope.

It also offers a possible explanation for the medium-field Q-slope observed in non-doped niobium cavities.

How might interstitial impurities improve the electron-phonon energy transfer mechanism? One potential explanation is the following: quasiparticles are heated above the lattice temperature by RF dissipation, releasing that energy to the lattice during inelastic collisions with impurities. As the concentration of impurities increases (*i.e.* as ℓ decreases), the scattering rate increases, improving the heat transfer rate from the electrons to the lattice phonons and mitigating the quasiparticle overheating effects.

This is an exciting conclusion, but more work will be necessary to confirm this explanation or offer an alternative. In the Center for Bright Beams, collaborative work is underway to use Density Functional Theory to build an *ab initio* picture of quasiparticle-phonon heat transfer in SRF cavities [MAG+19].

5.4 Optimal Nitrogen Doping Level

With the empirical relation between quasiparticle overheating and the electron mean free path found in our overdoping study, we can look towards finding an optimal level of nitrogen-doping. While the relative reduction of R_{BCS} with increasing RF field strength is strongest in cavities doped to the shortest electron mean free paths, the *overall* value of R_{BCS} depends on ℓ as well. As discussed in Sec. 3.2, for niobium, R_{BCS} has a minimum near $\ell = 20$ nm and increases steeply as the mean free path decreases. Furthermore, as discussed in Sec. 4.2.2, nitrogen-doped niobium exhibits an increased sensitivity of the residual resistance to trapped magnetic flux.

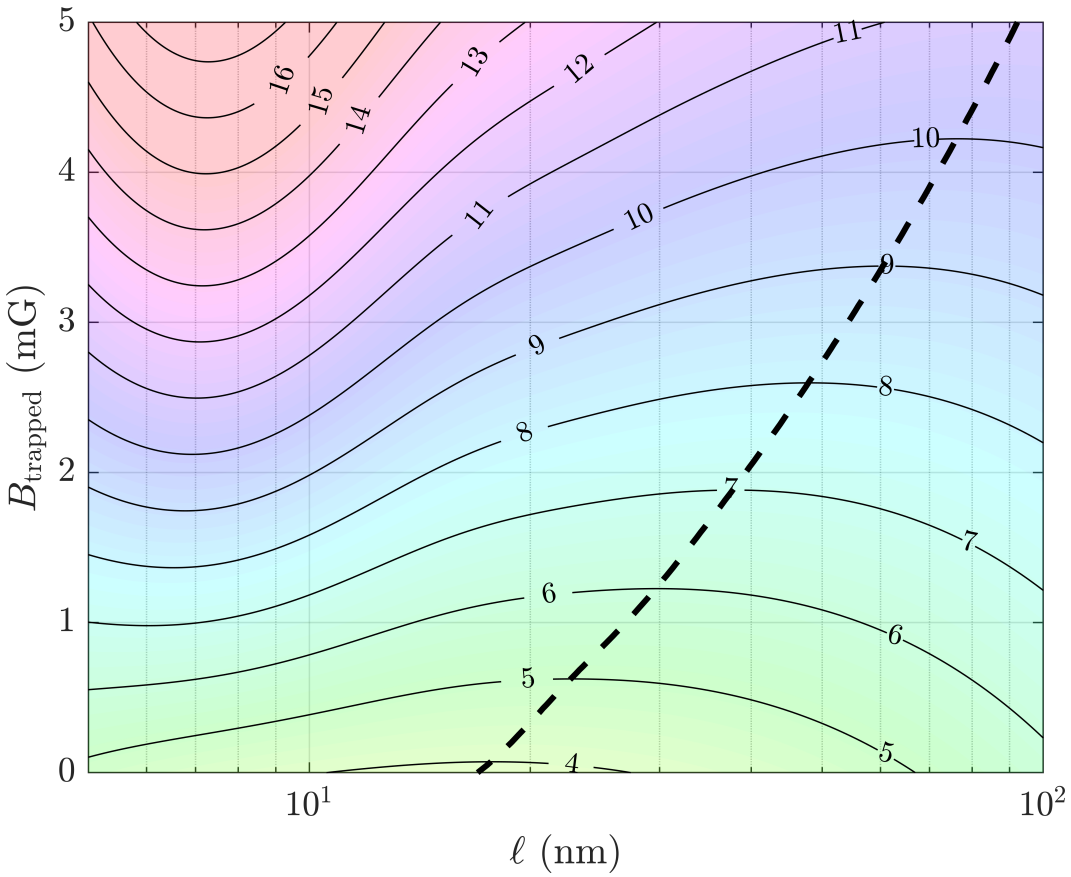

Figure 5.9: Calculation of $R_s = R_0 + R_{BCS}$, in units of nΩ, at $H_{pk} = 68$ mT for varying mean free path ℓ and trapped magnetic flux $B_{trapped}$. Line indicates optimal ℓ for a given amount of trapped flux.

We can combine the mathematical models for these effects, beginning with the base dependence of R_{BCS} on ℓ, then adding the Gurevich model of the anti-Q-slope, the ℓ-dependent quasiparticle overheating model developed above, and the model of the trapped flux sensitivity. Using this combined model we can calculate the total surface resistance in Eq. 3.42 for nitrogen-doped cavities at a given H_{pk}, T_0, ℓ, and $B_{trapped}$. From these results, we can find the mean free path ℓ that yields the lowest total surface resistance for the expected amount of trapped flux.

Figure 5.9 shows the results of this calculation for the LCLS-II design param-

eters, H_{pk} = 68 mT (E_{acc} = 16 MV/m in TESLA cavities) and T_0 = 2 K, for a range of values of ℓ and $B_{trapped}$. Data at extremely short ℓ has been excluded due to the strongly decreased quench fields observed in experiment for very strongly doped cavities [GEF+16]. The total surface resistance R_s at 2 K has strong contributions from both R_{BCS} (Gurevich model with quasiparticle overheating) and R_0 (trapped flux sensitivity); the dashed line indicates the optimal doping level as quantified by ℓ for a given "trapped flux budget". At an optimistically low $B_{trapped}$ of 1 mG or less, the strong overheating suppression and low overall R_{BCS} at short ℓ overcome the higher flux trapping sensitivity. However, as the trapped flux budget increases to a more conservative 5 mG, the benefit of minimizing R_0 at long ℓ overcomes the downsides of a weaker anti-Q-slope and increased overall R_{BCS}. In other words, if one can ensure that the trapped flux in an LCLS-II-style cryomodule will be kept near zero, then it is safe to use a strong doping to a mean free path of 15-20 nm and fully capitalize on the low starting R_{BCS} and strong anti-Q-slope; if, on the other hand, the trapped flux cannot be ensured to be lower than 3 mG or even 5 mG, R_0 becomes dominant and the optimal doping level compromise moves to higher ℓ.

5.5 Outlook

This overheating model has the potential to be an important tool in guiding future development of nitrogen-doping, both in terms of choosing accelerator design specifications and in terms of guiding future doping research.

In the next chapters, I will consider and build off of these results as I look towards understanding the anti-Q-slope effects in nitrogen-infused cavities; de-

velop a framework to model quasiparticle overheating in a more general case; and assess several theories of the anti-Q-slope, including the Gurevich theory discussed above, for their agreement with experimental results.

CHAPTER 6

THE ANTI-Q-SLOPE IN NITROGEN-INFUSED CAVITIES

As discussed in Ch. 4, nitrogen infusion is a variant to the nitrogen doping process that also promotes anti-Q-slope behavior in niobium cavities, but with dramatically different impurity content. In this chapter I will go over two studies performed at Cornell in which we investigated the properties of the anti-Q-slope in nitrogen-infused cavities and the potential role of interstitial impurities in controlling those properties, drawing connections to the quasiparticle overheating model developed in Ch. 5.

6.1 Quasiparticle Overheating in Nitrogen-Infused Cavities

In Sec. 4.3, I discussed the nitrogen infusion procedure, a variation on nitrogen doping of niobium cavities that replaces the 2-30 minute doping step at 800-990 °C with a days-long "infusion" step at 120-160 °C; in addition, the post-dope chemical etching step may be avoided, potentially simplifying and economizing the procedure as well as improving workplace safety by limiting acid usage. Nitrogen-infused niobium cavities show very similar RF performance to nitrogen-doped cavities, with strong anti-Q-slopes caused by a steep decrease in R_{BCS} with increasing H_{pk}.

We prepared several cavities in our initial study of nitrogen-infused niobium at Cornell, investigating their RF performance in our vertical test stand. All the cavities discussed in this chapter were treated at 160 °C. The upper portion of Table 6.1 summarizes the infusion protocols used. Like the cavities in the overdoping study, we used the techniques described in Sec. 3.3.3 to measure

Cavity	Infusion time (hr)	Anneal time (hr)	Doping gas	Post-dope etch	T_c (K)	Δ/k_BT_c	ℓ (nm)
C4(N1)[1]	48	168	N_2	none	9.2	1.931	7±2
C6(N1)[3]	48	0	N_2	none	9.14	2.179	1±0.5
C1(N1)[1]	48	0	Ar/CO_2[4]	HF rinse	9.2	1.784	9±3
C1(N2)[1]	24	0	N_2	none	9.1	1.886	9 ± 3
C1(N3)[1]	24	0	N_2	54 nm OP[5]	9.12	2.060	344 ± 103
C7(N1)[2]	48	0	N_2	none	9.0	1.886	5 ± 2
C7(N2)[2]	48	0	N_2	2× HF rinse	9.1	1.883	6 ± 2
C7(N3)[2]	48	0	N_2	2× HF rinse + 100 nm VEP[6]	9.1	1.982	14 ± 4
C8(N1)[2]	108	0	N_2	none	9.2	1.798	2 ± 1
C8(N2)[2]	108	0	N_2	HF rinse	9.2	1.845	2 ± 1
C8(N3)[2]	108	0	N_2	2× HF rinse	9.1	1.902	3 ± 1

[1] Single-cell TESLA cavity with niobium flanges.
[2] Single-cell TESLA cavity with NbTi flanges.
[3] Nine-cell TESLA cavity.
[4] 99.99999% purity Ar mixed with 10 ppm CO_2.
[5] Oxipolish.
[6] Vertical electropolish.

Table 6.1: Overview of cavity preparations for the nitrogen infusion studies in this chapter with final critical temperature, energy gap, and mean free path values. Each cavity was chemically reset by EP before baking; bakes started with a degas step as described in Sec. 4.3. The doping gas pressure and temperature were 40 mTorr and 160 °C, respectively, for all runs.

ℓ, T_c, $\Delta/k_B T_c$, $R_0(H_{pk})$, and $R_{BCS}(H_{pk}, T)$. I then used the routine from Ch. 5 to fit the model of the anti-Q-slope mediated by quasiparticle overheating to the experimental results and find a normalized quasiparticle overheating parameter α' for each of the nitrogen-infused cavities.

The first two cavities in this study, C4(N1) and C6(N1), were treated with a 48-hour infusion in a high-purity N_2 atmosphere at 40 mTorr [KHLM16, MKL17]. Cavity C4(N1) received an additional 168 hours of annealing in vacuum after the doping step. Both of these cavities exhibited a strong reduction in R_{BCS} with increasing H_{pk}, quite similar to that observed in the high-temperature nitrogen-doped cavities discussed in Ch. 5. Analysis of the RF measurements of these cavities found relatively short mean free paths, with $\ell = 1.0 \pm 0.5$ nm for C6(N1) and $\ell = 7 \pm 2$ nm for C4(N1).

The theoretical fitting using the anti-Q-slope model with quasiparticle overheating also yielded good results for these two initial nitrogen-infused cavities. The results of the $R_{BCS}(H_{pk})$ measurements and fits are shown in Fig. 6.1. For C4(N1), the best fit was achieved with a normalized overheating parameter $\alpha' = 0.4 \pm 0.2$ mK m^2/W; for C6(N1), $\alpha' = 0.5 \pm 0.4$ mK m^2/W. Looking back to Fig. 5.8, these values are consistent with the low quasiparticle overheating of cavities doped with high concentrations of nitrogen and short mean free paths; Fig. 6.2 shows a version of Fig. 5.8 updated with the results of the initial nitrogen-infusion study.

Figure 6.3 shows the concentration of C, N, and O impurities near the surface of a witness sample baked alongside C4(N1) [KFKL17]. Notably, the nitrogen content is very low except for a sharp spike in concentration near the surface up to about 0.2 at.%, in the range of nitrogen concentrations seen in

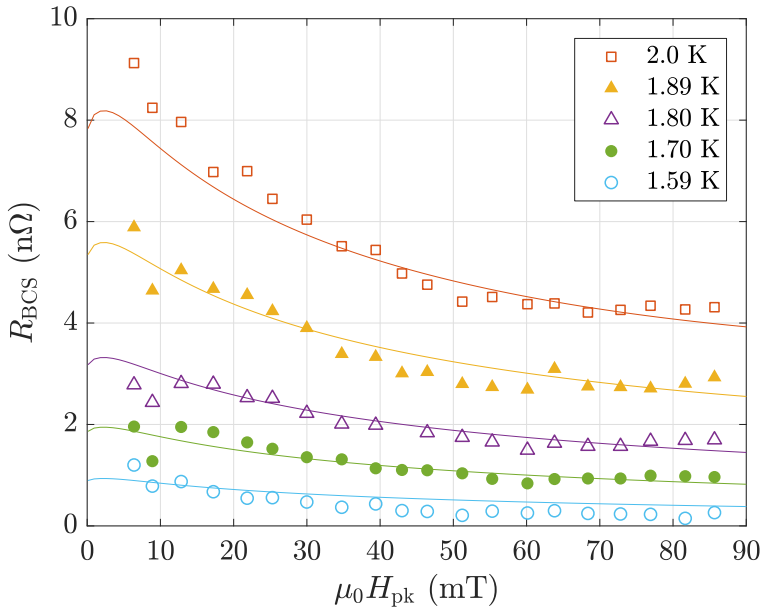

(a) C4(N1)
$\ell = 7 \pm 2$ nm

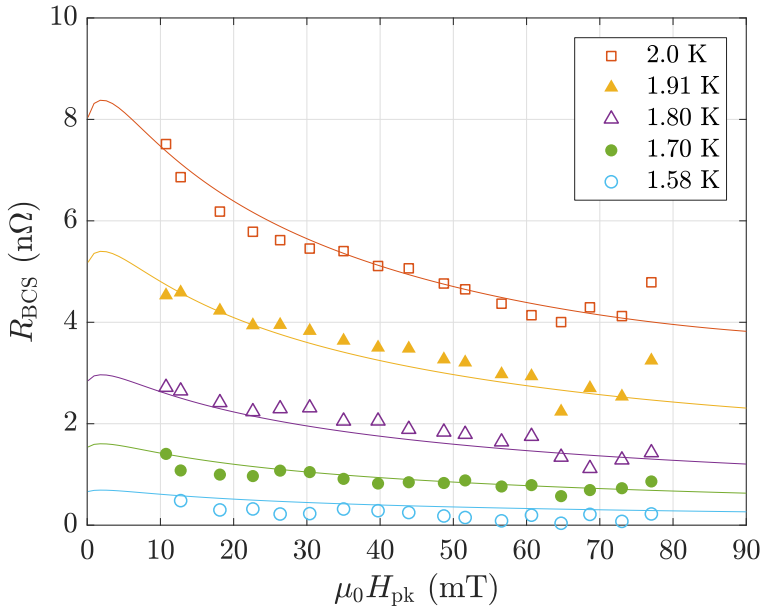

(b) C6(N1)
$\ell = 1.0 \pm 0.5$ nm

Figure 6.1: Experimental BCS surface resistance of nitrogen-infused cavities with theoretical fits using the Gurevich model with quasiparticle overheating.

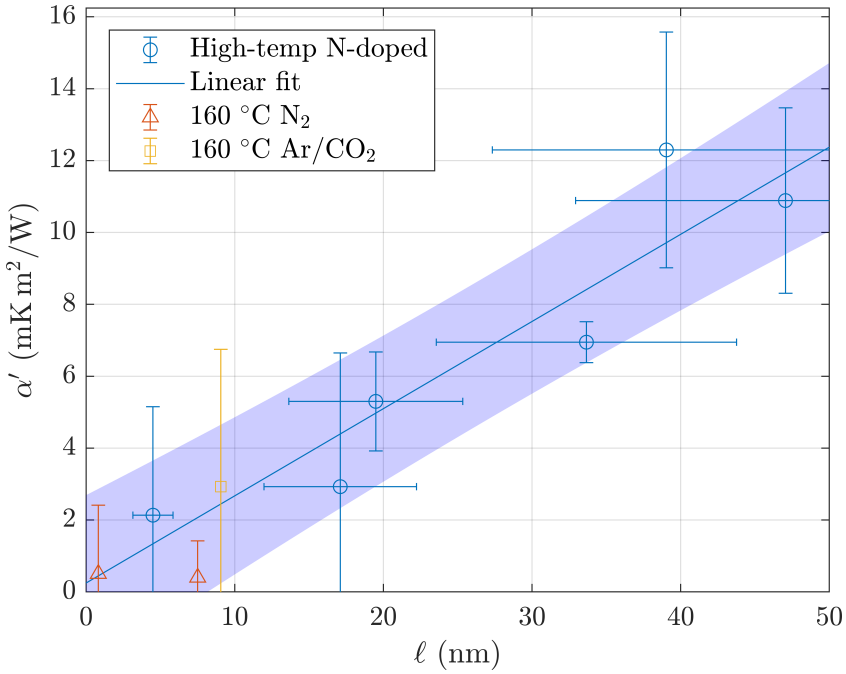

Figure 6.2: Updated version of Fig. 5.8, now including results from C1(N1), C4(N1), and C6(N1). The fit results from the nitrogen-infused cavities are consistent with the earlier model of quasiparticle overheating.

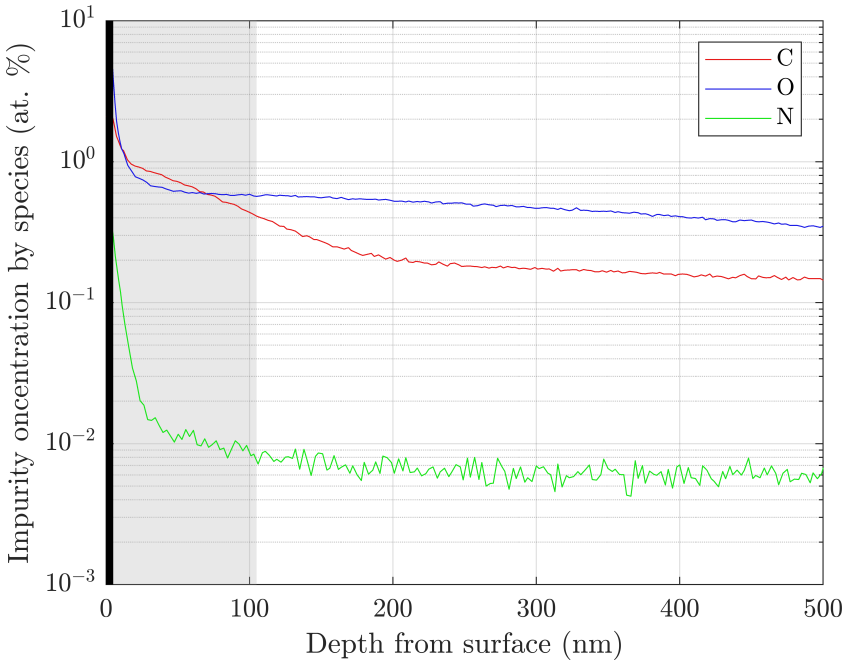

Figure 6.3: SIMS results of nitrogen, oxygen, and carbon content of cavity preparation C4(N1). Gray area approximates the RF penetration layer.

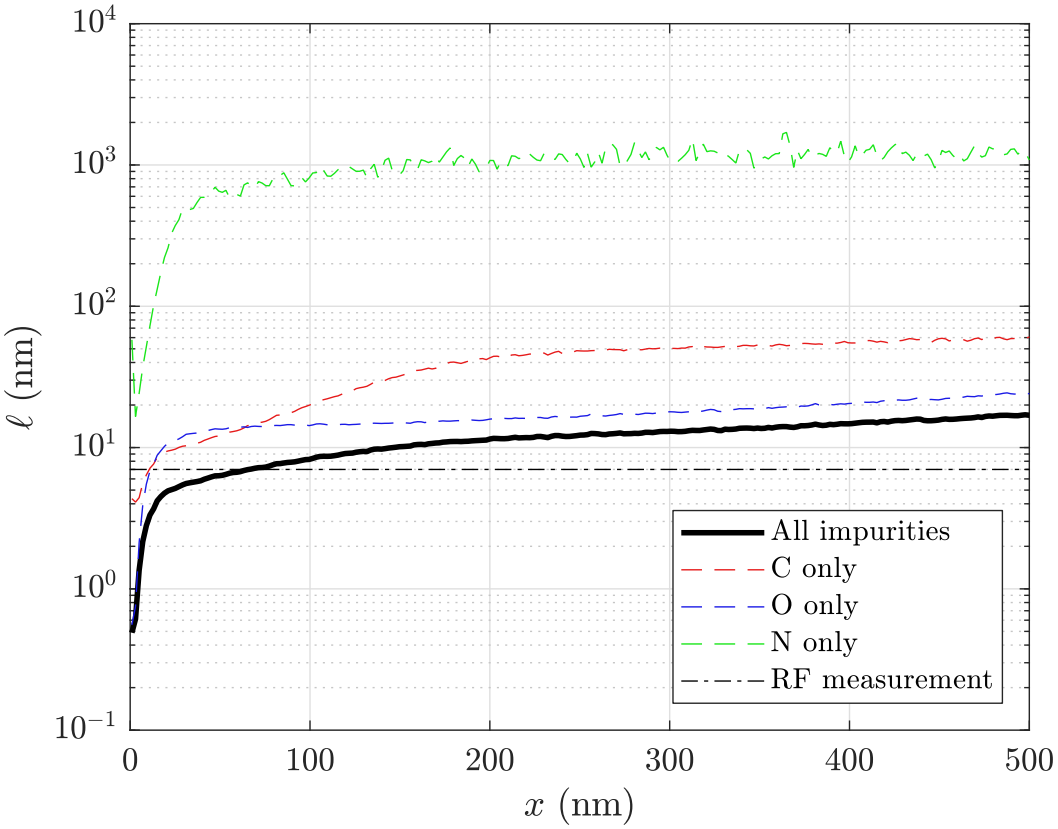

Figure 6.4: Calculation of the electron mean free path ℓ based on the concentrations of carbon, oxygen, and nitrogen impurities in the niobium sample baked with cavity C4(N1) as a function of depth x from the surface. Dashed lines indicate hypothetical contributions to ℓ from individual impurity species. The dash-dotted line indicates the value of ℓ obtained from RF measurements.

nitrogen-doped cavities; the spike decays quickly to a typical background level of 0.005-0.010 at.% over tens of nanometers. The oxygen and carbon levels, on the other hand, are quite elevated for hundreds of nanometers into the sample, reaching as high as 5 at.% near the surface and hovering near 0.1-0.5 at.% at deeper depths. This deeper concentration is at a similar level to that of nitrogen in doped cavities.

Figure 6.4 shows a depth-dependent calculation of the mean free path due to the nitrogen, carbon, and oxygen concentrations in the sample, similar to that

shown previously in Fig. 4.2. The value of ℓ changes through the depth due to the changing impurity concentrations, but the overall range near the surface within the first λ of depth is consistent with the value of ℓ determined from RF measurement analysis. Also shown in Fig. 6.4 are hypothetical calculations of ℓ for each impurity species taken separately. The high concentrations of carbon and oxygen make strong contributions to reducing ℓ, much stronger than the contribution of nitrogen.

We also prepared a third cavity in this initial study, C1(N1), attempting to remove the trace nitrogen and only load the cavity with oxygen and carbon interstitial impurities [KL18]. To achieve this, we replaced the nitrogen gas supply with a 10 parts per million mixture of carbon dioxide in a research-grade argon carrier gas (argon diffuses very slowly in metals compared to lighter elements [SR35]). The electron mean free path ℓ of this cavity was found by RF measurement to be $\ell = 9 \pm 3$ nm. The cavity showed a prominent anti-Q-slope, consistent with nitrogen-infused cavities with short ℓ; the experimental results and theoretical fits are shown in Fig. 6.5a. The fit yielded a normalized overheating parameter $\alpha' = 2.9 \pm 3.8$ mK m^2/W, again consistent with our earlier model considering the short mean free path. Unfortunately for our experiment, SIMS analysis revealed that nitrogen had still been absorbed into the surface, and in a similar quantity to that of our first nitrogen-infused samples; we presume that this nitrogen came from trace impurities in the argon or carbon dioxide supplies, or from a small leak in the furnace. Figure 6.5b shows the impurity concentrations in a witness sample baked with C1(N1).

Taken together, these RF test results, theoretical fits, and impurity concentration data tell quite an interesting story. As the experimental data and fits

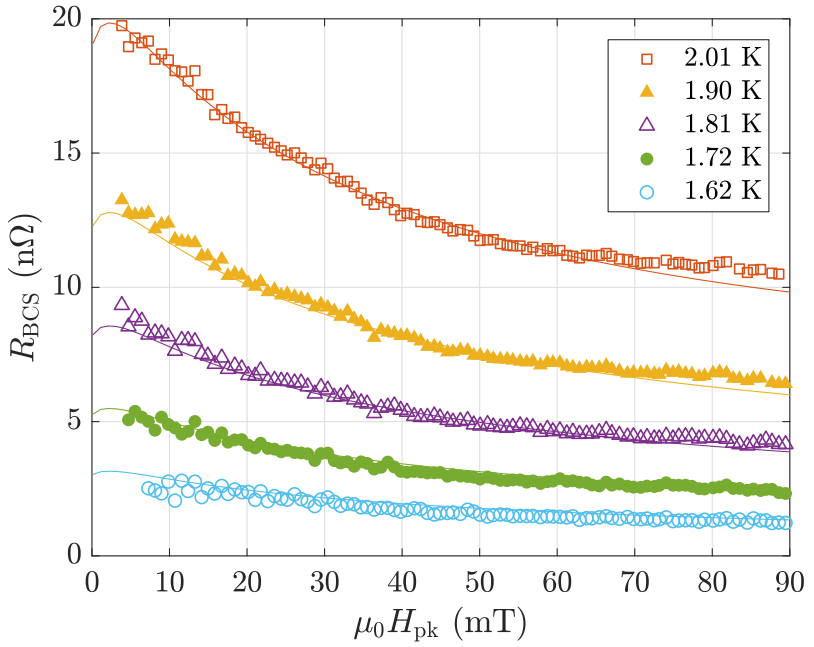

(a) C1(N1)
$\ell = 9 \pm 3$ nm

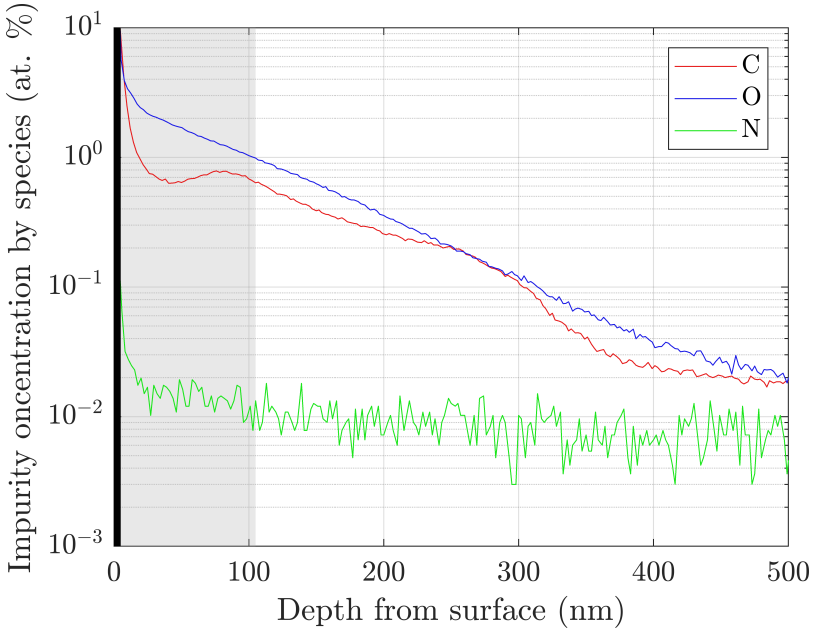

(b) C1(N1)
SIMS results

Figure 6.5: Experimental BCS surface resistance of a cavity treated with an Ar/CO_2 mixture with theoretical fits using the Gurevich model with quasiparticle overheating, as well as the SIMS results from a witness sample showing the concentrations of carbon, oxygen, and nitrogen in the surface.

reveal, the performance of these nitrogen-infused cavities was consistent with typical behavior of nitrogen-*doped* cavities. In terms of impurity content, the *total* impurity concentration level and the resulting electron mean free path ℓ was similar in the RF penetration layer for both treatments, but with different impurity species having the strongest presence. Considering our earlier model of the suppression of quasiparticle overheating by interstitial impurities, the high concentrations of oxygen and carbon in these nitrogen-infused cavities seem to be playing the role previously filled by nitrogen in high-temperature doped cavities. In Ch. 7 I will develop an advanced thermal modeling framework to further investigate this hypothesis.

These results also raise some interesting questions about the underlying anti-Q-slope behavior in nitrogen-infused cavities. Are the carbon and oxygen impurities causing the field-dependent reduction in R_{BCS}, or is the trace nitrogen (with a nanometers-thick spike near the surface) the true culprit? How will the properties of the anti-Q-slope vary as these impurity concentrations are changed?

6.2 Infusion Time and Surface Removal Study

In order to address these questions, we began a study investigating the performance of nitrogen-infused cavities with varying surface concentration of nitrogen, oxygen, and carbon [KMGL19, MAG+19]. We attempted to control this concentration in two ways: first, we varied the length of the infusion step, with the thought that longer infusion times would allow more of the impurities to diffuse into the niobium; second, we performed light chemical and electrochemical removals to etch away the regions of high impurity concentration and reveal

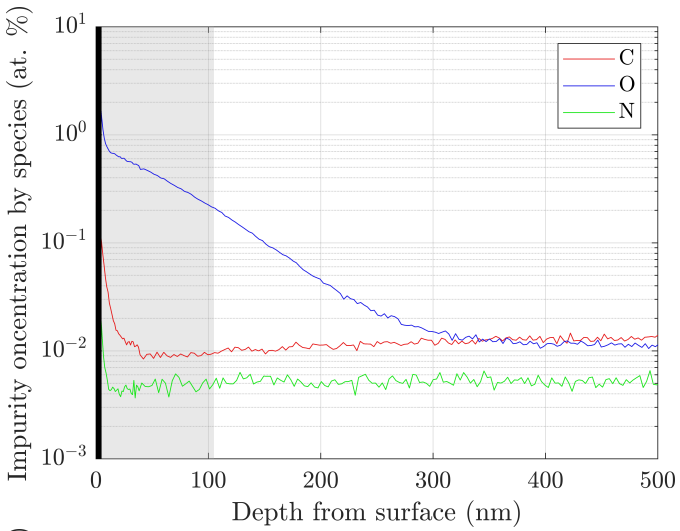

(a) C1(N2)

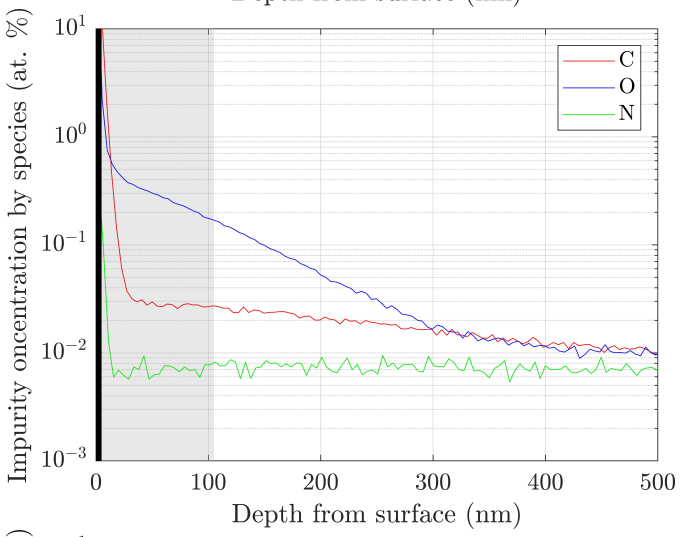

(b) C7(N1)

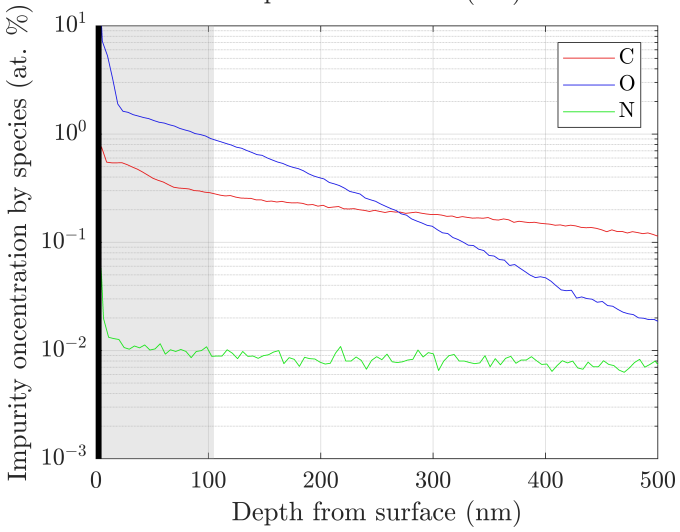

(c) C8(N1)

Figure 6.6: SIMS analysis results showing the concentrations of interstitial impurities in niobium witness samples baked alongside cavity preparations C1(N2), C7(N1), and C8(N1). Table 6.1 shows the protocols for these nitrogen infusion treatments.

lower concentrations beneath, analogous to the post-dope EP in the nitrogen-doped cavities discussed in Chs. 4 and 5. The lower portion of Table 6.1 gives an overview of the nitrogen infusion and surface removal protocols used in this study.

Figure 6.6 shows the results of SIMS analysis measuring the concentration of carbon, oxygen, and nitrogen in witness samples baked with C1(N2) (24-hour infusion), C7(N1) (48-hour infusion), and C8(N1) (108-hour infusion). Like the earlier nitrogen-infused samples, these showed a nanometers-wide spike of nitrogen at the 0.1 at.% level near the surface and a much lower concentration beneath the near-surface region. C1(N2) and C7(N1) show similar oxygen levels, while C7(N1) has a higher concentration of carbon than C1(N2). C8(N1), the cavity which received the longest infusion treatment, had higher concentrations of carbon and oxygen than the other two cavities.

6.2.1 Titanium Contamination

Under initial RF testing, cavities C7(N1) and C8(N1) behaved similarly but unusually for nitrogen-infused cavities. In particular, they exhibited a high R_{BCS} that did not decrease with increasing RF field strength, instead staying roughly constant with a slight increase. Figure 6.7 shows the 2 K R_{BCS} for these two cavity treatments. Optical inspection of the flanges of these cavities, made of niobium-titanium rather than the normal niobium used for the flanges of cavities C1-C5, found severe black speckling across the flange surface. Figure 6.8 shows an image of one of the afflicted cavity flanges. We again performed SIMS analysis on the witness sample for C8(N1), this time looking for titanium, with the hypoth-

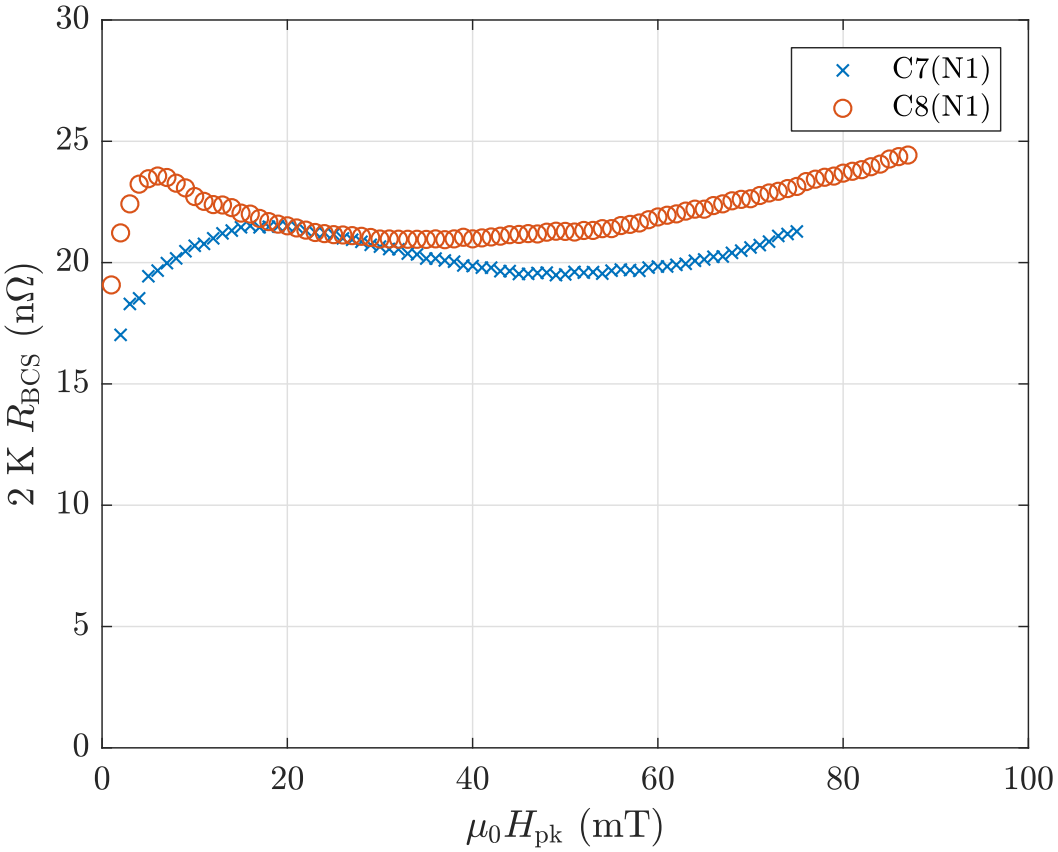

Figure 6.7: BCS surface resistance measurements at 2 K for the nitrogen-infused cavities that suffered titanium contamination.

esis that during the long infusion bake the flanges outgassed titanium that was then deposited onto the RF surface of the cavity (as well as the sample). Indeed, SIMS revealed a surface layer with a high concentration of titanium, as shown in Fig. 6.9. Over the first 2 nm, Ti was found at the 0.001-0.01 at.% level, steeply dropping to a background level at a depth of 40 nm.

6.2.2 HF Rinsing and Anti-Q-Slope Behavior

We performed an HF rinse on cavity C8(N1) in order to clean the titanium off of the niobium surface, yielding preparation C8(N2). HF rinsing removes the

Figure 6.8: Black speckling was observed on the NbTi flanges of C7(N1) as well as C8(N1), pictured here.

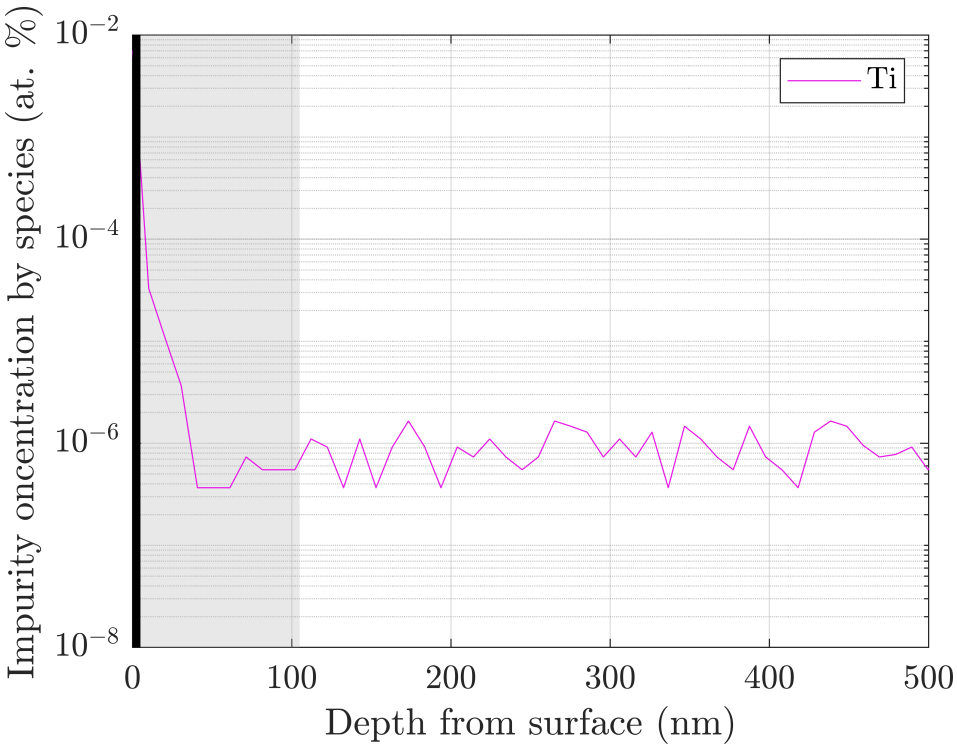

Figure 6.9: SIMS analysis revealing titanium contamination on the surface of a witness sample baked alongside C8(N1).

oxide layer atop the niobium surface, typically 5 nm in thickness; the first 2 nm of niobium underneath the removed oxide are converted into a fresh 5-nm oxide layer [GH80, AAC$^+$99, RGBO13]. The results of the RF test of C8(N2) revealed the expected strong anti-Q-slope typical of nitrogen-infused cavities, as shown in Fig. 6.10, indicating that the HF rinse succeeded in removing the titanium contamination layer and that the titanium suppressed the anti-Q-slope behavior. Based on the earlier SIMS results, this HF rinse also lowered the concentration of nitrogen at the surface from approximately 0.07 at.% to 0.04 at.%; the 2-5 nm scale of material removal by HF rinse is slightly smaller than the 10-15 nm scale of the nitrogen impurity presence in nitrogen-infused cavities.

We performed a second HF rinse to further reduce the nitrogen level and measure any possible changes in the field-dependent R_{BCS}. The resulting cavity preparation, C8(N3), did not show dramatically different performance except for a slightly decreased overall value of R_{BCS}; this is likely due to the slightly increased mean free path ℓ towards the minimum in R_{BCS} near $\ell = 20$ nm. The SIMS results indicate that the nitrogen concentration after the second HF rinse was approximately 0.02 at.%.

Based on the success of the HF rinse in curing the titanium contamination, we performed a double HF rinse on C7(N1), yielding cavity C7(N2). After rinsing, this cavity also showed anti-Q-slope behavior quite similar to that of C8(N3) for $\mu_0 H_{\mathrm{pk}} > 20$ mT, with a slightly lower R_{BCS} at lower fields.

Unlike C7(N1) and C8(N1), the 24-hour infusion run of C1(N2) yielded an anti-Q-slope under RF test without any chemical surface treatment. This further supports the titanium contamination hypothesis since the flanges on cavity C1 were constructed from pure niobium, not NbTi.

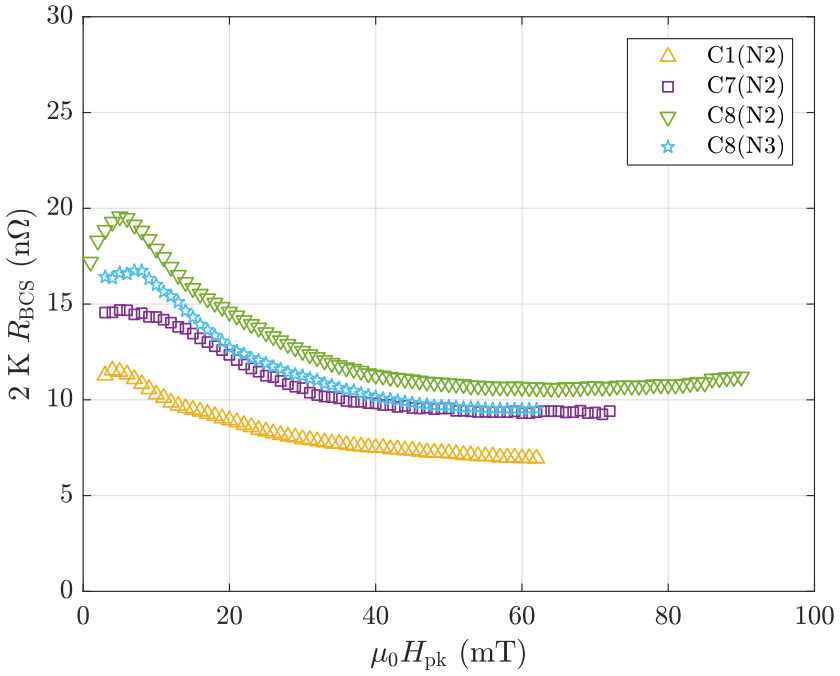

Figure 6.10: BCS surface resistance measurements at 2 K for the nitrogen-infused cavities C7 and C8 that had previously suffered titanium contamination and were subsequently treated with HF rinsing. Also shown is C1(N2) which did not suffer contamination or require HF rinsing.

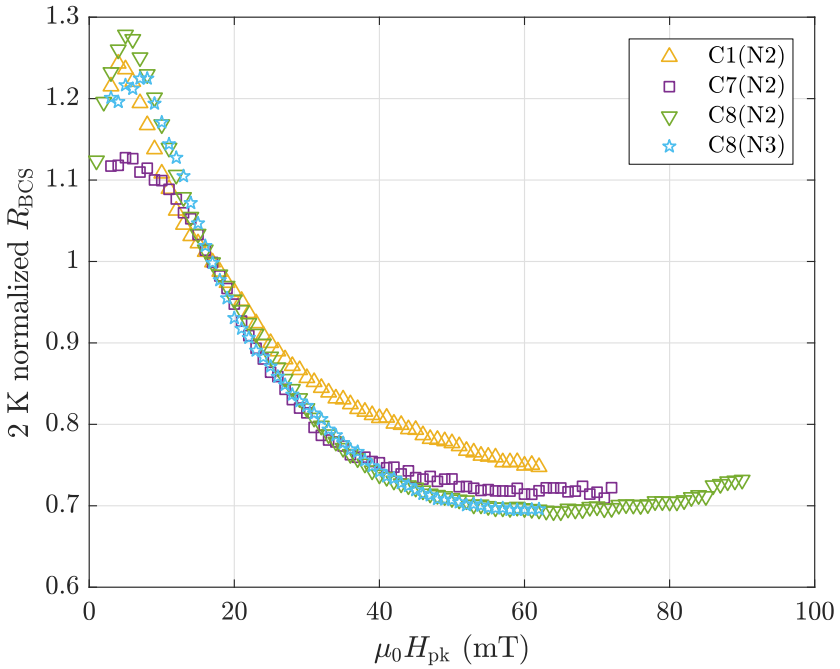

Figure 6.11: BCS surface resistance measurements from Fig. 6.10, normalized here at $\mu_0 H_{\mathrm{pk}} = 17$ mT.

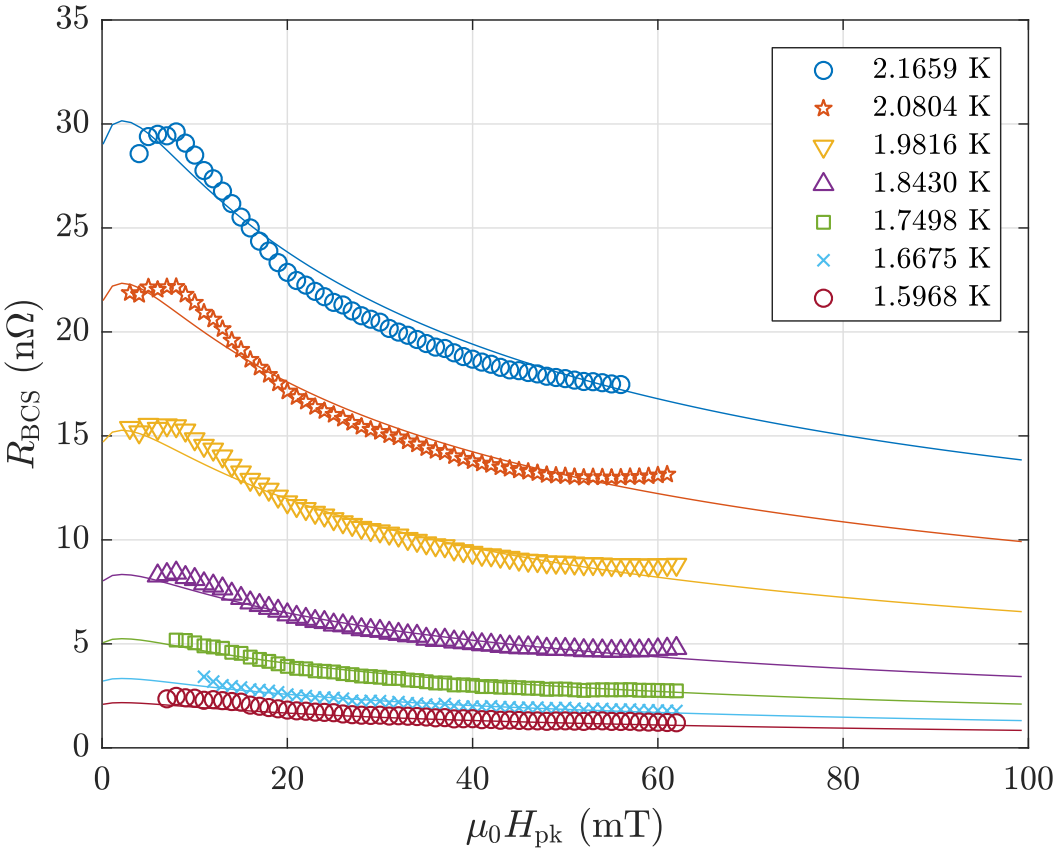

Figure 6.12: Measurements of R_{BCS} vs. H_{pk} for cavity C7(N2) at several temperatures with fitted predictions of the Gurevich model.

Figure 6.10 summarizes the anti-Q-slope results of these cavity preparations, showing the measurements of $R_{\mathrm{BCS}}(H_{\mathrm{pk}})$ at 2 K. Figure 6.11 shows the same curves normalized at 17 mT (E_{acc} = 4 MV/m); the anti-Q-slopes of these four cavity preparations show very similar relative reduction in R_{BCS} with increasing field strength. Fitting the $R_{\mathrm{BCS}}(H_{\mathrm{pk}})$ data for these cavities with the Gurevich model found only moderate success. Fig. 6.12 shows the fit results for cavity preparation C7(N2) as an example; in general, the theory was not able to predict both the steep decrease in R_{BCS} at low fields and the reversal of the field-dependence near 50 mT. This discrepancy between the predictions of the Gurevich model and experimental results of nitrogen-infused cavities will be discussed further in Chap. 8.

The similarity in the field-dependent reduction in R_{BCS} is quite interesting given the variation in infusion time across the cavities. these initial results indicate that the length of the infusion step does not strongly affect the magnitude of the anti-Q-slope in nitrogen-infused cavities; it should be noted, however, that the electron mean free path ℓ of all of the nitrogen-infused cavities in this study showing anti-Q-slope behavior falls within the low-overheating prediction of the earlier quasiparticle overheating model. The overall doping level does affect ℓ, due largely to the increased concentrations of carbon and oxygen. This in turn plays a large part in determining the overall BCS surface resistance. Further work is ongoing at Cornell to continue this investigation on infusion time and anti-Q-slope performance.

6.2.3 Deeper Surface Removal

After the HF rinse study above, we sought to perform deeper surface removal in order to isolate the roles of the different impurities in nitrogen-infused cavities. For cavity preparation C1(N3), we performed a 54 nm oxipolish [Die78, Hal17] on cavity C1. Based on the SIMS results in Fig. 6.6a, this fully removed the "spike" in the concentration of nitrogen near the RF surface; it also substantially reduced the concentration of carbon, but left the oxygen concentration near the 0.5 at.% level. Under RF test, this cavity showed no anti-Q-slope after the deeper removal, instead behaving much like a clean non-doped niobium cavity. As shown in Table 6.1, the electron mean free path ℓ was measured to be remarkably long given the high oxygen impurity content even at a depth of 54 nm.

We performed a similar test on cavity C7, removing 100 nm by VEP (per-

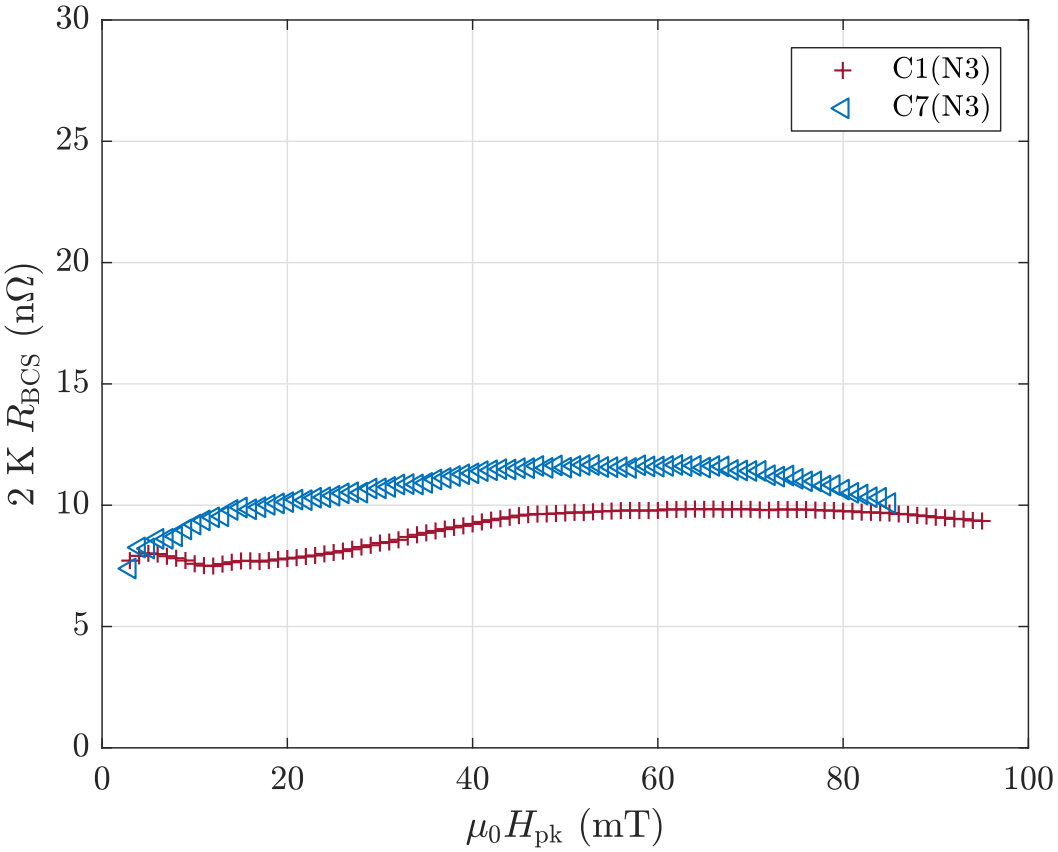

Figure 6.13: BCS surface resistance measurements at 2 K for the nitrogen-infused cavities that were treated with moderate surface removal by oxipolishing and electropolishing.

formed at a lower temperature of ~ 10 °C to slow the reaction rate) to yield cavity preparation C7(N3). Going by the earlier SIMS results shown in Fig. 6.6b, this polishing step again fully removed the surface nitrogen and substantially reduced the concentrations of carbon and oxygen. The carbon content for this cavity was higher than for C1(N3), and the oxygen content was lower. Like C1(N3), preparation C7(N3) showed no anti-Q-slope and instead behaved much like a non-doped niobium cavity, though the overall level of R_{BCS} was consistent with its short mean free path of 14 nm. Figure 6.13 summarizes the RF performance of these two cavities with moderate surface removal, showing the results of the measurements of $R_{\mathrm{BCS}}(H_{\mathrm{pk}})$ at 2 K.

These results begin to indicate that, despite its very limited presence in the RF layer except for the spike in concentration at the surface up to the 0.01-0.1 at.% level, nitrogen plays an essential role in the anti-Q-slope in nitrogen-infused cavities. These light surface removals were enough to completely remove the anti-Q-slope behavior and restore standard niobium behavior. What appears to be their most significant impact on the chemical composition of the RF surface layer is the near-total removal of the trace amounts of nitrogen, bringing its concentration at the surface below 0.01 at.%. This apparent correlation between the removal of the nitrogen surface layer and the removal of the anti-Q-slope behavior is the subject of ongoing research at Cornell.

6.2.4 Discussion

Together, the results of the three stages of the surface removal study indicate that the physics of the anti-Q-slope in nitrogen-infused cavities is highly dependent on the properties of the first hundreds if not the first tens of nanometers of the RF surface layer. A mild case of titanium contamination (0.001-0.01 at.% at the surface, rapidly decreasing to 1×10^{-5} at.% at a depth of 15 nm and 1×10^{-6} at 40 nm) prevented the field-dependent reduction in R_{BCS}. Light removal of single-digit-nanometer-thickness layers then fully restored the anti-Q-slope behavior expected for these cavity treatments. This is quite remarkable and may be the most important finding of this study: something located right on the surface of the cavity appears to turn the anti-Q-slope on and off. Finally, deeper chemical etching/polishing of tens of nanometers again removed the anti-Q-slope. While the high concentration of oxygen and carbon impurities match well the suppression of quasiparticle overheating, the correlation between the

reduction of the surface nitrogen concentration to below 0.01 at.% and the removal of the anti-Q-slope points towards nitrogen as the source of the underlying anti-Q-slope behavior.

A second lesson to draw from this surface removal study is that the length of the 160 °C infusion step does not strongly affect the relative reduction in R_{BCS} with increasing RF field, though the overall impurity content does affect the overall magnitude R_{BCS} (as expected by Eq. 3.41). In terms of impurity content, the unifying trend across the cavities in this study which did show anti-Q-slope is a thin layer of nitrogen at or above a concentration of 0.01 at.%. This also points towards nitrogen as the source of the underlying anti-Q-slope behavior.

On a more practical note, another lesson learned from this study is that the nitrogen infusion procedure is sensitive to surface contamination. Because the treatment does not nominally call for post-doping surface chemistry (as is usually included in the high-temperature nitrogen-doping procedure), the cavity is stuck with any surface contamination acquired during the furnace treatment step until its deleterious effects are revealed under RF test. Alternatively, HF rinsing could be included as part of the standard procedure for nitrogen infusion to reduce surface contamination issues.

This is promising initial work, but the evidence suggesting nitrogen's role in the anti-Q-slope remains somewhat circumstantial. As mentioned in Secs. 6.2.2 and 6.2.3 above, further research on the anti-Q-slope in nitrogen-infused niobium cavities is currently underway in the Cornell SRF group. In particular, these studies are looking towards finding more solid evidence for the role of nitrogen in the field-dependent reduction of the BCS resistance, continuing the studies of light surface removal and varied infusion step times as well as infu-

sion temperatures.

CHAPTER 7

ADVANCED THERMAL MODELING OF NIOBIUM SRF CAVITIES

At the extremely low temperatures where niobium SRF accelerators operate, the thermal properties of the accelerator cavities can have a large impact on the performance of the accelerator. The BCS surface resistance is exponentially dependent on temperature, and as discussed in Sec. 3.3.5, inefficient heat transfer from the interior RF surface to the exterior cooling bath can significantly increase the temperature of the RF surface, thereby increasing R_{BCS} and decreasing the accelerator efficiency Q_0.

The work presented in Ch. 5 investigated the electron-phonon heat transfer efficiency parameter Y in nitrogen-doped cavities, finding an empirical link between interstitial impurity content (quantified by the electron mean free path ℓ) and improved thermal efficiency: the high impurity content of strongly nitrogen-doped niobium cavities suppresses surface heating and promotes high-Q_0 performance. Likewise, shown in Ch. 6 were results indicating strong overheating suppression in nitrogen-infused cavities. This similarity in apparent surface heating behavior arises despite the dramatic differences in impurity content between the two similarly named cavity treatment protocols. Nitrogen-*doped* cavities have a relatively flat concentration of nitrogen for hundreds of nanometers into the surface (see Fig. 4.2), while nitrogen-*infused* cavities have concentration profiles of nitrogen, carbon, and oxygen that change drastically on the scale of *tens* of nanometers into the surface (as seen, for example, in Fig. 6.6).

So far, these surface heating studies have used a relatively simple thermal model, assuming linearized quasiparticle overheating quantified by a single

parameter α' independent of temperature and field strength; Eqs. 5.5 and 5.6 essentially express the full extent of the calculation. The results suggest a deep connection between high impurity content and improved thermal transfer, but in order to study this effect more thoroughly a more advanced thermal model is desirable.

I set out to develop such a model for niobium cavities, with a more detailed simulation of thermal effects and with greater adaptability to different models of R_s and Y. In particular, I sought to include several important features:

1. **Support for arbitrary surface resistance model –** While previous thermal models have been purpose-built for certain underlying models of the surface resistance R_s (such as the model in Ch. 5 for the Gurevich anti-Q-slope theory or the HEAT code [VXP07] for the Mattis-Bardeen theory), I wanted the new modeling framework to allow for the use of any microscopic/local calculation.
2. **Support for depth-dependent material parameters –** The impurity concentration profiles in nitrogen-infused cavities vary dramatically with depth, as discussed above, and the same can be said of a variety of other cavity treatments as well [KFKL17, BJ15, RG11]; this depth-dependent concentration gives rise to depth-dependent ℓ, λ, ξ, and other important parameters. I wanted the model to consider these depth-dependent properties especially in building an understanding of the electron-phonon heat transfer efficiency Y.
3. **Incorporation of existing models of thermal effects –** Some aspects of thermal transfer in niobium cavities cooled by liquid helium baths have been studied and modeled parametrically [VXP07, KB96, AF00, BF95]. I

wanted to incorporate these models of κ and h_K into the new framework in order to break apart the terms grouped in α' in Eq. 5.5 and isolate the electron-phonon effects encapsulated in Y for more detailed modeling.

4. **Consideration of quasiparticles in thermal equilibrium –** As mentioned in Sec. 5.3, the model of quasiparticle overheating used in the overdoping study made the implicit assumption that the quasiparticle temperature T_{quasi} was local and strictly dependent on the local field strength; for the advanced thermal model, I wanted to include the ability to calculate the thermal transfer given an equilibrium T_{quasi} through the RF layer.

The framework consists of two computational "grids" where different portions of the physics of the thermal model are calculated; for simplicity, the thermal framework operates in one dimension, under the assumption that the material is uniform across the surface and defect-free. On the first grid, representing points near the RF surface, the framework calculates the power dissipated by the RF field given local material parameters, an underlying model of R_s, and an equilibrium quasiparticle temperature T_{quasi}. On the second grid, representing points deeper in the niobium bulk and extending out to interface between the cavity and the helium bath, the model simulates thermal transfer through the cavity wall and into the bath, arriving at a quasiparticle temperature T_{quasi} given the magnitude of the RF power dissipated in the surface. The framework then repeats these measurements for varying T_{quasi}, arriving at a self-consistent result where the heat flow is matched across the two computational grids. In the next few sections I will outline these principal components.

7.1 Depth-Dependent Power Dissipation

The framework's computation routine begins on the near-surface grid representing the material in the first ~ 1 μm of the cavity wall, calculating the power per unit area dissipated by the RF field. The one-dimensional "grid" is made of up exponentially spaced points with a high density near the surface and a decreasing density extending into the depth of the material. This varying surface density improves calculation accuracy and efficiency by focusing computational resources near the surface where the RF field strength is highest (see Eq. 3.6) and where, in nitrogen-infused cavities, the depth-dependent material parameters change most rapidly (see for example Figs. 6.3 and 6.4).

Using a depth-dependent electron mean free path $\ell(x)$ that is either entered manually or calculated from SIMS results, the framework calculates a depth-dependent local $\xi(x)$ with Eq. 3.9 and $\lambda(x)$ using Eq. 3.10. Figure 7.1 shows an example calculation of these depth-dependent parameters using the SIMS results from cavity C4(N1) in Chap. 6. As an additional option, T_c and $\Delta/k_B T_c$ can be set as depth-dependent parameters or be given uniform values.

To calculate the depth-dependent peak RF magnetic field strength $\mu_0 H_{pk}(x)$, the framework uses the following:

$$\frac{dH_{pk}}{dx} = -\frac{H_{pk}(0)}{\lambda(x)} \exp\left(\frac{-x}{\lambda(x)}\right) \tag{7.1}$$

Integrating this over x yields the relative field profile:

$$\frac{H_{pk}(x)}{H_{pk}(0)} = \frac{1}{H_{pk}(0)}\left(1 + \int_0^x \frac{dH_{pk}}{dx} dx\right) \tag{7.2}$$

$$= 1 + \int_0^x -\frac{1}{\lambda(x)} \exp\left(\frac{-x}{\lambda(x)}\right) dx \tag{7.3}$$

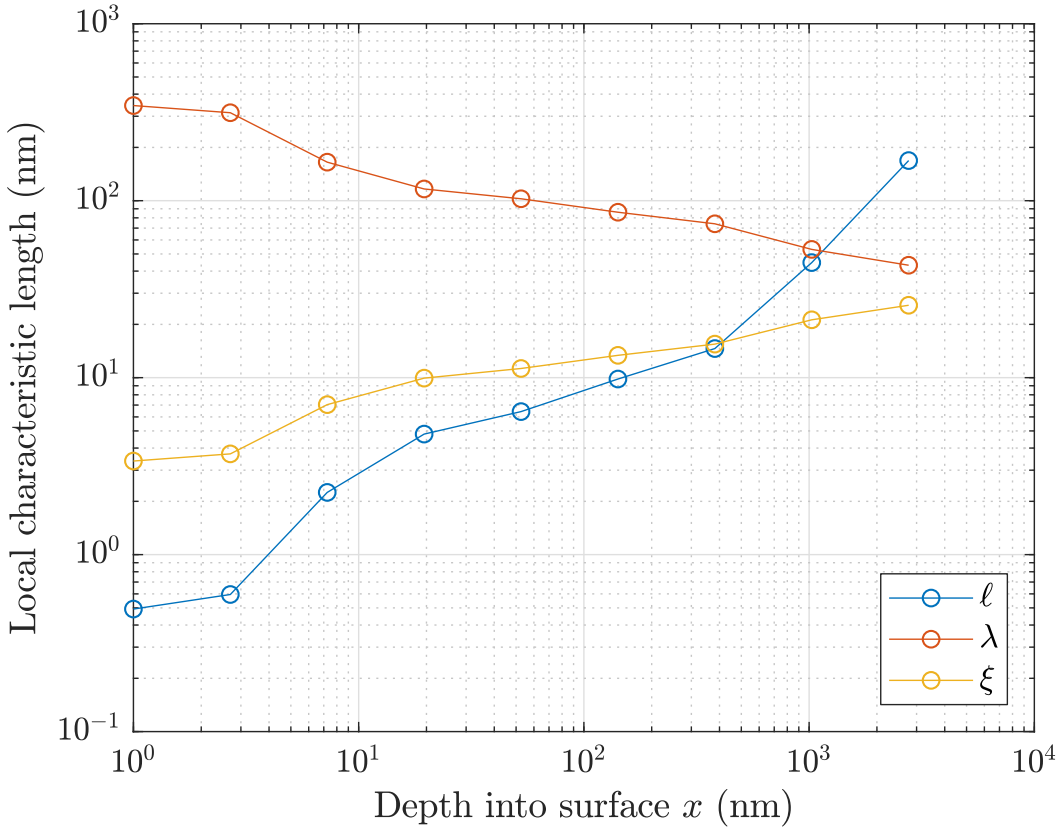

Figure 7.1: Depth-dependent mean free path ℓ, penetration depth λ, and coherence length ξ evaluated on the near-surface grid. Data generated from SIMS results for C4(N1), shown in Fig. 6.3.

Here the added 1 is an integration constant to satisfy the boundary condition that $H_{\mathrm{pk}}(x)/H_{\mathrm{pk}}(0) = 1$ at $x = 0$. Figure 7.2 shows the depth-dependent relative field strength $H_{\mathrm{pk}}(x)/H_{\mathrm{pk}}(0)$ for C4(N1), corresponding to the depth-dependent parameters shown above in Fig. 7.1.

Once the material parameters are established, the simulation begins with an ansatz quasiparticle temperature T_{quasi} and a peak surface magnetic field $H_{\mathrm{pk}}(0)$. At each point on the grid, the local volume density of dissipated power $\frac{d}{dx}\left(\frac{P}{A}\right)$ is calculated given the local material parameters, local field level $H_{\mathrm{pk}}(x)$, the ansatz T_{quasi}, and the chosen model of the surface resistance.

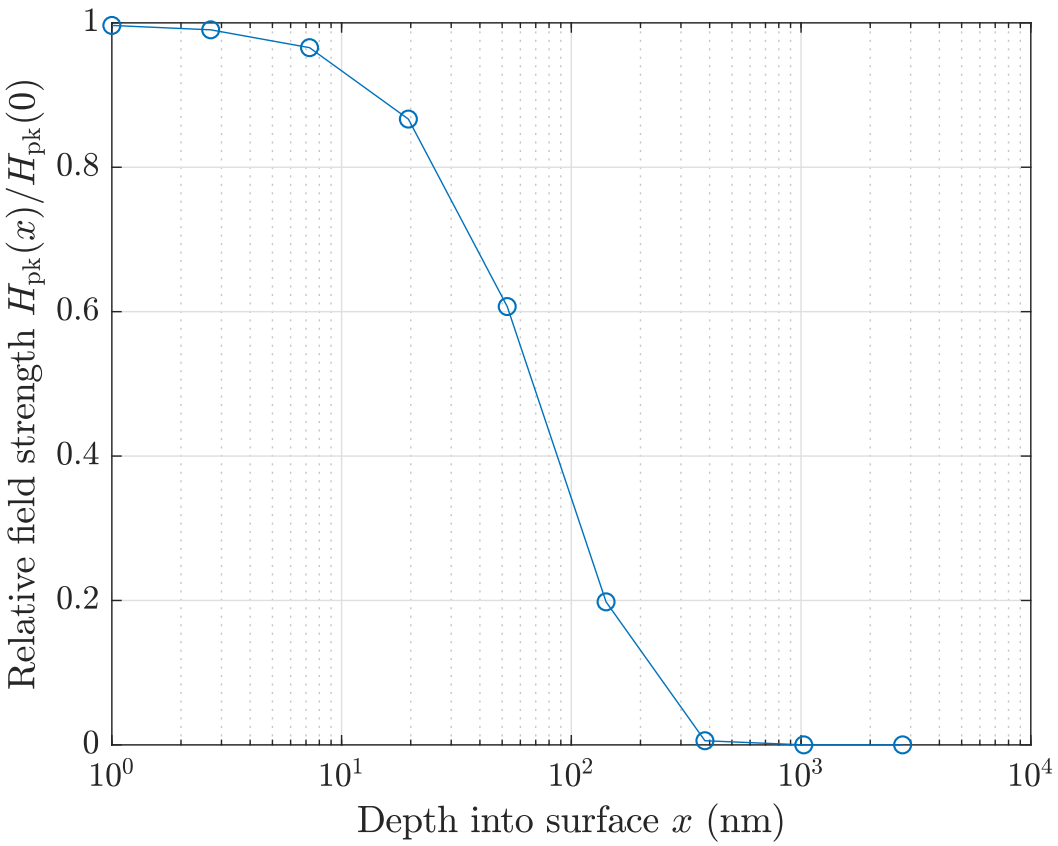

Figure 7.2: Depth-dependent relative field strength evaluated on the near-surface grid. Data generated from SIMS results for C4(N1), shown in Fig. 6.3.

For surface resistance models that do not explicitly calculate a local dissipated power volume density, one can be generated for each grid point by calculating R_s for a uniform material with the material properties of the desired grid point. This should be calculated with a surface field equal to the local field at the grid point and at the ansatz T_{quasi}. The Joule heating from a current decaying exponentially into the depth x with decay constant λ is equal to that in a slab of

thickness $\lambda/2$ and uniform current[1]:

$$\frac{P}{A} = \mathrm{Re}\left[\int_0^\infty \frac{J^2}{\sigma} dx\right] \tag{7.4}$$

$$= \mathrm{Re}\left[\frac{J_{\mathrm{pk}}^2}{\sigma}\right] \int_0^\infty \exp\left(-\frac{2x}{\lambda}\right) dx \tag{7.5}$$

$$= \frac{\lambda}{2} \mathrm{Re}\left[\frac{J_{\mathrm{pk}}^2}{\sigma}\right] \tag{7.6}$$

As such, the dissipated power volume density at the surface of the uniform material is given by the following, substituting in the expression for $\frac{P}{A}$ used in Eq. 3.35:

$$\frac{P}{A} = \frac{1}{2} R_{\mathrm{s,uni}} H_{\mathrm{pk}}^2 \tag{7.7}$$

$$\frac{d}{dx}\left(\frac{P}{A}\right) = \frac{P}{A}\frac{2}{\lambda} = \frac{1}{\lambda} R_{\mathrm{s,uni}} H_{\mathrm{pk}}^2 \tag{7.8}$$

Then, in the local approximation, this power density is equivalent to the dissipated power volume density at the grid point x:

$$\left.\frac{d}{dx}\left(\frac{P}{A}\right)\right|_x = \frac{1}{\lambda} R_{\mathrm{s,uni}} H_{\mathrm{pk}}(x)^2 \tag{7.9}$$

Once the local dissipated power volume density is found for all grid points, the total dissipated power per unit area can be calculated by integrating over x:

$$\frac{P}{A} = \int_0^\infty \frac{d}{dx}\left(\frac{P}{A}\right) dx \tag{7.10}$$

$$= \int_0^\infty \frac{1}{\lambda} R_{\mathrm{s,uni}} H_{\mathrm{pk}}(x)^2 dx \tag{7.11}$$

Here, $H_{\mathrm{pk}}(x)$ can be acquired from Eq. 7.2. This integral can be approximated by integrating up to a finite limit x_{end} if $H_{\mathrm{pk}}(x_{\mathrm{end}}) \ll H_{\mathrm{pk}}(0)$.

[1] See Eqs. 3.29-3.32 for a similar calculation.

7.2 Thermal Propagation

After an ansatz quasiparticle temperature T_{quasi} has been chosen and the dissipated power per unit area P/A of the RF surface has been calculated, the framework moves to calculating the propagation of this heat through the cavity wall and out to the helium bath. The system separates the thermal effects that were grouped in the earlier model presented in Chap. 5, with independent models of κ and h_{K}. For the electron-phonon heat transfer parameter Y, we do not yet have a conclusively predictive model, but we can draw on our earlier empirical model to set Y based on the material parameters as in Eq. 5.9.

The thermal propagation simulation calculates from the helium bath inwards, using a fixed value of the bath temperature T_{bath}. The simulation begins with finding the Kapitza resistance h_{K}, using a model developed by Vines and based on earlier experimental data presented by Mittag [VXP07, Mit73]. The framework uses the model for annealed niobium cooled by superfluid helium ($T_{\text{bath}} < 2.17$ K), considering T_{bath} as well as the temperature of exterior surface of the cavity wall T_{wall}:

$$h_{\text{K}}(T_{\text{wall}}, T_{\text{bath}}) = \left(200 \frac{\text{W}}{\text{m}^2\,\text{K}}\right)\left(\frac{T_{\text{bath}}}{1\ \text{K}}\right)^{4.65} f\left(\frac{T_{\text{wall}} - T_{\text{bath}}}{T_{\text{bath}}}\right) \tag{7.12}$$

$$f(t) = 1 + \frac{3}{2}t + t^2 + \frac{1}{4}t^3 \tag{7.13}$$

When $T_{\text{bath}} > 2.17$ K, the framework instead uses the model for niobium cooled by nucleate boiling in normal liquid helium:

$$h_{\text{K}}(T_{\text{wall}}, T_{\text{bath}}) = \left(1.2 \times 10^4 \frac{\text{W}}{\text{m}^2\,\text{K}}\right)\left(\frac{T_{\text{wall}} - T_{\text{bath}}}{1\ \text{K}}\right)^{0.45} \tag{7.14}$$

The heat flux q, by symmetry equal to the dissipated power per unit area on the RF surface P/A, is related to the Kapitza resistance and the temperatures of the

outer niobium wall and helium bath:

$$q = \frac{P}{A} = (T_{\text{wall}} - T_{\text{bath}})\, h_{\text{K}} \tag{7.15}$$

The Vines/Mittag model maps the wall temperature T_{wall} to P/A; as such, for a fixed T_{bath} we can generate a map of P/A values for a likely range of T_{wall}, such as $T_{\text{bath}} \leq T_{\text{wall}} \leq T_{\text{c}}$, and then numerically invert the map to find T_{wall} for the value of the dissipated power density P/A calculated in the near-surface grid.

Once the framework has calculated T_{wall} given the earlier P/A, it uses the parametric model of Koechlin and Bonin to calculate the thermal conductivity through the cavity wall [KB96]. This calculation takes place on a second computational "grid" with linearly spaced points representing the bulk niobium in the cavity wall[2]. Since doping and similar treatments affect only the first tens of micrometers of depth in the cavity wall, the majority of the 3 mm thickness is clean high-RRR niobium.

At very strong levels of doping, the reduced κ in these first few micrometers may start to make a significant impact on the overall thermal transport; one possible improvement for the model would be to include a region of poor thermal conductivity near the interior and exterior surfaces.

The Koechlin-Bonin model calculates the thermal conductivity κ for superconducting niobium as follows, depending on the local niobium temperature T_{Nb}, RRR, and the phonon mean free path ℓ_{ph}:

$$\kappa = R(y)\left(\frac{1}{A\,\text{RRR}\,T_{\text{Nb}}} + aT_{\text{Nb}}^2\right)^{-1} + \left(\frac{1}{D\,T_{\text{Nb}}^2\exp(y)} + \frac{1}{B\,\ell_{\text{ph}}T_{\text{Nb}}}\right)^{-1} \tag{7.16}$$

[2]Due to the details of the computation, these points are spaced linearly in *temperature* but approximately represent linear spacing in spatial coordinates; see Eq. 7.27.

Here a, A, B, and D are fit constants:

$$a = 7.52 \times 10^{-7}\ \mathrm{m/W\,K} \tag{7.17}$$

$$A = 0.141\ \mathrm{W/m\,K} \tag{7.18}$$

$$B = 4.34 \times 10^{3}\ \mathrm{W/m^2K^4} \tag{7.19}$$

$$D = 2.34 \times 10^{2}\ \mathrm{m\,K^3/W} \tag{7.20}$$

For the RRR of the material I have used the typically-cited value of 300; the framework allows for adjustment a custom value. For ℓ_{ph}, a reasonable value is 200 μm, a typical grain size for niobium cavities (phonon scattering in clean niobium is dominated by grain boundary effects) [VXP07]. The parameter y is the energy gap Δ divided by the local temperature normalized to units of energy $k_{\mathrm{B}}T_{\mathrm{Nb}}$, with the following approximate value given by Vines *et al.* [VXP07]:

$$y \approx \frac{\Delta}{k_{\mathrm{B}}T_{\mathrm{c}}}\frac{T_{\mathrm{c}}}{T_{\mathrm{Nb}}}\left(\cos\left(\frac{\pi T_{\mathrm{Nb}}^2}{2T_{\mathrm{c}}^2}\right)\right)^{1/2} \tag{7.21}$$

$R(y)$ is the ratio of the thermal conductivity in the superconducting state to that in the normal state, and is given by Bardeen *et al.* [BRT59]:

$$R(y) = \frac{12}{\pi^2}\left(f(y) + y\ln\left(1+\exp(-y)\right) + \frac{y^2}{2\left(1+\exp(y)\right)}\right) \tag{7.22}$$

In turn, $f(y)$ relates to the Fermi-Dirac distribution of electrons:

$$f(y) = \int_0^\infty \frac{z}{1+\exp(y+z)}dz \tag{7.23}$$

This can be expressed as a second-order polylogarithm (Jonquière's function) [Wei], which is efficiently calculable:

$$f(y) = \mathrm{Li}_2\left(-\exp(-y)\right) \tag{7.24}$$

To work towards finding the temperature of the niobium lattice at the RF surface T_{surf}, we note that the thermal conductivity is related to the heat flow

$q = P/A$ as follows:

$$q = \kappa\left(T_{\mathrm{Nb}}\right) \frac{dT_{\mathrm{Nb}}}{dx} \tag{7.25}$$

We can integrate both sides of Eq. 7.25 with respect to x across the thickness of the cavity wall d. For the left-hand side we have the following, noting that q does not change over x by the symmetry of the simulation:

$$\int_0^d q\, dx = q\, d = \frac{P}{A} d \tag{7.26}$$

On the right-hand side we have the following, using the chain rule of integration:

$$\int_0^d \kappa\left(T_{\mathrm{Nb}}(x)\right) \left.\frac{dT}{dx}\right|_x dx = \int_{T_{\mathrm{wall}}}^{T_{\mathrm{surf}}} \kappa\left(T_{\mathrm{Nb}}\right) dT \tag{7.27}$$

The framework performs the integral on the right-hand side of Eq. 7.27 cumulatively from the previously-calculated T_{wall} up to a range of reasonable values of T_{surf}, such as the range $T_{\mathrm{wall}} \leq T_{\mathrm{surf}} \leq T_{\mathrm{c}}$. Then, knowing d and P/A, the framework finds the value of T_{surf} such that Eqs. 7.26 and 7.27 are equal.

Finally, having calculated T_{wall} and T_{surf} given the ansatz T_{quasi}, the framework considers the quasiparticle-phonon overheating mechanism in order to find an "output" T'_{quasi} (note the primed variable). Again using the near-surface grid, the framework calculates a local $Y(x)$ based on $\ell(x)$ and the model in Eq. 5.9. Y may also depend on other parameters, such as the temperature [KLT57] or local field level, and the framework is adaptable to such a model of $Y(x)$.

Since the quasiparticles are considered to be in thermal equilibrium, Y must be averaged over the RF penetration layer. The choice of weighting for this average is not obvious; as a plausible option, the framework uses the field kernel:

$$Y = \frac{\int_0^\infty Y(x) H_{\mathrm{pk}}(x) dx}{\int_0^\infty H_{\mathrm{pk}}(x) dx} \tag{7.28}$$

Then, using this average Y, the lattice temperature T_{surf}, and the heat flow $q = P/A$, the system calculates the output T'_{quasi}:

$$T'_{\text{quasi}} = T_{\text{surf}} + \frac{P}{A}\left(\frac{1}{Y}\right) \tag{7.29}$$

Since the framework considers quasiparticles in thermal equilibrium, unlike the simpler model from Chap. 5, the additional dissipated power for a given value of Y will be much higher: in the new model, quasiparticles are overheated across the entire RF layer as a function of the averaged field strength, not only as a function of the local field strength. This results in a larger overall number of overheated quasiparticles.

As such, the value for β in Eq. 5.9 must be lower in the new framework to match experimental results. In general I have used Y as a free fitting parameter in this framework, including the $(T^5_{\text{quasi}} - T^5_{\text{surf}})$ dependence predicted in theory (see for example [TGK+09]). Figure 7.3 shows an example calculation of T_{wall}, $T_{\text{Nb}}(x)$, T_{surf}, and T'_{quasi} given an ansatz $T_{\text{quasi}} = 2.33$ K, experimental parameters T_{bath} and H_{pk}, and $Y^{-1} = 1 \times 10^{-1}$ mK m^2/W. These results as well as the results presented in the remainder of this chapter were calculated using RRR = 300 and $\ell_{\text{ph}} = 200$ μm.

7.3 Self-Consistent Heating

The routine described in Secs. 7.1 and 7.2 begins with an ansatz T_{quasi} and yields an output T'_{quasi}. The framework repeats this routine with varying ansatz T_{quasi}, adaptively refining the mesh of input temperature until a self-consistent result is achieved, *i.e.* an input temperature that gives the output $T'_{\text{quasi}} = T_{\text{quasi}}$.

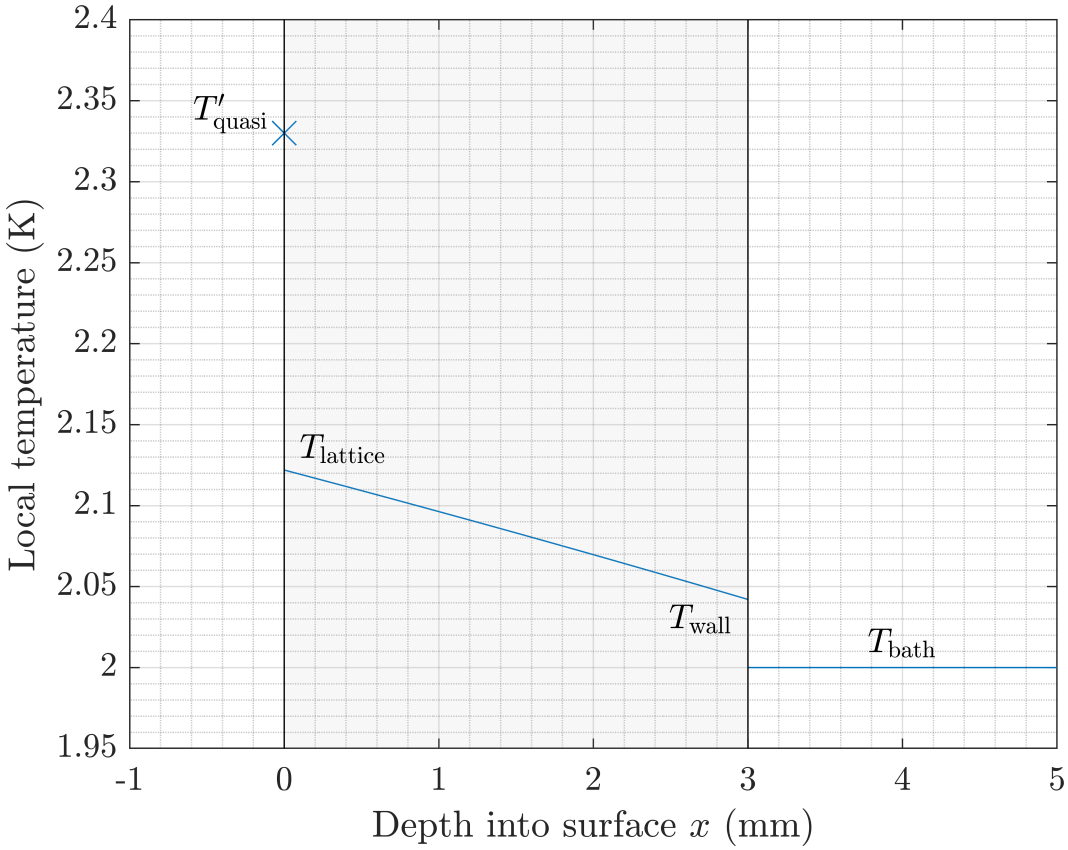

Figure 7.3: Depth-dependent temperature from example simulation using the Gurevich model and the material parameters and field distribution of C4(N1) shown in Figs. 7.1 and 7.2, with $\mu_0 H_{\mathrm{pk}} = 131$ mT, $Y^{-1} = 0.1\ \mathrm{mK\,m^2/W}$, and the ansatz $T_{\mathrm{quasi}} = 2.33$ K.

Once this result is found, the framework records the self-consistent quasiparticle temperature T_{quasi}, the niobium boundary temperatures T_{surf} and T_{wall}, and the surface resistance R_{s} given the starting values of T_{bath} and H_{pk}.

Figure 7.4 shows an example set of the results of the framework, plotting the output T'_{quasi} as a function of the ansatz T_{quasi} for a range of peak field levels. In general, these curves are concave upwards, with $T'_{\mathrm{quasi}} > T_{\mathrm{quasi}}$ at low ansatz values and $T'_{\mathrm{quasi}} < T_{\mathrm{quasi}}$ at higher ansatz values. Also illustrated in Fig. 7.4 is the identity output $T'_{\mathrm{quasi}} = T_{\mathrm{quasi}}$; the stable self-consistent solutions occur at the first intersection of this identity line with each of the curved simulation lines.

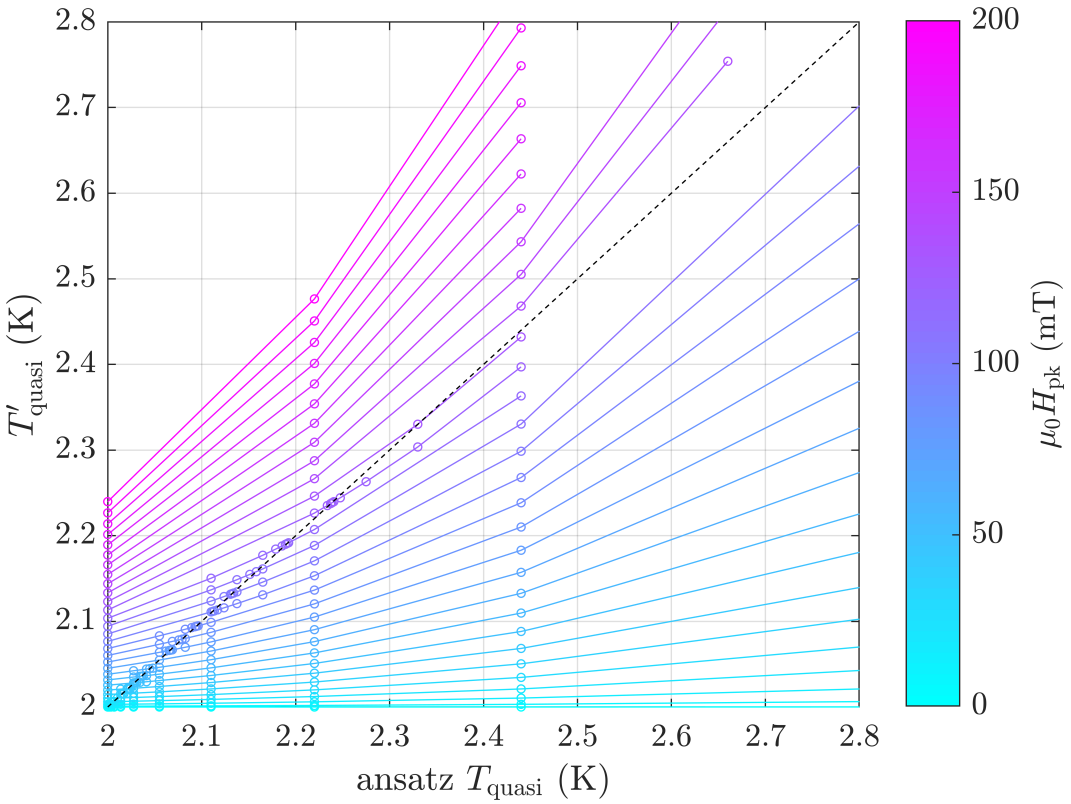

Figure 7.4: Simulation output temperature T'_{quasi} as a function of ansatz temperature T_{quasi} for varying RF field strength $\mu_0 H_{\mathrm{pk}}$, generated using the Gurevich model with the material parameters of cavity C4(N1) and $Y^{-1} = 0.1$ mK m^2/W. Intersections of colored curves with the dashed line indicate self-consistent solutions where $T'_{\mathrm{quasi}} = T_{\mathrm{quasi}}$; curves that do not intersect the dashed line have no self-consistent solutions (global thermal instability).

Simulation lines that do not intersect the identity line (*i.e.* solutions where $T_{\mathrm{quasi}'} = T_{\mathrm{quasi}}$ is never satisfied) indicate surface field levels H_{pk} with no self-consistent solutions. In such a case, the RF dissipation is high enough and thermal effects strong enough that the material goes into a thermal runaway and quenches. This is an interesting emergent property from the simulation and illustrates the "global thermal instability", a potential quench mechanism for SRF cavities [Mül87, Gra93, PHK98]. Of particular interest is the fact that the stable solutions at the highest fields still have T_{quasi} near 2.2-2.3 K, a good deal lower

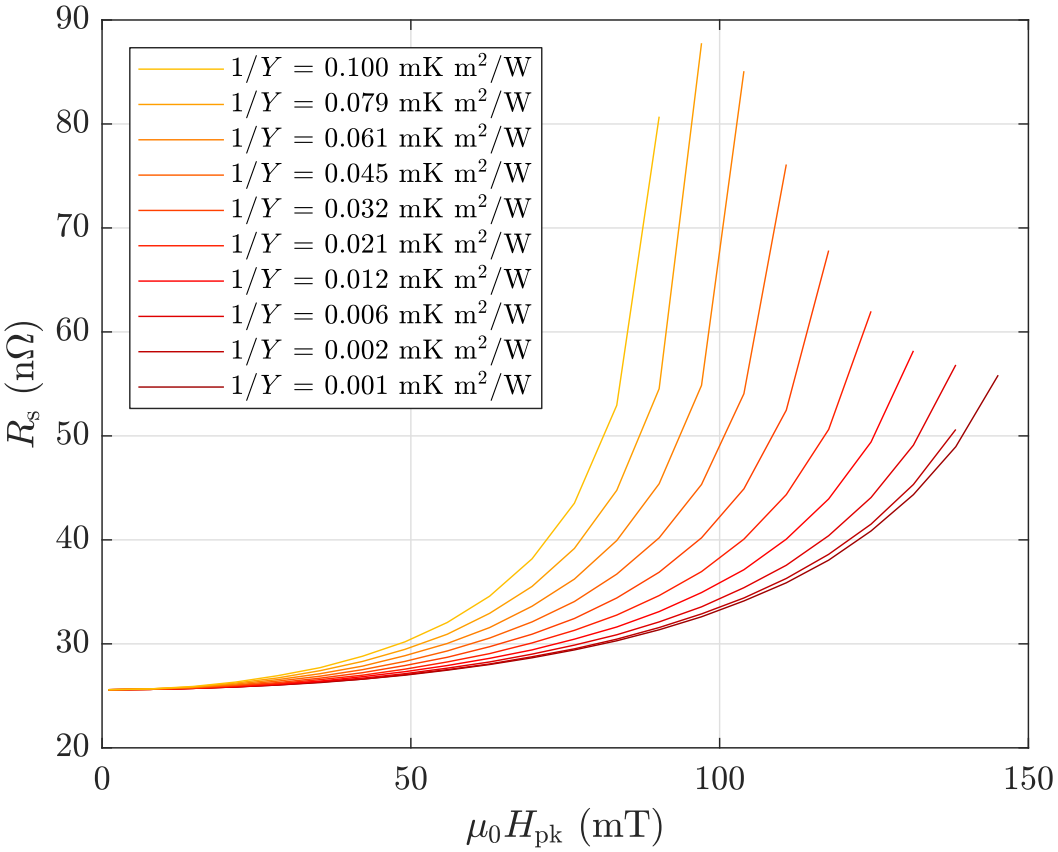

Figure 7.5: Simulated Mattis-Bardeen surface resistance at $T_{\text{bath}} = 2$ K using the thermal framework and a range of values of $1/Y$, calculated with the same material parameters as in Fig. 7.4. Endpoints of curves indicate global thermal instability limits. Note that there is a significant overheating effect even with $1/Y \approx 0$, likely due to the high initial R_{BCS} given the short average ℓ.

than T_c.

Figure 7.5 shows the results of a calculation of R_s vs. $\mu_0 H_{pk}$ using the Mattis-Bardeen surface resistance model with several values of the electron-phonon parameter Y; Figure 7.6 shows the corresponding quasiparticle temperature T_{quasi}, and Figure 7.7 shows those same results converted by Eq. 3.50 into the intrinsic quality factor Q_0 for a TESLA-shape cavity [ABB+00]. The three figures indicate thermal runaway quench fields where they occur.

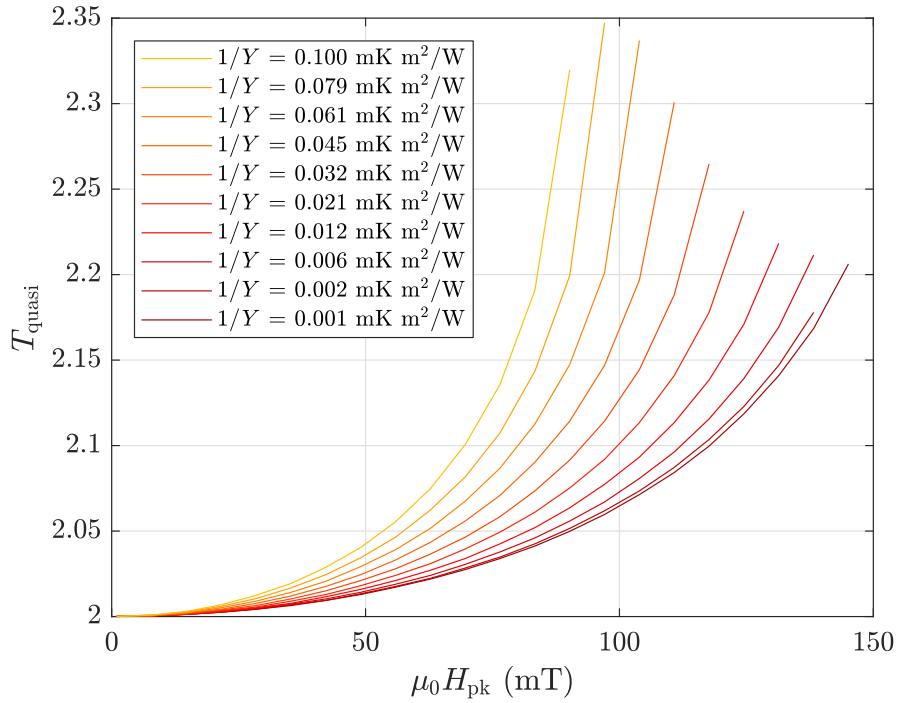

Figure 7.6: Quasiparticle temperature for the simulation results shown in Fig. 7.5.

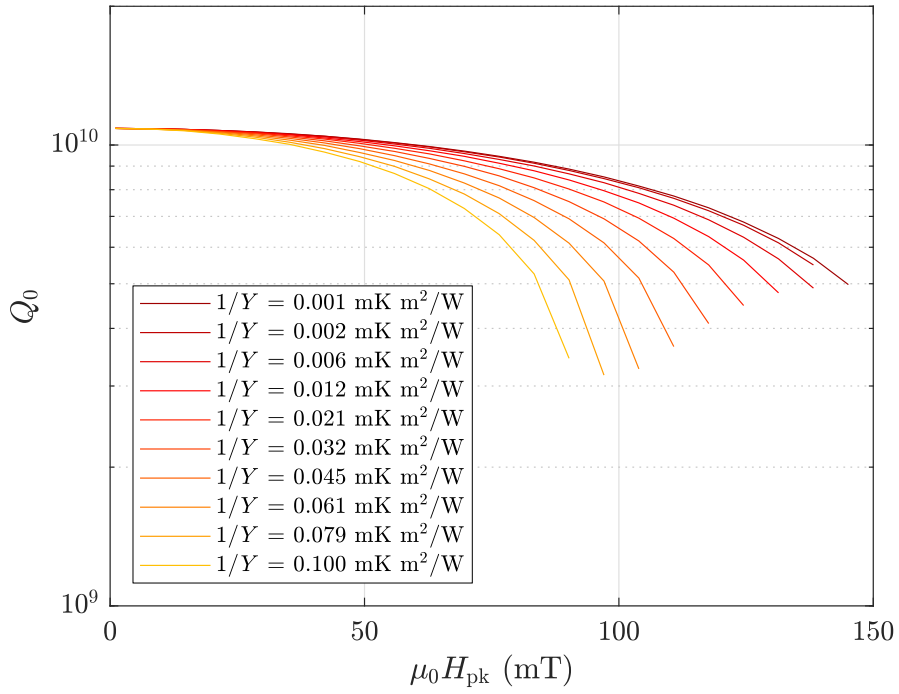

Figure 7.7: Simulated intrinsic quality factor Q_0 for a TESLA cavity using with the surface resistance shown in Fig. 7.5.

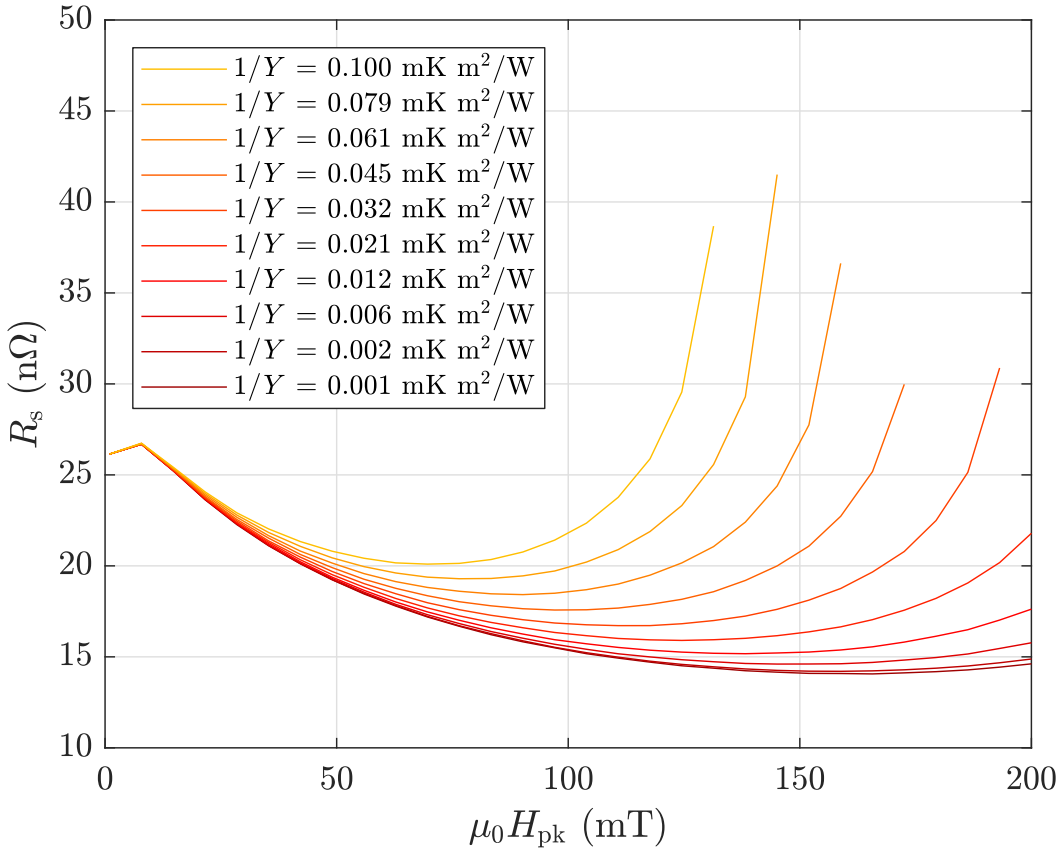

Figure 7.8: Simulated Gurevich model surface resistance at $T_{bath} = 2$ K using the thermal framework and a range of values of $1/Y$. The sharp corner is due to a low mesh density in H_{pk}. Endpoints of curves indicate global thermal instability limits. Compare to Fig. 5.3.

Figure 7.7 illustrates another interesting result of this simulation: the thermal effects cause a medium-field Q-slope comparable in magnitude to that observed in experiment (see for example the 800 °C data in Fig. 3.13). Some earlier studies found similar agreement between experimental Q-slope measurements and thermal feedback simulations (such as [DCM17]), though others only found such agreement by greatly varying the value of the bulk thermal conductivity (see for instance [Pad09, GFG+13]). Here the addition of the electron-phonon effects encapsulated in Y allows for a wide range of realistic Q-slope results with realistic thermal parameters.

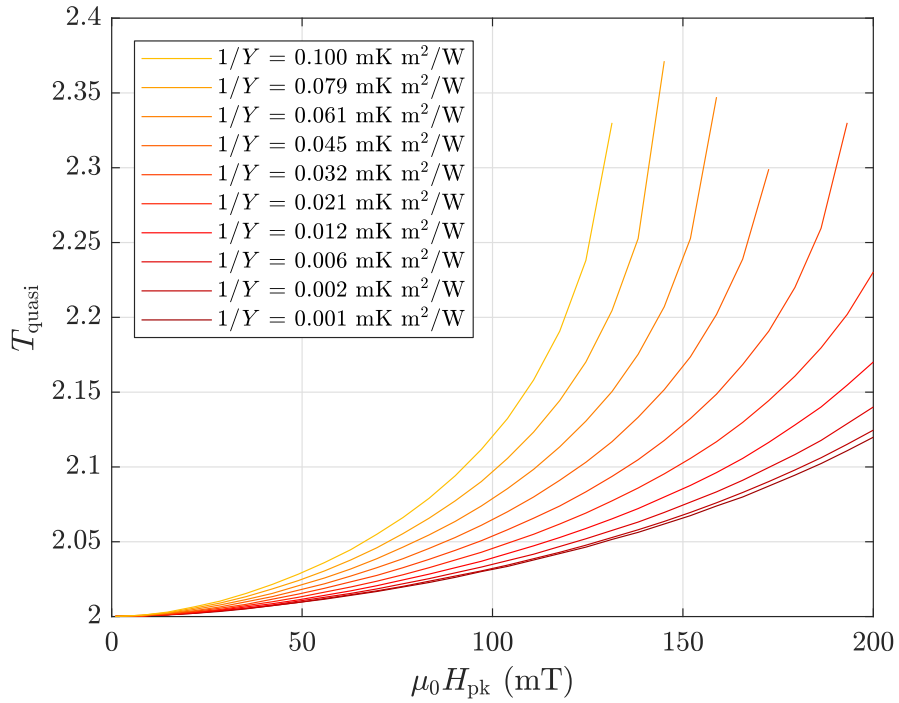

Figure 7.9: Quasiparticle temperature for the simulation results shown in Fig. 7.8.

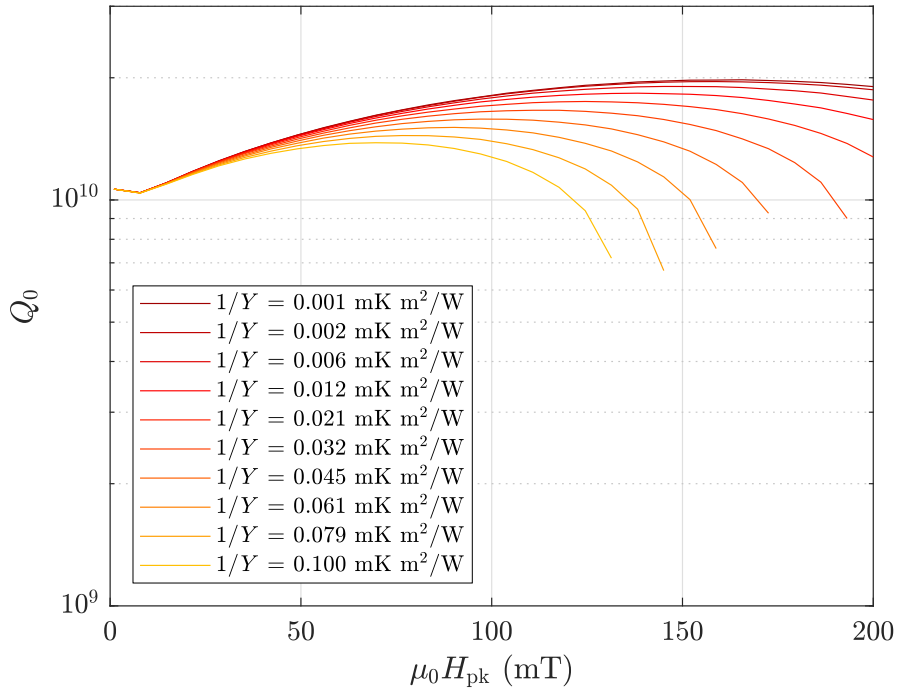

Figure 7.10: Simulated intrinsic quality factor Q_0 for a TESLA cavity using with the surface resistance shown in Fig. 7.8.

Figure 7.8 (comparable to the results from the earlier model shown in Fig. 5.3) shows the R_s vs. $\mu_0 H_{pk}$ results of a calculation using the Gurevich theory as the base model of R_s; T_{quasi} is shown in Fig. 7.9 and the Q_0 calculations are shown in Fig. 7.10. Here the thermal framework produces results that are consistent with the earlier findings in Chap. 5. As anticipated above, the values of Y in the new simulation are significantly lower than those used in the overdoping study for similar anti-Q-slope predictions; for example, compare the values of $1/Y$ in Fig. 7.10 to those in Fig. 6.2. The increased heating for a given value of Y is due to the fact that the quasiparticles in the advanced framework are in thermal equilibrium: the quasiparticles are overheated throughout the RF layer, not only near the surface, so losses are higher for the same value of Y.

7.4 Outlook and Applications

This new thermal framework is a highly adaptable system that will be useful for future studies of thermal Q-slope and thermal mediation of the anti-Q-slope as well as more detailed studies of Y, κ, and h_k. As it stands, the framework treats Y as a free parameter with an optional temperature dependence $Y \propto (T_{quasi}^5 - T_{surf}^5)$; building a deeper model of Y as a function of local material parameters is the subject of ongoing study at Cornell and within the Center for Bright Beams [MAL+19]. For our continuing studies of the anti-Q-slope and theoretical models thereof, this framework will allow for the consideration of thermal effects in any local model of the surface resistance under investigation.

Further future improvements would be to extend the model to a simulation of "hotspot" heating in two or three dimensions. This will increase computa-

tional complexity but allow for the study of surface defects in the context of advanced models of the surface resistance. Additional local effects which might be considered are field emission, multipacting, and magnetic vortex entry, which would contribute to R_s due to thermal effects and as loss mechanisms in their own right [Pad09, Hal17].

In the next chapter, I will circle back to the earlier discussion of the anti-Q-slope from Chaps. 4-6; among other tools, I will use the framework outlined in this chapter to study the predictions of several competing models of the anti-Q-slope in nitrogen-doped and nitrogen-infused niobium, assessing their performance against experimental data and working towards establishing a fundamental understanding of the physics of the anti-Q-slope.

CHAPTER 8

ASSESSMENT OF ANTI-Q-SLOPE THEORIES

The work presented in Chaps. 5 and 6 found good agreement between the experimental performance of nitrogen-doped and nitrogen-infused niobium cavities and the theoretical predictions from the Gurevich theory [Gur14] of the anti-Q-slope modulated by a linear model of quasiparticle overheating. This work found an empirical connection between the magnitude of the thermal effects and the electron mean free path ℓ, with shorter ℓ (higher impurity content) corresponding with better thermal transfer between overheated quasiparticles and lattice phonons.

In addition to the Gurevich model, several other theories have recently gained attention in the field of SRF as possible explanations for the anti-Q-slope. One of these models, proposed by Goldie and Withington [GW12], introduces quantum-mechanical effects that modify the quasiparticle distribution function in such a way that the microwave surface resistance decreases with increasing field. Another, proposed by Weingarten [Wei18], uses proximity coupling and an effective-medium approximation of a disordered composite superconductor to describe a field-dependent surface resistance. In this chapter, I will assess some of the merits and deficiencies of these models, introducing new evidence to the discussion and returning to the Gurevich model for a deeper assessment.

8.1 The Frequency-Dependence of the Anti-Q-Slope

In the last few years (2017-2019), new evidence has been measured in the field of SRF indicating a dependence of the anti-Q-slope effect on frequency. At Cornell,

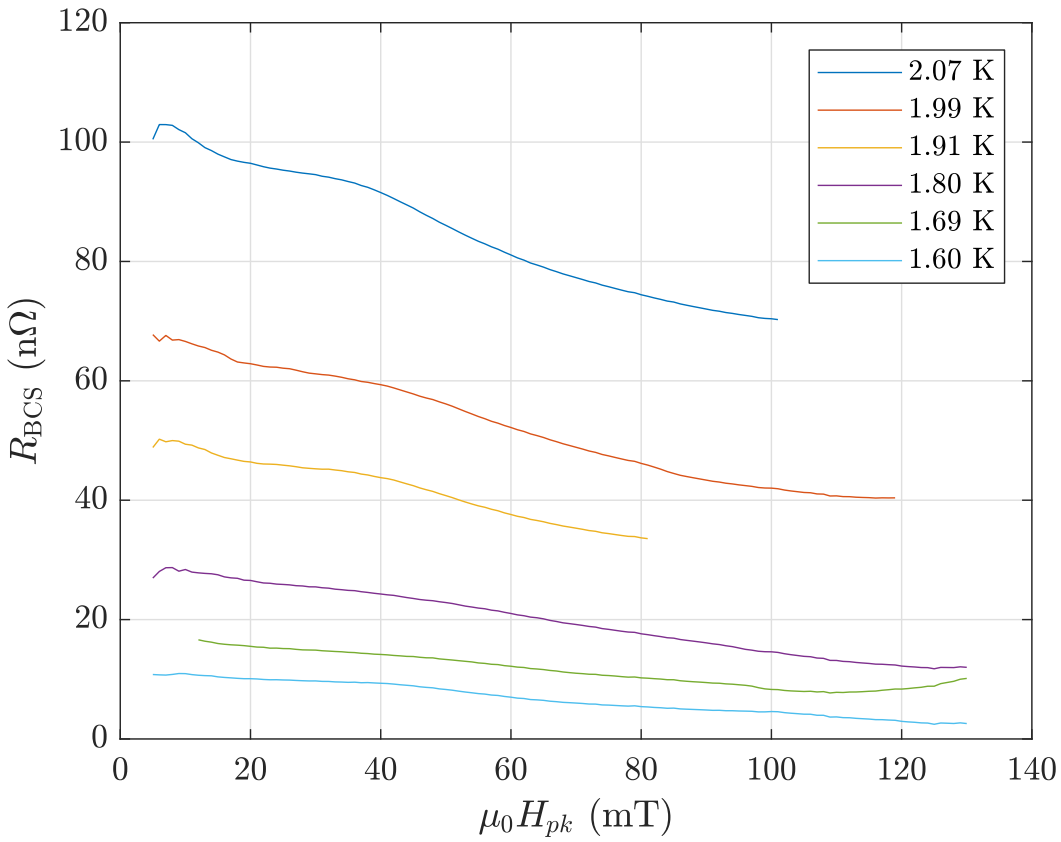

Figure 8.1: BCS surface resistance measurements for a 3.9 GHz non-doped clean niobium cavity ($\ell > 1000$ nm), indicating anti-Q-slope behavior.

our studies on nitrogen doping and infusion at 2.6 GHz find that the anti-Q-slope for cavities with these treatments is more pronounced at high frequencies, with a peak intrinsic quality factor Q_0 near $2{\times}10^{10}$ at fields $\mu_0 H_{\mathrm{pk}} \approx 80$ mT for a "'2/6" nitrogen-doped cavity [MKL18, MAG+19]. Moreover, our studies of a 500 MHz cavity treated with the 2/6 recipe showed an improved overall R_{BCS} but no anti-Q-slope at all [FGG+18].

Quite interestingly, early results of a 3.9 GHz clean niobium cavity ($\ell > 1000$ nm) measured at Cornell also find a reduction in R_{BCS} with increasing RF field strength, as shown in Fig. 8.1. This cavity received bulk EP and a 5-hour 800 °C degas bake. This is the first indication from Cornell results that

the anti-Q-slope is not only to be found in impurity-doped niobium, and places some theoretical limits on what the underlying physics might entail. Further studies of these frequency-dependent effects are ongoing at Cornell.

Outside of Cornell, other laboratories have shown similar frequency-dependent results. FNAL reported a strong frequency dependence of the anti-Q-slope, with the relative reduction in R_{BCS} increasing at higher frequencies [MCR+18]. Their study found an anti-Q-slope in nitrogen-doped cavities at frequencies above 1 GHz, with their 650 MHz cavity showing no field-dependent reduction in R_{BCS}. They also reported an anti-Q-slope at 3.9 GHz for cavities treated with BCP and for cavities treated with the EP/120 °C bake procedure, with lower-frequency cavities exhibiting a field-dependent R_{BCS} with positive slope that decreased with increasing frequency. For cavities that received EP only, they did not report a 3.9 GHz result but saw a mild anti-Q-slope at 2.6 GHz, again finding increasingly positive slopes in R_{BCS} at decreasing frequency.

Exploring studies at other laboratories not focused on nitrogen doping, we find conflicting results in terms of the presence of an anti-Q-slope at 3.9 GHz. Studies of the 3.9 GHz EXFEL cavities showed mostly flat Q vs. H curves, with some variation in slope such that some of the cavities tested could be classified as having anti-Q-slopes while others could not [BBB+19]. These cavities were treated with bulk removal by BCP, 800 °C vacuum degas, and post-bake "flash" BCP. R&D reports from the development of the 3.9 GHz LCLS-II cavities report an anti-Q-slope after EP for one cavity and none for a second cavity with the same treatment [SAC+18]. After 120 °C baking, both cavities showed a very mild increase in Q_0 with increasing field strength, though a third cavity with

the same treatment showed only a standard medium-field Q-slope. An earlier study of 3.9 GHz cavities for FLASH showed a very minor anti-Q-slope for cavities treated with BCP and none for a cavity treated with EP.

Moving forward, these results and the results of ongoing and future studies of this frequency dependence will be essential for improving our understanding of the physics of the anti-Q-slope.

8.2 Weingarten Model

The first alternative model of the anti-Q-slope that I will discuss here is the theory proposed by Weingarten [Wei18]. The model expands on an earlier proposal which treats impure niobium surfaces as disordered composite superconductors [EGH+14]. This composite is made up of a clean niobium bulk "host" peppered with mesoscopic defects in a disordered configuration in a layer of thickness d^*. The defects are themselves composite, made up of a volume fraction x_1 of a normal-conducting material with the remainder being a dirty superconductor. At low fields/surface currents, these defects are proximity-coupled to the clean host, but as the local magnetic field strength H passes above a defect critical field H^*, the defects begin to decouple and become normal-conducting; a growing number of defects decouple as the field increases up to H_c^*, above which all the defects in the defect layer are normal-conducting. This change modifies the overall quasiparticle conductivity σ_n in a manner dependent on both field strength and frequency, which in turn changes R_{BCS}.

Weingarten shows agreement between the predictions of his model and the frequency-dependent experimental results from FNAL mentioned above, repro-

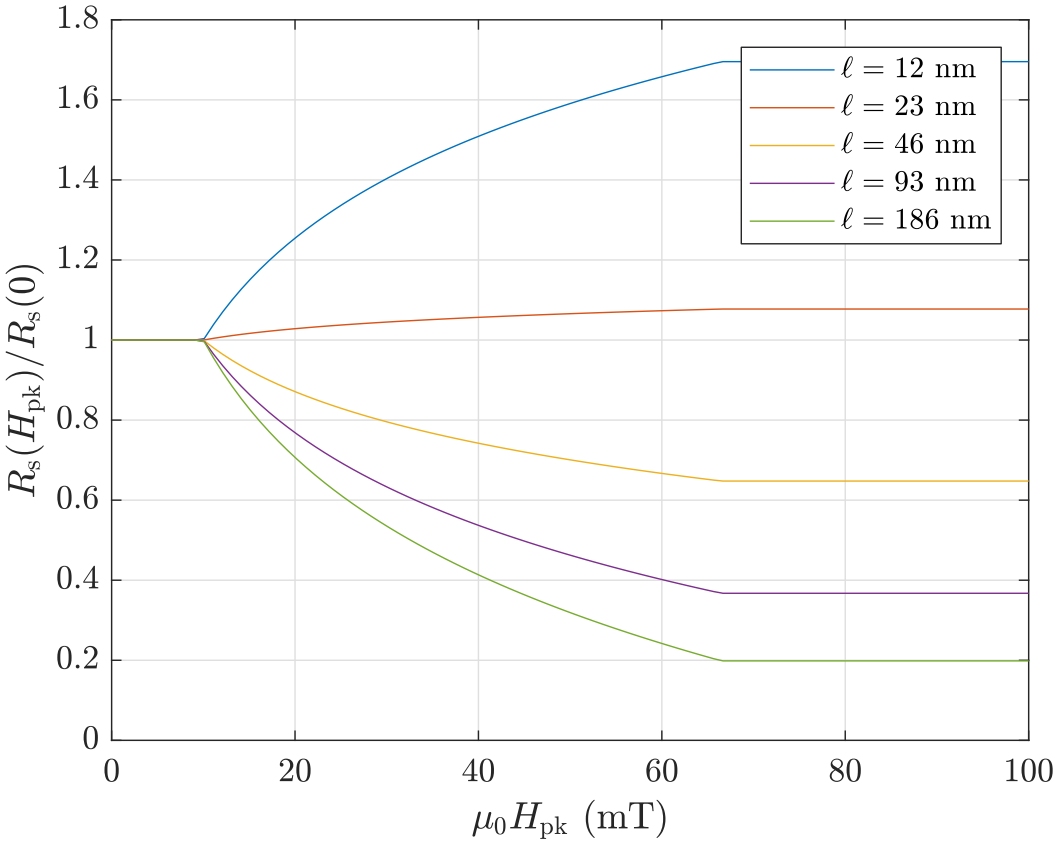

Figure 8.2: Theoretical predictions of the field-dependent surface resistance from the Weingarten model for varying electron mean free path ℓ. Results calculated with $\mu_0 H_c^* = 66$ mT, $\mu_0 H^* = 10$ mT, $x_1 = 2/3$, $\sigma_{Nb} = \ell \cdot 1.94 \times 10^7$ Sv/m, $T = 2$ K, and $f = 1.3$ GHz.

ducing the R_{BCS} vs. H_{pk} results for 2/6 nitrogen-doped cavities and non-doped cavities treated with BCP [MCR+18]. To assess this model ourselves, we made several calculations to test the predictions of the Weingarten model for varying material properties.

In our investigation, we found a discrepancy between the predictions of the model and known experimental results. By the predictions of the model, as the electron mean free path ℓ increases, the relative strength of the field-dependent drop in R_s also increases; simulations with very short ℓ show in fact a field-dependent *increase* in R_s. Figure 8.2 illustrates this finding. This is in opposition

to the body of experimental evidence, which shows an anti-Q-slope that gets stronger at *decreasing* ℓ and vanishes for $\ell > 200$ nm at 1.3 GHz, as discussed in the previous chapters of this dissertation.

In our assessment of this model, we also found several other factors that decreased our confidence in its applicability. One of these is the non-differentiable "corners" in R_{BCS} at H^* and H_{c}^*, which do not occur in the experimental results. Moreover, it appears that the lower field H^* fitted in the paper describing the model corresponds to 5 MV/m in a TESLA cavity, the lowest field presented in the experimental results from FNAL (indeed the field where the R_{BCS} results were normalized) [MCR+18]. Other results from the same laboratory [BCG+18], Cornell [GEF+16], and elsewhere [DCM+13] show that the effect begins continuously from very low fields and does not stop abruptly at some higher field, as suggested by the model in question. A further issue is the model's dependence on a number of finely-tuned parameters; while this is not strictly a reason to shake confidence in the theory, small adjustments to the critical fields H^* and H_{c}^* and especially to the defect volume fraction x_1 and the derived defect conductivity s_1 lead to dramatic changes in the calculated surface resistance. These parameters are also somewhat arbitrarily defined. In particular, the argument for setting $x_1 = 2/3$ is simply that the most dramatic changes in R_{s} occur there, where the mixed-state conductivity σ_{m} is maximized.

Because of the discrepancies and issues enumerated above, we do not have high confidence in this model as a description of the anti-Q-slope in nitrogen-doped niobium cavities, despite its correct prediction of the dependence of the effect on frequency. Perhaps future work[1] will improve the model and demand

[1] In private communication, the author of this model has informed us of a new interpretation of the model that may correctly predict the dependence on ℓ.

its reassessment; for now, we shall look to the other proposed theories.

8.3 Goldie-Withington Model

Another theory for the field-dependent surface resistance in nitrogen-doped niobium cavities is the model proposed by Goldie and Withington [GW12]. In their model, the increasing strength of the RF field on the surface of a superconductor drives the quasiparticles into a non-thermal distribution as they absorb photons of energy $\hbar\omega$. A brief discussion of the Mattis-Bardeen theory is in order to see the impact of this non-thermal distribution:

In the microscopic picture of the microwave surface resistance in the BCS context, the Mattis-Bardeen theory finds that R_s is proportional to the following integral [MB58]:

$$R_s \propto \int_{\Delta}^{\infty} \left|M^2\right| N(\epsilon)N(\epsilon+\hbar\omega)\left[f(\epsilon)-f(\epsilon+\hbar\omega)\right] d\epsilon \tag{8.1}$$

Here N is the quasiparticle density of states, evaluated at quasiparticle energies ϵ and $\epsilon + \hbar\omega$, representing the absorption of an RF photon of energy $\hbar\omega$. The function f is the quasiparticle distribution function. M is the matrix element for the interaction.

The non-thermal quasiparticle distribution proposed in the Goldie-Withington model differs from the standard Fermi-Dirac distribution function, introducing large spikes spaced at intervals of $\hbar\omega$ representing "sequential single-photon absorption"; in the regime where the results in the paper describing the model are calculated, $[f(\epsilon) - f(\epsilon + \hbar\omega)]$ is smaller on average than in the Fermi-Dirac case. The magnitude of this effect increases as the magnitude of the

RF field increases and more photons are absorbed, driving the system further out of the standard thermal distribution.

Recent work from de Visser *et al.* reported agreement with the Goldie-Withington model in an aluminum stripline resonator (T_c = 1.17 K) [dGD+14]. Their results, taken at ~ 5.29 GHz and over the temperature range 0.05-0.35 K, show an intrinsic quality factor Q_0 of the resonator increasing with increasing RF power at $T > 0.2$ K; at lower temperatures, Q_0 instead decreases as the level of RF power increases.

These findings are exciting, but there are some potential issues with applying this model to the typical parameters and conditions of SRF niobium accelerator cavities. In particular, the theory relies on the RF photon energy $\hbar\omega$ being on the same scale as or larger than the temperature (in units of energy) $k_B T$. In this regime, absorption of photons from the RF field drives the quasiparticles significantly out of the standard thermal distribution. In contrast to this, for the typical niobium SRF cavity operation parameters T = 2 K and f = 1.3 GHz, $\hbar\omega \approx 0.03 \cdot k_B T$, well outside of the predicted regime of the effect. The $\hbar\omega$-spaced spikes in the distribution function, were they to be present, would result in a much smaller deviation from the standard thermal distribution function. Moreover, there is as yet no proposed reason why the model might describe nitrogen-doped niobium but not other dirty-limit niobium cavities.

We have not yet completed calculations of the Goldie-Withington model in our range of SRF operation parameters; the calculations entail extensive kinetic equations that are computationally intensive and would require a large effort to program. As such, we cannot say for certain whether the model describes the anti-Q-slope as seen in nitrogen-doped and nitrogen-infused cavities and in

niobium cavities at higher frequencies. That being said, the dramatic differences between the regime of the theoretical calculations presented in [GW12] and the experimental results of [dGD+14] on the one hand and that of SRF accelerator cavities on the other indicate that this model is not appropriate to describe the the anti-Q-slope.

8.4 Gurevich Model

We now turn back to the Gurevich model [Gur14], for which we found good agreement with experimental results of the anti-Q-slope in strongly nitrogen-doped and some of the nitrogen-infused niobium cavities at 1.3 GHz. A brief explanation of the model can be found in Sec. 5.2. In terms of the Mattis-Bardeen theory, where the Goldie-Withington model modifies the quasiparticle distribution function f in Eq. 8.1, the Gurevich model modifies the quasiparticle density of states N, "smearing" the singularity at Δ as the RF surface currents in the superconductor break Cooper pairs [Bar62, Ful65]. The model predicts these effects in dirty-limit Type-II superconductors where $\hbar\omega \ll k_B T$ and $T \ll T_c$, appropriate assumptions for the regime where the anti-Q-slope has been observed in nitrogen-doped cavities.

Some of our earlier findings suggested that the Gurevich model had issues with accurately predicting the anti-Q-slope behavior observed in some cavities. As shown in Chap. 5, our results with fitting the model to experimental data from nitrogen-doped 1.3 GHz cavities were largely successful, though the theory does not accurately predict the behavior of cavities doped to intermediate mean free paths $\ell > 60$ nm. For nitrogen-infused cavities, as discussed in

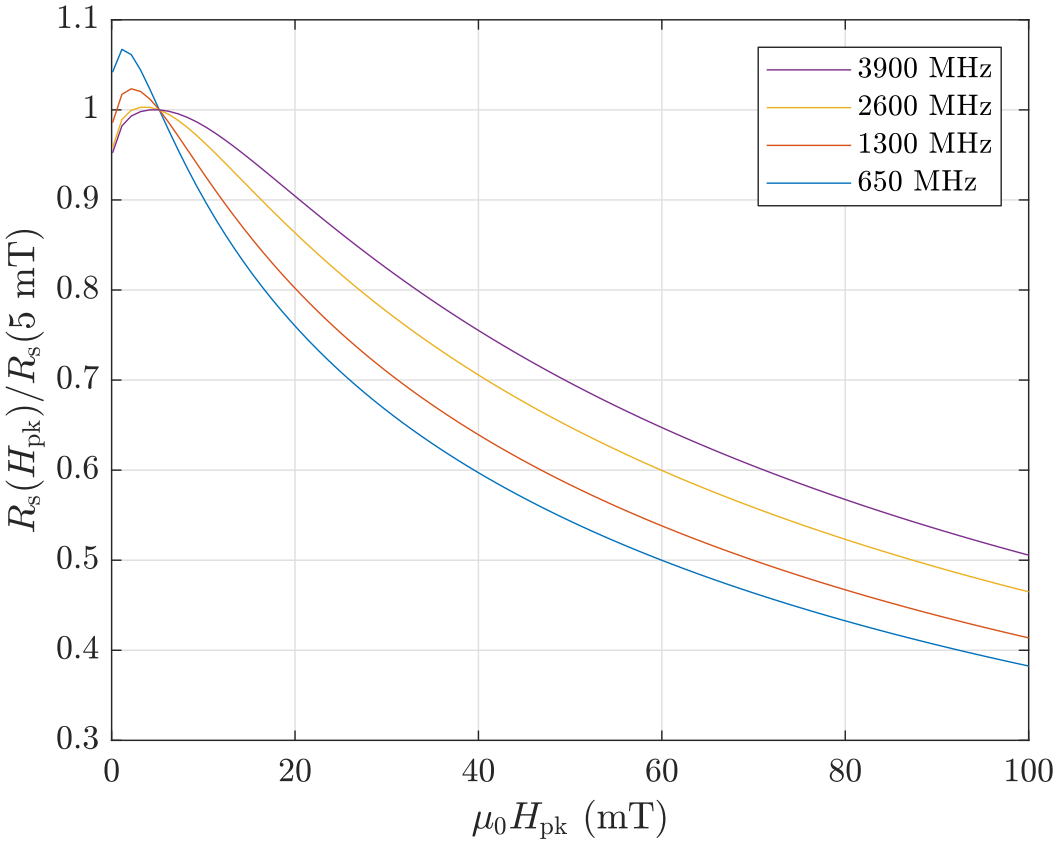

Figure 8.3: Frequency-dependent results of the relative field-dependent reduction in surface resistance predicted by the Gurevich model, calculated with $T_c = 9.1$ K, $\Delta/k_B T_c = 1.886$, $\ell = 9$ nm, and $T_{bath} = 2$ K.

Chap. 6, the predictions of the Gurevich theory matched some of the cavity test data well, while the predictions for other cavities showed less agreement with experiment.

The new frequency-dependent results cast new light on this model and its applicability. While the experimental findings show that the magnitude of the field-dependent reduction in R_s increases with increasing frequency, the Gurevich model predicts the opposite, with stronger reduction at lower frequencies. Figure 8.3 shows the results of calculations of the Gurevich model for several frequencies over the range from 650 MHz to 3.9 GHz. Here, the quasiparticle

overheating effects have been omitted to maximize the reduction in R_s. This stark contrast strongly suggests that, despite the very good agreement between theory and experiment at 1.3 GHz, the Gurevich model may not truly describe the physics of the anti-Q-slope.

This result and the discrepancies found earlier prompted us, in our collaboration with the Sethna group in the Center for Bright Beams, to reexamine the Gurevich model and perhaps find where it might be improved to account for the new frequency-dependent results [MAL+19]. Instead, this study found further issues with the model, particularly with the quasiparticle distribution function; the issue can be summarized as follows. In the model as written, the total density of quasiparticles is assumed to be constant in time due to the long lifetime of quasiparticles compared to the frequency of the RF field; each quasiparticle state has a particular energy $\tilde{\epsilon}$ that changes over time. The model then enforces that the distribution function be equal to the Fermi-Dirac thermal distribution when the sinusoidally-oscillating RF field passes through zero. This condition, however, ignores the additional quasiparticles excited by absorption of RF photons. Using detailed balance, we can make a correction to f to account for the additional quasiparticles. Instead of the purely thermal distribution $f(\tilde{\epsilon}) = \exp(\tilde{\epsilon}/k_B T)$, we have the following [Lia]:

$$f(\tilde{\epsilon}) = f(\epsilon, t) = \frac{\int_0^{\pi/\omega} \left(1 + \exp(-\epsilon/k_B T)\right)\left(1 + \exp(\epsilon/k_B T)\right)^{-1} dt}{\int_0^{\pi/\omega} \left(1 + \exp(-\epsilon/k_B T)\right) dt} \tag{8.2}$$

This correction leads to a dramatically different calculation of the field-dependent R_s.

Figure 8.4 compares the predictions of the surface resistance of the new distribution function against those of the original calculation for a range of magnitude of quasiparticle overheating; these calculations used the new thermal

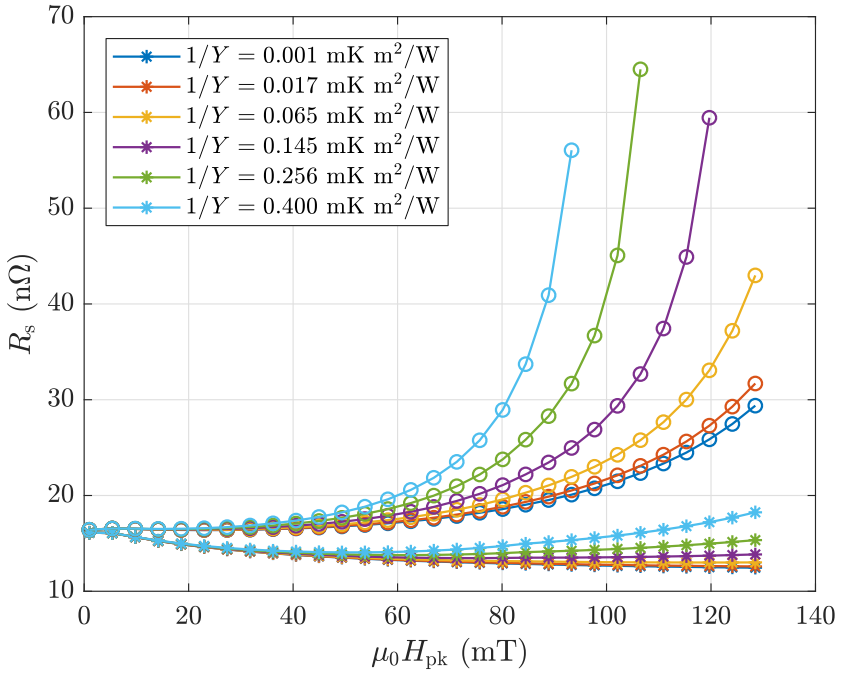

Figure 8.4: Simulations of the field-dependent surface resistance from the original Gurevich model (asterisks) and the version with corrected distribution function (open circles), for varying levels of quasiparticle overheating. Results calculated at $T = 2$ K with $R_0 = 10$ nΩ, $\ell = 20$ nm, $f = 1.3$ GHz, $\Delta/k_B T_c = 1.98$, and $T_c = 9.14$ K.

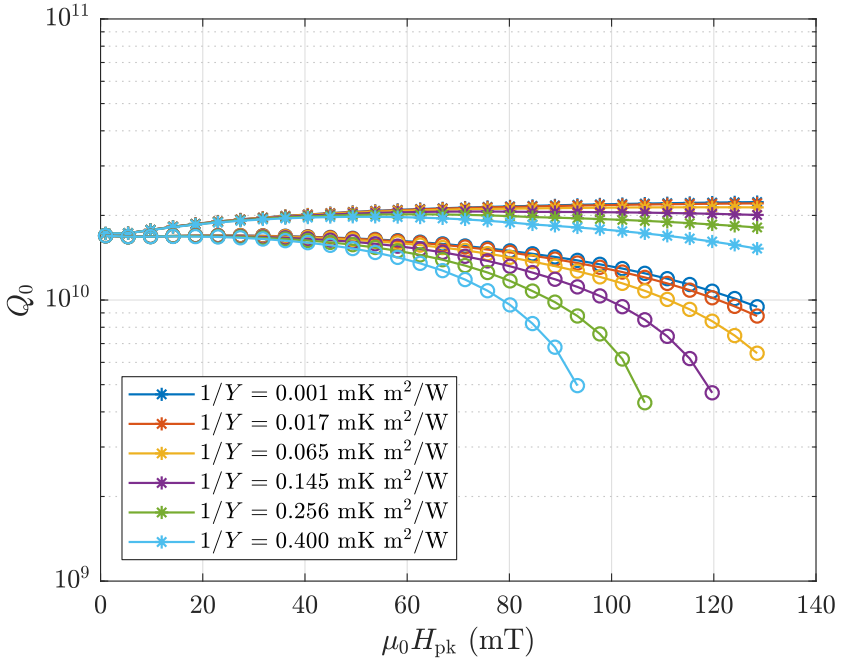

Figure 8.5: Simulations of the field-dependent intrinsic quality factor from the results in Fig. 8.4 for a TESLA-shape cavity.

framework developed in Chap. 7. Figure 8.5 shows the same results converted to the quality factor Q_0. The correction to the distribution function results in the total removal of the anti-Q-slope prediction.

In private communication with members of this collaboration, Gurevich has informed us that he has taken our findings into consideration and is making refinements to the model to account for the distribution function issue and the frequency dependence of the anti-Q-slope [GL]. We hope that these adjustments are fruitful and restore the initial success of the model at 1.3 GHz and extend it to other frequency regimes.

It is quite important to note here that this adjustment to the distribution function does not affect the results of the weak RF/strong DC field case of this model. In that regime, where the strong DC magnetic field modulates the quasiparticle density of states in such a way that the surface resistance changes in a field-dependent manner, the weak RF field does not significantly contribute to the excitation of quasiparticles; as a result, the distribution function largely does not vary in time and can be expressed as the Fermi-Dirac distribution. The new experimental apparatus presented in the next chapter will explore this particular regime of RF and DC fields for SRF materials.

8.5 Outlook

While each of the above-mentioned theories has its merits, each also has distinct issues that may limit its ability to describe the anti-Q-slope observed in niobium SRF cavities. Looking towards alternative explanations of the phenomenon, a potential model must address the frequency-dependence of the anti-Q-slope as

well as its apparent dependence on nitrogen content. Several empirical sketches come to mind: perhaps there is a threshold frequency above which niobium exhibits an anti-Q-slope, and interstitial nitrogen near the RF surface decreases this threshold; perhaps instead interstitial nitrogen prevents the growth of some other defect material with deleterious effects, such as nanoscopic hydride clusters (also called "nanohydrides", as discussed in [RGBO13, TGMR15]), revealing a "native" anti-Q-slope not otherwise reliant on the presence of nitrogen. On another note, each of the theories discussed in this chapter discuss effects in *bulk* superconductors; the evidence from the surface removal studies in Chap. 6 showing that nanometer-scale surface treatments can turn the anti-Q-slope on and off indicate that the anti-Q-slope may instead be a *surface* effect. Within the Center for Bright Beams, promising research is ongoing on yet another tack, working to develop a model of the field-dependent surface resistance using the Floquet approach to analyzing driven quantum systems.

From an experimentalist's point of view, the dearth of satisfying theories of the anti-Q-slope in SRF cavities can be seen as an opportunity to design new experiments and drive theoretical development with new evidence. In the next chapter, I will describe the development of such an experiment, a new "DC field-dependence cavity" which will investigate the dependence of the surface resistance on strong DC magnetic fields with the goal of establishing a new body of evidence to improve our understanding of the physics of the anti-Q-slope.

CHAPTER 9

THE DC FIELD DEPENDENCE CAVITY

As fundamental SRF research and development pushes the quality factor frontier higher with treatments like nitrogen doping and nitrogen infusion, it is important to understand the dependence of the superconducting microwave surface resistance on the strength of the electromagnetic fields present on the RF surfaces of cavities. Why does the surface resistance decrease with increasing RF field strength in nitrogen-doped and nitrogen-infused niobium cavities, resulting in the anti-Q-slope? Why does this behavior improve at frequencies above 1.3 GHz, but disappear at lower regimes? Why does a similar effect appear in some high-frequency cavities and not others? Do DC magnetic fields have a similar effect on the surface resistance? How can we push the surface resistance even lower?

Several theories have been proposed to explain the anti-Q-slope, but with somewhat unsatisfying results: as discussed in Chap. 8, all either miss key predictions of observed anti-Q-slope behavior, like the dependence on electron mean free path or frequency, or make assumptions about experimental conditions that do not apply to SRF cavities, like frequency and temperature. In order to experimentally explore the physics of the field-dependent surface resistance from a new angle, and to perform a deeper investigation of the predictions of the aforementioned models, we have designed and constructed a novel apparatus which tests the behavior of superconducting materials under strong DC magnetic fields superimposed over a relatively low RF field. This new experiment, the DC Field Dependence Cavity, measures the RF surface resistance as a function of the DC magnetic field strength on a superconducting surface. In

this chapter I will document the main components and features of this cavity, detailing and motivating the design and function of this new window into anti-Q-slope physics.

9.1 Prior Art and Motivation

A number of prior experiments have investigated the dependence of the microwave surface resistance on the strength of the electromagnetic field incident on the superconducting surface. In the case of radio-frequency fields, as discussed earlier in this dissertation, there exists a large amount of experimental data from tests of accelerator cavities, especially single-cell cavities, with a variety of treatment protocols. Because these tests are performed in the context of SRF research programs, they are typically (and somewhat by default) carried out at frequencies of interest for SRF studies. These studies include tests of full cavities prepared with a certain protocol, such as the ones presented in Chaps. 5 and 6, as well as tests of "sample host cavities": SRF structures with removable components that can be treated with novel protocols and reassembled onto the host cavity where the properties of the novel material can be examined under RF excitation. Often these removable samples are smaller and geometrically simpler than a full cavity, allowing for relatively inexpensive rapid testing of materials. The Cornell Sample Host Cavity family, most recently in its third generation [Xie13, HLGM14, MCG+15, MHL+16, MHLP17, OGL+18], is an example of such an apparatus, as are the quadrupole resonators at CERN [BHM98, dBG+17] and HZB [KBK+15].

On the contrary, there have been only a very limited number of experiments performed to study the effect of strong DC magnetic fields on the microwave

surface resistance for SRF materials. Numerous studies have been performed on stripline resonators, but these have largely treated materials not relevant for SRF applications such as tin, lead, and high-T_c superconductors like YBCO (for example, see [ROLL+94, ETDS16]). Those studies which did consider niobium stripline resonators did so at microwave frequencies outside the typical range of $\sim$ 100 MHz-4 GHz used in modern SRF cavities (for example, [KRB+18] presents measurements at 10 GHz). Another study investigated the effects of a DC magnetic field on a large superconducting surface more similar to an SRF cavity, but the experiment was performed on samples of tin and indium, not niobium, and again at 10 GHz [SM86]. In general, these studies found R_s to increase with the strength of the applied DC magnetic field, though [SM86] measured a reduction in R_s with applied DC magnetic field when $T < 0.9T_c$.

The promise of the new DC Field Dependence Cavity is to bridge the gap between these two bodies of evidence. As yet, the anti-Q-slope in SRF cavities has only been studied under varying RF field strength; experimental measurements of the DC field dependence of the surface resistance of SRF materials such as nitrogen-doped and nitrogen-infused niobium, niobium with other treatments, and alternative materials such as Nb_3Sn will help to guide our understanding of the mechanism underlying the anti-Q-slope and the field-dependent surface resistance in general. While the Gurevich model explicitly predicts a similar reduction in surface resistance due to strong DC magnetic fields parallel to the RF surface [Gur14], nearly any experimental measurement of this effect (or lack thereof) at relevant frequencies and temperatures and on relevant materials will improve our knowledge of this striking physics, hopefully leading us towards yet higher efficiencies.

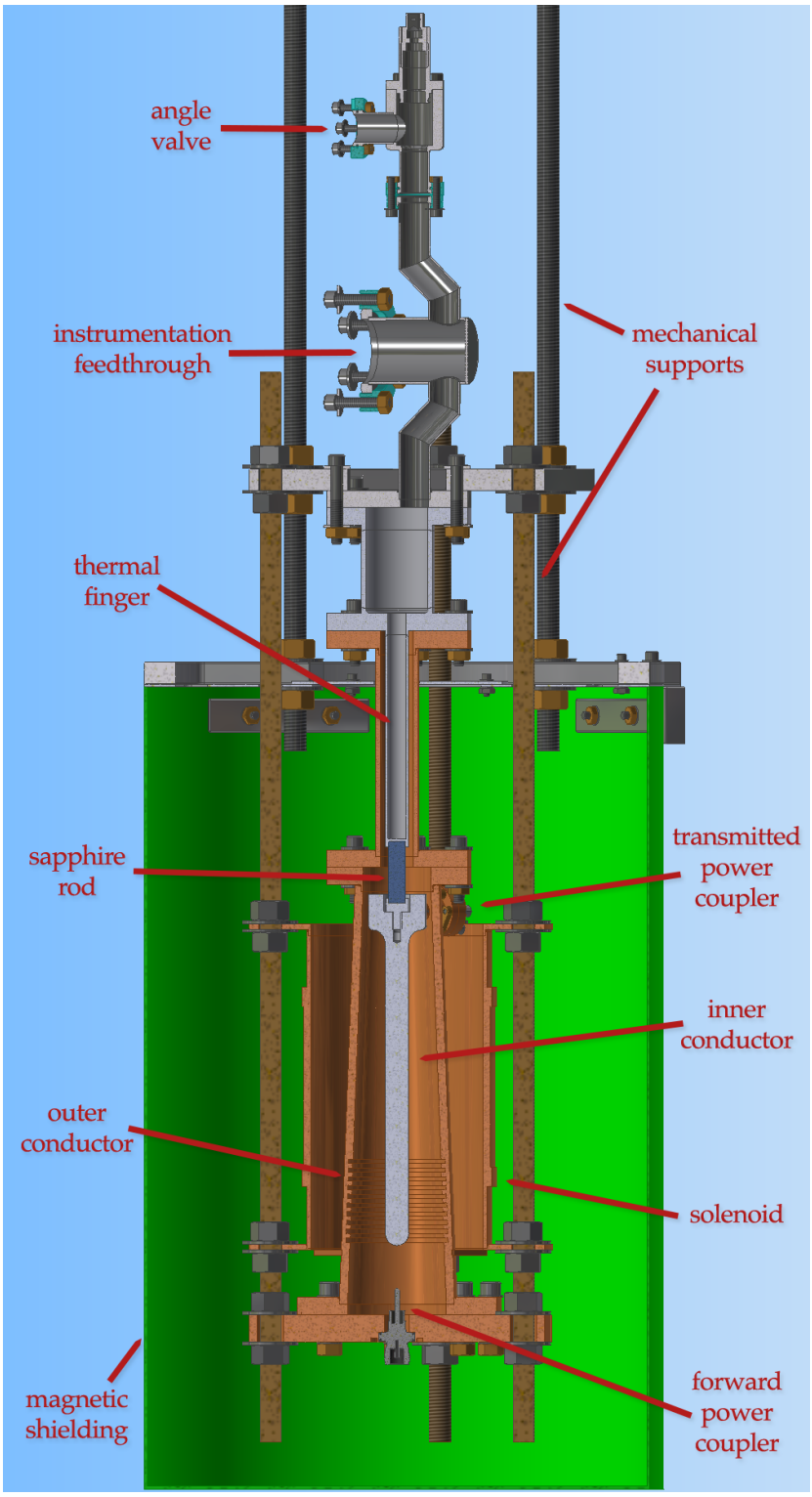

Figure 9.1: Computer illustration of the DC Field Dependence Cavity, with notes highlighting the features of the apparatus.

9.2 Overview of Apparatus

The DC Field Dependence Cavity is a coaxial resonator featuring a removable central superconducting sample. Figure 9.1 shows an overview of the design of the apparatus. The sample, a rod 20 cm long and 1.4 cm in diameter with a rounded tip on one end and flaring out to a diameter of 3.4 cm at the other, is held inside a conical outer conductor made of copper, a normal conductor. These two coaxial components form a resonant cavity; at the base of the assembly is a forward power coupler for exciting an RF field in the cavity, and near the flared end of the inner conductor, transverse to the cavity axis, is a transmitted power coupler for probing the field strength and driving the phase-locked loop (see Sec. 3.3.4). The resonator sits inside a superconducting solenoid that excites a highly uniform DC magnetic field on the surface of the inner conductor. The inner conductor is affixed to a narrow niobium "thermal finger" with thermometers and a heater; these components are used for calorimetric measurements of the RF power dissipated on the inner conductor. Between the inner conductor sample and the thermal finger is a sapphire rod that serves to thermally anchor the inner conductor to the finger while electrically isolating one from the other, preventing the propagation down the finger of RF power which might disrupt the calorimetric measurements.

Outside of the RF region of the cavity, a set of flanges hold a feedthrough for connecting the thermometers and heater to the data acquisition system and an angle valve through which the cavity can be pumped to vacuum. In addition, a large region surrounding the solenoid and resonator are enclosed in a superconducting niobium cylinder, protecting other equipment in the laboratory from the high magnetic fields generated by the solenoid. The entire assembly is

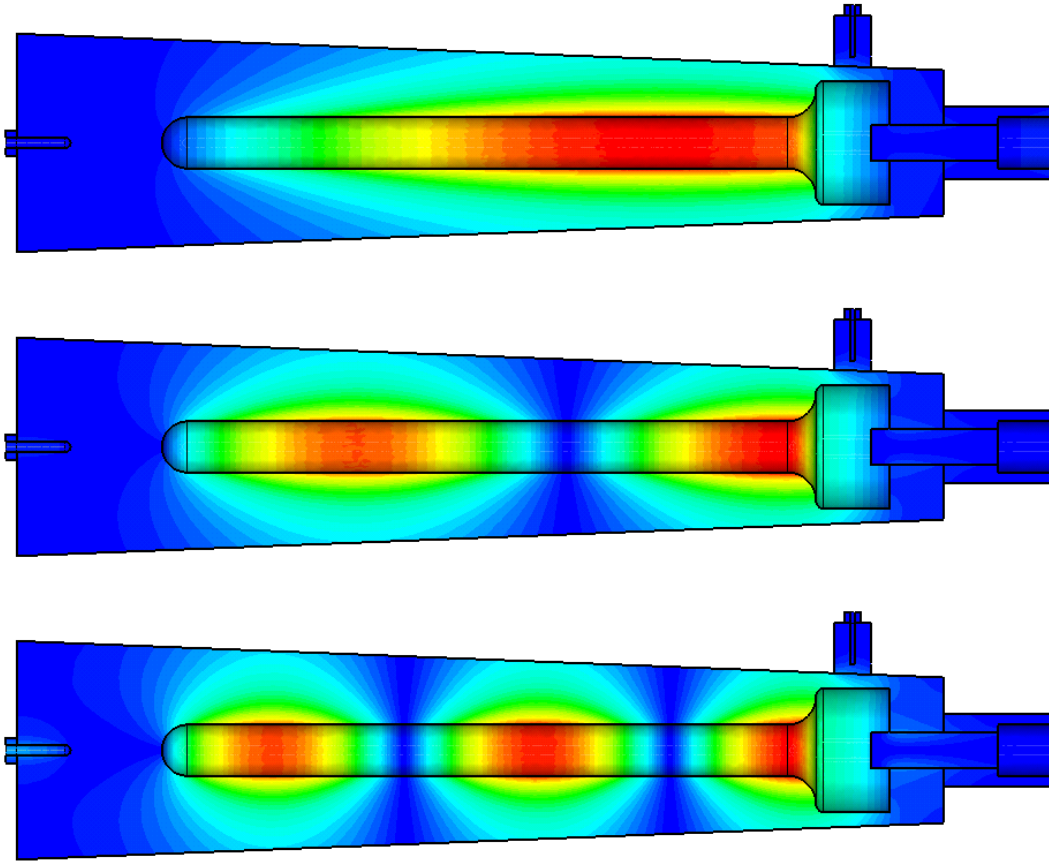

Figure 9.2: Simulations of the RF magnetic field distributions in the 550 MHz, 1.3 GHz, and 2.0 GHz modes of the DC Field Dependence Cavity. The magnetic field is aligned azimuthally.

immersed in a liquid helium bath.

The resonator is optimized for operation at three frequencies: 550 MHz, 1.3 GHz, and 2.0 GHz. The RF field distributions are shown in Fig. 9.2. These modes are the first three quarter-wave modes, with the length of the inner conductor $L \approx \Lambda/4$ at 550 MHz, $\approx 3\Lambda/4$ at 1.3 GHz, and $\approx 5\Lambda/4$ at 2.0 GHz, where $\Lambda = c/f$ is the RF wavelength[1]. The RF magnetic field is entirely azimuthally aligned, while the RF electric field is aligned in the r-z plane.

[1]Here I have used the uppercase Λ instead of the usual λ for the wavelength in order to avoid confusion with the notation for the penetration depth.

In the typical use case, a sample is prepared with a desired treatment, such as nitrogen doping. The cavity is assembled in a clean room, mounted onto the test insert, and pumped down to about 1×10^{-7} Torr. The assembly is loaded into a cryogenic dewar and cooled with liquid helium below the critical temperature T_c of the superconducting sample. A weak RF field is excited in the cavity, with $\mu_0 H_{pk} \approx 3$ mT on the surface of the inner conductor; this dissipates a small amount of power (at 1.3 GHz and 2 K, a clean niobium sample would dissipate around 100 μW), which excites a temperature gradient along the thermal finger. In order to keep the sample temperature consistent through the experiment, some additional power is provided by the heater. The difference in temperature between the two thermometers is measured, and by calibration with the heater this measurement is converted into a measure of the dissipated power. In turn, this measurement can be used to determine the microwave surface resistance of the inner conductor sample from simulations of the cavity geometry, just as measurements of Q_0 are used to the same end in other cavity tests (see Sec. 3.3.1); the specific method of calculation will be described below. The solenoid is then switched on, exciting a DC field of strength H_{DC} on the surface of the inner conductor, potentially changing the surface resistance. The calorimetric measurements are repeated at many values of H_{DC}, building up a map of the surface resistance as a function of DC field strength. This procedure is then repeated at multiple temperatures and for each mode of the cavity.

9.2.1 Calculation of Surface Resistance

Because of the unusual design of the apparatus, the standard methods of determining the surface resistance by way of measurements of the intrinsic quality

factor Q_0 as described in Sec. 3.3.1 are not possible for the DC Field Dependence Cavity. In particular, since the outer conductor is made of copper, a normal-conducting metal, the total intrinsic quality factor of the cavity is dominated by the RF losses on the copper where the surface resistance is up to five orders of magnitude higher (high-purity copper has a surface resistance at 1.3 GHz of 1.4 mΩ at cryogenic temperatures, compared to 18 nΩ for clean superconducting niobium at 2 K). Just as the loaded quality factor Q_L can be expressed as the inverse sum of Q_0 and the coupling quality factors (see Sec. 3.3.3), Q_0 can be expressed as the inverse sum of "local" quality factors for the outer and inner conductors. Beginning by using Eq. 3.48, normalizing to H_{pk}, and substituting in Eq. 3.44, we have the following:

$$Q_0 = 2\omega U \left(\int_S dS\, R_{\text{s}} H^2 \right)^{-1} \tag{9.1}$$

The domain of the integral can be split into two regions covering the surfaces of the inner and outer conductors:

$$Q_0 = 2\omega U \left(\int_{S_{\text{inner}}} dS\, R_{\text{s}} H^2 + \int_{S_{\text{outer}}} dS\, R_{\text{s}} H^2 \right)^{-1} \tag{9.2}$$

$$= \left(\frac{1}{Q_{\text{inner}}} + \frac{1}{Q_{\text{outer}}} \right)^{-1} \tag{9.3}$$

Compare the above to Eq. 3.68. Then, under the assumption that the surface resistance is uniform over the surface (likely a good approximation at the low RF field strengths in the new cavity), we can pull R_{s} out of the two integrals as before in Eq. 3.49, yielding local geometry factors G_{inner} and G_{outer}:

$$Q_0 = 2\omega U \left(R_{\text{s,inner}} \int_{S_{\text{inner}}} dS\, H^2 + R_{\text{s,outer}} \int_{S_{\text{outer}}} dS\, H^2 \right)^{-1} \tag{9.4}$$

$$= \left(\frac{G_{\text{inner}}}{R_{\text{s,inner}}} + \frac{G_{\text{outer}}}{R_{\text{s,outer}}} \right)^{-1} \tag{9.5}$$

The values of the local geometry factors are given in Table 9.1. Since $R_{\text{outer}}/G_{\text{outer}} \gg R_{\text{inner}}/G_{\text{inner}}$ (indeed $R_{\text{outer}} \gg R_{\text{inner}}$), $Q_0 \approx Q_{\text{outer}}$, and the majority of

Local geometry factor	550 MHz	1.3 GHz	2.0 GHz
G_{inner} (Ω)	35.8	83.5	135
G_{outer} (Ω)	118	273	424

Table 9.1: Local geometry factors for the inner and outer conductors of the DC Field Dependence Cavity.

the RF power is dissipated on the outer conductor. As a numerical example, at 1.3 GHz and 2 K where $R_{\text{s,Cu}} \approx 1.4$ mΩ and $R_{\text{s,Nb}} \approx 18$ nΩ, we find $P_{\text{diss,inner}}/P_{\text{diss,outer}} \approx 4 \times 10^{-5}$.

As a result, the RF Off measurement technique described in Secs. 3.3.3 and 3.4.2, with our assumed 10% uncertainty in Q_0, is not precise enough to measure fractional changes in R_{inner} that might occur due to the strong DC magnetic field. Instead, the DC Field Dependence Cavity is designed for direct measurements of the power dissipated on the inner conductor through calorimetry.

As shown in Fig. 9.1, the inner conductor is suspended inside the outer conductor and anchored to the cryogenic bath through the thermal finger. At cryogenic temperatures, thermal radiation is minimal, so the heat generated on the inner conductor is thermally conducted down the finger, creating a temperature gradient along the finger:

$$\frac{dT}{dz} = \frac{P_{\text{diss,inner}}}{\kappa(z)A(z)} \tag{9.6}$$

Here κ is the thermal conductivity and A is the cross-sectional area of the finger, both presented as functions of position z along the length of the finger. This thermal gradient results in a finite difference in temperature ΔT between the two thermometers affixed to the finger. The precise values of κ and A may have slight variations along z, so ΔT is calibrated as a function of $P_{\text{diss,inner}}$ by using the calibration heater on the thermal finger (located between the inner conductor and the first thermometer). With the calibration curve in hand, measurements

of ΔT between the two thermometers can be used to determine $P_{\text{diss,inner}}$ on the inner conductor.

An RF Off measurement yields the stored energy in the cavity U, as described in Sec. 3.3.3 (see Eq. 3.78). These can be put together with the calibrated measurement of $P_{\text{diss,inner}}(\Delta T)$ to find the surface resistance:

$$R_{\text{s,inner}} = \frac{G_{\text{inner}}}{Q_{\text{inner}}} \tag{9.7}$$

$$= \frac{P_{\text{diss,inner}}(\Delta T)\, G_{\text{inner}}}{\omega U} \tag{9.8}$$

Since the inner conductor is cooled conductively through the finger, its temperature increases when RF fields are present. The magnitude of this increase in temperature is slightly more than the ΔT measured between the thermometers. In order to keep this temperature stable and isolate the dependence of R_s on the DC field strength from its strong dependence on temperature, the calibration heater can be powered to provide a small amount of additional heat P_{heater}; then, as R_s changes with the DC field, P_{heater} is adjusted to keep ΔT constant. By the earlier calibration, the change in P_{heater} with changing H_{DC} can be used to calculate $R_s(H_{\text{DC}})$.

9.3 Design and Construction

Many of the components of the DC Field Dependence Cavity required particular attention in their design to ensure optimal functioning of the apparatus under test. In the following subsections I will detail the critical elements of the design and construction of these components.

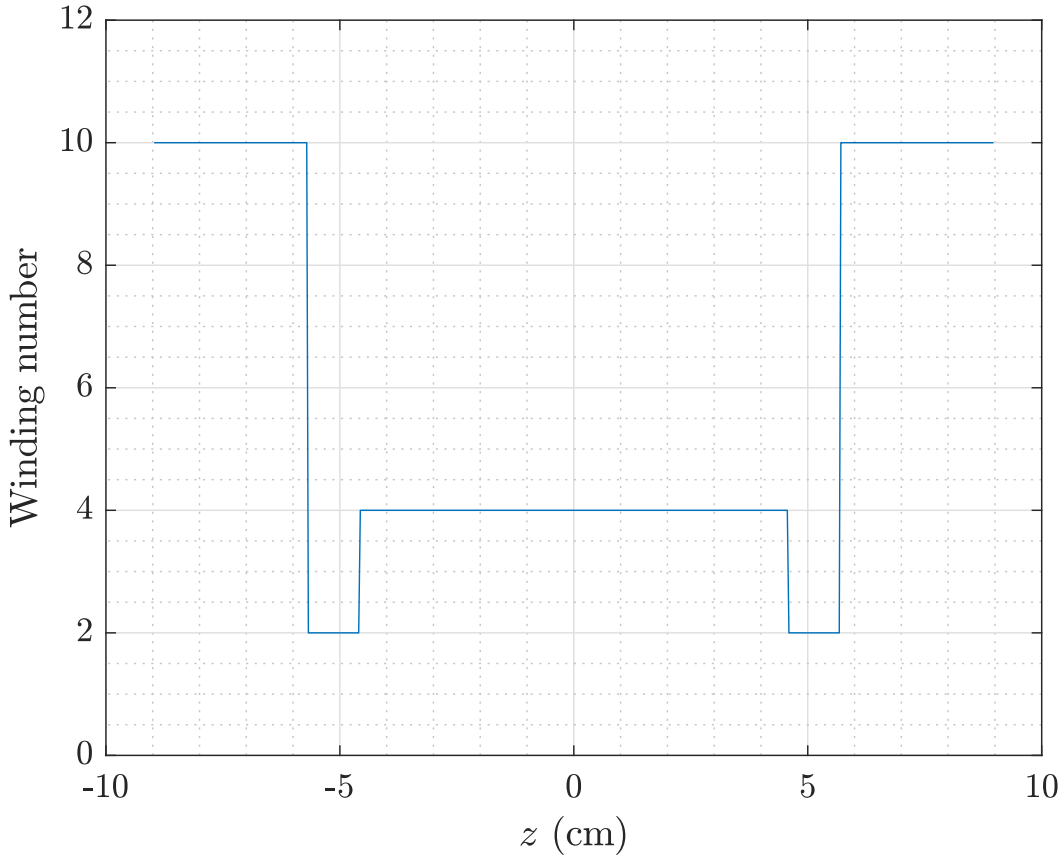

Figure 9.3: Optimized winding number (number of wire layers per wire diameter) of the superconducting solenoid over its length in z.

9.3.1 Solenoid Subsystem

The superconducting solenoid is wrapped around a mandrel that is 11.4 cm in diameter and 18 cm in length. These dimensions, constrained by the dimensions of the copper outer conductor of the resonator and the locations of other components such as the transmitted power feedthrough, bring the solenoid well away from the long solenoid approximation: a solenoid of these dimensions with a uniform winding density would have a highly nonuniform field. To combat this, I designed the solenoid with a nonuniform winding density, increasing the number of winding layers near the ends of the electromagnet to improve uniformity in the interior of the solenoid.

To optimize the placement and sizes of the additional winding layers, I developed a Matlab program that uses a genetic algorithm[2] to find the ideal winding pattern for the solenoid. The algorithm simulates "steps" cut into the mandrel with depths an even integer multiple of the wire diameter, using the Biot-Savart law to find the axial magnetic field considering the additional contribution from the extra windings in the steps, and comparing this against an ideal uniform field. Figure 9.3 shows the results of this optimization, plotting the winding number as a function of position z along the axis of solenoid.

For construction, the core of the mandrel was machined from copper tube stock. Two end plates were machined from copper plate and brazed onto the mandrel core to contain the wires and provide a mechanical support structure to hold the magnet in place. Figure 9.4 shows the finished solenoid mandrel with the steps cut in, mounted on the coil winding setup at Cornell. The solenoid was wound with superconducting NbTi wire; the wire, acquired from Supercon, Inc., features 54 superconducting NbTi filaments held in a copper "matrix" of diameter 0.30 mm. The wire is insulated with Formvar enamel, bringing the total wire thickness to about 0.33 mm. At the deepest step, the solenoid is wound in ten layers; at the shallowest, only two layers are wound. Figure 9.5 shows the solenoid after final winding, mounted on the test insert.

I tested the uniformity of the field along the magnet axis in air in the normal-conducting state. Figure 9.6 shows the results of the measurement along with the field strength predicted from calculation with the Biot-Savart law. The strength of the DC field relative to the excitation current is approximately 15 mT/A. The theoretical prediction has been scaled here to 95% of its original value; the discrepancy in scale between the experimental results and the theoret-

[2]See [BNK97] for a thorough treatment of genetic algorithm optimization techniques.

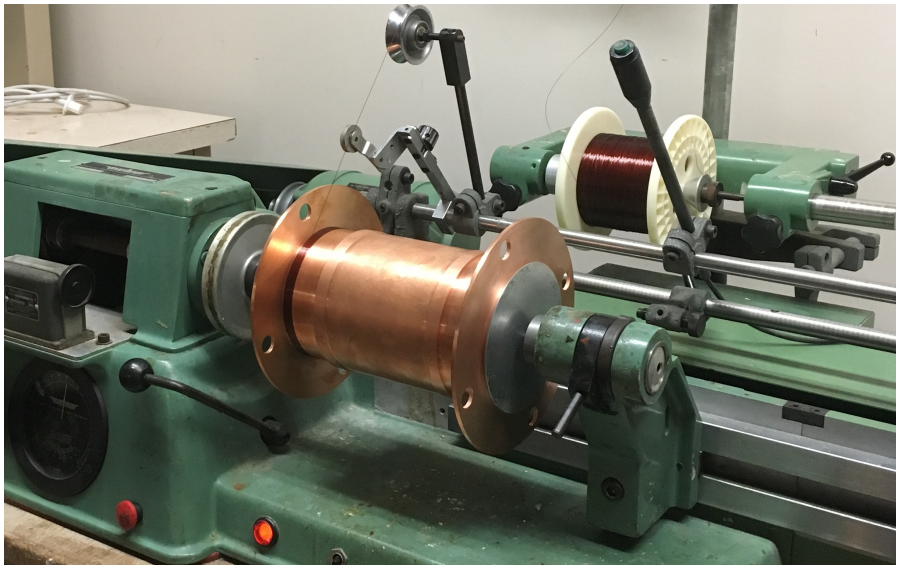

Figure 9.4: Mandrel of the superconducting solenoid, mounted on the coil winding setup at Cornell, with optimized steps visible.

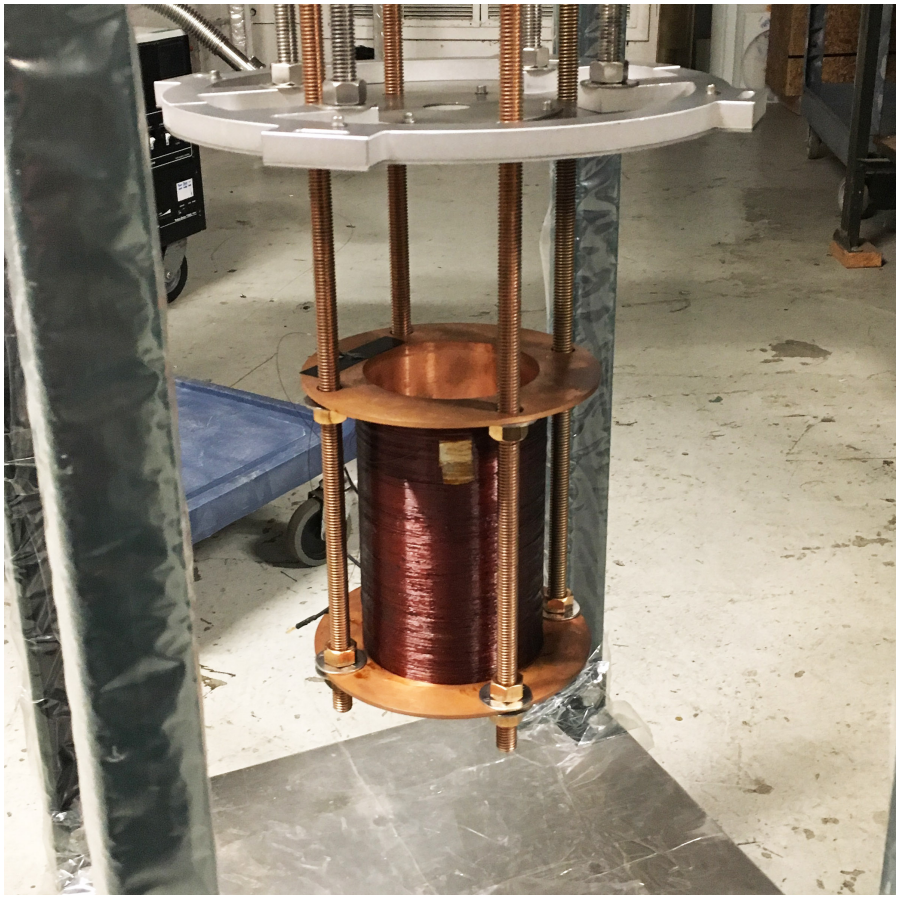

Figure 9.5: Completed solenoid, mounted on the cryogenic test insert in preparation for the cold test.

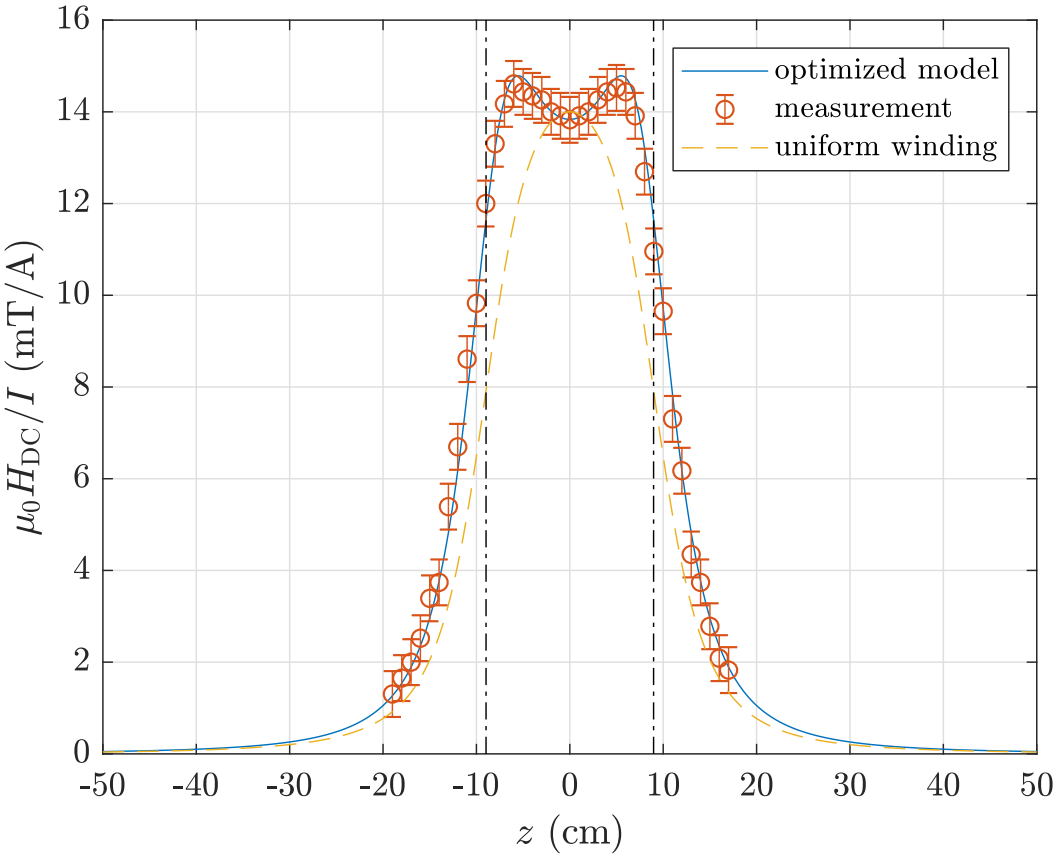

Figure 9.6: Simulation of the axial DC magnetic field generated by the superconducting solenoid, compared to experimental measurements. Also plotted is the simulated field from a solenoid with uniform winding density. Black dash-dotted lines indicate the left and right ends of the solenoid.

ical prediction may be due to a slight misalignment of the magnetic field sensor used for the measurement, from a slight mismatch in theoretical and experimental wire diameter, or otherwise; thankfully, the discrepancy is quite small and the wound solenoid exhibits good field uniformity otherwise in agreement with the prediction. Also depicted in Fig. 9.6 is the axial field for a solenoid of the same dimensions with uniform winding, showing strongly decreased fields near the ends of the solenoid (represented by dashed lines). Figure 9.7 shows the theoretical strength of the DC magnetic field in the *r*-*z* plane; the field has no azimuthal component.

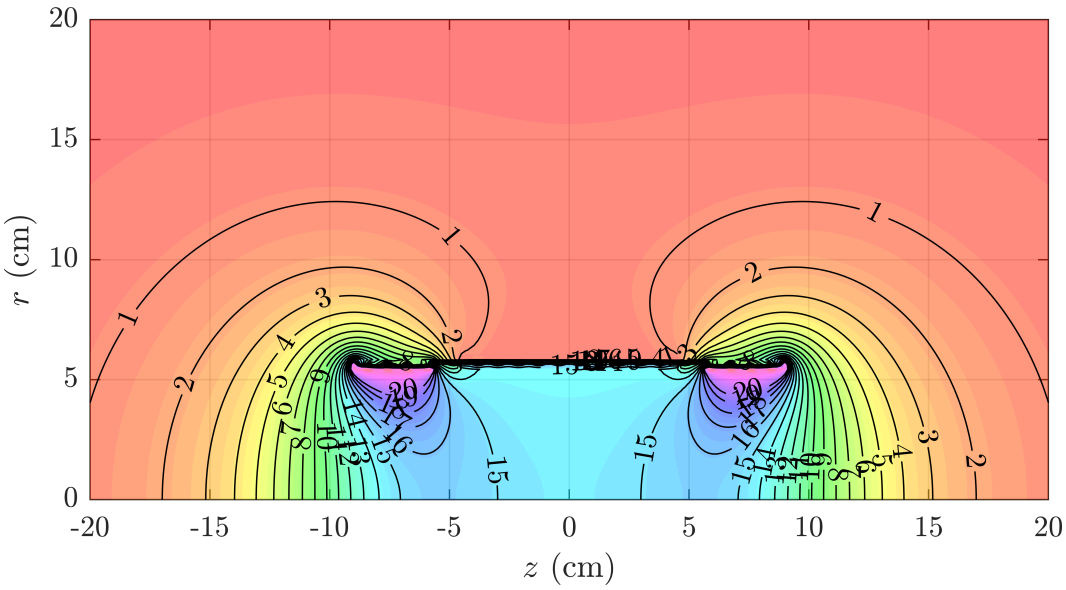

Figure 9.7: Simulation of the DC magnetic field strength of the superconducting solenoid in mT with an excitation current of 1 A.

Under cold test, the solenoid exhibited high linearity with excitation current, as expected. The magnet was tested up to an axial field of 52 mT; the results of this test of H_{DC} vs. I are shown in Fig. 9.8. Note that the field probe was placed off-axis, flush with the inner diameter of the mandrel, where the field level is slightly reduced from its on-axis value.

For superconducting operation of the solenoid, the excitation circuit includes a quench protection mechanism to protect people and equipment in the laboratory from high voltages that might be generated in a quench: during a quench, the resistance R of part or all of the solenoid increases dramatically as it turns to the normal state; due to the magnet's self-inductance, the current briefly remains at the same level, so by Ohm's law $V = IR$ a spike of high voltage is generated across the terminals of the solenoid. To give a numerical example, if a complete quench of the solenoid occurred at a field of 50 mT (I$\approx$ 4 A), the resistance of the wire would jump up to roughly 100 Ω, resulting in a spike of

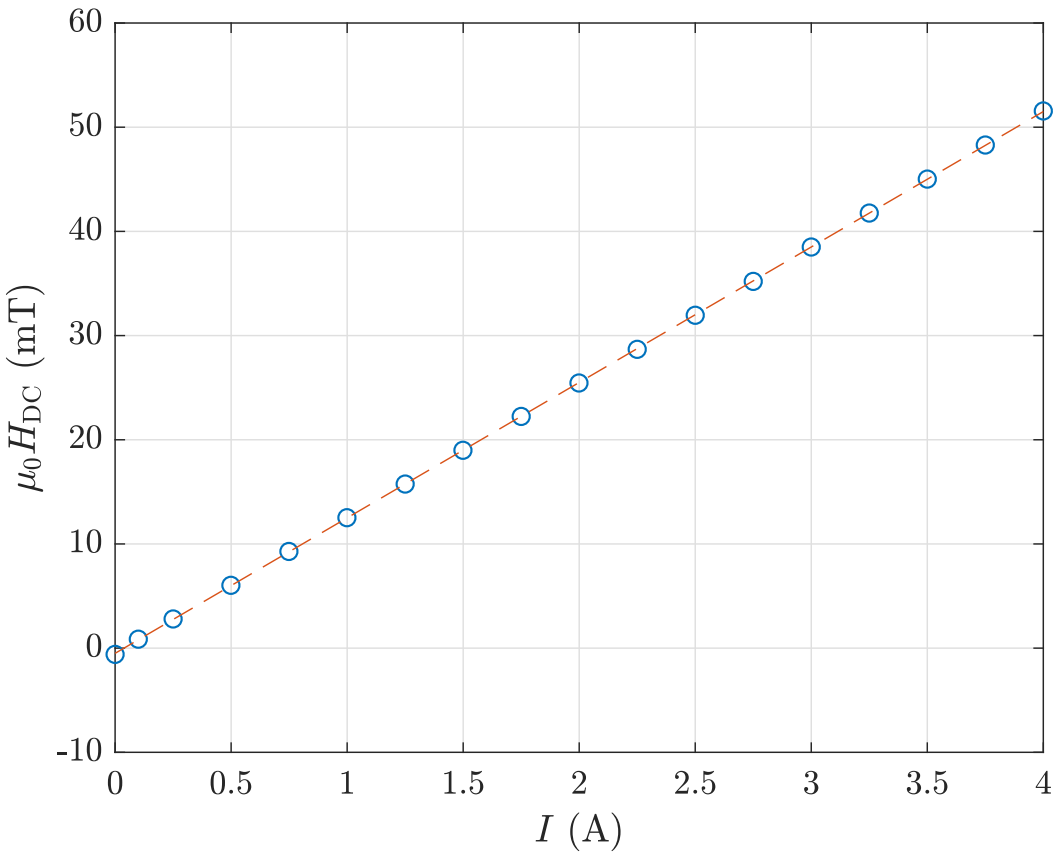

Figure 9.8: Measurements of the DC magnetic field strength of the solenoid, measured off-axis, as a function of applied current. Dashed line indicates a linear fit to $\mu_0 H_{\mathrm{DC}} = a * I + b$, with $a = 13.00 \pm 0.02$ mT/A and a background offset of $b = -0.50 \pm 0.04$ mT.

400 V. At the peak design field of 300 mT, this would be a spike of 2400 V.

The quench protection system is a set of high-voltage, high-current, hyper-fast switching diodes shorting the two terminals of the solenoid; below a threshold voltage, the diodes do not activate, and the magnet is energized as normal. In case of a quench, the voltage spike activates the diodes and shorts out the solenoid, until the quench event finishes and the solenoid returns to the superconducting state. Figure 9.9 shows a circuit diagram of the solenoid circuit including the quench protection system.

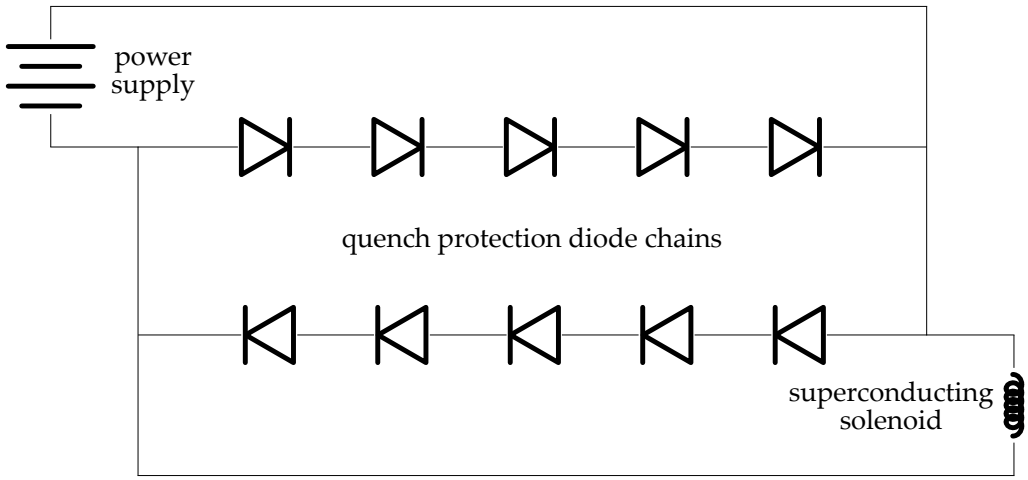

Figure 9.9: Diagram of the superconducting solenoid quench protection circuit with hyperfast switching diodes.

9.3.2 Superconducting Magnetic Shielding

For the safe operation of the superconducting solenoid, it is necessary to protect people and equipment in the laboratory from the strong magnetic fields produced by the electromagnet. In particular, the vertical test dewars in the Cornell SRF laboratory are lined with a layer of Mu-metal, a material with high magnetic permeability; typical values are quoted near $\mu = 100,000 \times \mu_0$ [Mag]. The Mu-metal serves to protect the cavities under RF test from ambient magnetic fields (such fields might become trapped during cooldown, leading to high residual resistance). This material can itself become magnetized if exposed to fields above a saturation threshold, quoted near $\mu_0 H_s = 800$ mT [Mag]; this threshold can be lowered by deformation and welding [Sgo11]. Since the target maximum field in the solenoid is 300 mT, additional shielding is necessary to prevent the saturation and permanent magnetization of the Mu-metal shielding.

As mentioned above, the cavity and solenoid are placed inside a capped

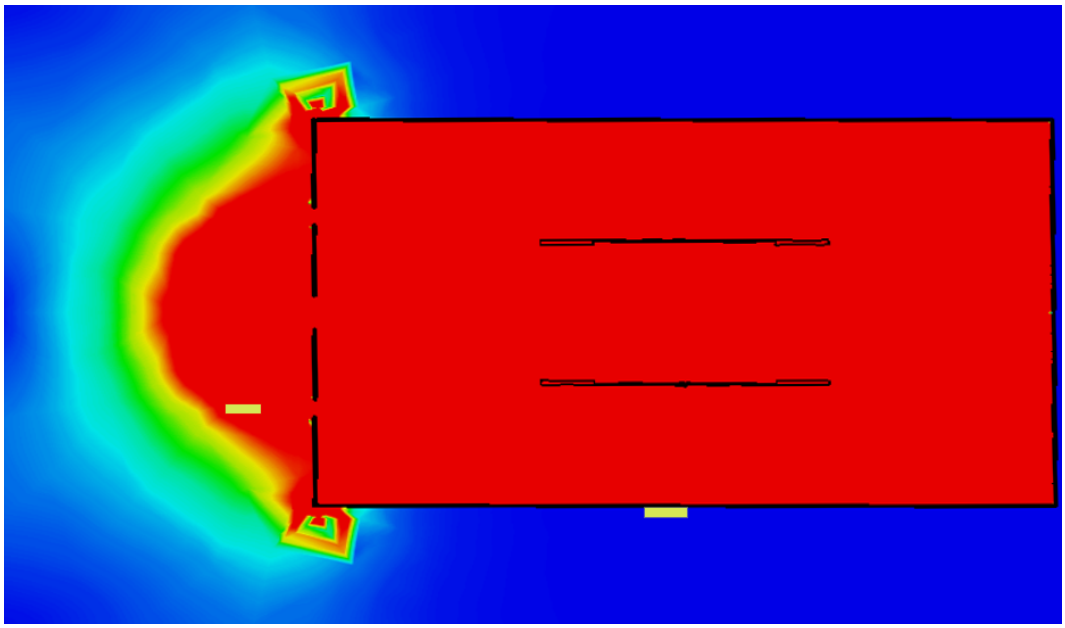

Figure 9.10: Simulation of the DC magnetic field generated by the superconducting solenoid inside the magnetic shielding cylinder with an excitation current of 1 A. Red areas indicate $\mu_0 H_{DC} > 100$ mG; yellow rectangles indicate locations of fluxgate magnetometers in test.

cylindrical shell of niobium. The cylindrical shell is welded to the lower cap; the upper cap is affixed separately during test preparation and has several half-inch-scale holes that allow cavity and solenoid instrumentation cables as well as mechanical support components to pass out of the shielding enclosure. At cryogenic temperatures, the niobium cylinder enters the superconducting Meissner state, expelling trapped flux and resisting the penetration of external magnetic fields. Superconducting cylinders have been found to provide excellent magnetic shielding due to the Meissner screening currents excited on the surface exposed to the field [KHS63, WMMS89]. This has largely been used to protect the interior of the cylinder from external fields, but the shielding works equally well to keep a field excited inside the cylinder from affecting the region outside.

Figure 9.10 shows the results of a simulation of the magnetic field produced by the solenoid with a 1 A excitation current (a peak field on axis of approxi-

mately 15 mT), including the effects of the superconducting magnetic shielding. The red area in the figure indicates a field level greater than 100 mG = 0.01 mT. The superconducting shielding was used in the cold test of the solenoid and performed to expectations. Two fluxgate magnetometers were placed outside the shielding cylinder during the test; their approximate positions are indicated in Fig. 9.10. When the field was excited to 15 mT, the sensor placed on the outer wall of the cylinder read a field of 0.24 mG, while a second sensor placed approximately one inch above one of the instrumentation feedthrough holes read a field of 175 mG. These readings are consistent with the simulation and indicate satisfying shielding by the superconducting cylinder.

9.3.3 Outer Conductor

In order for the DC magnetic field for the solenoid to reach the superconducting inner conductor sample, the outer conductor of the resonator needs to be a normal-conducting metal (as discussed above, superconducting cylinders make very efficient magnetic shields). For normal-conducting accelerating structures, high-purity oxygen-free copper is a common material of choice due to its comparatively low RF losses for a normal metal, high mechanical strength, high breakdown field, and low outgassing [ITK+00]; we chose to use this material for the outer conductor of the resonator.

Coaxial structures like the resonator in the DC Field Dependence Cavity are susceptible to "multipacting" [SPP95]. This phenomenon, which can also affect more traditional SRF structures, occurs at certain field levels when field-emission electrons are accelerated by the cavity to collide into the cavity wall.

Multipacting has several conditions that must be satisfied for it to take effect: the electron must have enough energy to cause secondary electron emission; the secondary electron yield on the surface must be greater than 1; the impact of the emitted electron (or the final impact of a chain of emissions and impacts) must happen at or near the original emission site; and the (final) impact must happen at the same time in the RF cycle as the initial emission. If these conditions are met, the process repeats resonantly, with the number of electrons ejected each time growing exponentially. This avalanche of electrons may produce enough heat to quench the cavity; the peak achievable field in the cavity is limited by this multipacting onset field. Multipacting can be "processed", which involves purposefully inducing the multipacting state in order to clean the surface and reduce the local secondary electron coefficient, but this produces heat and, moreover, is not guaranteed to work.

There are a number of techniques that can limit multipacting in resonant structures. One is to introduce a DC magnetic field: the electron trajectories are perturbed by cyclotron forces in the presence of the magnetic field, disrupting the multipacting conditions [GBC+03]. For the DC Field Dependence Cavity, the superconducting solenoid will likely provide enough of a disruption to suppress multipacting when it is switched on. However, when the solenoid is set to a low field or switched off, additional multipacting mitigation techniques are required. The design of the outer conductor includes two features that serve in this function; I used the Multipac program to optimize the parameters of the design [LAL+08].

The first multipacting mitigation feature of the outer conductor is its conical cross-section. Tapered structures have been shown to suppress multipact-

ing [Pro12]. Over its length of 25 cm, the outer conductor of the DC Field Dependence Cavity tapers from a diameter of 6 cm at the wide end to a diameter of 4 cm on the narrow end.

The second multipacting mitigation feature is a set of grooves cut into the interior of the conical outer conductor near the high-electric-field region at the tip of the inner conductor. Like the taper, grooves have been shown to reduce multipacting in coaxial structures [Pro12]. In total there are 10 grooves in the outer conductor; the grooves have a square cross-section of side length 5 mm and are spaced at 1 cm increments. The convex corners are rounded with a 0.5 mm radius.

Multipac simulations of the cavity, screenshots of which are shown in Figs. 9.11a-9.11c, indicate that these multipacting mitigation measures were successful. The "distance maps", which depict the potential multipacting sites along the cavity wall and the RF phase where the multipacting trajectories begin, show nearly complete suppression of multipacting in the 550 MHz and 1.3 GHz modes. In the 2.0 GHz mode, several possible multipacting trajectories were found, but all of these are of high order (*i.e.* many RF cycles between initial emission and final impact). Figure 9.11d shows one such high-order trajectory for the 2.0 GHz mode.

The exterior of the outer conductor also features several copper tabs that serve as alignment structures for the superconducting solenoid. In assembly, the solenoid is mounted flush to the tabs, which ensures that the high-uniformity DC field is correctly positioned with respect to the inner conductor sample.

For construction, the conical section of the outer conductor was machined

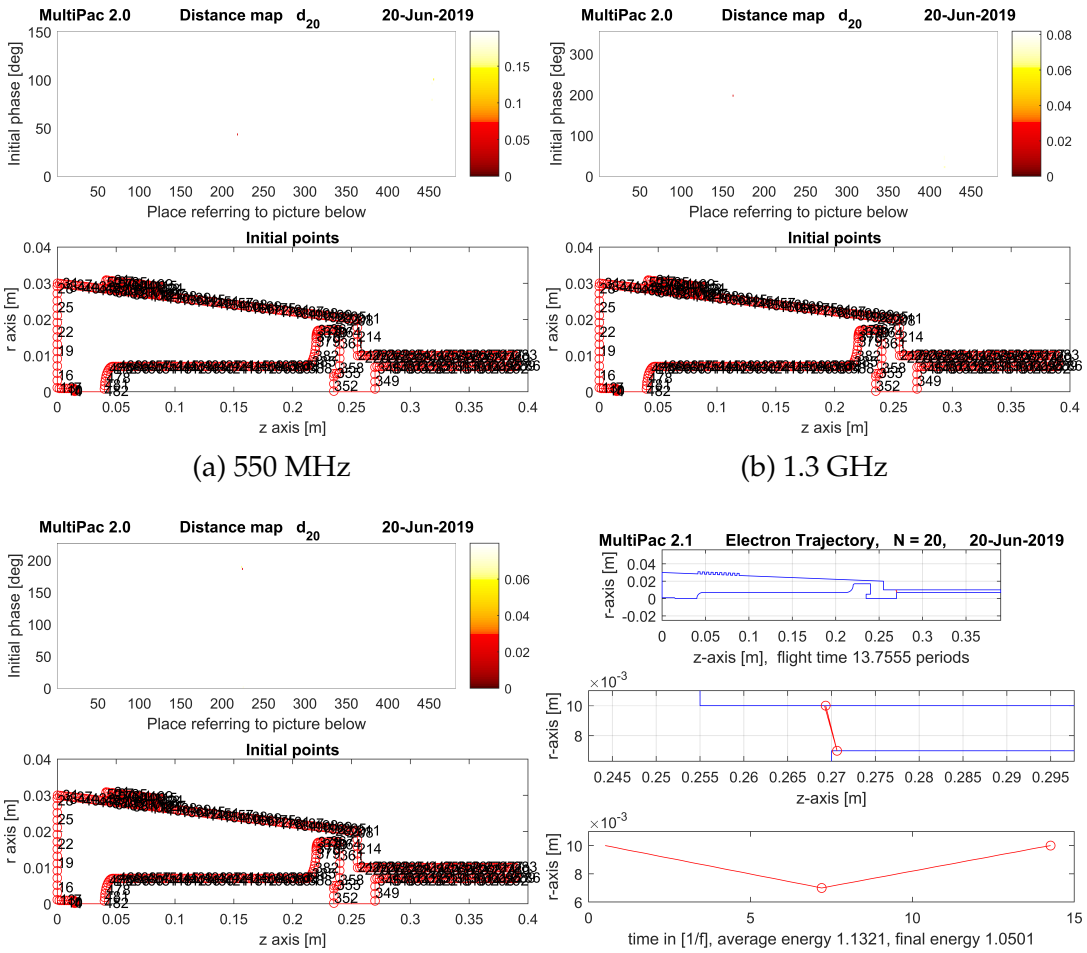

(a) 550 MHz (b) 1.3 GHz

(c) 2.0 GHz (d) High-order trajectory at 2.0 GHz

Figure 9.11: Multipac simulations of multipacting in the DC Field Dependence Cavity. Distance maps in Figs. 9.11a-9.11c show limited multipacting in the conical coaxial resonator (note the small red dots and their scarcity). Figure 9.11d shows an example of the remaining multipacting electron trajectories; all remaining trajectories were of high-order.

from high-purity oxygen-free copper bar stock. The transverse transmitted power port was machined separately and brazed onto the central structure, as were the two vacuum flanges on either end of the cone. The alignment tabs were then welded into place. Figure 9.12 shows the completed outer conductor assembly.

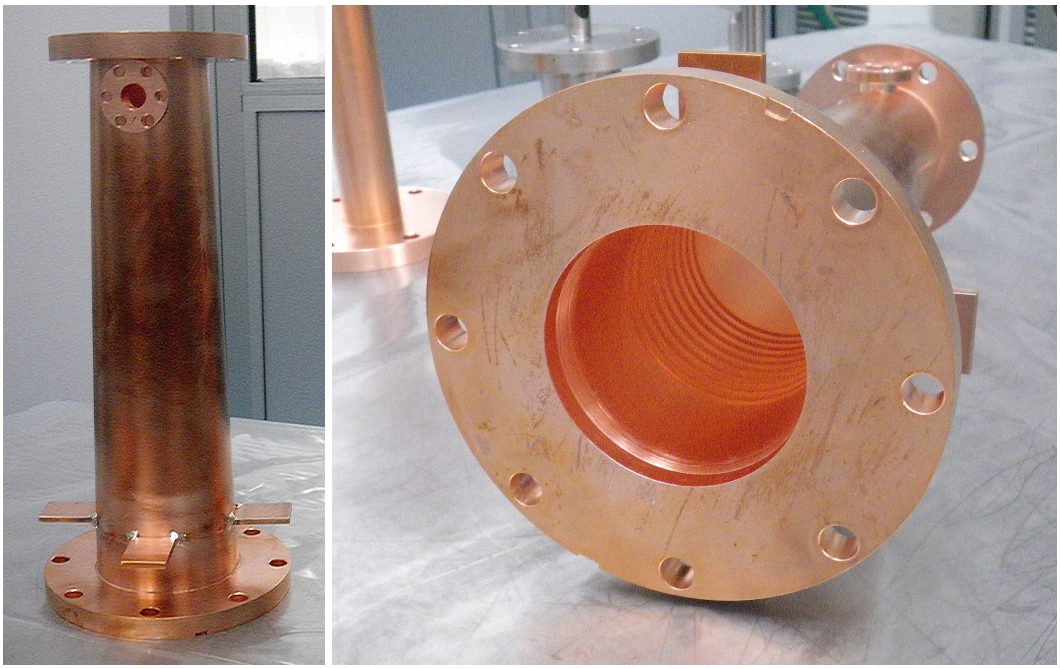

(a) Exterior (b) Interior and P_f coupler flange

Figure 9.12: Several views of the copper outer conductor of the DC Field Dependence Cavity.

9.3.4 Calorimetric Measurement System

The normal-conducting outer conductor of the coaxial resonator imposes some constraints on other elements of the DC Field Dependence Cavity. As mentioned earlier, the comparatively high surface resistance of the copper outer conductor makes standard RF Off measurements of Q_0 ineffective at measuring the surface resistance of the superconducting inner conductor. Instead, the DC Field Dependence Cavity uses a calorimetric measurement system where high-precision temperature measurements along a thermal finger anchoring the inner conductor yield a measurement of the power dissipated on the inner conductor (see Sec. 9.2.1 above).

In order to perform those high-precision measurements, the DC Field Dependence Cavity employs Cernox senors [Laka]. These sensors are calibrated to

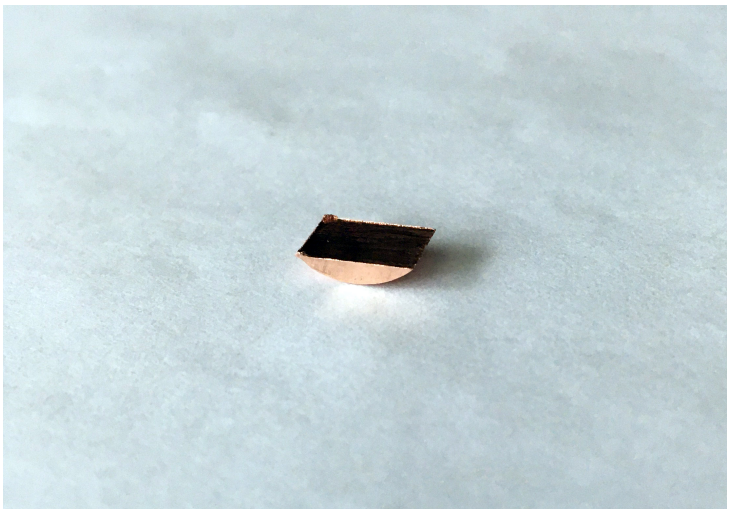

Figure 9.13: One of the copper shims used for mounting the instrumentation in the thermal finger assembly.

the ±3 mK level over the temperature range of 1.4-300 K. For the new apparatus, two Cernox sensors are mounted on copper cylindrical segment shims with varnish; the radius of the shims is cut to match the inner radius of the thermal finger. Figure 9.13 shows one of the copper shims. The shims are then affixed to the inner surface of the thermal finger with low-vapor-pressure two-part epoxy.

Also mounted inside the thermal finger, flush with the end of the niobium tube, is a carbon composition resistor that serves as the calibration heater. The resistor measures 900 kΩ at room temperature, rising to 3 MΩ at cryogenic temperatures. For mounting on the apparatus, the otherwise cylindrical resistor has been sanded on one side to have a flat face. This face is affixed to another copper cylindrical segment shim with varnish, and the shim is affixed to the interior of the thermal finger with the same two-part epoxy.

The Cernox thermometers and calibration heater are connected to a six-conductor ribbon cable that provides the excitation current for the three electronic components. The ribbon cable wires are 28 AWG (0.32 mm diameter)

silver-plated copper; the narrow diameter of the wires prevents interference with the calorimetric measurements. The other end of the ribbon cable connects by a set of clips to a matching ribbon cable in the feedthrough weldment, which in turn is connected to a 19-pin bayonet feedthrough. An instrumentation cable then connects to this feedthrough for four-point resistance measurements of the thermometers and a four-point excitation of the heater (two leads for excitation, two leads for a measurement of voltage across the heater).

The niobium tube of the thermal finger features two holes 1 cm in diameter that serve as access points for mounting the thermometers and calibration heater as well as vacuum pumping ports to the cavity. At the end of the tube opposite the inner conductor sample is a vacuum flange for mounting to the copper tube surrounding the thermal finger; this copper tube in turn features a vacuum flange for mounting to the conical outer conductor. This flange thermally anchors the assembly to the liquid helium bath. After the vacuum flange, the thermal finger assembly has a small section of niobium tube and a second vacuum flange. This wider tube encloses a space for clipping the instrumentation ribbon cable to the matching cable in the feedthrough weldment, which is attached at the second vacuum flange.

For construction, the niobium tube was machined from reactor-grade niobium tube stock. The flanges and wide tube were also machined from reactor-grade niobium. The four parts of the thermal finger assembly were electron-beam welded together.

Figure 9.14a shows the thermal finger with mounted instrumentation, and Fig. 9.14b highlights one of the mounted thermometers. Figure 9.14c shows the matching clips and instrumentation feedthrough on the feedthrough weldment.

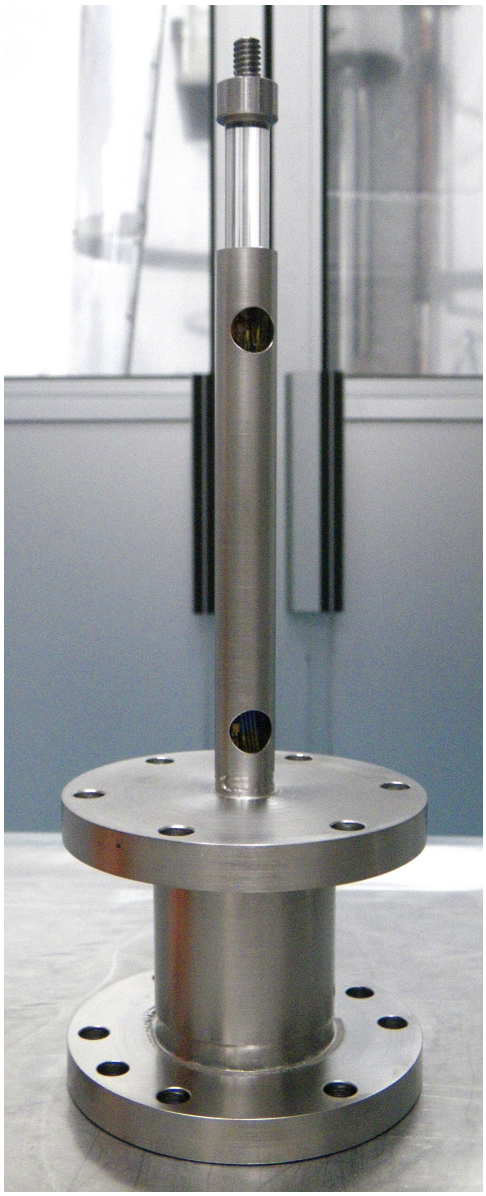

(a) Thermal finger assembly

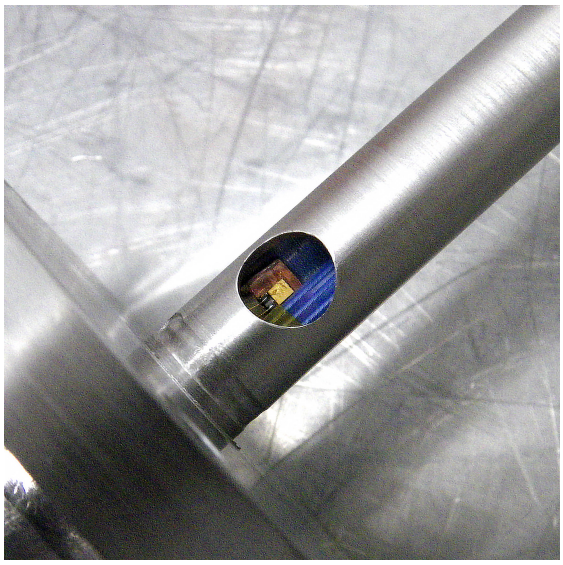

(b) Closeup of mounted thermometer

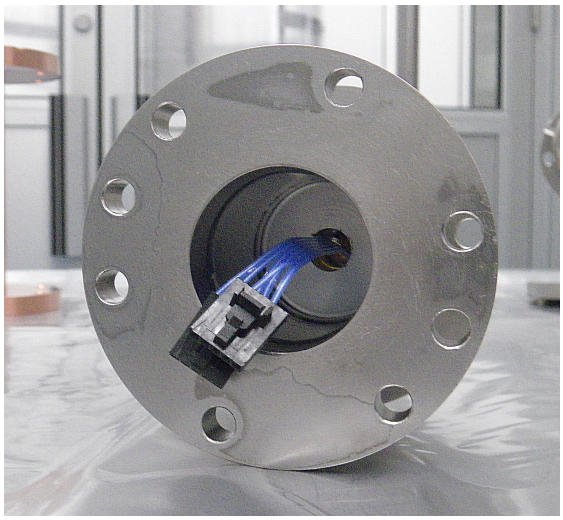

(c) Instrumentation clips

Figure 9.14: Several views of the thermal finger assembly of the DC Field Dependence Cavity.

Also shown in Fig. 9.14a are the sapphire rod and NbTi mounting screw, which were brazed into place before the internal instrumentation was installed. These additional parts will be described later in Sec. 9.3.

9.3.5 Power Couplers and Sensitivity

The DC Field Dependence Cavity features two RF couplers. The first, the forward power coupler, serves to excite an RF field in the cavity and is used for measurements of P_{f}, P_{in}, P_{r}, and P_{e} as described in Sec. 3.3.3. These measurements are used to calculate the the peak surface magnetic field H_{pk}.

For mechanical simplicity and to avoid the use of hard-to-clean bellows structures, the forward power coupler has a fixed length (as opposed to the variable couplers used for the cavity tests in Chaps. 4-6). This simplicity comes at a cost: the length of the coupler must be optimized for all three resonant modes.

For the optimization criterion we chose to us the sensitivity of measurements of relative change in the surface resistance $\delta R_{\mathrm{s}}/R_{\mathrm{s}}$ in all three modes. This sensitivity is affected by a number of factors: the coupling factor of the mode used for the measurement and the intrinsic quality factor of that mode of the cavity, which govern the peak field achievable in the cavity given a fixed maximum forward power; the surface resistance of the sample at that frequency and at the temperature under test, which determines the dissipated power $P_{\mathrm{diss,inner}}$ transmitted as heat down the thermal finger; the thermal conductivity of the thermal finger at the test temperature, which determines ΔT as a function of $P_{\mathrm{diss,inner}}$; and the sensitivity of the thermometers.

To determine the coupling factor for a given P_{f} coupler length, I used CST Studio [Das], a 3D electromagnetic modeling system. Into these simulations went the surface resistance of the copper outer conductor, which accounts for approximately 100% of the RF losses in the cavity. To calculate an

appropriate surface resistance, I used the equations that describe the anomalous skin effect in metals with the clean-limit interpolation by Bruynseraede *et al.* [PHK98, RS48, BGLM71]. In these equations, reproduced below, α is a dimensionless parameter expressing the magnitude of the anomalous skin effect for metals with long ℓ:

$$\alpha = \frac{3}{4}\mu_0\omega\left(\frac{1}{\rho\ell}\right)\ell^3 \tag{9.9}$$

$$R_\infty = R(\ell \to \infty) = \left(3\pi\left(\frac{\mu_0\omega}{4\pi}\right)^2\rho\ell\right)^{1/3} \tag{9.10}$$

$$R_s(\ell) \approx R_\infty\left(1 + 1.157\alpha^{-0.2757}\right) \tag{9.11}$$

High-RRR copper such as the high-purity oxygen-free copper saturates in the limit of R_∞ at cryogenic temperatures. At the three resonant frequencies of the 550 MHz, 1.3 GHz, and 2.0 GHz, the calculations above yield surface resistances of 0.830 mΩ, 1.44 mΩ, and 1.93 mΩ, respectively.

Given the geometry of the cavity and the surface resistance of the copper in each mode, the CST simulations yielded the reflection coefficients $\Gamma = \sqrt{P_r/P_f}$ for a range of coupler lengths at the three RF modes of the cavity. Figure 9.15 shows the results of these simulations; Γ is minimized at $L \approx 1.0$ cm, $L \approx 1.5$ cm, and $L \approx 2.25$ cm for modes 1, 2, and 3, respectively. For each value of Γ we can calculate P_{in}/P_f:

$$\frac{P_{in}}{P_f} = 1 - \frac{P_r}{P_f} = 1 - \Gamma^2 \tag{9.12}$$

Noting that in the steady state $P_{in} = P_{diss}$ and that $P_{diss} \approx P_{diss,outer}$, the energy in

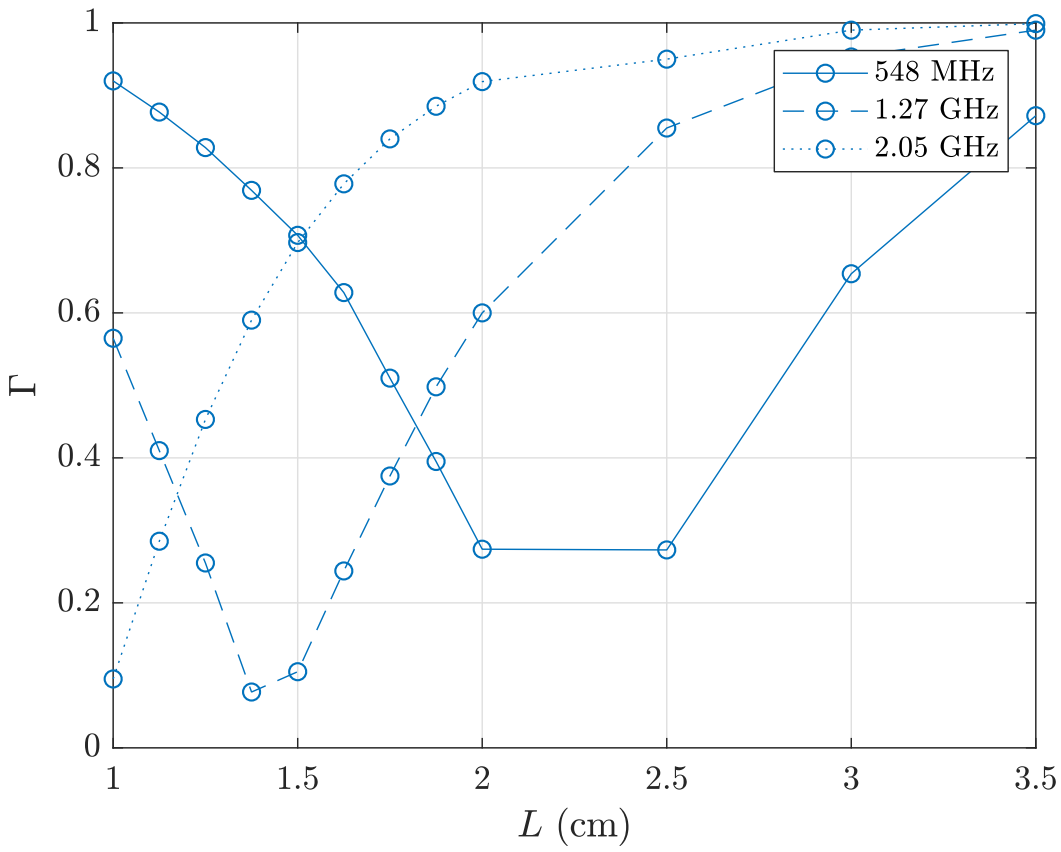

Figure 9.15: Simulated reflection coefficient Γ as a function of coupler length L in the three modes of the DC Field Dependence Cavity.

the cavity can then be determined as a function of the forward power:

$$\frac{U}{P_\mathrm{f}} = \frac{U}{P_\mathrm{in}}\frac{P_\mathrm{in}}{P_\mathrm{f}} \tag{9.13}$$

$$= \frac{U}{P_\mathrm{diss,outer}}\left(1-\Gamma^2\right) \tag{9.14}$$

$$= \frac{G_\mathrm{outer}}{\omega R_\mathrm{s,outer}}\left(1-\Gamma^2\right) \tag{9.15}$$

The CST simulations also yielded the field strength normalization coefficient $H_\mathrm{pk}/\sqrt{U}$ for each mode.

To simulate the power dissipated on the superconducting inner conductor, I used the SRIMP code[3] [Hal70] with $T_\mathrm{c} = 9.2$ K, $\Delta/k_\mathrm{B}T_\mathrm{c} = 1.81$, and $\ell = 20$ nm,

[3]See Sec. 3.2.

within the typical parameter ranges of doped niobium. Then, assuming uniform R_s over the surface of the inner conductor sample and rearranging Eq. 9.8, we can calculate the power dissipated on the inner conductor relative to the energy stored in the cavity:

$$\frac{P_{\text{diss,inner}}}{U} = \frac{\omega R_{\text{s,inner}}}{G_{\text{inner}}} \tag{9.16}$$

Here G_{inner} is again the "local geometry factor" of the inner conductor, determined from the RF simulations; the values for the three modes are given in Table 9.1.

To simulate the thermal conductivity κ of the niobium thermal finger, I used the Koechlin-Bonin parameterization with RRR=170 and $\ell_{\text{ph}} = 50$ μm as example parameters[4] [KB96]. From this I simulated the thermal gradient along the finger using its geometric properties (a hollow cylinder with outer radius $r_{\text{outer}} = 7$ mm, inner radius $r_{\text{inner}} = 5.5$ mm, and distance between thermometers $d = 10$ cm):

$$\Delta T = \frac{P_{\text{diss,inner}}\, d}{\kappa \pi \left(r_{\text{outer}}^2 - r_{\text{inner}}^2\right)} \tag{9.17}$$

Combining the above with Eqs. 9.15 and 9.16, we get the temperature gradient for a given forward power and reflection coefficient:

$$\Delta T = \frac{d}{\kappa \pi \left(r_{\text{outer}}^2 - r_{\text{inner}}^2\right)} \frac{R_{\text{s,inner}}}{G_{\text{inner}}} \frac{G_{\text{outer}}}{R_{\text{s,outer}}} \left(1 - \Gamma^2\right) P_{\text{f}} \tag{9.18}$$

The Cernox thermometers used in the thermal finger have an absolute calibration sensitivity of ±3 mK but are much more sensitive to relative changes in temperature; for the measurement equipment used in the Cornell SRF laboratory, the manufacturer reports a temperature resolution of $\delta T = 0.052$ mK [Laka,

[4]This RRR is somewhat high for reactor-grade niobium, but the thermal conductivity with these parameters is consistent with the measurements presented later in Sec. 9.5.3. The high-temperature vacuum braze outlined in Sec. 9.3.6 bake may have cleaned up the material in the thermal finger and raised the RRR.

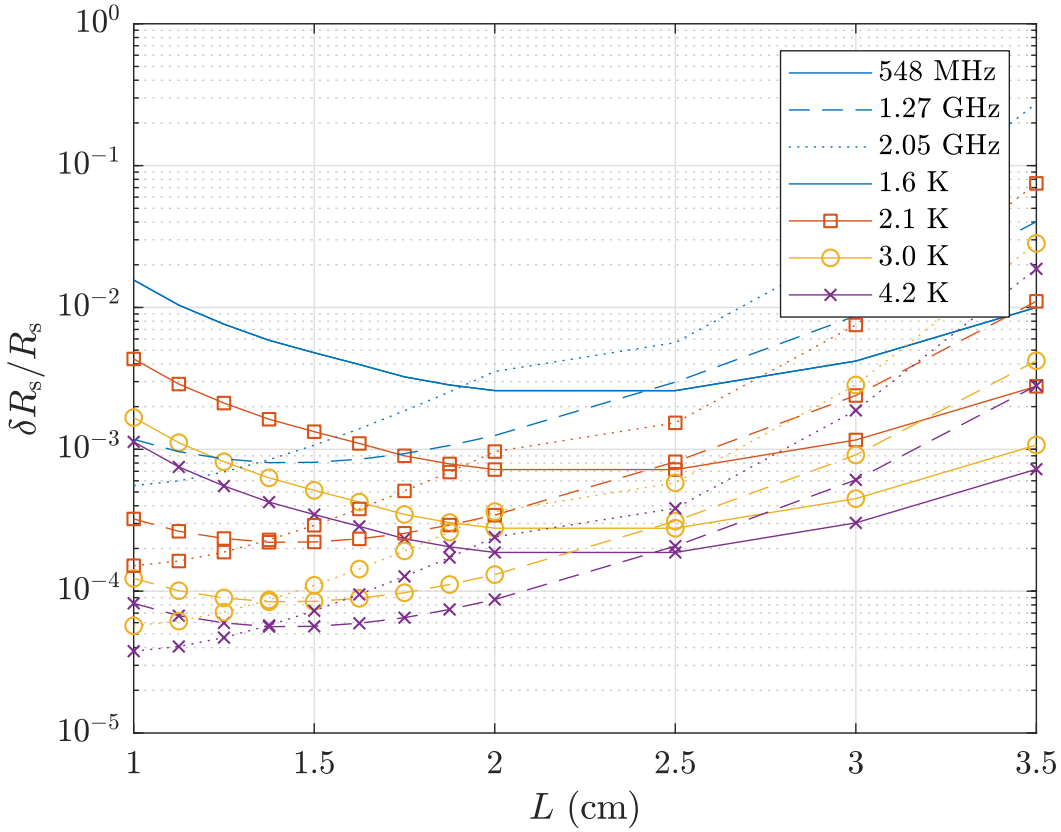

Figure 9.16: Simulation of the sensitivity of the measurement of relative change in surface resistance $\delta R_s/R_s$ with $P_f = 10$ W.

Lakb]. Considering Eq. 9.18, the sensitivity of the apparatus to relative changes in $R_{s,inner}$ is given by the following:

$$\delta R_{s,inner} = \delta T \frac{\kappa \pi \left(r_{outer}^2 - r_{inner}^2\right)}{d} \frac{G_{inner}}{G_{outer}} R_{s,outer} \left(1 - \Gamma^2\right)^{-1} P_f^{-1} \tag{9.19}$$

Figure 9.16 shows the results of the above calculation for varying length of the forward power coupler, simulated for the three modes of the cavity at a range of temperatures from 1.6 K to 4.2 K with $P_f = 10$ W. The sensitivity of each mode is optimized at different coupler lengths, due to the minimization of Γ seen above in Fig. 9.15. Based on these results, as a compromise between the three modes, we chose a coupler length of 1.5 cm; at that length the calculated relative sensitivity $\delta R_{s,inner}/R_{s,inner}$ is enough to measure changes of surface

resistance smaller than 0.5% in all modes.

It is important to note here that the sensitivity of *absolute* measurements of $R_{s,inner}$ is limited by the calibration uncertainty of ±3 mK as well as the uncertainties in the RF power measurements and in the calculated local geometry factors. These factors do not affect the *relative* measurements of $R_{s,inner}$ if the RF power is kept constant.

The length of the transmitted power probe was similarly optimized, but with a slightly different optimization criterion. As with the P_t probes used in standard vertical tests of single-cell cavities (see Sec. 3.4.2), this probe serves to measure the field level in the cavity and to excite the phase-locked loop used for RF testing. For the design, I wanted to ensure that Γ_t was greater than 0.98, corresponding to $\beta_t < 0.01$. This condition was satisfied by an off-the-shelf antenna assembly mounted so that its tip was set back from the flared section of the inner conductor by 6.5 mm.

For construction, we acquired an off-the-shelf antenna for the forward power coupler and modified it to fit the final design. We acquired the transmitted power probe antenna used in the design of that coupler. Both antennas were welded into vacuum flanges machined from copper plate stock. Figure 9.17 shows the completed forward and transmitted power coupler assemblies.

9.3.6 Sapphire Rod

The inner conductor is connected to the thermal finger by a sapphire rod; the rod serves to electrically isolate the two niobium pieces, preventing the propagation

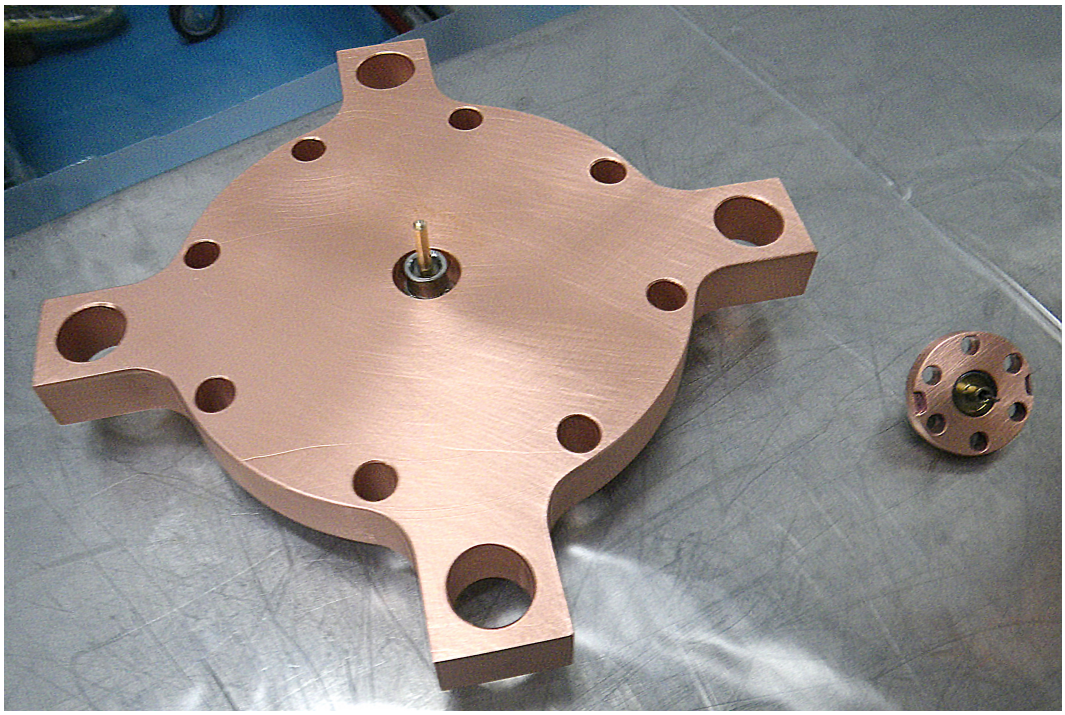

Figure 9.17: Completed forward power (left) and transmitted power (right) coupler flange assemblies.

of the RF modes down the thermal finger (such propagation could disrupt the calorimetric measurements).

Several key factors drive the choice of material for the rod. To serve its role in trapping RF modes inside the resonator region, the rod must be electrically insulating. To ensure that the inner conductor sample is not dramatically heated above the temperature of the thermal finger, the rod must have a thermal conductivity similar to or better than superconducting niobium. The rod must be a mechanically strong material that can support the weight of the inner conductor without deforming. The rod must be able to be brazed to niobium. Perhaps most importantly, the rod must not dissipate a significant amount of heat under RF excitation compared to the inner conductor sample; as such, it must have an extremely low loss tangent $\tan(\delta)$ at cryogenic temperatures. From simulations,

we chose as a threshold that the dissipated power in the rod should be less than 1% of the power dissipated on the inner conductor sample due to the surface resistance; this translates to $\tan(\delta) \approx 1 \times 10^{-9}$.

Artificial sapphire is considered to be one of the best dielectric materials for low-loss-tangent applications [BAP94]. At liquid helium temperatures and GHz-range frequencies, its $\tan(\delta)$ has been measured to be as low as $2{\times}10^{-10}$ [BAP94]. It has been reported in other SRF-related work [Pog11] that to minimize the loss tangent it is necessary to carefully clean the sapphire before use; in particular, exposing the sapphire to water could result in the growth of a layer of amorphous aluminum oxide, which has a much higher loss tangent of approximately $2{\times}10^{-3}$ [Ott15].

We implemented the sapphire cleaning procedure reported in N. Pogue's dissertation[5] [Pog11] in the preparations for construction of the cavity. Our implementation of the procedure went as follows:

1. Immerse sapphire piece in a 25% nitric acid solution in a beaker; ultrasonically clean for 5 minutes.
2. Heat nitric acid solution with immersed sapphire until it boils, then remove from heat and allow to cool for 20 minutes.
3. Remove sapphire from solution and rinse with deionized (DI) water.
4. Place sapphire in a beaker of acetone; ultrasonically clean for 5 minutes.
5. Remove sapphire from acetone and rinse with isopropanol. Place sapphire in a beaker of isopropanol and ultrasonically clean for 5 minutes.

[5] It appears that this procedure originally came from NASA/JPL but was not published and instead reached the author of [Pog11] by private communication from R. Wang.

6. Remove sapphire from isopropanol and rinse with 200-proof ethanol. Place sapphire in a beaker of 200-proof ethanol and ultrasonically clean for 5 minutes.
7. Keep sapphire piece immersed in 200-proof ethanol until needed.
8. Dry sapphire piece with dry nitrogen gas before use.

After cleaning, we affixed the sapphire rod to the niobium thermal finger and to the NbTi inner conductor mounting screw in a simultaneous direct vacuum braze. For the braze filler we used Nicoro (BAu3), a commercially available gold-based brazing material with solidus temperature 1000 °C and liquidus temperature 1030 °C. We performed the braze in vacuum at the 1×10^{-9} Torr level, adapting a standard procedure from the literature [WTW10]:

1. Ramp to 500 °C (15 minutes) and equilibrate (1 hour).
2. Ramp to 850 °C (5 minutes) and equilibrate (1 hour).
3. Ramp to 980 °C (5 minutes) and equilibrate (30 minutes).
4. Ramp above liquidus to 1060 °C (5 minutes) and soak (35 minutes).
5. Ramp back to room temperature.

An initial prototype braze showed good adhesion, rigidity, and tensile strength to the brazes [MGHL19]; after that successful test, we used the same cleaning and braze procedures for the final part. Figure 9.18 shows the sapphire rod brazed into place on the thermal finger assembly.

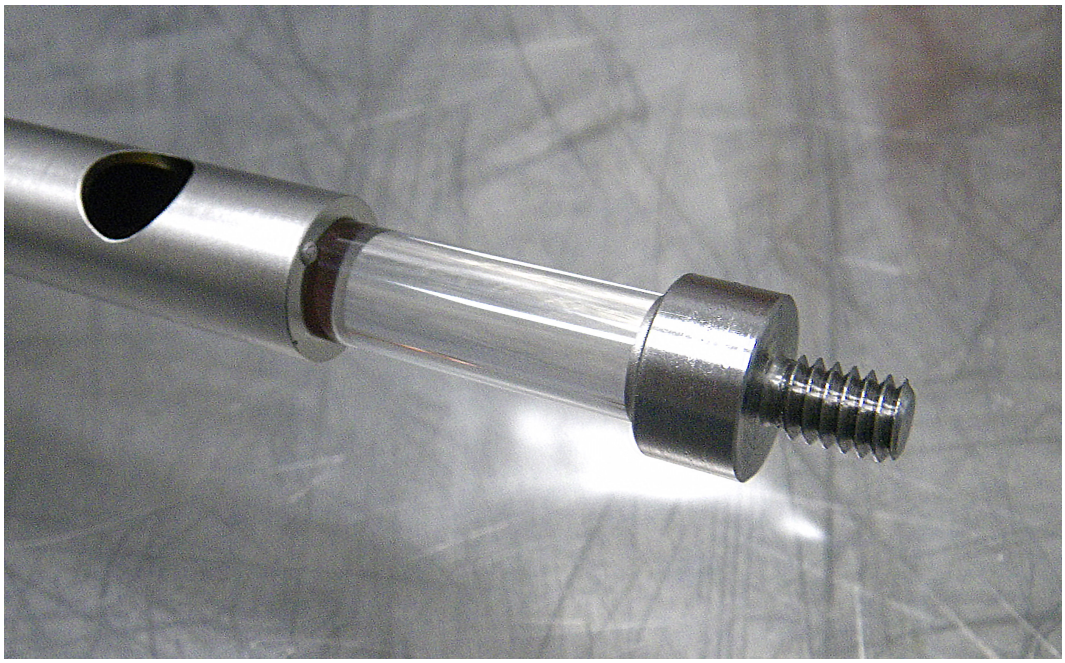

Figure 9.18: Close-up image of the sapphire rod installed in the thermal finger assembly.

9.3.7 Inner Conductor Sample

The design of the inner conductor sample in the DC Field Dependence Cavity is relatively straightforward. Most of its length is a cylinder of radius 7 mm; this constant radius encourages uniformity of the externally applied DC magnetic field on the surface of the inner conductor. The "tip" of the sample is rounded to prevent field enhancement, as is the edge of the flared portion at the other end of the sample. The flare serves geometrically to trap the quarter-wave family of RF modes in the resonator.

The sample is designed to be mounted to the thermal finger by a NbTi mounting screw attached to the sapphire rod. The flared end of the sample features a socket on the face aligned away from the RF cavity with a threaded blind hole. During assembly of the cavity, the sample is threaded onto the mounting

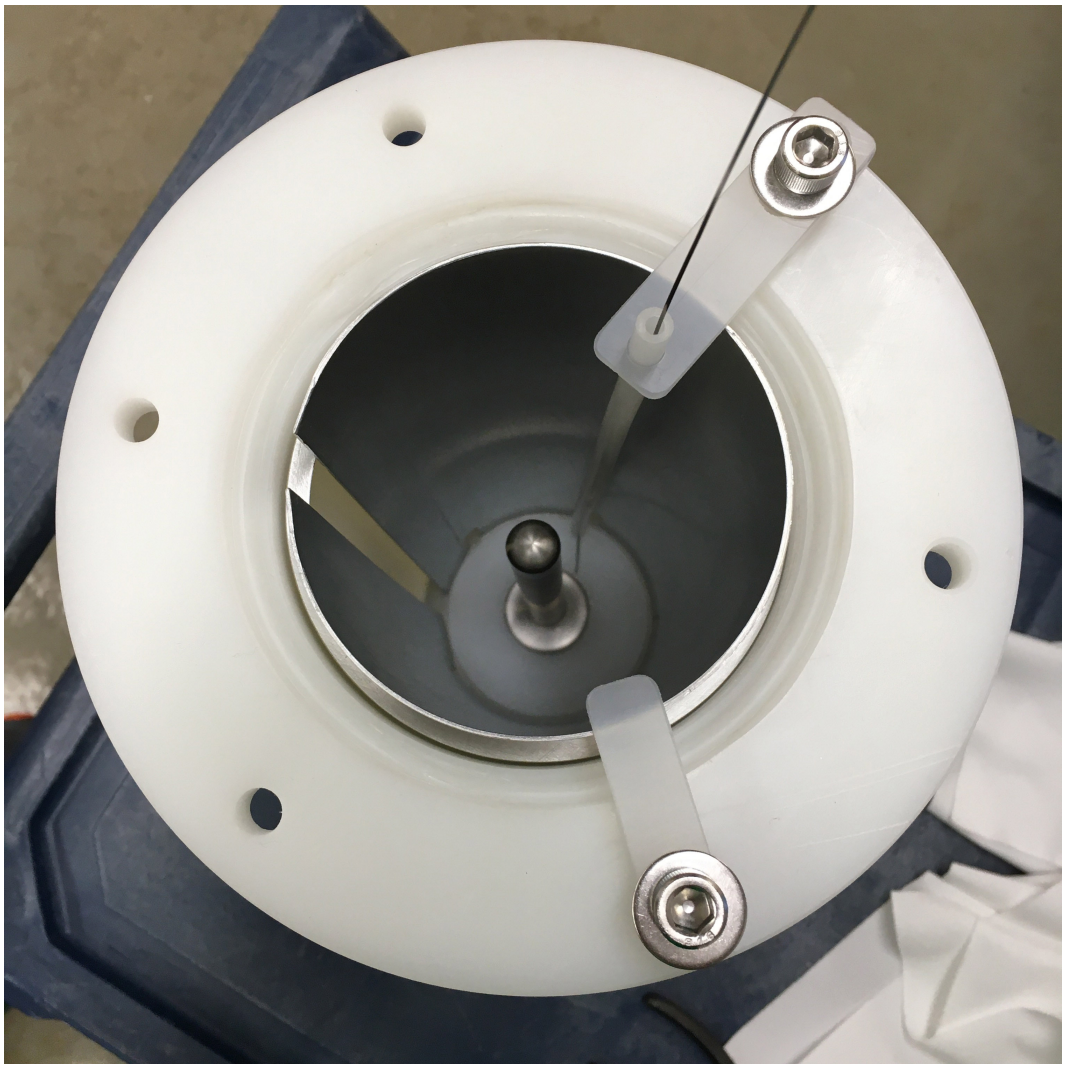

Figure 9.19: A niobium inner conductor sample for the DC Field Dependence Cavity mounted in the custom fixture for chemical etching.

screw.

The initial sample for commissioning the new cavity was machined from high-RRR fine-grain niobium bar stock. After machining, the preparation procedure for the sample followed a standard recipe used at Cornell for niobium single-cell cavities. The piece was first lightly scrubbed with soap and deionized water to remove machining residue. After this, we performed a vertical electropolish of the sample in a custom-built acid bath fixture; Fig. 9.19 shows

the inner conductor sample mounted in the custom fixture. This VEP removed 100 μm from the surface over approximately 12 hours. The VEP gave the sample a near mirror finish. After VEP, we cleaned the sample in an ultrasonic bath of detergent and deionized water. We followed this with a second ultrasonic bath in deionized water with no detergent. For the ultrasonic cleaning, we suspended the sample in the bath by threading a clean silver-plated support screw into the mounting point, wrapping clean stainless steel wire around the screw, and holding the wire with a support structure over the bath of deionized water. This process ensured that no metal parts touched the RF surface of the inner conductor sample, as such contact might result in detrimental surface scratches or metal contamination. After cleaning, we dried the sample with dry nitrogen gas and sealed it in a plastic bag for transport to the furnace.

We then performed a vacuum degas bake of the inner conductor sample at 800 °C for five hours. Figure 9.20 shows the inner conductor in the furnace before the bake. After the bake, the furnace was vented with filtered dry air and the sample was removed and sealed in a new plastic bag for transport to the clean room for assembly. Figure 9.21 shows the inner conductor just before the full apparatus was assembled.

9.3.8 Instrumentation Feedthrough Weldment

One final detail of the DC Field Dependence Cavity is the instrumentation and vacuum pumping structure located on the other side of the thermal finger from the RF resonator. As mentioned earlier, this component features a 19-pin bayonet vacuum instrumentation feedthrough connecting the internal instrumenta-

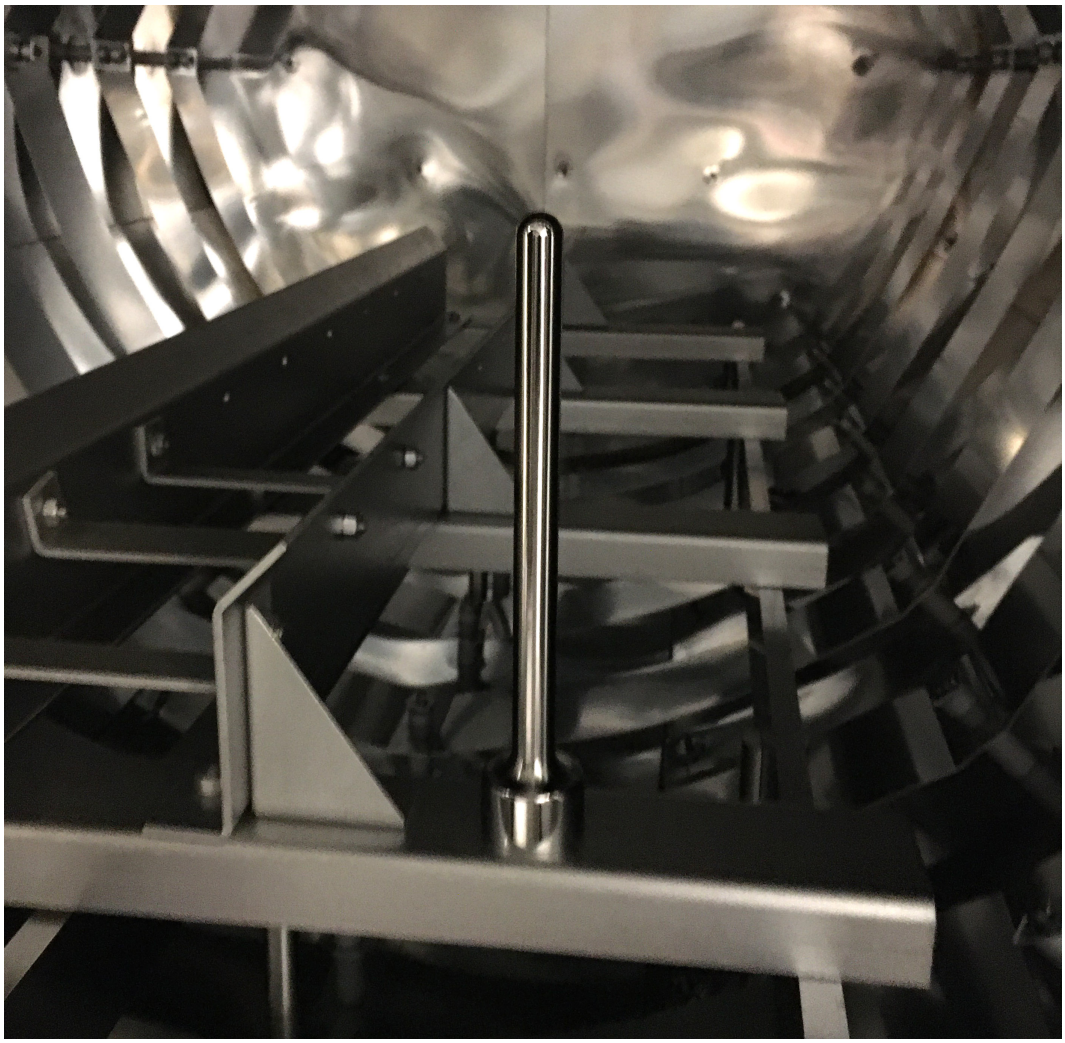

Figure 9.20: A niobium inner conductor sample for the DC Field Dependence Cavity installed in the vacuum furnace before an 800 °C degas bake.

tion to the external measurement system and is mounted to the thermal finger assembly by vacuum flange. The weldment also features a second line where an all-metal angle valve is mounted; a hose can be connected to this valve for pumping the interior of the cavity to vacuum.

We designed the feedthrough weldment to fit inside the bore of the superconducting solenoid, which must be mounted onto the apparatus after the assembly of the vacuum space. This is meant to preserve the cleanliness of the

Figure 9.21: A niobium inner conductor sample for the DC Field Dependence Cavity after chemical processing and vacuum degas bake, just before assembly into the cavity.

RF surfaces in the cavity, protecting it from any potential dirt or dust on the difficult-to-clean solenoid. The vacuum components are first assembled with the angle valve closed. After the solenoid is mounted, the angle valve is connected to the vacuum pumping system and opened again.

For construction, the weldment was built from 316-grade non-magnetic stainless steel. The weldment is connected to the cavity by an indium seal. The 19-pin feedthrough and angle valve are connected by knife-edge copper gasket flanges. Figure 9.22 shows the weldment, angle valve, and feedthrough prior to

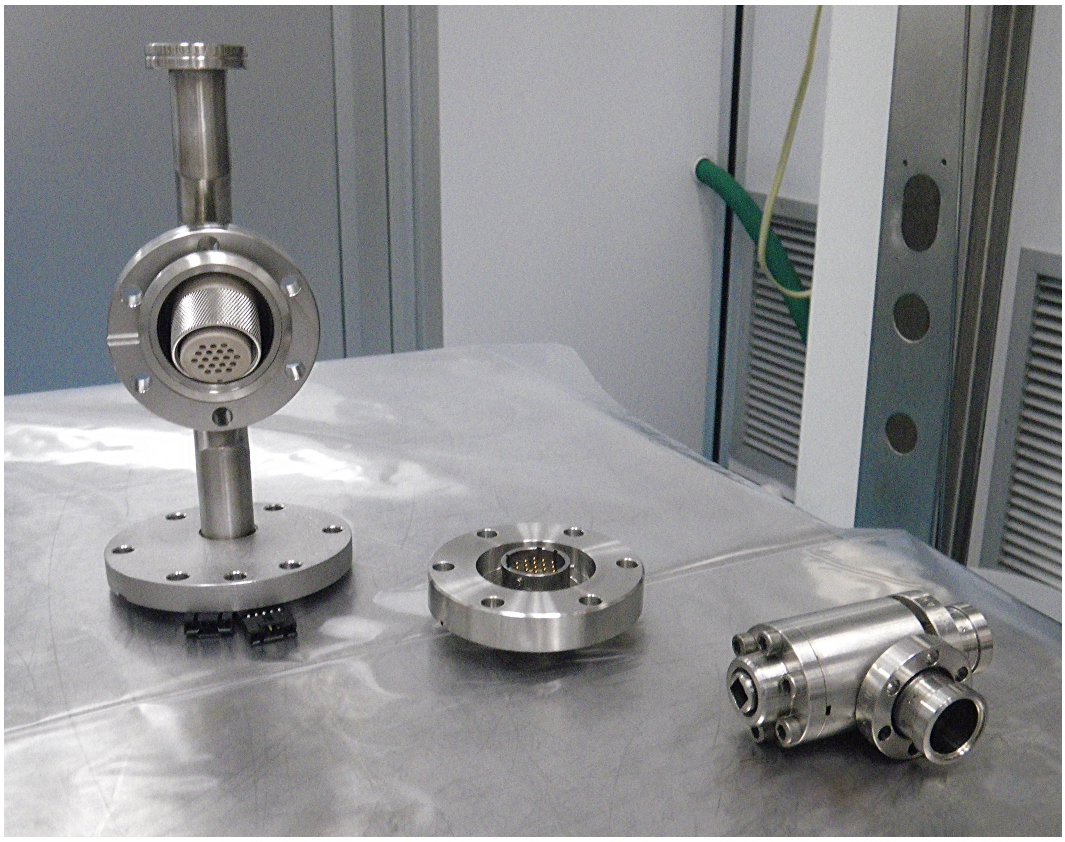

Figure 9.22: The instrumentation feedthrough weldment, instrumentation feedthrough, and all-metal angle valve for the DC Field Dependence Cavity.

the assembly of the full cavity structure.

9.4 Assembly

After the component parts of the DC Field Dependence Cavity were constructed, cleaned, and (when relevant) checked for leak-tightness, we transported them to the clean room for assembly of the full structure. Figure 9.23 shows the component vacuum pieces before assembly.

All of the vacuum connections of the cavity, excluding the 19-pin

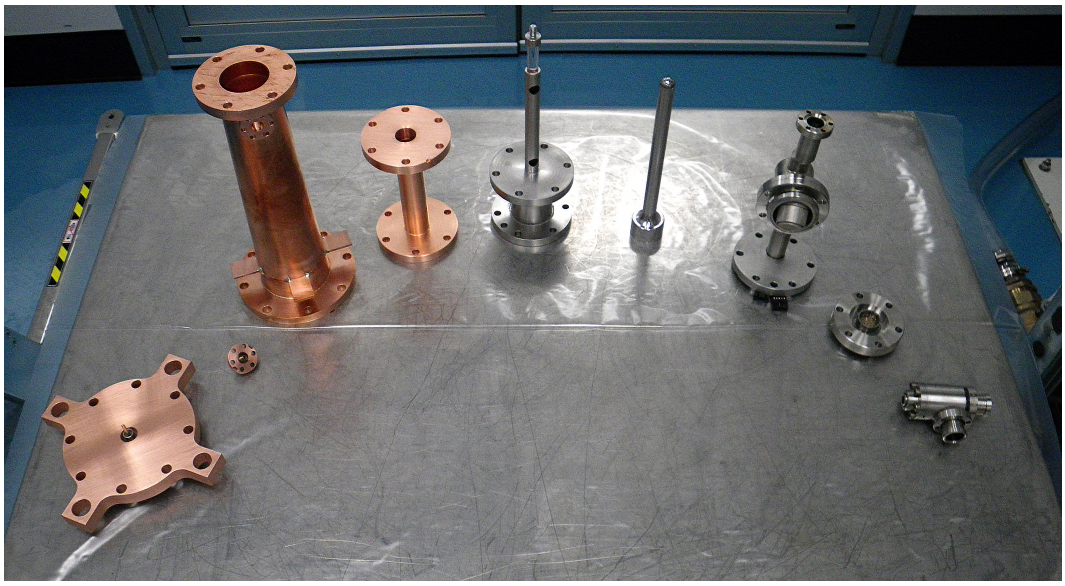

Figure 9.23: The component parts of the DC Field Dependence Cavity gathered in the clean room before assembly.

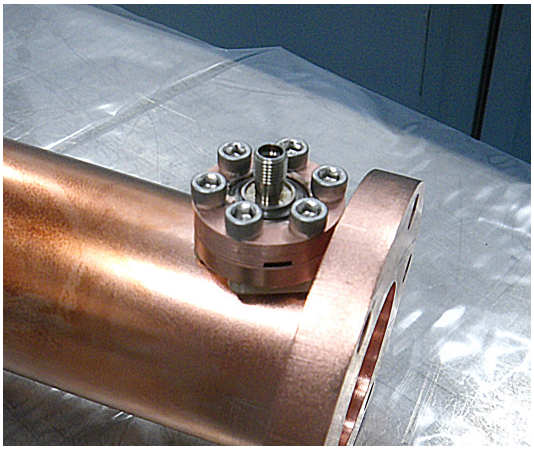

(a) P_f port

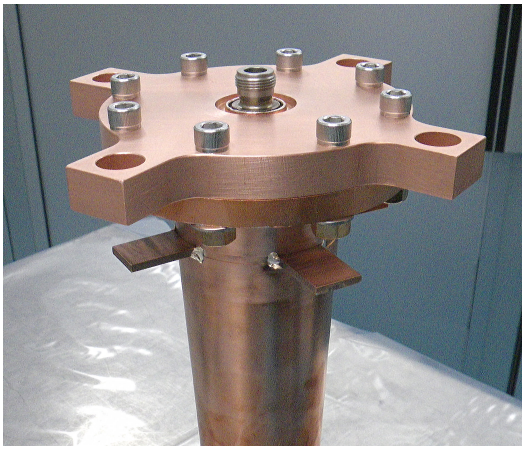

(b) P_f port

Figure 9.24: Sealed transmitted and forward power ports of the outer conductor.

feedthrough flange and the connection to angle valve, are indium wire seals. I used indium wire 0.02" (0.5 mm) in diameter for these connections. To seal off the cavity, I first installed the transmitted power coupler and forward power coupler flanges onto the conical outer conductor. Figure 9.24 show these two seals after completion. Next, I connected the niobium thermal finger assembly

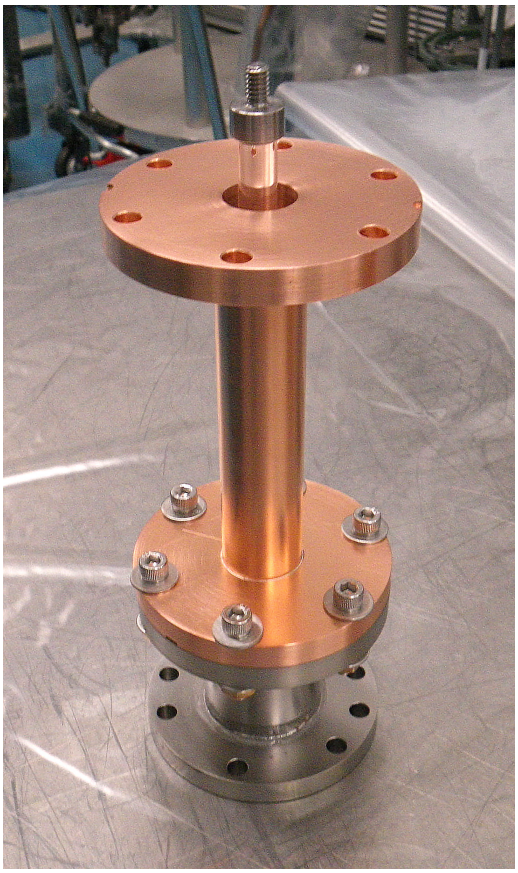

(a) Coaxial copper tube attached to the thermal finger assembly.

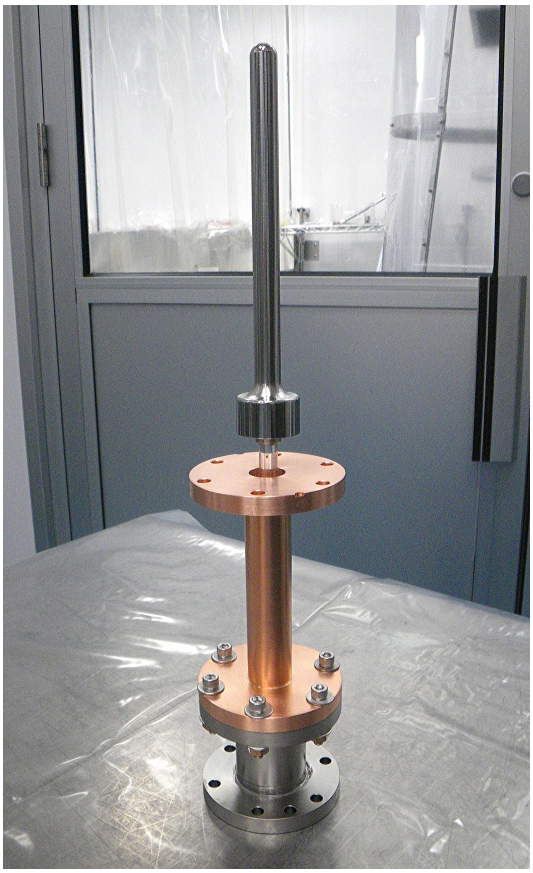

(b) Inner conductor mounted on NbTi screw, with visible misalignment.

Figure 9.25: Intermediate assembly stages of the thermal finger and inner conductor components of the DC Field Dependence Cavity.

to the cylindrical copper tube, as shown in Fig. 9.25a. I then attached the niobium inner conductor sample onto the mounting screw on the thermal finger assembly.

After the inner conductor was installed, there appeared to be a misalignment issue in the construction of the cavity, with the inner conductor tilted at approximately 0.5° with respect to the copper cylinder. Figure 9.25b shows the installed inner conductor and demonstrates the misalignment issue: the sapphire rod is not centered with respect to the opening in the copper tube. After noticing the misalignment, I continued with the assembly in the hopes that the small degree

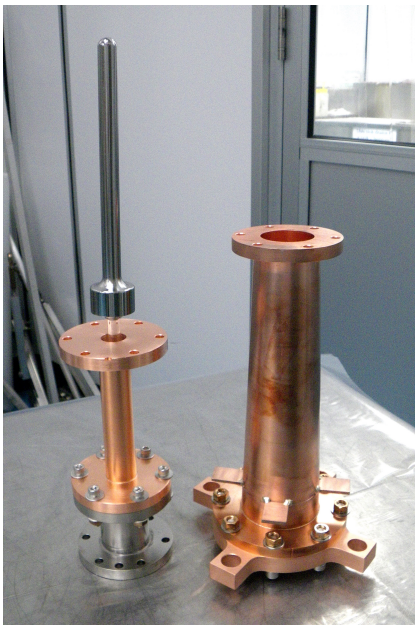

(a) Inner and outer conductor assemblies before joining.

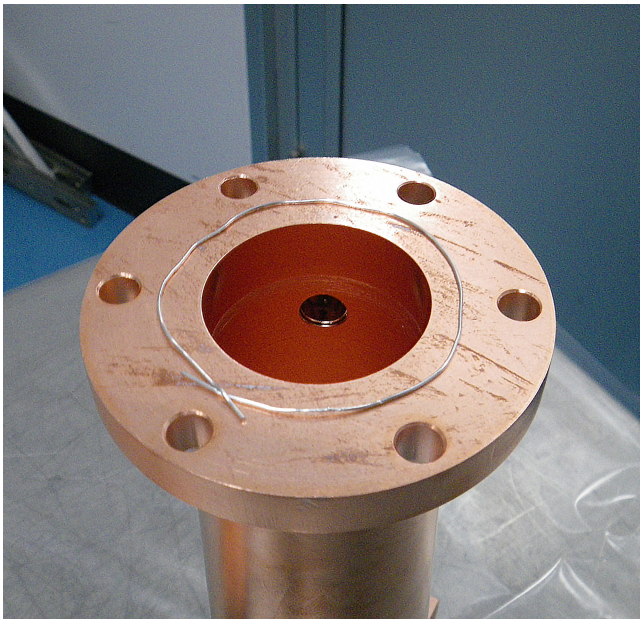

(b) Closeup of indium wire gasket.

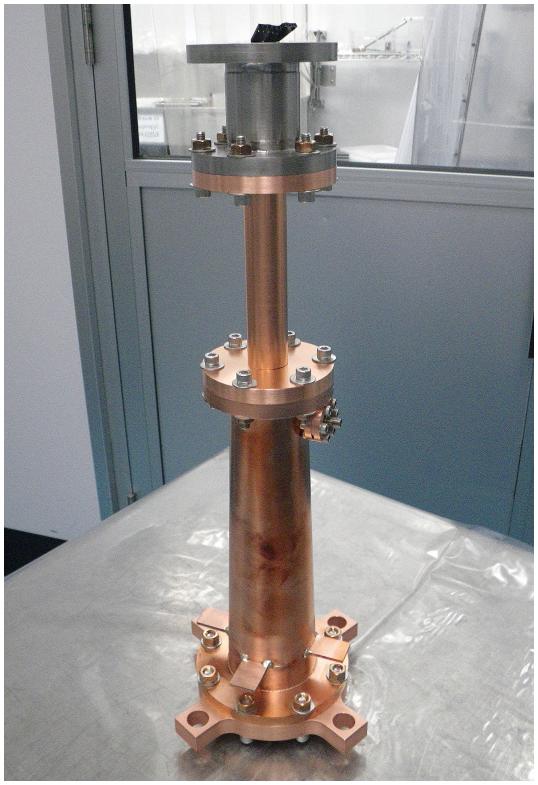

(c) Joined inner and outer conductor assemblies.

Figure 9.26: Intermediate assembly stages of the thermal finger and inner conductor components of the DC Field Dependence Cavity.

of misalignment would only result in a slight perturbation of the RF fields and not greatly affect the commissioning measurements. In future assemblies of the apparatus, we might make a slight adjustment to the thermal finger or to the copper tube to realign the inner and outer conductors.

Once the inner and outer conductor assemblies were sealed, I attached them at the interface between the cylindrical and conical outer parts. Figure 9.26a shows these parts side-by-side before assembly, and Fig. 9.26b shows a close-up image of the indium wire installed on the outer conductor flange before completing the seal. Figure 9.26c shows the combined assembly after the indium seal was completed. Also visible in Fig. 9.26c are the instrumentation clips in the thermal finger assembly.

The main interior of the cavity having been completed, I next worked on the instrumentation feedthrough. I began by installing the 19-pin feedthrough connection, sealed by a 2-3/4" ConFlat knife-edge copper gasket flange. I then installed the indium wire gasket onto the thermal finger flange, connected the clips between the thermal finger instrumentation and the instrumentation feedthrough weldment, and closed and sealed the connection. Figure 9.27a shows the feedthrough weldment installed onto the assembly. Finally, I attached the all-metal angle valve onto the feedthrough weldment, sealed with a 1-1/3" Mini ConFlat knife-edge copper gasket flange. Figure 9.27b shows the installed angle valve.

This completed the assembly of the vacuum components of the DC Field Dependence Cavity apparatus. Continuing onward, I closed the angle valve to seal the interior of the cavity and installed non-magnetic silicon-bronze support rods to prepare for mounting the solenoid and installing the full assembly

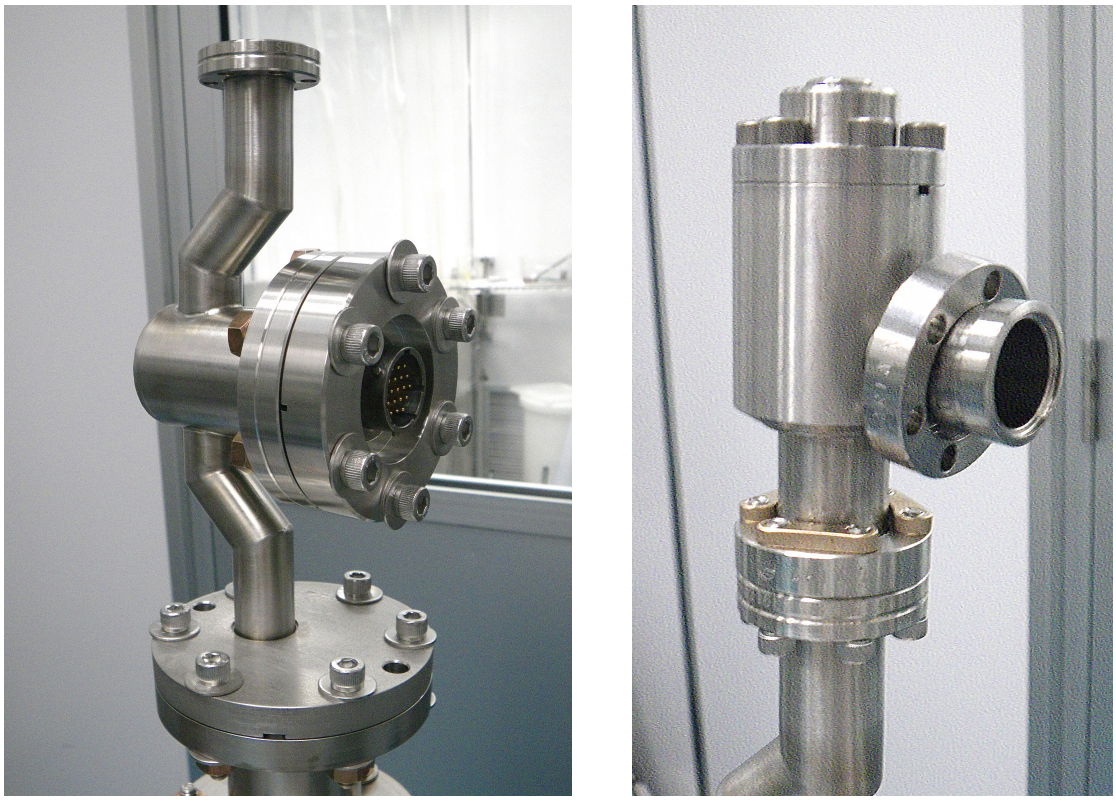

(a) Feedthrough weldment (b) All-metal angle valve

Figure 9.27: Vacuum and instrumentation feedthrough components installed onto the DC Field Dependence Cavity.

onto the cryogenic test insert prepared for the apparatus. Figure 9.28 shows the completed vacuum assembly with support rods.

I then moved the cavity to the equipment lock area of the clean room to install the superconducting solenoid. The support rods ensure that the solenoid is aligned axially with the cavity, and the tabs on the outer conductor ensure the correct positioning of the solenoid along the length of the cavity. Figure 9.29a shows the solenoid installed onto the assembly. Next, I installed a mounting bracket onto the assembly, as shown in Fig. 9.29b, and mounted the assembly onto the test insert. I connected the angle valve to the vacuum system on the test insert by a metal vacuum hose with Mini ConFlat and VCR metal gasket fit-

Figure 9.28: The fully assembled vacuum components of the DC Field Dependence Cavity apparatus with silicon-bronze support rods.

tings. Figure 9.29c shows the assembly mounted onto the insert with all vacuum connections completed.

After the assembly was complete, I opened the angle valve and used a turbo pump to pull vacuum inside the cavity, bringing the pressure to the 1×10^{-8} Torr level. I performed a leak check by spraying helium gas onto each of the indium seals, ConFlat seals, VCR fittings, brazes, and welds, reading the helium signal from a residual gas analyzer (RGA) connected to the pumping system. The procedure showed that the cavity was indeed leak-tight. Once this was completed,

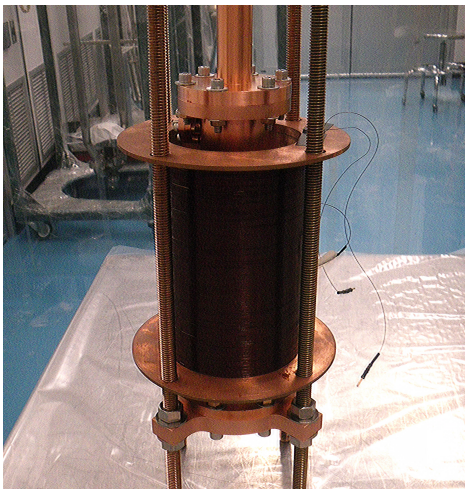

(a) Solenoid

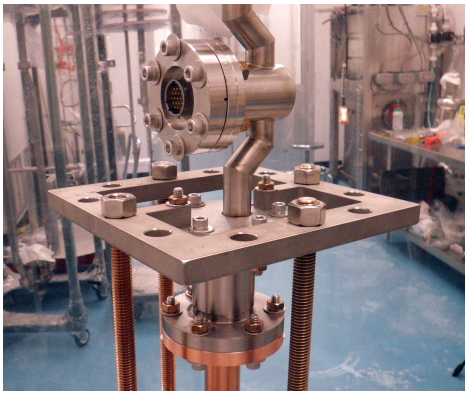

(b) Mounting bracket

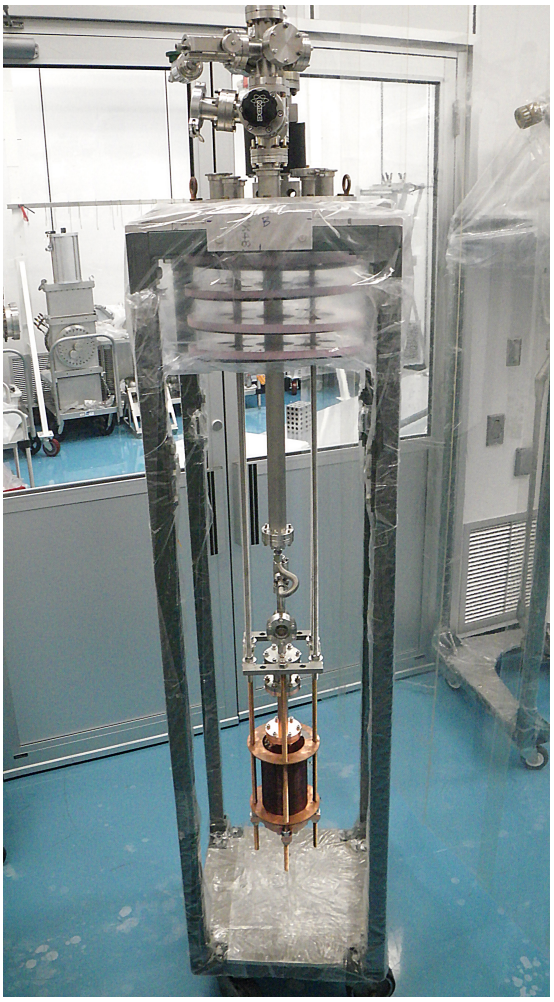

(c) Installed onto test insert

Figure 9.29: Final steps of the assembly of the DC Field Dependence Cavity.

I disconnected the pumping system and continued to pump the cavity using an ion pump installed on the test insert.

Outside the clean room, I installed two Cernox thermometers for reading the temperature of the exterior of the cavity, forward and transmitted power cables, a Hall probe for measuring the magnitude of the field strength of the solenoid, and the magnet power supply cable. I then installed the superconducting magnetic shielding around the cavity and solenoid. Finally, I installed the exterior instrumentation, including two flux-gate magnetometers for mea-

suring the magnetic field strength outside the shielding "can", with one sensor mounted on the exterior of the can and one mounted two inches above the can on one of the support rods. Figure 9.30 shows the installed shielding can and exterior instrumentation.

9.5 First Commissioning Test

9.5.1 Cooldown

After the assembly of the DC Field Dependence Cavity was completed, the apparatus was ready for the first commissioning test. I installed the insert into the cryogenic dewar, connected the instrumentation to the data acquisition system, and began the standard vertical test procedures for pumping the cryogenic dewar to vacuum and filling with liquid helium.

The exterior of the cavity cooled rapidly as cold helium gas flowed past during the helium fill. The interior sensors on the thermal finger, cooled by conduction instead of convection, cooled more slowly to approximately 120 K as the exterior of the cavity reached 5 K. As the level of liquid helium in the dewar reached the bottom of the RF cavity, the cooling rate increased due to the increased thermal conductivity of liquid helium compared to gaseous helium. As the exterior stabilized at 4.2 K, the thermal finger sensors cooled slowly to that equilibrium temperature. When the niobium inner conductor cooled below its critical temperature of approximately 9.2 K, its heat capacity dramatically decreased; with the decreased thermal mass, the thermal finger thermometers rapidly cooled to the bath temperature of 4.2 K.

Figure 9.30: The DC Field Dependence Cavity installed on the vertical test insert with superconducting magnetic shielding can and external instrumentation.

At one point during the cooldown, as the dewar filled with liquid helium and surrounded the cavity, the pressure in the cavity spiked upwards and tripped off the ion pump. We connected a turbo pump to the cavity to pump out the leaking helium. The pressure in the cavity peaked in the range of 1×10^{-3} Torr before we connected the turbo pump, indicating a small leak. The level of the liquid helium in the dewar at the time of the leak indicated that the leak took place at the VCR fittings of the vacuum hose connected to the angle valve. The turbo pump pressure stabilized near 1×10^{-5} Torr; because of the high pump impedance of the narrow vacuum lines in the instrumentation feedthrough weldment as well as the cryopumping action of the cavity itself, the pressure in the cavity was likely closer to 1×10^{-3} Torr. Furthermore, there was likely a layer of gas adsorbed onto the cavity wall. We limited the remainder of the commissioning test to operation at 4.2 K.

9.5.2 Reflection and Transmission Coefficients

With the cavity fully cooled to 4.2 K, we used a network analyzer to measure the reflection and transmission coefficients Γ and T for the three modes. These coefficients are defined as follows:

$$\Gamma = \sqrt{\frac{P_\mathrm{r}}{P_\mathrm{f}}} \tag{9.20}$$

$$\mathrm{T} = \sqrt{\frac{P_\mathrm{t}}{P_\mathrm{f}}} \propto \sqrt{\frac{U}{P_\mathrm{f}}} \tag{9.21}$$

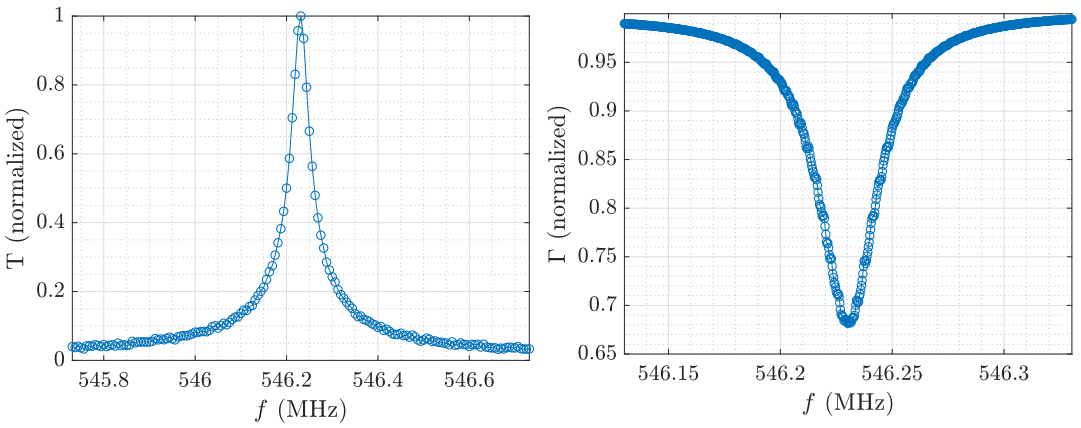

(a) Transmission coefficient

(b) Reflection coefficient

Figure 9.31: Reflection and transmission coefficients for the first mode of the DC Field Dependence Cavity.

Measurements of Γ and T can be used for estimates of β_e and Q_L for the cavity [PHK98]:

$$\beta_e = \frac{1 \mp \Gamma}{1 \pm \Gamma} \tag{9.22}$$

$$Q_L = f_r/\Delta f \tag{9.23}$$

In Eq. 9.22, the upper signs are used when the cavity is undercoupled and the lower signs are used when the cavity is overcoupled. In Eq. 9.23, f_r is the resonance frequency (where T is maximized) and Δf is the full-width half-maximum of the resonance peak of $U \propto \mathrm{T}^2$ with respect to frequency.

Figure 9.31a shows the transmitted power coefficient T, normalized to a maximum of 1, as a function of excitation frequency. The resonance frequency of the first mode of the cavity was measured to be 546 MHz. The full-width half-maximum of the transmitted power curve was 35.5 kHz. From these, we can estimate a loaded quality factor for the cavity $Q_L = 1.54 \times 10^4$.

The reflected power coefficient Γ for the first mode is shown in Fig. 9.31b. At the resonance frequency, Γ was measured to be 0.68. This corresponds to a

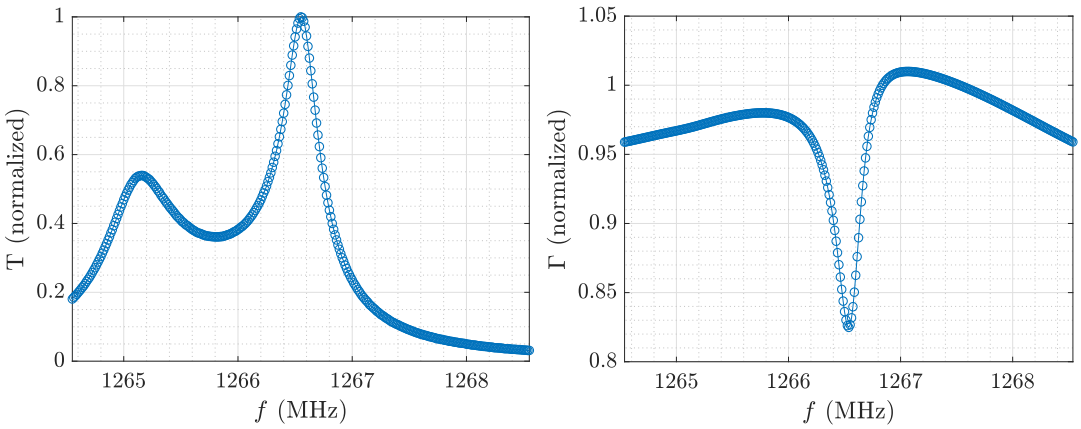

(a) Transmission coefficient

(b) Reflection coefficient

Figure 9.32: Reflection and transmission coefficients for the second mode of the DC Field Dependence Cavity.

coupling factor of $\beta_e = 5.3$ in the overcoupled case and $\beta_e = 0.19$ in the undercoupled case. By Eq. 3.73, the above measurements of Q_L and β_e yield $Q_0 = 9.7 \times 10^4$ in the overcoupled case and $Q_0 = 1.8 \times 10^4$ in the undercoupled case.

In the second mode, we observed some apparent mode splitting in the measurement of T, as shown in Fig. 9.32a. The measurement of Γ, shown in Fig. 9.32b, found only one resonance, corresponding with the higher of the two transmitted power peaks. For this peak, we measured the resonance frequency to be 1.267 GHz and the full-width half-maximum of T to be 289 kHz, leading to an estimated $Q_L = 4.38 \times 10^3$. At the resonant frequency, Γ was 0.83, corresponding to $\beta_e = 10$ in the overcoupled case and $\beta_e = 0.10$ in the undercoupled case. These yield $Q_0 = 4.8 \times 10^4$ in the overcoupled case and $Q_0 = 4.8 \times 10^3$ in the undercoupled case.

In the third mode, we again observed mode splitting in the measurement of T, as shown in Fig. 9.33a. Again, the measurement of Γ found only one resonance peak, as shown in Fig. 9.33b. Here the "true" resonance was the lower of the two peaks observed in T. At that peak, the resonance frequency

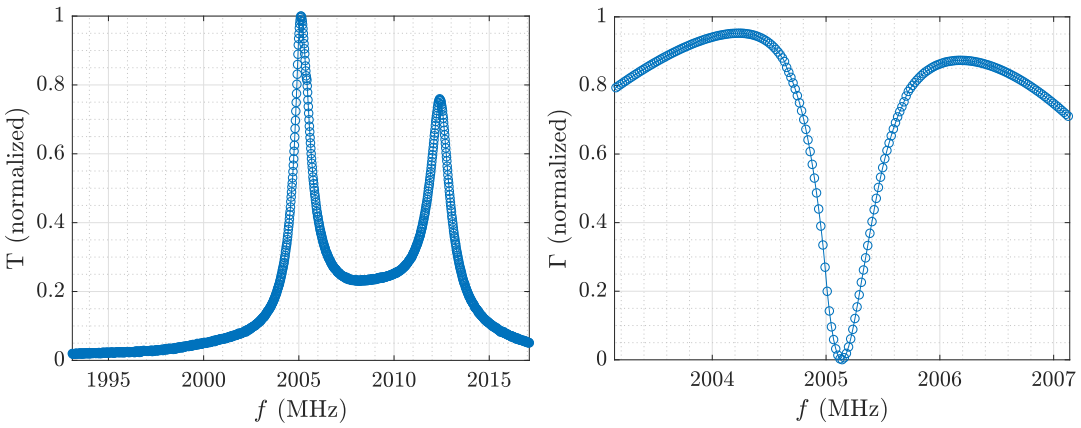

(a) Transmission coefficient (b) Reflection coefficient

Figure 9.33: Reflection and transmission coefficients for the third mode of the DC Field Dependence Cavity.

was 2.005 GHz; the full-width half-maximum of T was 443 kHz, yielding an estimate of $Q_L = 2.88 \times 10^3$. At the resonance frequency, Γ was 2.4×10^{-3}, corresponding to $\beta_e = 1.05$ in the overcoupled case and $\beta_e = 0.95$ in the undercoupled case. These yield $Q_0 = 5.9 \times 10^3$ in the overcoupled case and $Q_0 = 5.6 \times 10^3$ in the undercoupled case.

These coupling factors are somewhat different from the expected coupling factors of 0.13, 1.2, and 4.5 expected for modes 1, 2, and 3 from the CST simulations, though they are all close enough to unity coupling that the RF amplifier system in the Cornell SRF laboratory will be powerful enough to supply peak RF surface magnetic fields in the range of 1-5 mT on the inner conductor. The mismatch may be due to systematic errors in the CST software.

For the first and second modes, the calculations of Q_0 in the overcoupled cases indicate $R_{s,outer} = 1.2$ mΩ and 5.7 mΩ, respectively, reasonable values for cryogenic copper (if a bit higher than the expected values used above in Sec. 9.2.1). For the third mode, the calculated Q_0 is quite low, nearly one tenth the value of Q_0 in the second mode. If all the intrinsic losses are on the cop-

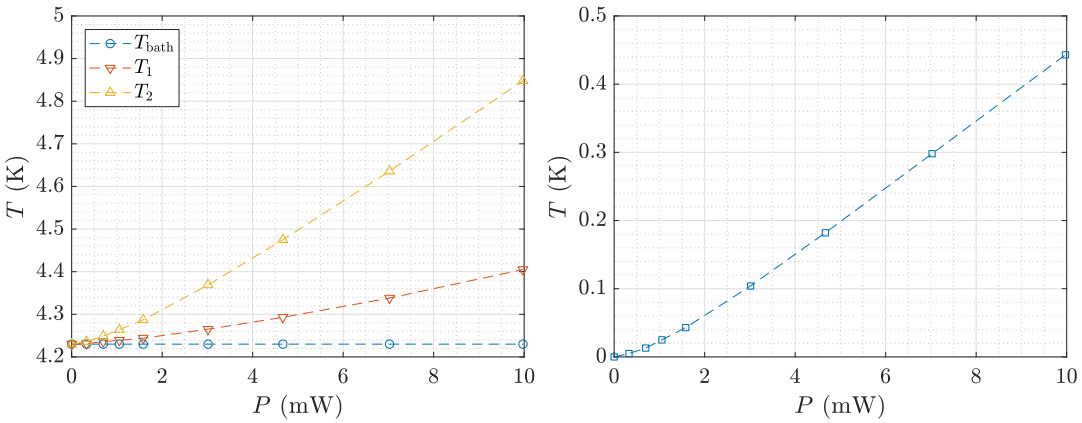

(a) Sensor temperatures

(b) Thermal finger gradient

Figure 9.34: Temperature measurements of the thermal finger and bath thermometers as a function of the applied power on the calibration heater.

per outer conductor, this corresponds to $R_{\text{s,outer}} = 72$ mΩ, high even for room-temperature copper. This puzzling feature must be investigated further.

9.5.3 Heater Calibration

After taking measurements of Γ and T, I next moved onto calibration measurements of the heater. Figure 9.34a shows the temperatures of the helium bath and the two internal thermometers in the thermal finger assembly as a function of power applied on the heater, and Fig. 9.34b shows the temperature difference ΔT on the thermal finger as a function of the heater power. The gradient increases approximately linearly with heater power, as is expected from the standard thermal gradient expression given in Eq. 9.17. The nonlinearity in ΔT vs. P_{heater} may indicate that the system was not fully equilibrated for the measurements and that the appropriate values of T_1, T_2, and ΔT are somewhat higher than those presented in Fig. 9.34.

We can estimate κ for the thermal rod to be 30-40 W/m K between 4 K and 5 K. This is higher than expected for reactor-grade niobium, which typically has RRR in the range of 20-50; as shown in Fig. 3.11, we might expect $\kappa \approx 10$ W/m K for reactor-grade niobium. As mentioned in Sec. 9.3.5, the vacuum bake for the braze may have improved the RRR of the thermal finger assembly and thus improved the thermal conductivity.

9.5.4 Commissioning at 1.3 GHz

Once the heater calibration was completed, we progressed on to commissioning in the 1.3 GHz mode under RF power with the phase-locked loop circuit. I began with no DC field from the superconducting solenoid.

We encountered some noise issues in the measurements of reflected power, exemplified in Fig. 9.35. This noise included a number of spikes that made it difficult to make continuous Q vs. H measurements. The traditional measurements of Q_L clustered around $4.28 \pm 0.10 \times 10^3$, consistent with the value calculated from the network analyzer measurements of T.

The measurements of the main coupling factor β_e were also subject to the noise in the reflected power measurements, resulting in high uncertainty, with $\beta_e = 5.8 \pm 3.3$. This measurement is somewhat lower than the calculation of β_e in the overcoupled case from the network analyzer measurements of Γ. Using the RF power measurements of β_e and Q_L yields an intrinsic quality factor $Q_0 = 2.9 \pm 1.4 \times 10^4$, also lower than the calculation from the network analyzer measurements.

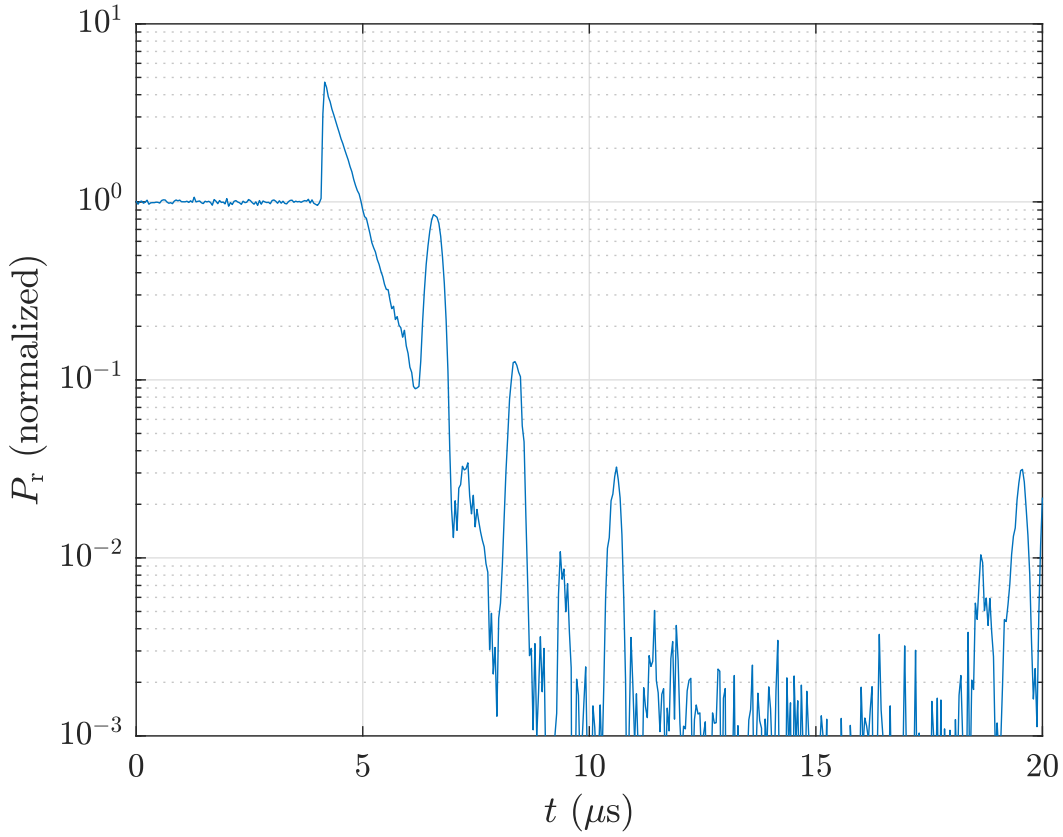

Figure 9.35: Example reflected power decay measurement of the DC Field Dependence Cavity, highlighting the noise issues encountered during the first commissioning test.

We then excited a steady RF field in the cavity. Based on the power measurements and calibrated attenuation factors of the cables in the RF circuit as well as the above RF power measurements of Q_0 and β_e, the peak magnetic field on the inner conductor was $\mu_0 H_{pk} = 10 \pm 3$ μT. Using the network analyzer measurements of β_e, Q_L, and Q_0 with the RF measurement of P_f also yields $\mu_0 H_{pk} = 10$ μT.

With no DC field applied, the temperature gradient on the thermal finger from this applied RF field was 0.019 K. Based on the earlier calibration, this corresponds to a dissipated power of 8.76×10^{-4} W. In turn, from the earlier field distribution simulations, this indicates $Q_{inner} = 1.1 \pm 0.7 \times 10^6$ and $R_{s,inner} = 7 \pm 5 \times 10^{-5}$ Ω. This is a substantially higher resistance than the 1.1×10^{-6} Ω

expected at 4.2 K. This may indicate additional sources of surface resistance on the niobium sample, such as hydride Q-disease or trapped magnetic flux due to the unusual cooldown dynamics. Another potential reason for the high dissipated power given the field strength in the cavity is a larger-than-expected $\tan\delta$ of the sapphire rod; for example, $\tan\delta = 8 \times 10^{-5}$ instead of the expected $\tan\delta < 1 \times 10^{-9}$ would account for the additional losses.

Despite the unexpectedly high losses, we continued with the commissioning test, applying a DC magnetic field with the superconducting solenoid and measuring the temperature gradient along the thermal finger. We ramped the solenoid field up to an excitation current of 4 A, corresponding to an axial field of 60 mT.

At low DC field, up to approximately 20 mT, the thermal gradient showed minimal change. Above 20 mT, the thermal gradient ΔT made a sudden dramatic increase of 33%. At the same field, the steady-state transmitted and reflected power measurements also changed, with P_t increasing by 2% and P_r decreasing by 2%. At approximately 23 mT, P_t and P_r dramatically and suddenly decreased, by 11% and 92%, respectively. For increasing DC magnetic field up to 60 mT, ΔT and P_t varied slowly, generally decreasing to a minimum at 56 mT with a slight increase up to 60 mT. Over the same scale, P_r gradually increased to a maximum, also at 56 mT, with a slight decrease up to 60 mT. Figure 9.36 shows ΔT as a function of the applied DC magnetic field, and Fig. 9.37 shows the reflected and transmitted power measurements (normalized to their low-field values).

This apparent dependence of ΔT (and by extension P_diss), P_r, and P_t on the DC magnetic field strength is interesting and puzzling. The magnitude of the

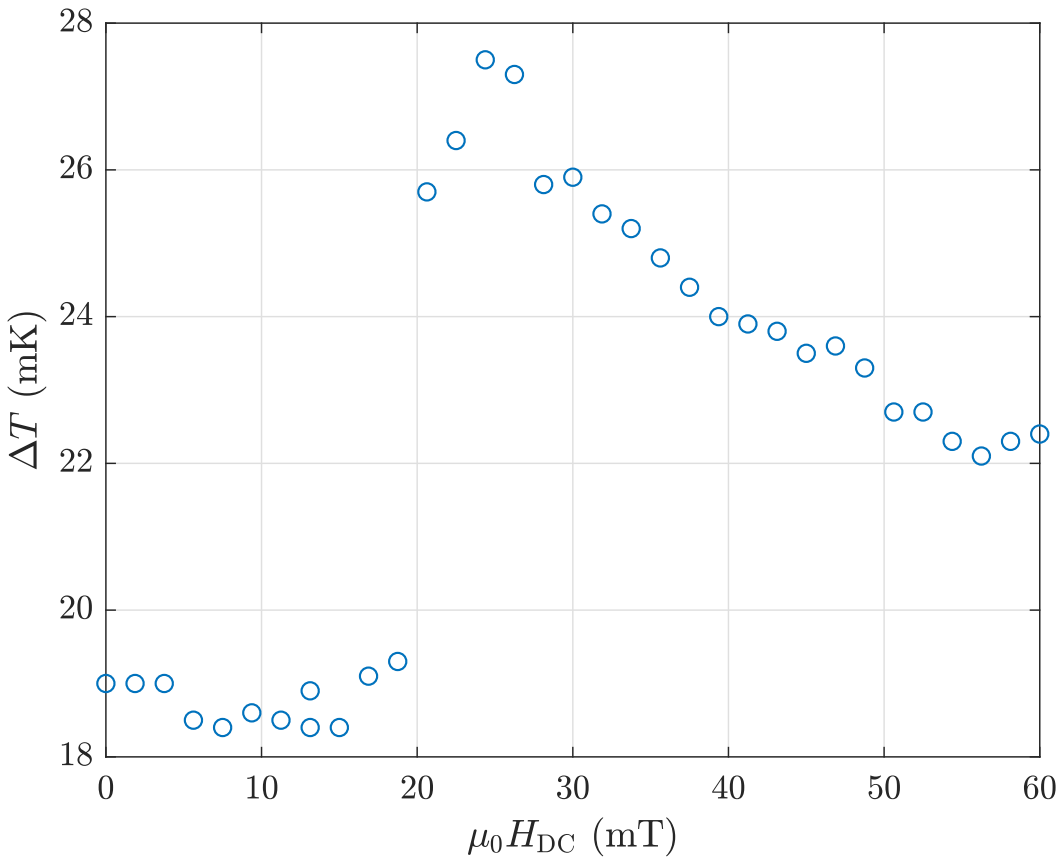

Figure 9.36: Temperature gradient measured on the thermal finger as a function of applied DC magnetic field.

drop in P_t relative to that in P_r may indicate multipacting in the transmitted power port or between the inner conductor and transmitted power coupler; the P_t port, which breaks the azimuthal symmetry of the resonator, was not included in the 2D Multipac simulations and may require additional mitigation factors, such as ridges on the antenna. In addition, the helium gas leak may have helped bring about multipacting: the adsorbed gas on the cavity walls may have increased the secondary electron coefficient [KNTS12]. Multipacting would act as an additional loss mechanism in the cavity, reducing P_r, and if incident on the inner conductor would dissipate heat there, increasing ΔT. If the multipacting involved the transmitted power coupler, it could greatly reduce the strength of the TEM wave coupled out of the cavity, thereby reducing P_t.

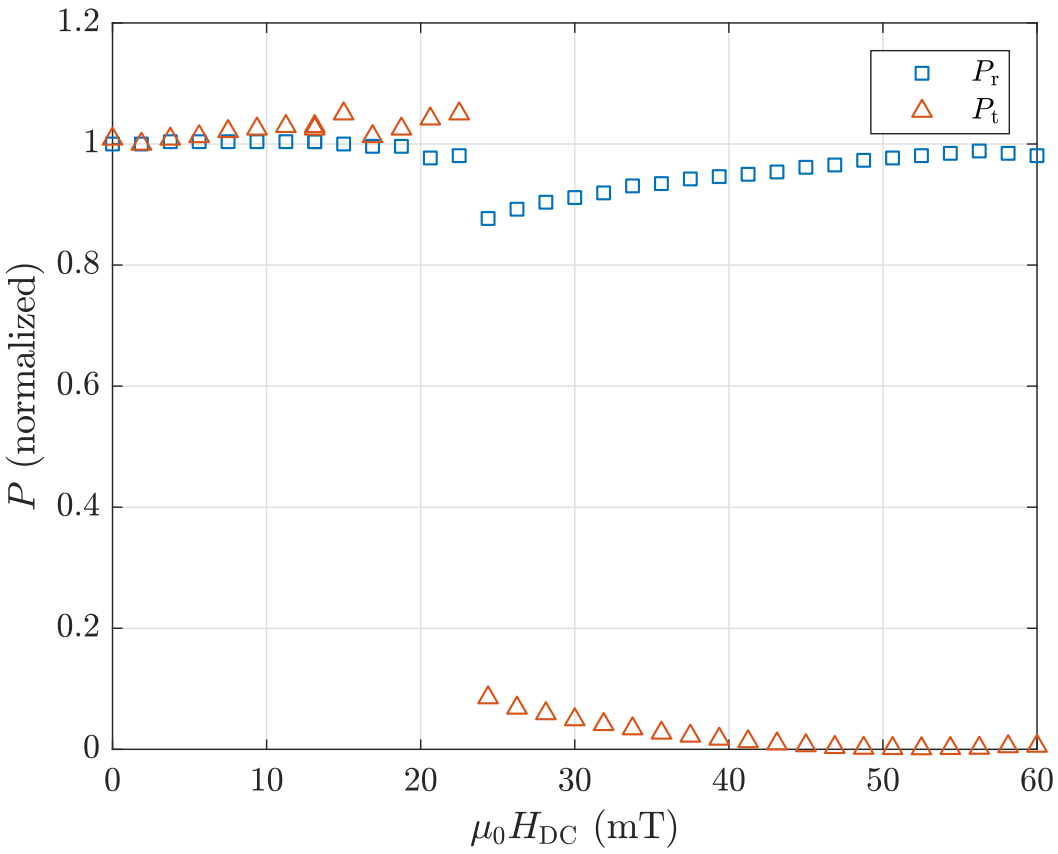

Figure 9.37: Reflected and transmitted power measurements in the DC Field Dependence Cavity as a function of applied DC magnetic field.

The DC magnetic field may have controlled the magnitude of multipacting by distorting the trajectories of secondary electrons.

After the DC-field-dependent measurement of ΔT at 4.2 K was completed, we warmed the apparatus back up to room temperature, not wanting to risk pumping to lower temperatures and potentially making the leak more severe (particularly at temperatures below the superfluid transition temperature of helium T_{lambda} = 2.17 K).

9.5.5 Outlook and Further Commissioning Tests

The first test of the DC Field Dependence Cavity showed promising early results. The three main modes of the cavity are accessible at reasonable (but unexpectedly high) coupling factors, as indicated by the measurements of Γ and T. The calorimetric measurement system also works as expected and has been calibrated with the resistive heating element. However, several issues and questions must be resolved before commissioning can continue at lower temperatures and in the other RF modes.

First, the liquid helium leak must be located. As mentioned above, there is a strong possibility that the source of the leak is one of the VCR fittings on the vacuum hose connected to the angle valve, so the first step in eliminating the leak will be to investigate and potentially replace these fittings.

Another early improvement should be upgrading the quench protection circuit to a higher current threshold. As built, the system is limited to a potential of 1 V across the solenoid; the approximately 0.25 Ω resistance of the normal-conducting portion of the circuit limits the excitation to 4 A and 60 mT. Increasing the number of diodes in the quench protection circuit to allow for an excitation of 20 A would allow an excitation of the solenoid up to 300 mT, greatly extending the experimental range of the apparatus. At higher fields, the apparent multipacting may also be suppressed [GBC+03]. Further, at these high fields, the apparatus could be used to measure the superconducting critical fields of the inner conductor, in particular H_{sh}.

In the short term, with the leak fixed and quench protection system upgraded, testing can continue in the other modes where the apparent multipact-

ing in the transmitted power port may not be triggered, at 4.2 K and lower temperatures. In the longer term, perhaps by changing the geometry of the port (adding ridges to the inner or outer conductor of the P_t port or shortening the port's inner conductor). Fixing the leak may also improve the apparent multipacting: reducing the amount of gas adsorbed onto the cavity walls at cryogenic temperatures may reduce the secondary electron coefficient [KNTS12].

Another issue that must be understood is the higher-than-expected dissipated power on the inner conductor. This may be due to a high loss tangent in the sapphire rod, as discussed above. To address this, it may be necessary to re-treat the sapphire rod, perhaps repeating the cleaning procedure outlined in Sec. 9.3.6. As an alternative hypothesis, the cryogenic loss tangent of sapphire has been reported to depend strongly on the growth method for the crystal [GFGD16]; it may help to rebuild the thermal finger assembly with a new sapphire rod grown by one of the low-loss methods.

The measurements of T and Γ also raise some interesting questions. What is the cause of the apparent mode-splitting in the 1.3 GHz and 2.0 GHz modes? Curiously, the secondary peaks in T did not appear to correspond to troughs in the reflection coefficient Γ; also curiously, the trough in the reflection coefficient measurements of the second mode indicated that the lower-frequency peak in the transmission coefficient was the "true" peak, while the opposite was true in the third mode. Another unexpected outcome of these measurements was the low Q_0 calculated for the third mode.

Deeper investigation of this mode-splitting is necessary. To speculate, perhaps a closer look at the second and third modes will reveal secondary, shallower troughs in Γ corresponding to the secondary peaks in T, indicating

stronger overcoupling and thus higher Q_0 and $R_{s,outer}$ closer to the expected values. This would help solve the puzzle of the particularly low Q_0 of the third mode. The mode-splitting and low Q_0 may also be linked to multipacting.

On a similar note to the observed mode-splitting, the thermal finger and inner conductor assembly should be re-aligned with the copper tube and conical outer conductor. By restoring azimuthal symmetry to the cavity, this will promote DC and RF field uniformity and may also reduce the mode-splitting effect.

Overall, this is a promising start for this new apparatus.

CHAPTER 10

CONCLUSION

Chapters 5-9 of this dissertation have detailed several research projects aimed at improving our understanding of the field-dependent surface resistance in nitrogen-doped niobium. These include experimental results from tests of single-cell cavities and theoretical analysis of those test results; an assessment of several models of the field-dependent surface resistance; and the development of new computational and experimental tools to for deeper investigation of the properties of doped niobium. In this final chapter, I will summarize the findings of the earlier chapters, present some concluding remarks to connect the results, and give an outlook on future directions for investigation.

10.1 1.3 GHz Cavity Tests and Analysis

In the study of strongly nitrogen-doped niobium cavities presented in Chap. 5, our research found that the magnitude of the field-dependent reduction in the BCS surface resistance was strongly dependent on the electron mean free path ℓ, with shorter ℓ linked to stronger relative reduction of R_{BCS}. We found good agreement between these 1.3 GHz experimental results and the predictions of the Gurevich model of the field-dependent surface resistance. We established a theoretical link between the strength of the observed change in relative reduction of R_{BCS} and the electron mean free path ℓ through the effect of quasiparticle overheating, in which inefficient heat transfer from the quasiparticles in the RF surface to the cryogenic bath leads to an increase in the temperature of the quasiparticles, counteracting the field-dependent reduction in R_{BCS}. Our findings suggested that the electron-phonon heat transfer rate is strongly depen-

dent on ℓ and has a large effect on quasiparticle overheating, and that doping cavities with nitrogen to $\ell < 20$ nm can help to maximize the field-dependent reduction in R_{BCS}. Collaborative work in the Center for Bright Beams is underway using Density Functional Theory to build an *ab initio* model of the link between interstitial impurities and the suppression of quasiparticle overheating.

We combined the results of this study with earlier work investigating the sensitivity of the residual resistance to trapped magnetic flux in nitrogen-doped cavities. By balancing the effects of ℓ on the low-field value of R_{BCS}, the magnitude of the field-dependent reduction in R_{BCS}, and the flux trapping sensitivity of R_0, we can calculate an optimal nitrogen doping level (as quantified by ℓ) for a given set of accelerator parameters and expected trapped flux density. When trapped flux can be kept to a minimum, short mean free paths of $\ell \approx 20$ nm give the best performance, where the low-field R_{BCS} is minimized and the field-dependent reduction in R_{BCS} is maximized. On the other hand, as trapped flux becomes an issue, longer mean free paths become more appropriate, where the flux trapping sensitivity of R_0 decreases.

In the study of nitrogen-infused cavities presented in Chap. 6, we found similar performance between nitrogen-infused and nitrogen-doped cavities despite dramatic differences in the impurity content. While nitrogen-doped cavities have a relatively flat concentration profile of interstitial nitrogen on the scale of micrometers, nitrogen-infused cavities show N, C, and O concentrations that vary by orders of magnitude on the scale of tens of nanometers. In particular, nitrogen appears to be present above background levels only very near the surface in nitrogen-infused cavities, with a concentration at or above 0.01 at.% at the surface and rapidly decaying below that threshold after approximately 10 nm. The

nitrogen-infused cavities with field-dependent reductions in R_{BCS} did not agree with the Gurevich model predictions as well as the nitrogen-doped cavities, but the best fits indicated strong overheating suppression. This suppression is consistent with the earlier model of quasiparticle overheating considering the short mean free path ℓ of these cavities. The weaker agreement with the Gurevich model may be related to the rapid variation in material properties through the RF layer.

In our surface removal study, we used several chemical methods to minutely etch the RF surfaces of several nitrogen-infused cavities, including two that initially suffered from titanium contamination at a surface concentration of approximately 0.001 at.%. This study found that a removal of 2 nm of material from the surface by HF rinsing was enough to cure the titanium contamination and restore anti-Q-slope behavior to the infused cavities, that the anti-Q-slope persisted after at least two HF rinses, and that deeper removal of 50-100 nm removed the anti-Q-slope behavior again.

Linked together, the results of the nitrogen-doping and nitrogen-infusion studies point to several interesting conclusions. It appears that the unifying feature across all the 1.3 GHz niobium cavities which showed anti-Q-slope behavior is a surface concentration of nitrogen at or above 0.01 at.%. Cavities with nitrogen concentration below this threshold as well as cavities with a thin contamination layer on the surface did not show anti-Q-slope behavior. This indicates that the link between nitrogen doping and the anti-Q-slope may be a *surface* effect involving nitrogen, sensitive to contamination. One possibility is that nitrogen suppresses the presence of some detrimental surface feature, such as nanohydrides, revealing a "native" anti-Q-slope. Future studies should

investigate this possibility, continuing the sequential HF rinse study to better understand the nitrogen concentration threshold.

While the concentrations of oxygen and carbon in the surface appear not to be correlated to the presence of the anti-Q-slope, the nitrogen infusion study indicates that these impurities may work as well as nitrogen for improving the electron-phonon heat transfer coefficient Y, thereby suppressing quasiparticle overheating. The mechanism of the link between impurity concentration and electron-phonon heat transfer efficiency remains a key open question in this study. Looking forward, it will be important to study this quasiparticle overheating with experimental and theoretical tools in order to minimize detrimental thermal effects in anti-Q-slope cavities as well as cavities with more traditional Q-slopes that may be related to quasiparticle overheating.

10.2 Theoretical Tools and Assessment

In Chap. 7, I outlined a new thermal modeling framework for studying the field-dependent surface resistance in niobium accelerator cavities. This new framework is designed to improve upon earlier thermal models in several capacities. The framework supports arbitrary local models of R_s, considering depth-dependent material parameters such as ℓ, ξ, λ, Δ, and T_c. It adds upon previous models of quasiparticle overheating that have included the effects of thermal conductivity of the cavity wall and the Kapitza resistance to the helium bath by including the electron-phonon thermal resistance. Given a set of experimental conditions, the framework uses a self-consistent method to find the equilibrium surface quasiparticle temperature, the increase of which can mediate an anti-

Q-slope or drive medium-field Q-slope and eventually lead to a global thermal instability quench.

The results of calculations using the Mattis-Bardeen theory found reasonable agreement with the behavior of non-doped niobium cavities, with the electron-phonon heat transfer mediating the medium-field Q-slope over a range of experimentally realistic magnitudes. Calculations using the Gurevich model of the anti-Q-slope with the new framework also showed reasonable agreement with experimental results. In all, the new framework is highly adaptable and can be used as a tool for future studies of the field-dependent surface resistance in SRF cavities, particularly for testing local models of R_s against experimental results.

In Chap. 8, I presented an assessment of several recent theoretical models of the field-dependent surface resistance, taking into account recent early measurements of the frequency dependence of the anti-Q-slope in nitrogen-doped and nitrogen-infused niobium cavities as well as high-frequency clean niobium cavities: the magnitude of the reduction in R_{BCS} increases with increasing cavity frequency for a given cavity preparation, appearing in non-doped clean niobium cavities above approximately 3 GHz. The assessment covered three models of R_s, and found that none were satisfying descriptions of the anti-Q-slope observed in niobium SRF cavities. We first investigated the model proposed by Weingarten, for which we found agreement with the experimentally observed frequency dependence of the anti-Q-slope, but disagreement with observations of the dependence on electron mean free path. We then studied the model proposed by Goldie and Withington, finding that the physical principles employed appear to rely on experimental conditions not satisfied by niobium cavities, par-

ticularly the relative values of T, T_c, Δ, and ω. Finally, we reassessed the model proposed by Gurevich, for which we had found good agreement with experimental results of 1.3 GHz nitrogen-doped cavities; here, we found disagreement with the newly observed frequency dependence of the anti-Q-slope. Furthermore, we found a likely error in the model that, when corrected, nullified the anti-Q-slope prediction.

If there are no satisfying models of the anti-Q-slope in niobium cavities, where should we look next for building a new model? Based on the conclusions of the experimental studies of nitrogen-doped and nitrogen-infused cavities, a model of the anti-Q-slope must consider several apparent features. First is the frequency dependence of the strength of the reduction in R_{BCS}, including the apparent onset frequency (approximately 1 GHz for nitrogen-doped cavities and approximately 3 GHz for clean niobium cavities) below which the anti-Q-slope disappears. Another is the apparent relation of the anti-Q-slope to the surface properties, where at 1.3 GHz there is good correlation between the presence of an anti-Q-slope and nitrogen above the 0.01 at.% level at the surface, except in cavities with a surface layer of titanium contamination. Work is ongoing within the Center for Bright Beams to develop a model of the surface resistance in the Floquet formulation of driven quantum systems; this may also prove to be a fruitful direction of research.

Having no satisfying theory of the anti-Q-slope presents an opportunity to design new experiments to probe other aspects of the field-dependent surface resistance of niobium, generating new experimental data to drive the development of new models.

10.3 The DC Field Dependence Cavity

On that note, in Chap. 9 I introduced the DC Field Dependence Cavity, a new sample host cavity at Cornell designed to study the dependence of the surface resistance of niobium and nitrogen-doped niobium samples on the strength of an applied DC magnetic field. This apparatus will provide a new body of evidence to explore the anti-Q-slope, looking beyond the dependence of the surface resistance on the RF field strength studied so far in traditional accelerator cavities.

The cavity is a coaxial resonator with a removable superconducting inner conductor sample and a normal-conducting outer conductor body, resonating at 550 MHz, 1.3 GHz, and 2.0 GHz. This resonator is positioned inside a superconducting solenoid, which applies a strong DC magnetic field on the RF surface. Calibrated calorimetric measurements reveal the surface resistance of the inner conductor as a function of the applied field strength; it is expected that the cavity will be sensitive to changes in R_s on the 0.1% level.

The construction and first assembly of this new cavity have been completed at Cornell, and commissioning is underway. The superconducting solenoid works as expected, with good field uniformity and nominal performance of the solenoid and superconducting magnetic shielding up to the maximum tested field of 60 mT. With an upgrade to the quench protection system in the near future, we expect that the solenoid will reach 200-300 mT with nominal performance.

In the first cooldown of the cavity, a liquid helium leak appeared, probably on one of the vacuum hose fittings. This leak likely led to a helium gas pressure

near 1×10^{-3} Torr inside the cavity during the test, with gas adsorbed onto the cavity walls due to the cryopumping action. We restricted the test to 4.2 K to avoid further issues related to this leak.

I measured the transmission and reflection coefficients of the three cavity modes, which yielded measurements of β_e, Q_L, and Q_0. The values of these in the first and second modes indicated higher β_e than expected from simulations. In the third mode, we found β_e much lower than expected, near unity coupling; this may be related to multipacting, which might be greatly enhanced by the presence of adsorbed gas on the cavity walls. The transmission and reflection coefficient measurements also showed some unexpected mode-splitting in the second and third modes, which may be related to a slight misalignment of the inner conductor/thermal finger assembly with respect to the outer conductor of the cavity.

I calibrated the thermal finger measurement system and made the first measurements of the dependence of the thermal gradient (proportional to the surface resistance) on the applied DC magnetic field. This first test showed large heating which may indicate unexpected surface losses or a high loss tangent to the sapphire rod, a component in the thermal finger assembly. In this test I also measured the reflected and transmitted power as functions of the DC field. As I increased the DC field strength, I measured a large and sudden jump in ΔT and drops in P_t and P_r; these may indicate multipacting in the transmitted power coupler.

Overall, these are promising early results from this new apparatus. The fundamental mode of operation of the cavity, measuring the change in temperature gradient along the thermal finger as a function of the applied DC magnetic

field, has been shown to work with good sensitivity. However, there must be additional commissioning work for the cavity to address the several issues mentioned above. Top priorities are fixing the leak and improving the quench protection circuit. The first will allow for low-temperature operation, particularly below the superfluid transition of helium at 2.17 K, and may also help with the apparent multipacting. The second will greatly extend the range of achievable DC field on the RF surface. Multipacting might also be suppressed at higher DC fields as electron trajectories are disrupted.

The curious mode splitting must also be investigated, and the secondary peaks more closely studied. Perhaps these will have more ideal coupling constants, closer to the expected values. Realignment of the thermal finger assembly may also fix this issue.

With these addressed, commissioning of the cavity can continue at other modes and temperatures. Soon we will be ready to begin a sample-testing program to open wide this new window into the physics of the anti-Q-slope.

BIBLIOGRAPHY

[AAC+99] C. Z. Antoine, A. Aspart, J. P. Charrier, H. Safa, and B. Visentin. Alternative approaches for surface treatment of Nb superconducting cavities. In *Proceedings of the 9th International Conference on RF Superconductivity*, 1999.

[ABB+00] B. Aune, R. Bandelmann, D. Bloess, B. Bonin, A. Bosotti, M. Champion, C. Crawford, G. Deppe, B. Dwersteg, D. A. Edwards, H. T. Edwards, M. Ferrario, M. Fouaidy, P.-D. Gall, A. Gamp, A. Gössel, J. Graber, D. Hubert, M. Hüning, M. Juillard, T. Junquera, H. Kaiser, G. Kreps, M. Kuchnir, R. Lange, M. Leenen, M. Liepe, L. Lilje, A. Matheisen, W.-D. Möller, A. Mosnier, H. Padamsee, C. Pagani, M. Pekeler, H.-B. Peters, O. Peters, D. Proch, K. Rehlich, D. Reschke, H. Safa, T. Schilcher, P. Schmüser, J. Sekutowicz, S. Simrock, W. Singer, M. Tigner, D. Trines, K. Twarowski, G. Weichert, J. Weisend, J. Wojtkiewicz, S. Wolff, and K. Zapfe. Superconducting TESLA cavities. *Physical Review Special Topics - Accelerators and Beams*, 3(9), September 2000.

[ABB+16] S. Aull, M. Benedikt, A. Blondel, D. Bozzini, O. Brunner, J.-P. Burnet, A. Butterworth, R. Calaga, S. Gorgi Zadeh, E. Jensen, M. Koratzinos, V. Mertens, A. Milanese, M. Nonis, K. Oide, L. Rinolfi, N. Schwerg, L. Tavian, J. Wenninger, and F. Zimmermann. Electrical Power Budget for FCC-ee. In *Proceedings of the 7th International Particle Accelerator Conference*, pages 3828–3831, 2016.

[Abr57] A. A. Abrikosov. The magnetic properties of superconducting alloys. *Journal of Physics and Chemistry of Solids*, 2(3):199–208, January 1957.

[AF00] J. Amrit and M. X. François. Heat flow at the niobium-superfluid helium interface: Kapitza resistance and superconducting cavities. *Journal of Low Temperature Physics*, 119(1/2):27–40, 2000.

[ANAG36] L. C. van Atta, D. L. Northrup, C. M. van Atta, and R. J. van de Graaff. The Design, Operation, and Performance of the Round Hill Electrostatic Generator. *Physical Review*, 49:761–776, May 1936.

[Ano31] Anonymous. Minutes of the Schenectady Meeting September 10, 11 and 12, 1931. *Physical Review*, 38:1915–1924, November 1931.

[Ban19] M. Banks. Europe unveils successor to the Large Hadron Collider. https://physicsworld.com/a/europe-unveils-successor-to-the-large-hadron-collider/, January 2019. Accessed 2019-01-22.

[BAP94] S. N. Buckley, P. Agnew, and G. P. Pells. Cryogenic dielectric properties of sapphire at 2.45 GHz. *Journal of Physics D: Applied Physics*, 27(10):2203–2209, October 1994.

[Bar] Bartington Instruments. Mag-01H. Bartington.com. Accessed Aug. 13, 2019.

[Bar55] J. Bardeen. Theory of the Meissner Effect in Superconductors. *Physical Review*, 97(6):1724–1725, March 1955.

[Bar62] J. Bardeen. Critical fields and currents in superconductors. *Reviews of Modern Physics*, 34(4):667–681, October 1962.

[BBB+19] M. Bertucci, A. Bignami, A. Bosotti, P. Michelato, L. Monaco, C. Pagani, R. Paparella, D. Sertore, C. Maiano, P. Pierini, and J. Chen. Performance analysis of the European X-ray Free Electron Laser 3.9 GHz superconducting cavities. *Physical Review Accelerators and Beams*, 22(8), August 2019.

[BCC+97] C. Benvenuti, S. Calatroni, I. E. Campisi, P. Darriulat, C. Durand, M. A. Peck, R. Russo, and A.-M. Valente. Magnetic flux trapping in superconducting niobium. In *Proceedings of the 8th International Conference on RF Superconductivity*, 1997.

[BCG+18] D. Bafia, M. Checchin, D. Gonnella, A. Grassellino, O. S. Melnychuk M. Martinello, A. D. Palczewski, S. Posen, A. Romanenko, D. A. Sergatskov, and J. F. Zasadzinski. Understanding and pushing the limits of nitrogen doping. In *Proceedings of the 9th International Particle Accelerator Conference*, 2018.

[BCS57a] J. Bardeen, L. N. Cooper, and J. R. Schrieffer. Microscopic Theory of Superconductivity. *Physical Review*, 106(1):162–164, April 1957.

[BCS57b] J. Bardeen, L. N. Cooper, and J. R. Schrieffer. Theory of Superconductivity. *Physical Review*, 108(5):1175–1204, December 1957.

[BF95] A. Boucheffa and M. X. François. Kapitza conductance of niobium

for superconducting cavities in the temperature range 1.6 K, 2.1 K. In *Proceedings of the 7th International Conference on RF Superconductivity*, 1995.

[BGLM71] Y. Bruynseraede, D. Gorle, D. Leroy, and P. Morignot. Surface-resistance measurements in TE_{011}-mode cavities of superconducting indium, lead and an indium-lead alloy at low and high RF magnetic fields. *Physica*, 54(1):137–159, July 1971.

[BGS+19] D. Bafia, A. Grassellino, Z. Sung, A. Romanenko, O. S. Melnychuk, and J. F. Zasadzinski. Gradients of 50 MV/m in TESLA shaped cavities via modified low temperature bake. In *Proceedings of the 19th International Conference on RF Superconductivity*, 2019.

[BHM98] E. Brigant, E. Haebel, and E. Mahner. The quadrupole resonator, design considerations and layout of a new instrument for the RF characterization of superconducting surface samples. In *Proceedings of the 6th European Particle Accelerator Conference*, 1998.

[BJ15] A. Bose and S. C. Joshi. Study of impurity distribution in mechanically polished, chemically treated and high vacuum degassed pure niobium samples using the TOFSIMS technique. *Superconductor Science and Technology*, 28(7):075007, May 2015.

[BNK97] W. Banzhaf, P. Nordin, and R. E. Keller. *Genetic Programming: An Introduction*. Morgan Kaufmann Publishing, Inc., 1997.

[Bog58] N. N. Bogolyubov. On a new method in the theory of superconductivity. *Il Nuovo Cimento*, 7(6):794–805, March 1958.

[BRT59] J. Bardeen, G. Rickayzen, and L. Tewordt. Theory of the thermal conductivity of superconductors. *Physical Review*, 113(4):982–994, February 1959.

[CMS+10] G. Ciovati, G. Myneni, F. Stevie, P. Maheshwari, and D. Griffis. High field Q slope and the baking effect: Review of recent experimental results and new data on Nb heat treatments. *Physical Review Special Topics - Accelerators and Beams*, 13(2), February 2010.

[Coo56] L. N. Cooper. Bound Electron Pairs in a Degenerate Fermi Gas. *Physical Review*, 104(4):1189–1190, November 1956.

[Cra17] A. C. Crawford. Extreme diffusion limited electropolishing of niobium radiofrequency cavities. *Nuclear Instruments and Methods in Physics Research Section A: Accelerators, Spectrometers, Detectors and Associated Equipment*, 849:5–10, March 2017.

[CRD+18] A. D. Cahill, J. B. Rosenzweig, V. A. Dolgashev, S. G. Tantawi, and S. Weathersby. High gradient experiments with *X*-band cryogenic copper accelerating cavities. *Physical Review Accelerators and Beams*, 21:102002, October 2018.

[CSF12] A. Chandra, M. Sumption, and G. S. Frankel. On the mechanism of niobium electropolishing. *Journal of The Electrochemical Society*, 159(11):C485–C491, 2012.

[CW32] J. D. Cockroft and E. T. S. Walton. Experiments with High Velocity Positive Ions. II. The Disintegration of Elements by High Velocity Protons. *Proceedings of the Royal Society A*, 137:229–242, 1932.

[Dah97] P. F. Dahl. *Flash of the Cathode Rays: A History of J J Thomson's Electron*. Institute of Physics, Bristol and Philadelphia, 1997.

[Das] Dassault Systèmes. CST Studio Suite. 3ds.com. Accessed Nov. 20, 2019.

[dBG+17] V. del Pozo Romano, R. Betemps, F. Gerigk, R. Illan Fiastre, and T. Mikkola. Redesign of CERN's quadrupole resonator for testing of superconducting samples. In *Proceedings of the 18th International Conference on RF Superconductivity*, 2017.

[DCM+13] P. Dhakal, G. Ciovati, G. R. Myneni, K. E. Gray, N. Groll, P. Maheshwari, D. M. McRae, R. Pike, T. Proslier, F. Stevie, R. P. Walsh, Q. Yang, and J. Zasadzinzki. Effect of high temperature heat treatments on the quality factor of a large-grain superconducting radio-frequency niobium cavity. *Physical Review Special Topics - Accelerators and Beams*, 16(4), April 2013.

[DCM17] P. Dhakal, G. Ciovati, and G. R. Myneni. Role of thermal resistance on the performance of superconducting radio frequency cavities. *Physical Review Accelerators and Beams*, 20(3), March 2017.

[dGD+14] P. J. de Visser, D. J. Goldie, P. Diener, S. Withington, J. J. A. Baselmans, and T. M. Klapwijk. Evidence of a nonequilibrium distri-

bution of quasiparticles in the microwave response of a superconducting aluminum resonator. *Physical Review Letters*, 112(4), January 2014.

[DHL17] J. Ding, D. L. Hall, and M. Liepe. Simulations of RF field-induced thermal feedback in niobium and Nb3Sn cavities. *Proceedings of the 18th International Conference on RF Superconductivity*, 2017.

[Die78] H. Diepers. Method for the anodic polishing of surfaces of intermetallic niobium compounds and niobium alloys. *US Patent 4,072,588*, 1978.

[EGH+14] R. Eichhorn, D. Gonnella, G. Hoffstaetter, M. Liepe, and W. Weingarten. On superconducting niobium accelerating cavities fired under N_2-gas exposure. *ArXiv preprint*, 2014.

[EGLP47] F. R. Elder, A. M. Gurewitsch, R. V. Langmuir, and H. C. Pollock. Radiation from Electrons in a Synchrotron. *Physical Review*, 71:829–830, June 1947.

[ETDS16] N. G. Ebensperger, M. Thiemann, M. Dressel, and M. Scheffler. Superconducting Pb stripline resonators in parallel magnetic field and their application for microwave spectroscopy. *Superconductor Science and Technology*, 29(11):115004, October 2016.

[Euc17] Euclid Tech Labs. The SuperLANS Family of Codes for 2D RF Cavity Simulations. `http://www.euclidtechlabs.com/the-superlans-family-of-codes-for-2d-rf-cavity-simulations/`, May 2017. Accessed 04-10-2019.

[FGG+18] F. Furuta, F. Gau, M. Ge, T. Gruber, J. J. Kaufman, M. Liepe, J. T. Maniscalco, J. Rose, and J. Sears. RF test result of a BNL N-doped 500 MHz B-cell cavity at Cornell. In *Proceedings of the 9th International Particle Accelerator Conference*, 2018.

[FLS06] R. P. Feynman, R. B. Leighton, and M. Sands. *The Feynman Lectures on Physics*. Addison Wesley, second edition, 2006.

[Ful65] P. Fulde. Tunneling density of states for a superconductor carrying a current. *Physical Review*, 137(3A):A783–A787, February 1965.

[GAB+19] D. Gonnella, S. Aderhold, D. Bafia, A. Burrill, M. Checchin, M. Ge,

A. Grassellino, G. Hays, M. Liepe, M. Martinello, A. Palczewski, S. Posen, T. Raubenheimer, C. Reece, A. Romanenko, and M. Ross. The LCLS-II high Q and gradient R&D program. In *Proceedings of the 19th International Conference on RF Superconductivity*, 2019.

[GBC+03] R. L. Geng, S. Belomestnykh, R. G. Carter, P. Goudket, and H. Padamsee. Dynamics of multipacting in rectangular coupler waveguides and suppression methods. In *Proceedings of the 11th International Conference on RF Superconductivity*, 2003.

[GC13] A. Gurevich and G. Ciovati. Effect of vortex hotspots on the radio-frequency surface resistance of superconductors. *Physical Review B*, 87(5), February 2013.

[GCA33] R. J. van de Graaff, K. T. Compton, and L. C. van Atta. The Electrostatic Production of High Voltage for Nuclear Investigations. *Physical Review*, 43:149–157, February 1933.

[GEF+16] D. Gonnella, R. Eichhorn, F. Furuta, M. Ge, T. Gruber, G. Hoffstaetter, J. Kaufman, P. N. Koufalis, M. Liepe, and J. T. Maniscalco. Improved N-doping protocols for SRF cavities. In *Proceedings of the 7th International Particle Accelerator Conference*, 2016.

[Gei10] H. Geiger. The Scattering of the Formula-Particles by Matter. *Proceedings of the Royal Society A: Mathematical, Physical and Engineering Sciences*, 83(565):492–504, April 1910.

[Gen05] R. L. Geng. Review of New Shapes for Higher Gradients. In *Proceedings of the 12th International Conference on RF Superconductivity*, 2005.

[GFG+13] M. Ge, F. Furuta, D. Gonnella, G. H. Hoffstaetter, M. Liepe, and H. Padamsee. Investigation of the surface resistivity of SRF cavities via the HEAT and SRIMP program as well as the multi-cell T-map system. In *Proceedings of the 16th International Conference on RF Superconductivity*, 2013.

[GFGD16] V. Giordano, C. Fluhr, S. Grop, and B. Dubois. Tests of sapphire crystals manufactured with different growth processes for ultra-stable microwave oscillators. *IEEE Transactions on Microwave Theory and Techniques*, 64(1):78–85, January 2016.

[GH80] M. Grundner and J. Halbritter. XPS and AES studies on oxide growth and oxide coatings on niobium. *Journal of Applied Physics*, 51(1):397–405, January 1980.

[GHL+06] F. Giazotto, T. T. Heikkilä, A. Luukanen, A. M. Savin, and J. P. Pekola. Opportunities for mesoscopics in thermometry and refrigeration: Physics and applications. *Reviews of Modern Physics*, 78(1):217–274, March 2006.

[GK68] B. B. Goodman and G. Kuhn. Influence des défauts étendus sur les propriétés supraconductrices du niobium. *J. Phys. France*, 29:240–252, 1968.

[GKL16] D. Gonnella, J. Kaufman, and M. Liepe. Impact of nitrogen doping of niobium superconducting cavities on the sensitivity of surface resistance to trapped magnetic flux. *Journal of Applied Physics*, 119(7):073904, February 2016.

[GL] A. Gurevich and D. B. Liarte. Private communication. 2019.

[GL50] V. L. Ginzburg and L. D. Landau. On the Theory of superconductivity. *Zh. Eksp. Teor. Fiz.*, 20:1064–1082, 1950.

[GL13] D. Gonnella and M. Liepe. High Q_0 Studies at Cornell. In *Proceedings of SRF 2013*, 2013.

[Gok03] C. Gokcek. Tracking the resonance frequency of a series RLC circuit using a phase locked loop. In *Proceedings of 2003 IEEE Conference on Control Applications.* IEEE, 2003.

[Gol76] E. Goldstein. Vorläufige Mittheilungen über elektrische Entladungen in verdünnten Gasen. *Monatsberichte der Königlich Preussischen Akademie der Wissenschaften zu Berlin*, pages 279–295, May 1876.

[Gon16] D. Gonnella. *The Fundamental Science of Nitrogen-Doping of Niobium Superconducting Cavities*. PhD thesis, Cornell University, August 2016.

[Gor59] L. P. Gor'kov. Microscopic Derivation of the Ginzburg-Landau Equations in the Theory of Superconductivity. *Journal of Experimental and Theoretical Physics*, 9(6):1364, 1959.

[Gra93] J. Graber. *High Power RF Processing Studies of 3 GHz Niobium Superconducting Accelerator Cavities*. PhD thesis, Cornell University, May 1993.

[GRS+13] A. Grassellino, A. Romanenko, D. Sergatskov, O. Melnychuk, Y. Trenikhina, A. Crawford, A. Rowe, M. Wong, T. Khabiboulline, and F. Barkov. Nitrogen and argon doping of niobium for superconducting radio frequency cavities: a pathway to highly efficient accelerating structures. *Superconductor Science and Technology*, 26(10):102001, August 2013.

[GRT+17] A. Grassellino, A. Romanenko, Y. Trenikhina, M. Checchin, M. Martinello, O. S. Melnychuk, S. Chandrasekaran, D. A. Sergatskov, S. Posen, A. C. Crawford, S. Aderhold, and D. Bice. Unprecedented quality factors at accelerating gradients up to 45 MVm^{-1} in niobium superconducting resonators via low temperature nitrogen infusion. *Superconductor Science and Technology*, 30(9):094004, August 2017.

[Gur12] A. Gurevich. Superconducting Radio-Frequency Fundamentals for Particle Accelerators. *Reviews of Accelerator Science and Technology*, 05:119–146, January 2012.

[Gur14] A. Gurevich. Reduction of dissipative nonlinear conductivity of superconductors by static and microwave magnetic fields. *Physical Review Letters*, 113(8), August 2014.

[GW12] D. J. Goldie and S. Withington. Non-equilibrium superconductivity in quantum-sensing superconducting resonators. *Superconductor Science and Technology*, 26(1):015004, November 2012.

[HA63] J. L. Harden and V. Arp. The lower critical field in the Ginzburg-Landau theory of superconductivity. *Cryogenics*, 3(2):105–108, June 1963.

[Hal70] J. Halbritter. Ext. Bericht 3/69-2 Kernforschungszentrum, Karlsruhe, 1969. Computer program for the surface impedance: Ext. Bericht 3/70-6 Kernforschungszentrum Karlsruhe, 1970.

[Hal17] D. L. Hall. *New Insights into the Limitations on the Efficiency and Achievable Gradients in Nb_3Sn SRF Cavities*. PhD thesis, Cornell University, December 2017.

[HLGM14] D. L. Hall, M. Liepe, D. A. Gonnella, and I. S. Madjarov. SRF material performance studies using a sample host cavity. In *Proceedings of the 5th International Particle Accelerator Conference*, 2014.

[HLP+17] D. L. Hall, M. Liepe, R. D. Porter, D. B. Liarte, and J. P. Sethna. Field-dependence of the sensitivity to trapped flux in Nb_3Sn. In *Proceedings of the 18th International Conference on RF Superconductivity*, 2017.

[ITK+00] H. Ino, K. Tajiri, Z. Kabeya, T. Nakamura, Y. Yamanaka, K. Yoshino, F. Naito, T. Kato, E. Takasaki, and Y. Yamazaki. Advanced copper lining for accelerator components. In *Proceedings of the 20th Linear Accelerator Conference*, 2000.

[JAB+88] C. M. Jones, G. D. Alton, J. B. Ball, J. A. Biggerstaff, D. T. Dowling, K. A. Erb, D. L. Haynes, D. E. Hoglund, E. D. Hudson, R. C. Juras, S. N. Lane, C. A. Ludemann, J. A. Martin, M. J. Meigs, S. W. Mosko, D. K. Olsen, and N. F. Ziegler. The Holyfield heavy ion research facility. *Nuclear Instruments and Methods in Physics Research Section A: Accelerators, Spectrometers, Detectors and Associated Equipment*, 268(2):308–312, 1988.

[Jac99] J. D. Jackson. *Classical Electrodynamics*. Wiley, third edition, 1999.

[KB96] F. Koechlin and B. Bonin. Parametrization of the niobium thermal conductivity in the superconducting state. *Superconductor Science and Technology*, 9(6):453–460, June 1996.

[KBC+15] R. Kephart, S. Biederon, B. Chase, S. Chattopadhyay, I. Gonin, A. Grassellino, S. Kazakov, T. Khabiboulline, S. Milton, S. Nagaitsev, R. Pasquinelli, P. Piot, S. Posen, O. Pronitchev, A. Romanenko, N. Sipahi, and V. Yakovlev. SRF, Compact Accelerators for Industry & Society. In *Proceedings of the 17th International Conference on RF Superconductivity*, page FRBA03, 2015.

[KBK+15] R. Kleindienst, A. Burrill, S. Keckert, J. Knobloch, and O. Kugeler. Commissioning results of the HZB quadrupole resonator. In *Proceedings of the 17th International Conference on RF Superconductivity*, 2015.

[KFG+16] P. N. Koufalis, F. Furuta, M. Ge, D. Gonnella, J. J. Kaufman, M. Liepe, J. T. Maniscalco, and R. D. Porter. Low temperature nitrogen baking of a SRF cavity. In *Proceedings of the 28th Linear Accelerator Conference*, 2016.

[KFKL17] P. N. Koufalis, F. Furuta, J. J. Kaufman, and M. Liepe. Impact of duration of low temperature doping on superconducting cavity performance. In *Proceedings of the 18th International Conference on RF Superconductivity*, 2017.

[KHLM16] P. N. Koufalis, D. L. Hall, M. Liepe, and J. T. Maniscalco. Effects of interstitial oxygen and carbon on niobium superconducting cavities. *ArXiv preprint*, 2016.

[KHS63] Y. B. Kim, C. F. Hempstead, and A. R. Strnad. Magnetization and critical supercurrents. *Physical Review*, 129(2):528–535, January 1963.

[Kit04] C. Kittel. *Introduction to Solid State Physics*. John Wiley & Sons Inc, 2004.

[KL18] P. N. Koufalis and M. Liepe. Insights into the role of C, N, and O introduced by low-temperature baking on niobium cavity performance. In *Proceedings of the 9th International Particle Accelerator Conference*, 2018.

[Kla06] J. P. Klason. Presentation Speech by Prof. J. P. Klason, President of the Royal Swedish Academy of Sciences, on December 10, 1906. NobelPrize.org, Nobel Media AB 2019, 1906.

[KLT57] M. I. Kaganov, I. M. Lifshitz, and L. V. Tanatarov. Relaxation between electrons and the crystalline lattice. *Soviet Journal of Experimental and Theoretical Physics*, 1957.

[KMGL19] P. N. Koufalis, J. T. Maniscalco, M. Ge, and M. Liepe. Effect of low temperature infusion heat treatements and "2/0" doping on superconducting cavity performance. In *Proceedings of the 19th International Conference on RF Superconductivity*, 2019.

[KNTS12] A. Kuzucan, H. Neupert, M. Taborelli, and H. Störi. Secondary electron yield on cryogenic surfaces as a function of physisorbed gases. *Journal of Vacuum Science & Technology A: Vacuum, Surfaces, and Films*, 30(5):051401, September 2012.

[KRB+18] S. Kwon, A. Fadavi Roudsari, O. W B. Benningshof, Y.-C. Tang, H. R. Mohebbi, I. A. J. Taminiau, D. Langenberg, S. Lee, G. Nichols, D. G. Cory, and G.-X. Miao. Magnetic field dependent microwave losses in superconducting niobium microstrip resonators. *Journal of Applied Physics*, 124(3):033903, July 2018.

[Kro03] V. F. Kroupa. *Phase Lock Loops and Frequency Synthesis*. John Wiley & Sons, 2003.

[KWS70] M. L. Kinter, I. Weissman, and W. W. Stein. Chemical polish for niobium microwave structures. *Journal of Applied Physics*, 41(2):828–829, February 1970.

[Laka] Lake Shore Cryotronics. Cernox Specifications. LakeShore.com. Accessed Aug. 13, 2019.

[Lakb] Lake Shore Cryotronics. Negative Temperature Coefficient Temperature Sensors: Is Higher Resistance Better? LakeShore.com. Accessed Nov. 23, 2019.

[LAL+08] Y.-M. Li, S. An, Z. Liping, Y. S. Cho, and P. Ylä-Oijala. Multipac 2.1 - multipacting simulation package with a 2D FEM field solver for a Microsoft Windows system. In *Proceedings of the 11th European Particle Accelerator Conference*, 2008.

[LCS12] D. N. Leonard, G. W. Chandler, and S. Seraphin. *Scanning Electron Microscopy*, pages 1–16. Wiley, 2012.

[LHK+18] D. B. Liarte, D. L. Hall, P. N. Koufalis, A. Miyazaki, A. Senanian, M. Liepe, and J. P. Sethna. Vortex dynamics and losses due to pinning: Dissipation from trapped magnetic flux in resonant superconducting radio-frequency cavities. *Physical Review Applied*, 10(5), November 2018.

[Lia] D. B. Liarte. Private communication. 2018.

[Liv75] M. S. Livingston. The History of the Cyclotron. In *Proceedings of the 7th International Cyclotron Conference*, August 1975.

[LL32] E. O. Lawrence and M. S. Livingston. The Production of High Speed Light Ions Without the Use of High Voltages. *Physical Review*, 40:19–35, April 1932.

[LL35] F. London and H. London. The electromagnetic equations of the supraconductor. *Proceedings of the Royal Society of London. Series A - Mathematical and Physical Sciences*, 149(866):71–88, March 1935.

[Lun72] S. Lundqvist. Award ceremony speech. NobelPrize.org. Nobel Media AB 2019, 1972.

[Mag] Magnetic Shield Corp. Mumetal technical data. mu-metal.com. Accessed Nov. 18, 2019.

[MAG+19] J. T. Maniscalco, T. A. Arias, M. Ge, P. N. Koufalis, D. B. Liarte, M. Liepe, J. P. Sethna, and N. Sitaraman. The field-dependent surface resistance of doped niobium: new experimental and theoretical results. In *Proceedings of the 19th International Conference on RF Superconductivity*, 2019.

[MAL+19] J. T. Maniscalco, T. A. Arias, D. B. Liarte, M. Liepe, J. P. Sethna, and N. Sitaraman. Theoretical analysis of quasiparticle overheating, positive Q-slope, and vortex losses in SRF cavities. In *Proceedings of the 10th International Particle Accelerator Conference*, 2019.

[MB58] D. C. Mattis and J. Bardeen. Theory of the anomalous skin effect in normal and superconducting metals. *Physical Review*, 111(2):412–417, July 1958.

[MCG+15] J. T. Maniscalco, B. Clasby, T. Gruber, D. L. Hall, and M. Liepe. Recent results from the Cornell sample host cavity. In *Proceedings of the 17th International Conference on RF Superconductivity*, 2015.

[MCR+18] M. Martinello, M. Checchin, A. Romanenko, A. Grassellino, S. Aderhold, S. K. Chandrasekeran, O. Melnychuk, S. Posen, and D. A. Sergatskov. Field-enhanced superconductivity in high-frequency niobium accelerating cavities. *Physical Review Letters*, 121(22), November 2018.

[MGC+16] M. Martinello, A. Grassellino, M. Checchin, A. Romanenko, O. Melnychuk, D. A. Sergatskov, S. Posen, and J. F. Zasadzinski. Effect of interstitial impurities on the field dependent microwave surface resistance of niobium. *Applied Physics Letters*, 109(6):062601, 2016.

[MGHL19] J. T. Maniscalco, T. Gruber, A. Holic, and M. Liepe. Progress towards commissioning the Cornell DC Field Dependence Cavity. In *Proceedings of the 19th International Conference on RF Superconductivity*, 2019.

[MGL17] J. T. Maniscalco, D. Gonnella, and M. Liepe. The importance of the

electron mean free path for superconducting radio-frequency cavities. *Journal of Applied Physics*, 121(4):043910, January 2017.

[MHL+16] J. T. Maniscalco, D. L. Hall, M. Liepe, O. B. Malyshev, R. Valizadeh, and S. Wilde. New material studies in the Cornell sample host cavity. In *Proceedings of the 7th International Particle Accelerator Conference*, 2016.

[MHLP17] J. T. Maniscalco, D. L. Hall, M. Liepe, and R. D. Porter. Cornell sample host cavity: recent results. In *Proceedings of 8th International Particle Accelerator Conference*, 2017.

[Mit73] K. Mittag. Kapitza conductance and thermal conductivity of copper niobium and aluminium in the range from 1.3 to 2.1 k. *Cryogenics*, 13(2):94–99, February 1973.

[MKL17] J. T. Maniscalco, P. N. Koufalis, and M. Liepe. The importance of the electron mean free path for superconducting RF cavities. In *Proceedings of the 18th International Conference on RF Superconductivity*, 2017.

[MKL18] J. T. Maniscalco, P. N. Koufalis, and M. Liepe. Modeling of the frequency and field dependence of the surface resistance of impurity-doped niobium. In *Proceedings of the 9th International Particle Accelerator Conference*, 2018.

[ML18] J. T. Maniscalco and M. Liepe. A Computational Method for More Accurate Measurements of the Surface Resistance in SRF Cavities. *Proceedings of the 9th International Particle Accelerator Conference*, 2018.

[MO33] W. Meissner and R. Ochsenfeld. Ein neuer Effekt bei Eintritt der Supraleitfähigkeit. *Naturwissenschaften*, 21(44):787–788, 1933.

[Mül87] G. Müller. Superconducting niobium in high RF magnetic fields. In *Proceedings of the 3rd International Conference on RF Superconductivity*, 1987.

[Nis11] M. Nisenoff. Microwave Superconductivity Part 1: History, Properties and Early Applications. In *2011 IEEE MTT-S International Microwave Symposium*. IEEE, June 2011.

[Nor13] Th. Nordstrom. Award ceremony speech. NobelPrize.org, Nobel Media AB 2019, 1913.

[Odh01] C. T. Odhner. Presentation Speech by the former Rector of the National Archives C. T. Odhner, President of the Royal Swedish Academy of Sciences, on December 10, 1901. NobelPrize.org, Nobel Media AB 2019, 1901.

[OGL+18] T. Oseroff, M. Ge, M. Liepe, J. T. Maniscalco, S. McNeal, R. D. Porter, and M. Sowa. Performance of samples with novel SRF materials and growth techniques. In *Proceedings of the 9th International Particle Accelerator Conference*, 2018.

[O'L15] C. O'Luanaigh. First successful beam at record energy of 6.5 TeV. `https://home.cern/news/news/accelerators/first-successful-beam-record-energy-65-tev`, April 2015. Accessed 2019-01-22.

[OMFB79] T. P. Orlando, E. J. McNiff, S. Foner, and M. R. Beasley. Critical fields, Pauli paramagnetic limiting, and material parameters of Nb3Sn and V3Si. *Physical Review B*, 19(9):4545–4561, May 1979.

[Ott15] M. R. Otto. *Low-temperature characterization of dielectric loss at microwave frequencies in aluminum oxide*. PhD thesis, University of Waterloo, 2015.

[Pad09] H. Padamsee. *RF Superconductivity*. Wiley VCH Verlag GmbH, 2009.

[PHK98] H. Padamsee, T. Hays, and J. Knobloch. *RF Superconductivity for Accelerators*. Wiley series in beam physics and accelerator technology. Wiley, New York, NY, 1998.

[Pip53] A. B. Pippard. An experimental and theoretical study of the relation between magnetic field and current in a superconductor. *Proceedings of the Royal Society of London. Series A. Mathematical and Physical Sciences*, 216(1127):547–568, February 1953.

[Ple37] H. Pleijel. Presentation Speech by Prof. H. Pleijel, Chairman of the Nobel Committee for Physics of the Royal Swedish Academy of Sciences, on December 10, 1937. NobelPrize.org, Nobel Media AB 2019, 1937.

[Pog11] N. A. Pogue. *Dielectric-loaded microwave cavity for high-gradient testing of superconducting materials*. PhD thesis, Texas A&M University, May 2011.

[Por19] R. D. Porter. T-mapping, B-measurements and vertical diagnostics at Cornell. In *TESLA Technology Collaboration Meeting*, February 2019. `https://indico.desy.de/indico/event/21337/session/5/contribution/69`.

[Pro12] D. Proch. Multipacting. In A. W. Chao, K. H. Mess, M. Tigner, and F. Zimmermann, editors, *Handbook of Accelerator Physics and Engineering*, chapter 6.9. World Scientific, second edition, May 2012.

[RC97] P. Rai-Choudhury, editor. *Handbook of Microlithography, Micromachining, and Microfabrication. Volume 1: Microlithography*. SPIE Press, 1997.

[RECS13] A. Romanenko, C. J. Edwardson, P. G. Coleman, and P. J. Simpson. The effect of vacancies on the microwave surface resistance of niobium revealed by positron annihilation spectroscopy. *Applied Physics Letters*, 102(23):232601, June 2013.

[RG11] A. Romanenko and L. V. Goncharova. Elastic recoil detection studies of near-surface hydrogen in cavity-grade niobium. *Superconductor Science and Technology*, 24(10):105017, September 2011.

[RGBO13] A. Romanenko, A. Grassellino, F. Barkov, and J. P. Ozelis. Effect of mild baking on superconducting niobium cavities investigated by sequential nanoremoval. *Physical Review Special Topics - Accelerators and Beams*, 16(1), January 2013.

[ROLL+94] S. Revenaz, D. E. Oates, D. Labbé-Lavigne, G. Dresselhaus, and M. S. Dresselhaus. Frequency dependence of the surface impedance ofYBa2cu3o7-δthin films in a dc magnetic field: Investigation of vortex dynamics. *Physical Review B*, 50(2):1178–1189, July 1994.

[RS48] G. E. H. Reuter and E. H. Sondheimer. The theory of the anomalous skin effect in metals. *Proceedings of the Royal Society of London. Series A. Mathematical and Physical Sciences*, 195(1042):336–364, December 1948.

[SAC+18] N. Solyak, S. Aderhold, S. K. Chandrasekaran, E. Harms, T. Khabiboulline, A. Lunin, C. Grimm, O. Prokofiev, and G.Wu. Design and

test results of the 3.9 GHz cavity for LCLS-II. In *Proceedings of the 9th International Particle Accelerator Conference*, 2018.

[Saf01] H. Safa. High field behavior of SCRF cavities. In *Proceedings of the 10th International Conference on RF Superconductivity*, 2001.

[SDR92] N. J. Simon, E. S. Drexler, and R. P. Reed. *Properties of Copper and Copper Alloys at Cryogenic Temperatures*. National Institute of Standards and Technology (NIST), 1992.

[Sgo11] S. Sgobba. Physics and measurements of magnetic materials. March 2011.

[Sie39] K. M. G. Siegbahn. Award ceremony speech. NobelPrize.org, Nobel Media AB 2019, 1939.

[Sin14] W. Singer. SRF cavity fabrication and materials, 2014.

[SM86] S. Sridhar and J. E. Mercereau. Nonequilibrium dynamics of quasiparticles in superconductors. *Physical Review B*, 34(1):203–216, July 1986.

[SPP95] E. Somersalo, P.YläiOijala, and D. Proch. Analysis of multipacting in coaxial lines. In *Proceedings of the 18th Particle Accelerator Conference*, 1995.

[SR35] C. J. Smithells and C. E. Ransley. The diffusion of gases through metals. *Proceedings of the Royal Society of London. Series A - Mathematical and Physical Sciences*, 150(869):172–197, May 1935.

[SZY84] F. W. Sears, M. W. Zemansky, and H. D. Young. *University Physics, Part II*. Addison-Wesley, 1984.

[TCS11] M. K. Transtrum, G. Catelani, and J. P. Sethna. Superheating field of superconductors within Ginzburg-Landau theory. *Physical Review B*, 83(9), March 2011.

[TGK+09] A. V. Timofeev, C. Pascual García, N. B. Kopnin, A. M. Savin, M. Meschke, F. Giazotto, and J. P. Pekola. Recombination-limited energy relaxation in a bardeen-cooper-schrieffer superconductor. *Physical Review Letters*, 102(1), January 2009.

[TGMR15] Y. Trenikhina, A. Grassellino, O. S. Melnychuk, and A. Romanenko. Characterization of nitrogen doping recipes for the Nb SRF cavities. In *Proceedings of the 17th International Conference on RF Superconductivity*, 2015.

[Tin04] M. Tinkham. *Introduction to Superconductivity*. Dover Publications Inc., 2004.

[Tör03] H. R. Törnebladh. Presentation Speech by Dr. H. R. Törnebladh, President of the Royal Swedish Academy of Sciences on December 10, 1903. NobelPrize.org, Nobel Media AB 2019, 1903.

[Val14] N. R. Valles. *Pushing The Frontiers Of Superconducting Radio Frequency Science: From The Temperature Dependence Of The Superheating Field Of Niobium To Higher-Order Mode Damping In Very High Quality Factor Accelerating Structures*. PhD thesis, Cornell University, January 2014.

[Vel87] V. F. Veley. *Modern Microwave Technology*. Prentice-Hall, 1987.

[VKFS19] R. D. Veit, N. A. Kautz, R. G. Farber, and S. J. Sibener. Oxygen dissolution and surface oxide reconstructions on Nb(100). *Surface Science*, 688:63–68, October 2019.

[VXP07] J. Vines, Y. Xie, and H. Padamsee. Systematic trends for the medium field Q-slope. In *Proceedings of the 13th International Conference on RF Superconductivity*, 2007.

[Wal51] I. Waller. Presentation Speech by Prof. I. Waller, member of the Nobel Committee for Physics. NobelPrize.org, Nobel Media AB 2019, 1951.

[WBP16] M.St. Węglowski, S. Błacha, and A. Phillips. Electron beam welding – Techniques and trends – Review. *Vacuum*, 130:72–92, August 2016.

[Wei] E. W. Weisstein. Polylogarithm. `http://mathworld.wolfram.com/Polylogarithm.html`. From *MathWorld*–A Wolfram Web Resource. Accessed 2019-11-05.

[Wei18] W. Weingarten. N-doped surfaces of superconducting niobium cavities as a disordered composite. *IEEE Transactions on Applied Superconductivity*, 28(6):1–4, September 2018.

[Wid28] R. Wideröe. Über ein neues Prinzip zur Herstellung hoher Spannungen. *Archiv für Elektrotechnik*, 21(4):387–406, July 1928.

[Wie15] H. Wiedemann. *Particle Accelerator Physics*. Springer, fourth edition, 2015.

[Wil96] E. J. N. Wilson. Fifty years of synchrotrons. In *Proceedings of the 5th European Particle Accelerator Conference*, 1996.

[WMMS89] J. O. Willis, M. E. McHenry, M. P. Maley, and H. Sheinberg. Magnetic shielding by superconducting Y-Ba-Cu-O hollow cylinders. *IEEE Transactions on Magnetics*, 25(2):2502–2505, March 1989.

[WTW10] C. A. Walker, F. R. Trowbridge, and A. R. Wagner. Direct brazing of sapphire to niobium. *Welding Journal*, 89:50–55, March 2010.

[Xie13] Y. Xie. *Development of Superconducting RF Sample Host Cavities and Study of Pit-Induced Cavity Quench*. PhD thesis, Cornell University, January 2013.